APPLIED AXIAL MAGNETIC FIELD EFFECTS ON EXTENDED MAGNETOHYDRODYNAMICS LABORATORY PLASMA JETS: EXPERIMENTS AND SIMULATIONS

A Dissertation

Presented to the Faculty of the Graduate School

of Cornell University

in Partial Fulfillment of the Requirements for the Degree of

Doctor of Philosophy

by

Tom Byvank

May 2018

APPLIED AXIAL MAGNETIC FIELD EFFECTS ON EXTENDED MAGNETOHYDRODYNAMICS LABORATORY PLASMA JETS: EXPERIMENTS AND SIMULATIONS

Tom Byvank, Ph.D.

Cornell University 2018

Laboratory experiments can help validate and benchmark computer simulations. This laboratory plasma jet research focused on characterizing and quantifying the effects of extended magnetohydrodynamics (XMHD) and an externally applied axial magnetic field (B_z). In the present research, plasma jets were formed from Joule heating and ablation of radial foils (approximately 15 μm thin circular disks) using a pulsed power generator (COBRA) with 1 MA peak current and 100 ns rise time. Plasma dynamics of the jet were diagnosed under a change of current polarities, which correspond to current moving either radially outward or inward from the foil's central axis. The influence of the Hall effect on the jet development was observed under opposite current polarities, which changed the jet conical structure (width and angle). Additionally, we studied the effects on jet dynamics resulting from varying the B_z from 0 to 2 T. The plasma jet formation compressed the B_z as the plasma converged toward the central z-axis. The pressure from the B_z compression led to on-axis density hollowing of the jet. Experimental measurements of this compression were made using dB/dt (or "B-dot") magnetic probes placed in the center of the hollow plasma jet. Additionally, we found that the plasma jet formation disrupted from the ablating foil surface with a large enough applied B_z, meaning the jet was no longer well-collimated but was ejected as multiple bursts of plasma. We

observed that the critical B_z for disruption depended upon the foil material (Al, Ti, Ni, Cu, Zn, Mo, W) and correlated with material properties of the foil such as the electrical resistivity and equation of state. Experimental results were compared with predictions made by XMHD numerical simulations (PERSEUS). This study of 1) the Hall effect, 2) applied magnetic field effects, and 3) the process of foil ablation permitted further understanding of fundamental physics topics including 1) the importance of low-density plasmas within high-density plasma environments, 2) how magnetic forces influence plasma dynamics, and 3) the impact of material properties during transitions from the solid through plasma phases.

BIOGRAPHICAL SKETCH

Tom Byvank was born on May 7, 1990 at 10:52 pm on planet Earth. He weighed 5 pounds 12 ounces and was 19 inches long. It is now 2018, and Tom weighs more and is taller. Between 1990 and 2018, Tom went to school, did some other things, and did not do many other things. The questions "why?" and "how?" spawned Tom's interest in science. Dublin Coffman High School delivered Tom in its graduating class of 2008. Tom studied physics and astronomy at Ohio State and graduated in 2012 with various specifications, acronyms, and Latin words. Afterward, Tom went to Oak Ridge National Lab for an internship, and then he went to graduate school at Cornell from 2013 to 2018. That last part is what this document is about.

After grad school, life will continue, filled with uncertainty as always. Tom will try his best to contribute more goodness to the world than badness. He will try to create more positivity in this world than negativity– and, who knows, maybe even controlled nuclear fusion.

A Ballad to COBRA

by Tom Byvank

Working in the lab
of plasma studies,
fun is up for grabs,
just you wait and see.

Come clean the rings
of the mighty COBRA.
As you wipe, sing
"what a great aroma."

Choose your hardware,
wires, puffs, foils, or more.
What do you dare?
Challenges are in store.

Set up diagnostics.
Wear your laser goggles.
Adjust mirrors and optics,
do not just boondoggle.

XUV cameras tilt or straight,
interference patterns shear,
spectroscopy calibrates.
Did you forget something, you fear.

When hardware you remove,
beware the A-K gap.
Dexterity you prove,
else create a mishap.

Think, are O-rings greased?
Start the vacuum pump,
now drink tea in peace
or go take a dump.

Crossover to cryos,
check delay timings,
your lab notebook will grow,
shot soon approaching.

Turn on high voltage,
note pressure in torr.
Get reference laser image,
that's what the preshot is for.

Apply gas pressures,
set screen room and scopes,
stop oil and water.
Now build up your hope.

TG on and Arm,
HV on, TG-70,
max voltage no harm,
currents are falling.

Science is now on the verge,
count down 3, 2, 1, fire,
hear COBRA's roar and discharge
to get the shot you desire.

Acquire current traces,
circulate and debubble,
success in this case,
but will the next shot be trouble?

Reload and repeat.
A run on COBRA
is always a treat,
the joy of plasma.

Fusion fifty years away,
fifty years ago that was.
Please oh please do not dismay,
else be trapped in COBRA's jaws.

ACKNOWLEDGEMENTS

Some thanks are in order for this lucky life that I've been awarded, currently containing no famine, genocide, nor defenestration...

First of all, if you are reading this (and not by mistake), thank you.

Thanks to Mr. David Scott for introducing me to physics and for infecting me with whatever it is that still makes me enjoy this mysterious topic. Hopefully there is no cure for this enthusiasm.

Thanks to Dr. Ratnasingham Sooryakumar (Dr. Soory) for his guidance, support, introduction to research, and opportunities to let me explore.

Thanks to a teaching assistant (whose name I forget) in my undergrad differential equations class for reminding me that, in school, I will never learn anything more important than what I already learned by the time I was a kid (paraphrasing): how to travel on a bus (or live in daily life) without actively hurting anyone else, no matter what the other person looks like or their beliefs.

Thanks to Dr. Boyd Evans and Dr. Orlando Rios for their guidance and for the opportunity to continue learning to become a scientific researcher.

Thanks to Dr. Otto Octavius for his inspiration to study plasma physics and fusion.

Thanks to Dr. Pat Knapp and Dr. Matt Martin for letting me have fun checking out Sandia National Labs and New Mexico over the summer (2016).

Thanks to Dr. Dave Hammer for introducing me to the Lab of Plasma Studies, for teaching by example the importance of networking, and for his nuclear fusion course that simultaneously provided me with realism, pessimism, and hopeful conviction.

Thanks to my committee member, Dr. Michael Thompson, for his support with my materials science minor.

Thanks to my committee member, Dr. Charlie Seyler, for his patience and helpfulness in building some of my intuition about plasma physics. In particular, I am extremely grateful for his guidance in letting me play around with the PERSEUS code to support my experiments.

Thanks to my advisor, Dr. Bruce Kusse, for his meticulous questioning to understand the fundamental physics of complex phenomena, for encouragement to follow my interests, for dedication to his students (for both research and teaching), and for his sense of humor.

Thanks to the National Nuclear Security Administration (NNSA) Stewardship Sciences Academic Programs under Department of Energy (DOE) Cooperative Agreement DE-NA0001836, DE-NA0003764, and the National Science Foundation (NSF) Grant PHY-1102471 for supporting this research and for letting me travel to California, Louisiana, New Mexico, Turkey, Georgia (USA), Maryland, Canada, California again, Illinois, New Jersey, Nevada, Wisconsin, Maryland again, and also back to New York.

Thanks to all of the people I've interacted with in the Lab of Plasma Studies who made my grad school "work" entertaining, including but not limited to: Levon Atoyan, Jacob Banasek, Todd Blanchard, Adam Cahill, Dillan Chang, Joey Engelbrecht, Pierre Gourdain, John Greenly, Phil de Grouchy, Jason Hamilton, Nat Hamlin, Dan Hawkes, Cad Hoyt, Billy "Laser Doctor" Potter, Sophia "The Rock" Rocco, Peter Schrafel, Cindy VanOstrand, and Harry Wilhelm. Also, I want to thank Harry Wilhelm again for being a wizard in the lab, for being generally awesome, and for harnessing his inner mongoose to subdue the COBRA.

Thanks to everyone in the boxing club at Cornell for giving me a consistent outlet to relieve mental stress and for punching me in the face. Hakuna matata.

Thanks to my housemate and friend Ben Dolata (who is pretty metal) for be-

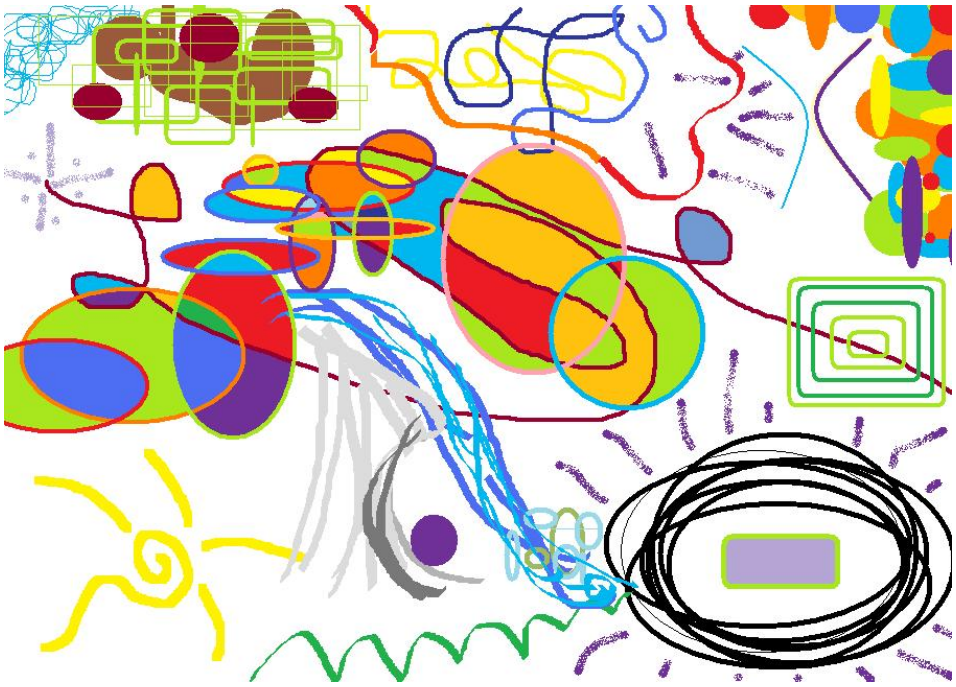

Figure 1: A present. B. Shrefler, 2011.

ing in the same general area as me for about 4 years and for his strange sense of humor. I still remember that time you bought all that stuff. While it's true that, in the end, the certainty of death invalidates everything, I have seen occasional glimpses of light and love within this dark abyss.

Thanks to my family for their encouragement, support, and love. In particular, thanks to my parents for letting me take them for granted. Even if I don't say it as much as I should, I love you. Thanks to my grandpa "Bakka" for being a role model of how to live a life filled with love and compassion. Thanks to my friends for being my friends. That's actually really important. Among many other people, thanks to my undergrad roommates Chris Cannizzaro, Kevin Rhodus, and Hok Hei Tam for their camaraderie and for helping me live in life rather than just survive. Thanks to my friend Brittany Shrefler for her optimism, hope, and for being inspirationally authentic in a way that challenges my life perspective (see Fig. 1).

TABLE OF CONTENTS

LIST OF TABLES

LIST OF FIGURES

CHAPTER 1

NONTECHNICAL SUMMARY

This section of the thesis is mom-approved for conceptual understanding.

My research area is "high energy density plasma physics" and, in particular, creating the plasma by using "pulsed power generators." Those are a lot of complicated words when mashed together, so here is a better description of my research.

All of the materials that you see are made of atoms. An atom is made of a nucleus at the center surrounded by electrons. A nucleus has a positive electric charge, and electrons have negative electric charge. The total electric charge of an atom is zero, meaning the atom is charge neutral. When enough energy is applied to a solid material, it can change into a liquid and then a gas. The atoms in solids, liquids, and gases are charge neutral. When even more energy is applied, the electrons can separate from the nucleus in the atom. Without some of the negatively charge electrons in the atom, the atom becomes positively charged and is called an ion.

A plasma is the energetic state of matter (like solid, liquid, or gas) that has these separated electrons and ions moving around. The word "plasma" was named analogously to blood plasma, which has red blood cells moving within the fluid. Some common examples of plasmas are the Sun, lightning, and neon signs. The Sun contains nuclear reaction explosions that exist as a plasma. A lightning strike is an electrical spark (discharge) between a cloud and the ground. Neon lighting tubes light up from electrical discharges within the neon gas.

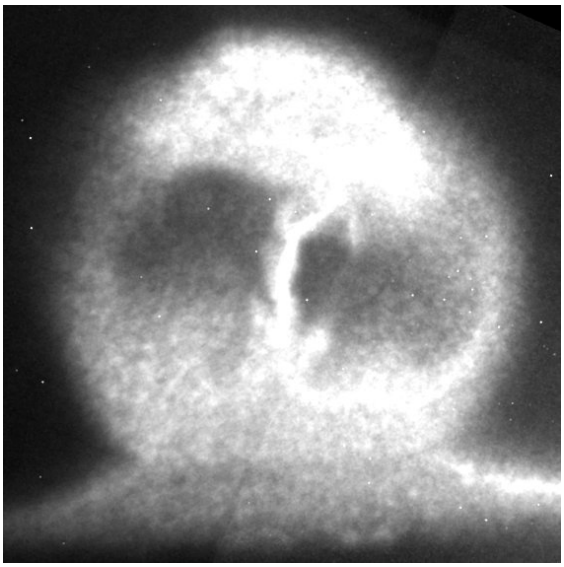

Figure 1.1: Optical self emission of shot 3585 at time t = 265 ns after the start of current rise.

Electrically charged particles (like ions and electrons) experience forces from electric and magnetic fields. These forces are why lightning strikes occur, why batteries provide electrical energy, and why compasses point North. In a plasma, the electric and magnetic forces act on the ions and electrons, and the moving charged particles can also create and modify the electric and magnetic forces. The interaction between the charged particles and the electric and magnetic forces leads to complicated behavior of the plasma. This complicated plasma behavior makes for some interesting scientific problems.

In my research, we send an electrical current through a piece of metal foil (like Reynolds Wrap Aluminum Foil). The energy passing through the foil causes the foil to heat up, explode, and create a plasma. The goal of my research is to understand what happens to this plasma under various conditions. Fig. 1.1 is a picture of one of my laboratory experiments that shows a plasma

similar to a lightning strike being formed.

To get an idea of how much energy we use to create the plasma, here are some comparisons. We send 100 kJ of energy through our plasma-generating-machine in a timespan of a few hundred nanoseconds. 100 kJ of energy is the same energy as 24 food Calories (about one milk chocolate Hershey's Kiss). A few hundred nanoseconds is more than a million times faster than the blink of a human eye. Luckily, your metabolism takes a lot more time to process your 24 Calories of food, so you don't explode. For your reference, the average total worldwide power consumption is about $20 * 10^9$ kJ per second, or only about 20 times larger than the energy produced by our plasma-generating-machine in the same amount of time. Additionally for a comparison, a lightning strike discharges about 10^6 kJ of energy in about a millionth of a second, or about one thousand times more energy than our plasma-generating-machine in the same amount of time. Lastly, as a final comparison, the Sun outputs about $4 * 10^{23}$ kJ of energy in one second, or about four trillion (four-million-million) times more energy than our plasma-generating-machine in the same amount of time.

Why should we care about my research to understand laboratory plasmas? Why should we care about creating plasmas in the laboratory? As previously mentioned, the Sun is an amazing plasma explosion. In astronomy, there are many other interesting objects, and many of these objects are also plasmas. We can only observe those objects from here on Earth, and that can make it difficult to understand why certain processes behave the way they do. We can't do full-scale "astronomy experiments" here on Earth, but the goal of a research area called "Laboratory Astrophysics" is to create situations in the laboratory that allow us to study the same physics as that which occurs on astronomical scales.

In my research, I study laboratory plasma jets, which are relevant to astrophysical plasma jets. A plasma jet is a collimated flow of plasma (meaning particles move in a parallel direction), like how a water jet is a collimated stream of water (like what comes out of a firehose). Astrophysical plasma jets are formed in many contexts, including outside of black holes. As matter is falling into a black hole, some of the matter is ejected away from the black hole at its North and South poles. These ejections of matter are plasma jets. There are still many unanswered questions as to why and how astrophysical plasma jets exist and develop. The goal of my research is to study plasma jets that are created in the laboratory to help understand the physics of why certain processes happen.

Another goal of plasma physics research is to help make controlled nuclear fusion a sustainable energy source. Currently, nuclear power plants use a process called nuclear fission that produces a lot of radioactive waste. In contrast, nuclear fusion reactions do not produce this radioactive waste as a byproduct. However, nuclear fusion power plants are currently not used because controlling the fusion reactions is very challenging. One goal of plasma physics research is to understand the reasons why fusion is so difficult and hopefully work toward solving the problems. My research of laboratory plasma jets will not create controlled nuclear fusion in the laboratory, but it can help to better understand some of the processes that occur. This better understanding can help solve some of the challenges of fusion, but I'm not making any promises for fusion power plants in the near future.

CHAPTER 2

MOTIVATION

2.1 Does Size Matter?

Laboratory Astrophysics

The idea behind Laboratory Astrophysics is that, given similar scaling relations and dimensionless quantities, laboratory experiments can be used to study the same physics as that which occurs on astronomical scales. [1, 2, 3, 4, 5] Astrophysical phenomena are much larger than any experiments conducted on Earth, but, if their geometry is similar and the controlling physical processes are in the same regimes, laboratory experiments can accurately describe the physics of the astronomical events. Furthermore, even if a laboratory experiment cannot fully replicate an astrophysical phenomena, the experiment can still explore parts of the physical processes. Consider the following terrestrial example of a laboratory experiment describing a larger system: designing an airplane by testing a model in a wind tunnel. The model can describe the airplane dynamics as long as both systems have similar conditions including the Mach number M, Reynolds number Re, and proportionally scaled geometric dimensions. In astrophysics, some additional scaling parameters that may impact the system dynamics include the magnetic Reynolds number R_M and Peclet number Pe.

We note that, for certain comparisons, the dimensionless numbers do not have to be exactly the same but just in the same regime; for example, a Reynolds number Re $\ll 1$ is in the laminar flow regime, and Re $> 10^4$ is in the turbulent flow regime, so a laboratory system with Re $= 10^5$ could have similar dynam-

ics to an astrophysical system with Re $= 10^8$. However, if other processes are important in the astrophysical system, like radiation effects for example, then a laboratory experiment with a similar Reynolds number but not a similar radiative cooling parameter $\chi_{rad} = t_{rad}/t_{hydro}$ (the ratio of radiative to hydrodynamic timescales) will not accurately describe the astrophysical phenomena. As previously mentioned, laboratory experimental scales are smaller than astrophysical spatial scales. Gravity is fundamental in the formation of many astrophysical bodies, and gravity is negligible in the formation of laboratory plasmas evolving over nanosecond timescales. Although gravity may be the fundamental cause of an astrophysical process, it may not be significantly important to the dynamics, in which case a laboratory experiment can still accurately correspond with the astrophysical event. An object's length scale may also be important for certain phenomena besides gravity like the Hall effect, as will be further discussed in Sec. 7.1.2. Lastly, we caution that if a laboratory experiment looks (morphologically) similar to an astrophysical process, that does not mean that the experiment provides useful information about the process; both phenomena must be in similar physical regimes.

The word ubiquitous is ubiquitously used to describe the astrophysical contexts in which plasma jets appear. The most basic definition of a jet is a collimated outflow. Astrophysical jets can form from geysers on comets, solar spicules in the chromosphere, stellar accretion disks, and radio galaxy nuclei. [6, 7, 8, 9] The plasma jet we create in the laboratory is approximately 1 cm long. Table 2.1 displays estimated parameters comparing our laboratory plasma jet (created on the COBRA pulsed power generator) with a laboratory experiment of "plasma at critical density in a modest-temperature hohlraum" on the Z machine (a pulsed power generator at Sandia National Laboratory) and astrophys-

Table 2.1: Laboratory Astrophysics Parameter Comparisons

Object	COBRA jet	Z exp	YSO jet	NS acc col	HH 110 jet
Size	1 cm	0.1 cm	$10^{16} - 10^{19}$ cm	$4 * 10^4$ cm	$7.5 * 10^{15}$ cm
M	1.5	1	10-50	40	30
Pe	4.4	10^{-2}	10^{11}	80	10^5
Re	$3.2 * 10^5$	$3 * 10^4$	10^{13}	$6 * 10^8$	10^5
R_M	3.5	$5 * 10^2$	10^{15}	$5 * 10^{13}$	n/a
β	10	30	1-10	$3 * 10^{-8}$	n/a
χ_{rad}	10^{-2}	0.5	n/a	$2 * 10^{-5}$	n/a

ical systems: a jet from a young stellar object (YSO), a neutron star (NS) accretion column, and a jet from Herbig-Haro (HH) object 110. [10, 11, 12, 13] See Appendix A for parameter calculations for our laboratory jet, other than the radiative cooling parameter χ_{rad} which is calculated by dividing thermal energy by radiative power loss (estimated using blackbody emission of a $\sim 1\ cm^3$ region).

Our laboratory jet is ejected from a disk of solid material (radial foil) that, given the right conditions, can look like a rotating accretion disk (see Fig. 2.1). However, the laboratory foils and astrophysical accretion disks have completely different physical mechanisms for looking similar– rotation due to the Lorentz force in radial foils rather than angular momentum conservation from gravitational collapse in accretion disks. Still, our laboratory plasma jets may be relevant to the physics of astrophysical jet formation, collimation, and propagation. In our research, we study the influence of an external magnetic field on laboratory jets that could provide information into how magnetic fields interact with and are embedded into astrophysical jets.

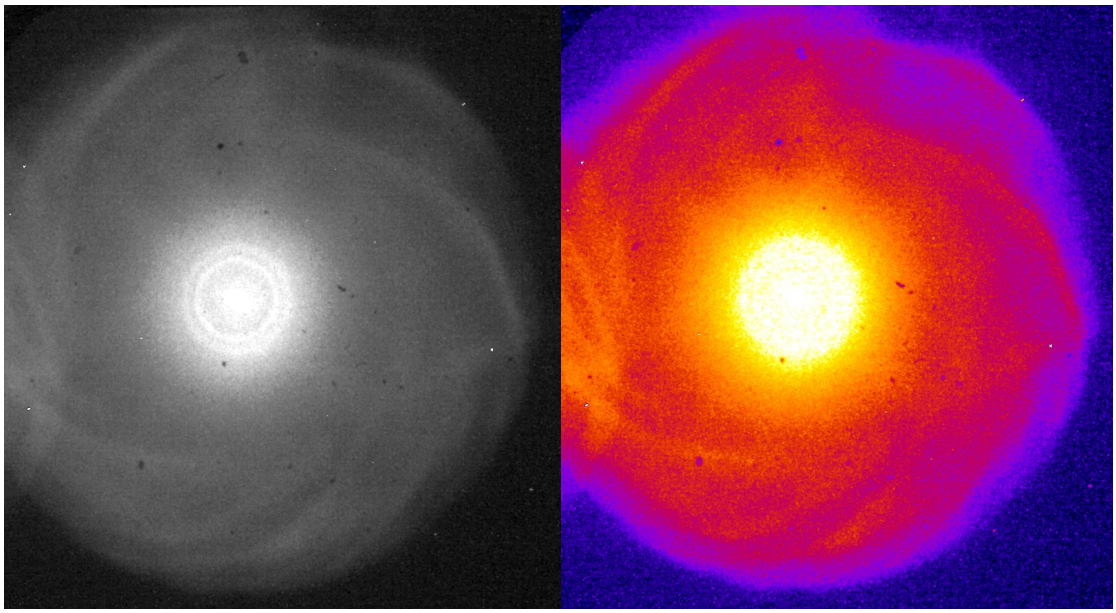

(a) (b)

Figure 2.1: Extreme ultraviolet self emission looking down onto the radial foil in a) grayscale and b) a "fire" colorscale. Shot 3698 at 150 ns after the start of current rise.

2.2 Zeros and Ones:

Benchmarking Computer Codes

"Experiments have perfect physics and imperfect diagnostics; simulations have imperfect physics and (can) have perfect diagnostics," to paraphrase John Greenly, personal communication, 2016 or so. Comparing experiments with numerical simulations helps uncover the important physical processes when trying to understand a phenomena. Experiments can help determine incorrect approximations, assumptions, or physical implementations in a simulation. Computer codes can suggest possible directions for experimental campaigns. "Good enough" numerical simulations may even be able to accurately predict what will happen in experiments. For example, "good enough" simulations of nuclear weapon explosions can permit detailed scientific understanding without

needing to actually explode nuclear bombs. When experiments and simulations do not agree, there is an opportunity for a deeper understanding of the physics involved.

We compare our plasma jet laboratory experiments with numerical simulations using the code PERSEUS (an acronym standing for: Plasma as an Extended-MHD Relaxation System using an Efficient Upwind Scheme). [14] One discovery that PERSEUS has helped demonstrate is how low density plasma can influence regions of high density plasma. Often in high energy density physics, researchers approximate that certain effects that are important in low density regions can be ignored; however, these effects can influence the high density regions as well, particularly when the high density regions are created by merging the initially low density plasma. One example of such an effect is the Hall effect (different in a plasma than in a solid), which both the PERSEUS code and laboratory jet experiments show drastically influences the plasma dynamics in the higher density regions. The higher density laboratory jet is formed from converging lower density regions.

2.3 Blowing Stuff Up:

Plasma Instabilities and Ablation Physics

Plasmas are dynamic phenomena that often display instabilities. For well-controlled and contained systems, like those hoped to be used for sustainable nuclear fusion reactions, plasma instabilities must be mitigated. In the laboratory, plasmas can be produced by energizing initially solid materials. The process going from a solid to plasma phase usually involves the ablation pro-

cess: heating, melting, vaporizing, and ionizing. The details of a material's conductivity and equation of state as it transitions from solid to liquid, vapor, and plasma phases can fundamentally affect the dynamics of the plasma. This dynamic process of ablation physics may closely relate to instability growth. Additionally, moving from relatively-low-energy solids to high-energy plasmas passes through the regime of warm dense matter physics– a regime that can be experimentally hard to diagnose and computationally challenging to model. [15]

We study the ablation physics of the radial foils used to generate the plasma jets. We also study plasma instabilities that occur on the foil and in the jet, in particular when we apply an axial magnetic field. In this research, the applied magnetic field is perpendicular to the direction of current flow, and it fundamentally affects the foil's surface plasma formation and further instability growth. The hope is that continuing to better understand instabilities can lead to the ability to better control and mitigate them (most optimistically for applications like controlled nuclear fusion).

CHAPTER 3

CONTEXT

3.1 High Energy Density Physics

The frontier of high energy density physics pushes the limits of how much energy can be put into an area within a certain (short) amount of time. The extreme state of high energy density matter produces some extreme numbers. High energy density can mean obtaining pressures over one million times the Earths atmospheric pressure, temperatures of millions of degrees Celsius, and densities of tens of times typical solid densities. Furthermore, these extreme conditions usually occur over short timescales on the scale of billionths of a second (read: they explode), and deposition of large energies in a short time lead to extremely large instantaneous power outputs that can reach over ten times the worldwide power consumption. [16]

General goals of high energy density physics research include studying: material properties like degenerate matter and radiation production, astrophysics like planetary interiors and solar phenomena, relativistic conditions like particle acceleration, and inertial confinement fusion for energy production. Additionally, high energy density physics can support national security through stockpile stewardship and weapons testing. High energy density physics can also explore fundamental physics including nonlinear effects, magnetic field generation, hydrodynamics, and material equations of state.

3.2 Pulsed Power

Obtaining high energy density states of matter requires energy deposition within a short amount of time. Two prominent methods of achieving this large power are using 1) pulsed power generators and 2) lasers. Pulsed power generators collect energy over relatively large timescales (say, minutes) and discharge it rapidly (say, within a couple hundred nanoseconds). The energy can be stored by capacitors in Marx generators or linear transformer drivers. Pulsed power is one of the most energy efficient methods to produce a large power output. Lasers can create high energy density conditions by irradiating matter. Some characteristics of the required laser are "good enough" energy, power, intensity, irradiance, and beam quality (uniformity).

Experiments conducted using pulsed power generators rather than lasers can have different geometries that permit diagnostic access of larger spatial scales (centimeters rather than millimeters of plasma) and longer time scales (hundreds of nanoseconds rather than a few nanoseconds) to more easily observe the evolution of plasma dynamics. Conversely, experiments conducted using (fast-pulse) lasers rather than pulsed power can probe smaller spatial scales (resolving hundreds of nanometers) and shorter time scales (resolving tens of femtoseconds) in order to investigate plasma phenomena including waves and laser-plasma interactions. The author would like to note that pulsed power and laser experiments are not mutually exclusive, although it is true that most facilities focus on only one method of obtaining high energy density conditions.

3.3 Radial Foils

One use for a pulsed power machine's current is to create a Z pinch. [17, 18, 19, 20] Typically in a Z pinch, an electrical connection between the anode and cathode permits an axial current ($J = J_z$) to flow and self-generate an azimuthal magnetic field ($B = B_\theta$) thanks to Ampere's Law. The Lorentz force ($J \times B$) acts radially inward and "pinches" the current-carrying load. This pinching implosion can create large energies, pressures, and x-ray bursts– assuming that instabilities (such as the Magneto-Rayleigh-Taylor instability, an arch-nemesis of the Z pinch) do not significantly degrade the implosion.

The electrical power load hardware of a pulsed power generator supports various geometries. Vertically (axially) spanning the anode and cathode electrodes, researchers can place wire arrays, liners (cylindrical tubes), planar foils, and gas puffs. These loads can implode as a Z pinch described above. Rather than orient the anode and cathode axially, loads can radially connect the electrodes, as in radial wire arrays or radial foils. Here, one of the electrodes is placed at the center of the load hardware (as a pin beneath the foil on-axis) and the other electrode is set as an outer annulus. In radial foil experiments, a thin circular disk spans and electrically connects the pin and annulus electrodes. The current flows radially through the foil and axially through the center electrode pin. The current Ohmically heats the foil; melts, vaporizes, and ablates the solid foil; and produces a surface plasma above the foil. The axial current through the center pin self-generates an azimuthal magnetic field. Thereby, $J \times B$ forces act upward and inward, creating a collimated flow of plasma on-axis above the foil– a plasma jet.

At Imperial College London, using the pulsed power generator MAGPIE (the Mega Ampere Generator for Plasma Implosion Experiments [21]), and at Cornell University, using the pulsed power generator COBRA (COrnell Beam Research Accelerator [22]), researchers using radial foils and radial wire arrays have investigated numerous phenomena, including: X-ray production from magnetic bubbles, plasma jet interactions with an ambient medium, jet contact with a target, effects of radiative cooling, the impact of the Hall effect, and effects of applied dynamic and uniform magnetic fields. [23, 24, 25, 26, 27, 28, 29, 30, 31, 32, 33, 34, 35, 36, 37, 38, 39, 40, 41, 42, 43, 44, 45, 46, 47]

CHAPTER 4

OVERVIEW

4.1 Questions Explored

This laboratory plasma jet research focuses on characterizing and quantifying the effects of extended magnetohydrodynamics (XMHD) and an externally applied axial magnetic field (B_z). We compare experimental results with numerical simulations using the XMHD code, PERSEUS. Experimentally, we investigate Hall physics– an XMHD effect– by changing the direction of current flow through the foil hardware, and we find differences in the jet dynamics and structure depending upon the current direction (current polarity). We explore how the applied B_z affects on-axis density hollowing of the jet (using interferometry), on-axis compression of the applied B_z (using magnetic dB/dt or "B-dot" probes), and azimuthal rotation of the jet and background plasma. In order to measure the azimuthal rotation of the jet, we use Thomson scattering; from those experiments, we observe an interaction between the probing laser and the plasma jet. Additionally, we consider what happens when we vary the magnitude of the applied B_z. We find that the plasma jet formation disrupts from the foil surface with a large enough applied B_z, meaning the jet is no longer well-collimated but is ejected as multiple bursts of plasma. We examine how varying the center pin diameter, foil thickness, and foil material influences the disruption of the plasma jet and of the ablating surface plasma.

4.2 Answers Uncovered

Both experiments and the PERSEUS extended magnetohydrodynamics (XMHD) code show differences in jet structures under a change in current polarities, while an MHD code shows identical jets. These polarity differences are particularly noticeable with an applied B_z. Reverse current polarity jets are wider, have a larger conical angle, and have more on-axis density hollowing than standard current polarity jets. The jet structure is determined by an approximate radial force balance between competing dynamical (ram) pressures, thermal pressures, and magnetic pressures. Additionally, we observe polarity effects (i.e. anode-cathode asymmetries) of the current filamentation that forms on the radial foil surface. The addition of the Hall term in the Generalized Ohm's Law permits the XMHD code to be more accurate than an MHD code.

As the plasma converges toward the central axis to form the jet, the plasma compresses the applied B_z. In both experiments and simulations, we find larger B_z compression at a height closer to the foil surface compared to higher up. Simulations predict a larger peak B_z compression than what is measured in the experiments (other than one case, for a Ti foil and a 0.7 T B_z). Simulations show compression starting earlier in time than in the experiments. Furthermore, simulations show a decrease in B_z strength at late enough times, but the experiments do not show this decrease and the compression measurements become questionably-reliable at late enough times. Both simulations and experiments show the same trend of a larger change in B_z (peak value minus initial value) for a smaller initial B_z. We also consider the effects on B_z compression of the current pulse shape, current polarities, the probe conductor, 2D vs 3D effects,

and foil materials. Differences between simulations and experiments are larger than the estimated experimental measurement uncertainty of $\sim$10%. Considering discrepancies between experiments and simulations can allow for better understanding of the physical effects involved in the plasma dynamics.

Applying the B_z creates a $J_r B_z$ component of the $\mathbf{J} \times \mathbf{B}$ force that causes azimuthal rotation of the plasma (of both the background plasma and of the plasma jet that is formed by the converging background plasma). Measurements of this rotation were conducted by other graduate students using optical spectroscopy and Thomson scattering (with my support, for the latter). When using the 10 J laser for Thomson scattering, the laser can interact with the plasma jet by heating from inverse bremsstrahlung absorption, which causes the plasma to expand and produce a low-density bubble. For an accurate measurement (e.g. of electron temperature), the goal is to minimize the plasma perturbation by the diagnostic.

Under application of a large enough B_z, rather than simply forming a wider jet as expected by the 2D PERSEUS simulations, we experimentally observe a disruption of the plasma jet collimation for which plasma erupts from the foil surface as discrete bursts early on in time. The critical B_z for the onset of the disruption correlates with material properties like electrical resistivity and equation of state. Lower resistivity materials like aluminum disrupt at a B_z for which higher resistivity materials like titanium produce well-collimated jets. 3D simulations of the ablation process of a slab (that represents a small section of the radial foil) that starts from the solid phase reproduce some of the experimental trends such as the material resistivity and B_z dependence on generation of current nonuniformities and plasma nonuniformities. Understanding the dy-

Table 4.1: COBRA Shot Statistics

Run	Dates	Shot Numbers	Shots
1	4/22 - 5/5/2014	3173 - 3187	15
2	6/30 - 7/10/2014	3218 - 3231	14
3	10/15 - 10/24/2014	3322-3332	11
4	1/5 - 1/15/2015	3377 - 3405, 3408	30
5	5/4 - 5/22/2015	3536 - 3571	36
6	6/15 - 6/25/2015	3584 - 3616	33
7	8/24 - 9/4/2015	3683 - 3703	21
8	1/4 - 1/21/2016	3814 - 3848	35
9	3/7 - 3/23/2016	3895 - 3938	44
10	11/8 - 12/2/2016	4275 - 4307	33
11	4/17 - 4/27/2017	4496 - 4515	20
12	6/7 - 6/22/2017	4530 - 4566	37
Total			329

namics of a plasma that is generated from a source (like a solid foil) can require detailed understanding of material phase transitions in the solid, liquid, and vapor states.

4.3 Experimental Shot Statistics

Table 4.1 displays the COBRA shots for which I was the principal investigator (PI). Fig. 4.1 displays how being the PI on COBRA occasionally felt.

Figure 4.1: Being on COBRA: Destruction. Acrylic on paper. T. Byvank, 2016.

CHAPTER 5

EXPERIMENTAL SETUP

5.1 Adventures of a COBRA Electron

For further detailed information about pulsed power, the author directs the reader to the book *Pulsed Power Systems* by H. Bluhm and various theses from previous graduate students. [48, 49, 50, 51, 52, 53, 54, 55, 56, 57]

At the Laboratory of Plasma Studies (LPS) at Cornell University (CU), we conduct our experiments in the vacuum chamber of the COrnell Beam Research Accelerator (COBRA) pulsed power generator. [22] COBRA provides a 1 MA peak current in a 100 ns zero-to-peak rise time. To achieve this power, we use pulse compression that sends the pulse from two Marx capacitor bank generators to two intermediate storage capacitors (ISC), to two main switches, to four pulse forming (coaxial transmission) lines (PFL), to four output switches, to one current adder (a triplate transmission line), to a (coaxial) magnetically insulated transmission line (MITL), and finally to the load chamber and experimental hardware. The main idea behind pulse compression is that stored energy is transferred into successively lower inductance and capacitance energy-storage-sections; the stored energy is constant, and the pulse time decreases ($t_{charge} \sim (\pi/2)(LC)^{1/2}$; 800 ns charging rise time ISC, 300 ns rise time PFL, 100 ns rise time load), so the power increases. COBRA is nominally a 0.5 Ω impedance machine that drives loads of order 10 nH inductance (more realistically, 20 nH). A schematic of COBRA is displayed in Fig. 5.1.

First, we discuss dielectric materials and voltage breakdown. Table 5.1

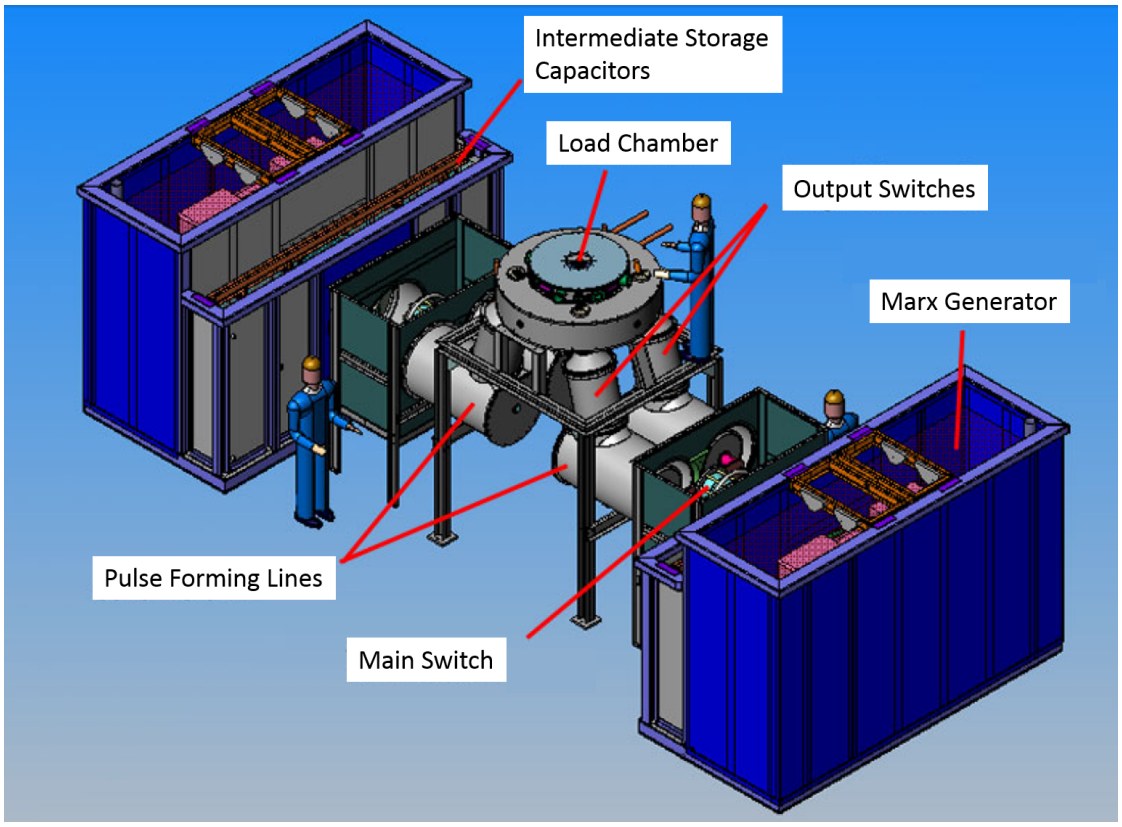

Figure 5.1: Computer-aided design drawing of the COBRA pulsed power machine.

Table 5.1: Dielectric Materials and Voltage Breakdown. Adapted from Bluhm. [48]

Material	Dielectric Constant ε	Breakdown Strength (MV/m)
Air	1.0	3.0
Kapton	3.6	275
SF_6	1.0	8 (per atm)
Transformer oil	2.2	10-40
Water	80	20 (for t<10 μs)

shows some materials and their voltage hold-off. These materials can be used to hold off voltage entirely during a process, or they can act within switches to determine the breakdown time. For example, oil may be used rather than water around a switch to reduce the capacitance across a switch's end plates, preventing a prepulse because of oil's lower dielectric constant. The Paschen curve

describes the minimum voltage for breakdown (y-axis, V) across a material relative to the product of pressure times distance (x-axis, Pd) between electrodes within a switch. Under this voltage or a larger voltage, a Townsend avalanche will ionize the material and create an arc across the electrodes. Qualitatively, the Paschen curve has a minimum V_{min} at some Pd_0. At lower Pd than Pd_0, there are not enough charge carriers to sustain a breakdown at a specific voltage. At higher Pd than Pd_0, too many charge carriers lead to high collisionality, so electrons do not acquire sufficient energy to sustain a breakdown (because they lose energy during the collisions). In practice, the switches used in COBRA operate at a Pd value larger than Pd_0.

Each Marx bank, held in an oil-dielectric, consists of sixteen 1.35 μF capacitors charged in parallel to 70 kV over a time of around 2 minutes. The total stored energy in each Marx bank is 53 kJ (for a total of 106 kJ in COBRA). Spark gap gas (SF6) switches (0.64 in gap) reconfigure the capacitor circuit from parallel to series. The capacitors discharge in series and output a voltage of 1.1 MV (16 * 70 kV), negative with respect to ground. See Fig. 5.2 for a diagram of the Marx generator configuration. The charging resistors (all in range of 1-10 kΩ; 9 g/L solution of $CuSO_4$ in H_2O) have long enough (millisecond) RC-times to allow for the in-series discharge. The Marx has a total capacitance of 84 nF and inductance of about 4 μH. A trigger Marx (containing charging resistors 520 Ω*cm; 4 g/L solution of $CuSO_4$ in H_2O) provides the signal (a voltage large enough for gas switches to arc) for the Marx to fire.

The discharge output from the Marx bank charges a 46 nF intermediate storage capacitor (ISC), held in a water-dielectric, for approximately 800 ns until the ISC discharges through a main self-breaking gas (SF6) spark gap switch (stack

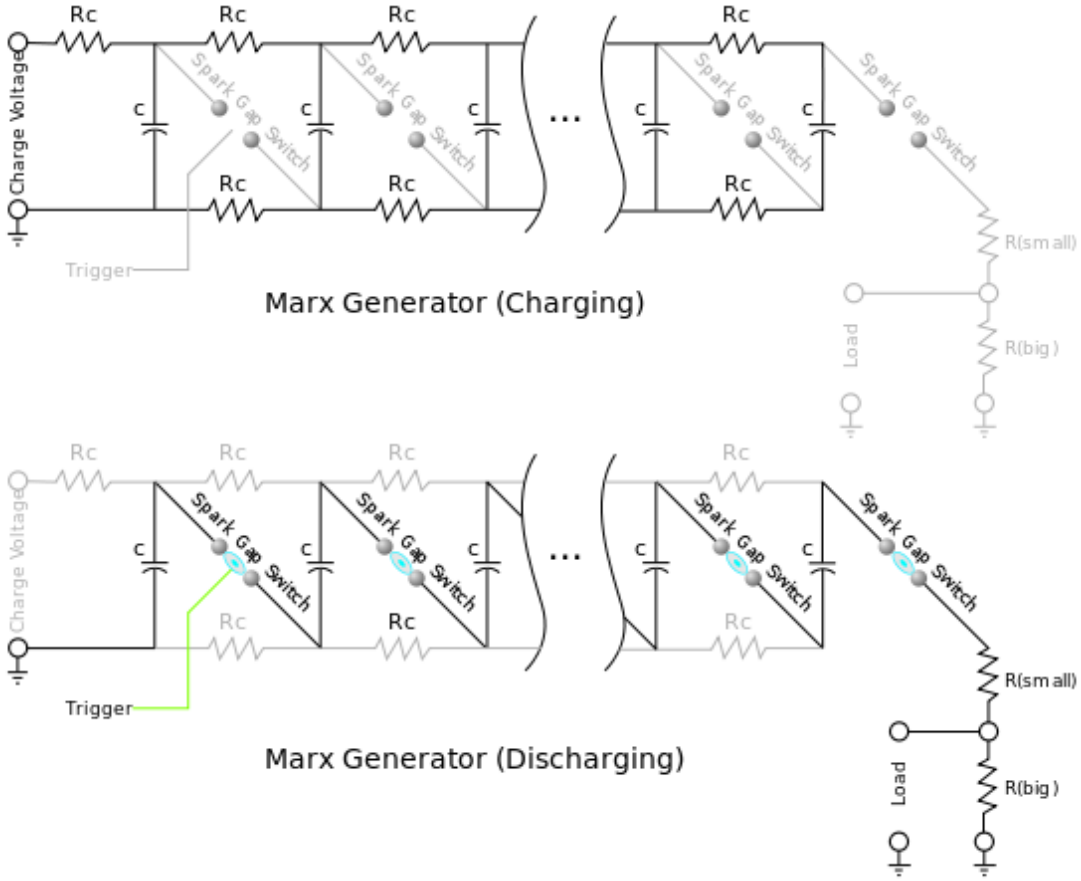

Figure 5.2: Diagram of charging and discharging Marx generator. Image from Wikipedia made by ZooFari, November 1, 2009, [Public domain], via Wikimedia Commons, https://commons.wikimedia.org/ wiki/File:Marx_Generator.svg

of stainless steel plates with 0.35 in gaps).

The pulse forming lines (PFL), held in a water-dielectric, are where the pulse compression occurs. The main switch discharges into two parallel PFLs, each with a 1.8 Ω impedance and 30 ns transit time. The PFLs charge for approximately 300 ns and discharge through output self-breaking gas (SF6) spark gap switches (stack of stainless steel plates and copper-tungsten electrodes with a 0.66 in gap), held in an oil-dielectric.

The output switches discharge into the adder (named because it adds the

current from the 4 output switches), held in a water-dielectric. The current passes from the adder to the center plate of a three-plate (anode-cathode-anode) geometry, held in vacuum. The anode is ground and the cathode is "hot." Insulator spacer rings (also called the diode stack) separate the anode and cathode plates by capacitive voltage division (meaning a smaller E-field is set up in between the rings compared with the total E-field between the anode and cathode without any rings, due to the rings becoming electrically polarized). There are 5 insulated rings in between both anode-cathode plate separations for a total of 10 rings. When these rings get dirty from deposited load material after many (est. 20, depending upon the load) experimental shots, current can arc across the dirt tracks and lead to current crowbarring, which is when, rather than being perfectly reflected, the reflected pulse gets sent back to the diode stack and instead rings (reflects) around the dirt tracks. Additionally, if an arc cracks the ring and breaks the vacuum-water interface, that is the end of the COBRA experimental run (at least). Therefore, as needed, we clean the dirt off the rings (using isopropanol for the 7 bottom rings [rexolite], diffusion pump oil (low vapor pressure) for the 3 top rings– made of a different material [lucite]– and also then oil the 7 bottom rings) and inhale more alcohol (isopropanol) fumes than a body typically wants to ingest during an afternoon.

The three-plate (or tri-plate) geometry feeds the current into a magnetically insulated transmission line (MITL). Magnetic insulation is achieved when current through the coaxial MITL self generates a perpendicular magnetic field that will deflect (by the Lorentz force) charged particles (most importantly, the electrons) emitted from electrode surfaces. The cyclotron motion causes the charged particles to return to the emitting conductor rather than discharge into the other electrode, which would result in current loss before reaching the load hardware.

Typical peak voltages at the load are of the order hundreds of kilovolts (say, 300-400 kV). For the closest anode-cathode (A-K) gap spacing of approximately 2 cm, the cathode diameter is 3.8 cm, and a 1 MA current would produce a 10.5 T B-field. With this B-field, the electron cyclotron radius for a 300 eV electron is $4 * 10^{-4}$ cm; therefore, the larger A-K gap spacing provides insulation from electrons arcing across the gap.

The current and voltage reaching the load are monitored with a Rogowski coil and inductive voltage monitor, respectively. The Rogowski coil is a helically wound wire (essentially an N turn dB/dt probe as explained in Sec. 5.4) placed outside of and around the cathode power feed, schematically shown in Fig. 5.3. The Rogowski coil voltage V_R is given by Eq. 5.1, with load current I(t), permeability of free space μ_0, number of turns in coil N, area of each loop A, and radius r from center of current to coil. The voltage monitor is a long, thin, high-inductance ($L_w \sim 1$ μH) wire connecting the cathode current feed to ground. A small amount of the COBRA current goes through the voltage monitor wire, creating a time-varying magnetic field that is measured by a dB/dt probe. The probe voltage V_p is related to the actual load voltage V by Eq. 5.2, ignoring resistive losses through the (conductive) voltage monitor wire, where L_w is the wire inductance.

$$V_R = \frac{dI}{dt}\frac{\mu_0 N A}{2\pi r} \tag{5.1}$$

$$V = L_w \frac{dI}{dt} = L_w \frac{2\pi r}{\mu_0 A} V_p \tag{5.2}$$

The COBRA driving current can be approximated by $I(t) = I_{max} * \sin^2(0.5 * \pi * t/100)$ for the initial 100 ns rise time with time t in nanoseconds. As shown

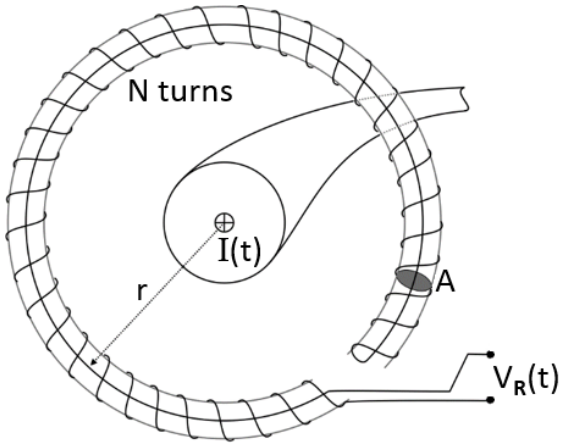

Figure 5.3: Diagram of Rogowski coil. Adapted from Wikipedia image by Luque alfredo, February 28, 2011, [CC BY-SA 3.0 (https://creativecommons.org/licenses/by-sa/3.0)], via Wikimedia Commons, https://commons.wikimedia.org/wiki/ File:Rogowsky_coil.png

in Eq. 5.3, the load voltage V measured by the voltage monitor depends upon the load resistance R, current I, and inductance L. The total inductance L = $L_{convolute} + L_{load}(t)$ is the sum of the COBRA convolute powerfeed inductance $L_{convolute}$ (based upon where the voltage monitor is attached to the COBRA machine) and the experimental load $L_{load}(t)$ (which, in this work, is the radial foil and plasma jet).

$$V = IR + L\frac{dI}{dt} + I\frac{dL}{dt} \tag{5.3}$$

The voltage wave is initially reflected from the high inductance load, travels back through the pulsed power machine transmission line (PFLs) until the voltage wave is reflected again back toward the load by the high inductance of the main switch, and returns to the load about 100 ns after peak current. This pulse reflection creates the characteristic double-hump current pulse shape seen on COBRA. For a lossless transmission line, the reflected voltage, V_{-}, is given by Eq. 5.4, with incident voltage V_{+}, load impedance Z_L, and transmission line

characteristic impedance $Z_0 = \sqrt{L/C}$. The total voltage is $V(x,t) = V_+ + V_-$.

$$V_- = \frac{Z_L - Z_0}{Z_L + Z_0} V_+ \tag{5.4}$$

For the process by which current gets to the load and diagnostics trigger to observe the experimental plasma, see Appendix B. For the operating instructions to fire COBRA, see Appendix C.

5.2 Radial Foil Load Hardware

We conduct our experiments in the vacuum chamber of COBRA (initially) at room temperature. The vacuum pressure of $\leq \ 5 * 10^{-5}$ Torr corresponds to $\leq \ 2 * 10^{12} \ cm^{-3}$ background gas particles with a mean free path of $\geq \ 0.8$ cm. [58] The chamber size is of order $\sim 1 \ m^3$.

The load hardware that connects the COBRA powerfeed electrodes is the "radial foil," which is a thin, solid, circular disk supported beneath its center z-axis by an electrode pin (solid cylinder with a flat top; brass) and supported at its outer annulus by an electrode ring (titanium). In order for the foil to make good electrical contact, the center pin is held at a height ~ 1 mm above the outer ring, thereby stretching the foil taught.

The COBRA current flows radially through the foil and axially through the center electrode pin. When the center pin is the cathode and the outer annulus ring is the anode, we refer to the setup as "standard current polarity." In standard polarity, current flows radially inward through the foil and down the pin. When the center pin is the anode and the outer ring is the cathode, we refer to

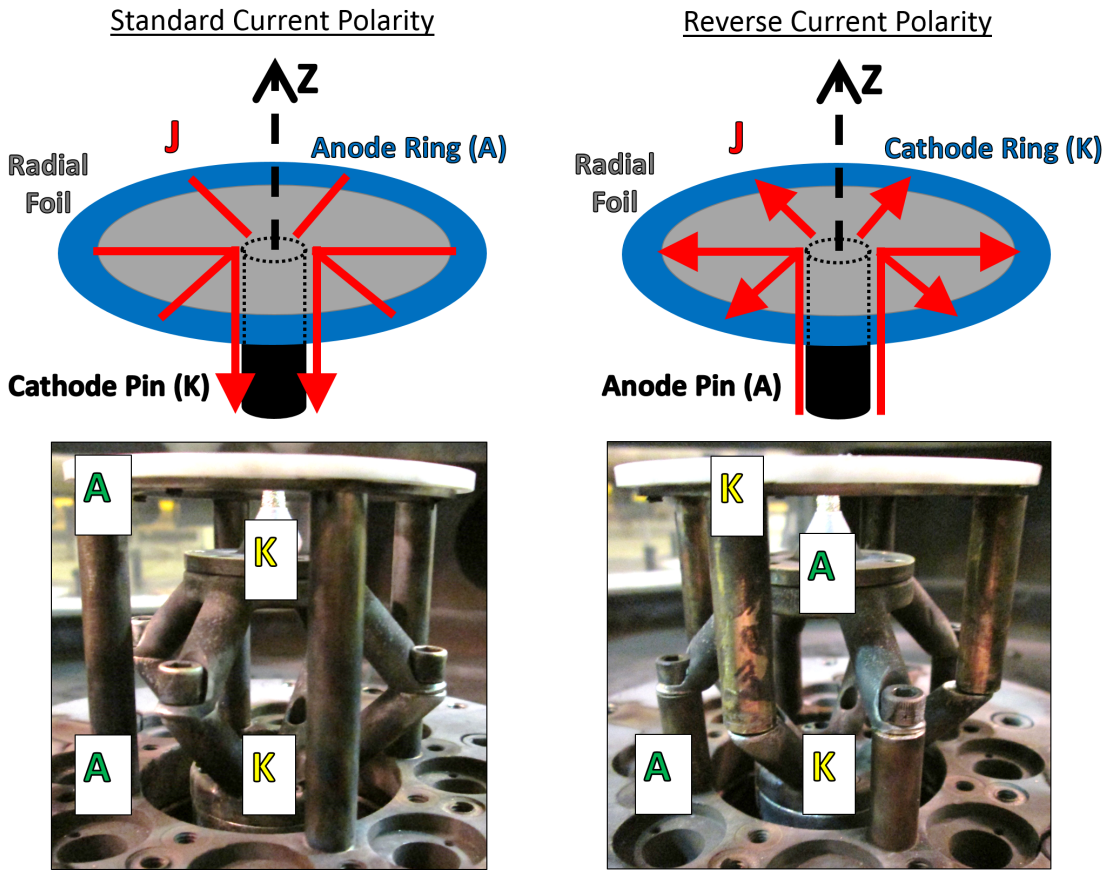

Figure 5.4: Diagrams and pictures of hardware for standard and reverse current polarities with labeled current direction (red) and electrodes (anode A and cathode K).

the setup as "reverse current polarity." In reverse polarity, current flows up the anode pin and radially outward through the foil.

The different current polarities are obtained by orienting a piece of hardware that can be rotated, connected by extension posts to the COBRA power feed cathode and to the chamber anode (ground). Using the same hardware for both current polarities minimizes any changes in load inductance and allows for consistent comparisons in plasma dynamics between experiments. See Fig. 5.4 for diagrams and pictures of both current polarities.

In this research, we use various load configurations: center pin diameters of

Table 5.2: Radial Foil Materials

Material	Thickness (μm)	Purity (%)
Al	4	99
Al	15	98 [Reynolds Wrap]
Al	38	99
Ti	12.5	99.5
Ti	15	99.5
Ni	12.5	99.95
Cu	12.5	99.9
Zn	25	99.95
Mo	15	99.97
W	25	99.5

2 mm, 5 mm, and 10 mm; foil thicknesses of 4 μm, 12.5 μm, 15 μm, 25 μm, and 38 μm; and foil materials of aluminum (Al), titanium (Ti), nickel (Ni), copper (Cu), zinc (Zn), molybdenum (Mo), and tungsten (W). The outer foil diameter (or inner diameter of the electrode ring that holds the foil) is 36 mm. Table 5.2 shows the foil materials we use and the material purity, although we note that gases (impurities) quickly adsorb to the foil surface and are present even under vacuum immediately before the experimental shot. For example, the surface of an aluminum foil is likely a thin layer of aluminum oxide.

The 5 mm pin, 15 μm thick Reynolds Wrap Al foil is the baseline configuration for this research. The skin depth δ of room temperature aluminum is given by Eq. 5.5 to be $\sim$40 μm, where η is the material resistivity, ω is the frequency of the COBRA current pulse (100 ns rise time, 400 ns period, $1.6 * 10^7$ rad/s frequency), and μ_0 is the permeability of free space. For titanium, a higher resistive material than aluminum, the room temperature skin depth is $\sim$150 μm. Additionally, we note the trend that solid materials' resistivities tend to increase with increasing temperature. Based on these calculated skin depths, we see that the COBRA current pulse fully penetrates the foil but only travels along the outside

of the center pin.

$$\delta \approx \sqrt{\frac{2\eta}{\omega\mu_0}} \tag{5.5}$$

In order to load the radial foil hardware as designed for the COBRA chamber, the author has some suggestions as follows. When using the Helmholtz coil, set up the anode post of the convolute (rather than the cathode post) near the location of the electrical feed wire bend in the lower Helmholtz coil. The other orientation may be more likely to arc to that "bend" spot, which already has some damage (and attempted repair). To ensure concentric-enough electrodes for symmetric current flow, if the foil holder is not well-enough centered on the pin, the anode plate in the COBRA chamber may be slightly shifted; another option is to switch around some of the anode and/or cathode posts (if they are not perfectly straight). When loading the foil into the foil holder, minimize extra solid foil material outside of the holder that may fall into the AK gap after the experiment. Cut the foil in an octagon shape with edges immediately interior to the holder's screw holes. Firmly press on the holder when connecting the two holder pieces (Delrin plastic top and titanium bottom) to ensure good electrical contact with the foil. As needed, use a smooth object like the handle end of a screwdriver or Allen key to press down on the outside edge of the foil in order to further make good electrical contact. Try to use a piece of foil with minimal creases; some nonuniformities do not matter, but deep grooves near the center pin region may influence the current distribution and corresponding jet development. Additionally, after each shot, the center pin will develop more bumps or rough spots. Depending upon the experiment, these bumps may be detrimental to the formation of an azimuthally symmetric jet because they may

help seed instabilities like the jet disruption. Therefore, depending on the experimental campaign, it may be good practice to replace the center pin for each shot. The pin surface can be smoothed by facing it with a lathe (or milling machine), and then the pin can be used for a subsequent shot.

5.3 Helmholtz Coil

A Helmholtz coil pulsed independently from the COBRA current pulse provides a uniform axial magnetic field (B_z from 0 to $\sim$2 T) in the region of interest (center z-axis location near pin and jet) over the experimental timescale of interest ($\sim$300 ns). The Helmholtz coil rise time is $\sim$140-150 μs, which is a factor of $\sim$1000 times longer than the COBRA current rise time of $\sim$100 ns. The $\sim$150 μs coil rise time permits field penetration through the foil hardware of 85% relative to the field with no hardware at the region of interest as measured before the experiments with dB/dt probes placed $\sim$1 mm above the foil. Eddy currents generated within the load hardware prevent full magnetic field penetration relative to vacuum. A longer coil rise time would permit more field penetration. At this 1 mm height above the foil, we measure no difference (within an acceptable uncertainty of $\sim$5-10%) in the penetrated field for the different foil materials used, despite their different resistivities (e.g. room temperature Ti is a factor of $\sim$10 more resistive than Cu or Al).

A substantial part of the remaining description in this section will summarize and restate the specifications in the thesis of Peter Schrafel, a previous graduate student. [57] See Appendix D for operating instructions to charge and fire the power supply for the Helmholtz coil.

The Helmholtz coil configuration has two circular solenoids (wire coils) oriented along the same (z-)axis. We use a Helmholtz coil rather than one full solenoid because the Helmholtz coil permits radial (and axial) diagnostic access. For a Helmholtz coil, the distance between the two coils equals the radius of the coil loops. When current flows in the same direction in both the top and bottom coils, the magnetic field B at the midpoint of the coils is given by Eq. 5.6, with permeability of free space μ_0, number of turns in each coil N, current through the coils I, and coil radius a.

$$B = \frac{8}{5\sqrt{5}} \frac{\mu_0 N I}{a} \tag{5.6}$$

As shown in Fig. 5.5a, We model the Helmholtz coil circuit as an underdamped RLC circuit with a switch, and, because of long timescales (150 μs) relative to the pulse travel time (<50 ns for an electrical signal to go <10 m at $\sim$66% the speed of light), we treat the electrical feeds as resistors rather than transmission lines. The electrical feeds outside of the experiment chamber connect to the coil inside of the vacuum chamber by utilizing vacuum feedthrough holes on a chamber port. Table 5.3 shows the Helmholtz coil parameters. The coil inductance is estimated as the sum of two wire coils. The stored energy in the capacitor bank should be about equal to the peak magnetic field energy plus the resistive loss through the electrical feeds throughout the entire damped sinusoid current. As is calculated in Table 5.3, the resistive loss until peak current is too high– larger than half the total stored energy– considering there are additional resistive losses after the peak of the damped sinusoid current, as well. However, a slight change in the actual resistance of the electrical feeds (take as $\sim 0.2 \pm 0.1\,\Omega$ one-way from the capacitor bank to the coil) can account for the

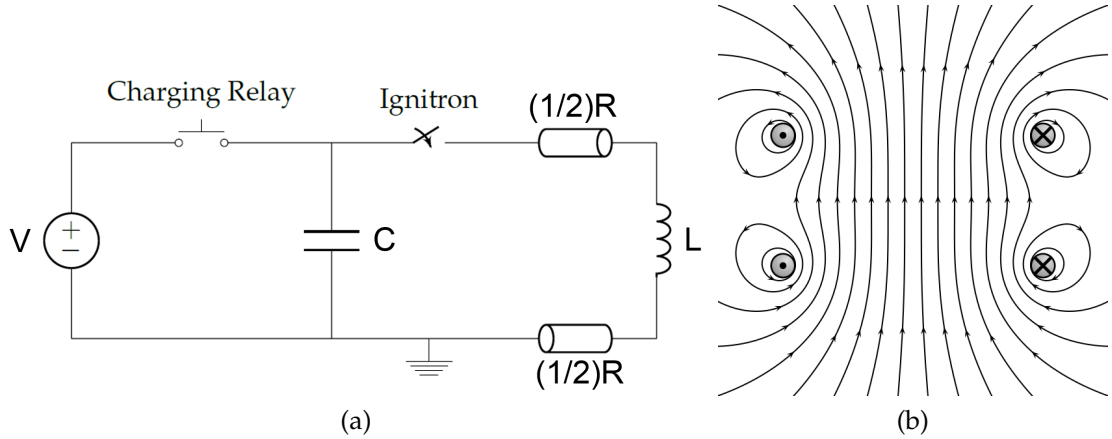

Figure 5.5: a) Simplified circuit diagram for the applied magnetic field: with capacitor bank capacitance and voltage, charging relay, ignitron switch, electrical feed resistance, and Helmholtz coil inductance. Adapted from P. Schrafel, 2014. [57] b) Cross section of magnetic field lines produced by Helmholtz coil loops in vacuum (no hardware within the coils), showing a uniform field within the central region between the coil loops. Image from Wikipedia made by Geek3, May 2010 [CC BY-SA 3.0 (https://creativecommons.org/licenses/by-sa/3.0)], via Wikimedia Commons https://commons.wikimedia.org/ wiki/File%3AVFPt_helmholtz_coil2.svg

needed energy balance.

The Helmholtz coil has a uniform magnetic field in the center of the coils and fringing fields outside, as illustrated in Fig. 5.5b. If the fringing fields were large enough, they could penetrate the COBRA MITL gap and undermine the vacuum electrical insulation. However, these radial fringing fields are smaller (by a factor of $\sim$0.01) than the azimuthal MITL fields.

Generating a magnetic field necessitates structural integrity of the coil to withstand the magnetic pressure (energy density). The pinching force from parallel wire loops will try to pull the wires together, and the magnetic pressure gradient will try to push the loops outward. Therefore, the Helmholtz coil was fabricated by winding wires (flat strip Cu-Be conductor), wrapping Kapton film around (for electrical insulation of high voltages between wire turns), and plac-

Table 5.3: Helmholtz Coil Design Parameters

Parameter	Formula	Value
radius, a		∼0.06 m
wire width, w		∼0.002 m
wire thickness, t		∼0.02 m
characteristic wire size, s	$\sim (w+t)/2$	∼0.01 m
height between loops, h		∼0.04 m
turns in each coil, N		12
voltage, V		8 kV
capacitance, C		196 μF
resistance, R*		0.4 Ω*
inductance, L	$2\mu_0 a N^2[\ln(8(2a)/s) - 2]$	56 μH
peak current, I (damped sinusoid)	$\sim 0.7V\sqrt{C/L}$	10.5 kA
peak midpoint magnetic field, B	$(8/5\sqrt{5})\mu_0 NI/a$ $\approx 0.22V\sqrt{\mu_0 C}/a^{3/2}$	1.9 T
rise time, $\tau_{1/4}$	$(\pi/2)\sqrt{LC}$	∼160 μs
stored energy	$CV^2/2$	6.3 kJ
B-field energy at peak	$\pi a^2(h+t)B^2/2\mu_0$	1.0 kJ
resistive energy loss until peak*	$< I^2 > R\tau_{1/4}$	3.5 kJ*

ing into a G10 fiberglass shell (that has good structural integrity able to withstand the magnetic pressure). The coil was potted in STYCAST 1264 A/B epoxy after the epoxy was debubbled in a vacuum chamber.

5.4 Magnetic dB/dt (B-dot) Probes

We use dB/dt (or Bdot, B-dot, $\dot{\text{B}}$) probes to measure compression of the axial magnetic field (B_z) produced by the Helmholtz coil. [59, 27] The dB/dt (time rate of change of the magnetic field) through the probe loop is proportional to the induced voltage determined by Faraday's law (and sign determined by Lenz's law); see Eqs. 5.7-5.9 with electric field E, magnetic field B (average value through the loop area), time t, loop segment length $d\ell$, loop area A, and voltage V. The loop is on one end of a coaxial cable and is made from the inner conduc-

tor, so, on our experiment timescales, the voltage difference is the "open circuit" voltage between the inner and outer conductors on each end of the loop; see Fig. 5.6 and the text below for a further description of the probe geometry. Only the dB/dt component normal to the loop surface induces a voltage; therefore, loop orientation within the changing magnetic field is important.

$$\nabla \times E = -\frac{\partial B}{\partial t} \tag{5.7}$$

$$\oint E \cdot d\ell = -\frac{\partial}{\partial t} \int B \cdot dA \tag{5.8}$$

$$taking \ \frac{\partial A}{\partial t} = 0, \ V = A\frac{dB}{dt} \tag{5.9}$$

Our dB/dt probes are made from semi-rigid coaxial cables (0.51 mm outer diameter (OD)). The loop areas are of order 0.5 mm^2, for which an average magnetic field change of 1 T in a time of 50 ns leads to voltage of 10 V. The outer conductor of the coaxial cable is at ground, so the oscilloscopes measure the induced voltage on the inner conductor. The probe loops are covered with Kapton tubing and the probe end filled with epoxy for electrical insulation. Kapton (polyimide) has a $\sim$275 MV/m electrical insulation rating; see, for example, Table 2.10 on page 43 of the book by Bluhm. [48] See Appendix E for instructions on how to make the dB/dt probes.

The loop orientation (surface normal) can be perpendicular to the coaxial cable length axis, called a "normal probe" or "theta probe," or the loop orientation can be parallel to the coaxial cable length axis, called a "z-probe." For the z-probe, the outer conductor extends to the side and past the loop to prevent penetration of some non-axial fringing field components. Furthermore, the z-probe loop orientation can be parallel or anti-parallel to the coaxial cable length

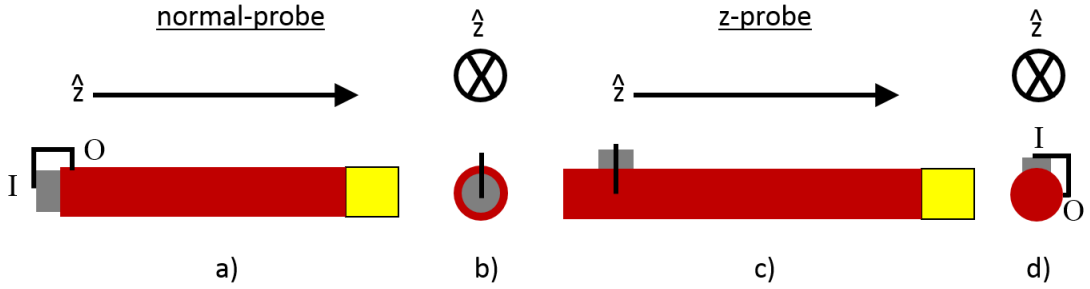

Figure 5.6: Schematic of dB/dt probes without the electrical insulation components (Kapton tubing, outer plastic insulation, and epoxy). Color code: black line: inner conductor (loop), gray: coaxial insulator, red: outer conductor, yellow: connector. The probe loop voltage is at the inner conductor end of the loop, $\sim$ point I. The outer conductor end of the loop, point O, is at ground. We define the loop orientation as the surface normal going from point I to point O. a) Normal probe side view. b) Normal probe end-on view. c) Z-probe side view. d) Z-probe end-on view; the loop direction from point I to O is clockwise, showing a "positive-z" orientation.

axis, and this orientation determines the sign of the induced voltage. We define the cable z-axis as the cable-length axis in the direction from the loop to the probe connector (which will be parallel to the z-axis of the COBRA experiment). The probe connector connects the probe coaxial cable to a cable (SMA) that is attached to an oscilloscope far outside of the experiment chamber. We define a positive-z loop orientation as when the inner conductor wire wraps around clockwise when looking down onto the z-axis (when looking in the negative z-direction); see Fig. 5.6 d). Given these defined orientations, a time-increasing B field in the positive z direction will produce a positive voltage signal for a loop with a positive-z orientation. Switching the direction of either the dB/dt or the loop orientation will switch the sign of the voltage signal.

To measure B_z compression in the plasma jet experiments, we can combine two z-probes of opposite loop orientations (counter-wound loops) in order to make a differential measurement. Using this combination, we can verify that

the probe voltage signal corresponds to dB/dt rather than pickup from some electric field. We expect that a dB/dt will create opposite voltage signals for opposite loop orientations. Subtracting the two signals and dividing by 2 (for the number of total loops) gives the magnetic dB/dt signal, and adding the two (ideally opposite) signals and dividing by 2 gives the (ideally zero) electrical pickup.

We can also measure B_z compression by combining a normal probe and a z-probe, so a dB/dt in only one direction leads to a voltage signal in one probe and a null (zero) signal in the other. Using this combination, we can verify that the probe voltage signal corresponds with a dB/dt in only the z (axial) direction rather than some non-axial component.

Additionally, we can measure B_z compression using only one z-probe. Here, there are less measurement safeguards and checks compared to a differential measurement. However, opposite loop orientations can be still used for different COBRA shots and the results compared for agreement.

To convert a voltage to dB/dt, before the experiment each dB/dt probe area is calibrated using a well-characterized pulser; see Appendix F. Because the loop is small, it is difficult (especially when the loop is enclosed in Kapton and epoxy) to directly and accurately measure the area. The loop area calibration has an estimated uncertainty for the dB/dt measurement of $\sim 5\%$ that we conservatively take to be $\sim 10\%$ to account for some probe orientation shift in the experimental setup. An actual $\sim 10\%$ change in the effective loop area corresponds to an orientation shift larger than a 25° angle, which is far larger than any realistic misalignment. Furthermore, the off-axis components of the loop area can be accounted for by calibrating the area in multiple orientations (i.e. along with

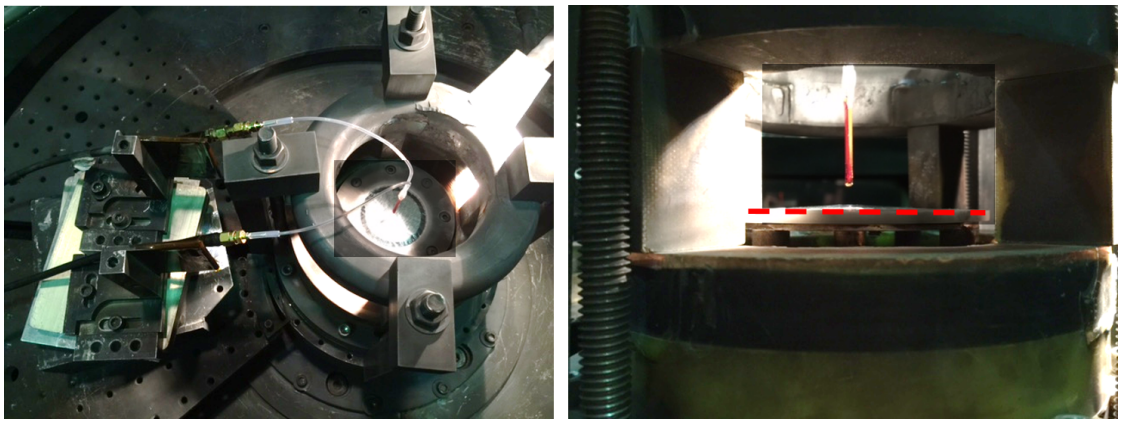

Figure 5.7: Experimental setup for measurement of magnetic field compression. Left: top view showing double-loop probe, radial foil, and Helmholtz coil in the COBRA chamber. Right: side view showing probe tip position (orange Kapton) relative to radial foil (dashed red line).

calibrating a z-probe loop parallel to the coaxial cable z-axis, also calibrate in orthogonal directions).

In order to measure the compression of the axial magnetic field, we use dB/dt probes placed in the central hollow region of the jet. This central placement minimizes any perturbation of the jet, limits any shock formed around the probe, and reduces any current in the plasma around the probe. See the results in Section 7.3 for more detail and discussion about the probe measurements.

When loading dB/dt probes for an experiment, one determines by eye (and ruler, as needed) the final probe position (height, angle, loop orientation, etc.) relative the foil hardware. The outer plastic of the probe can be bent as needed and hardened with a heat gun after bending. Despite this hardening, the probe may still shift under vacuum or by gravity if enough time passes (e.g. overnight). Making larger probes with more epoxy on the outside for electrical insulation and structural support can make the probe more stable to shifting; however, a larger probe can also physically perturb a plasma more than a

smaller probe. See Fig. 5.7 for (preshot) setup pictures of a magnetic field compression experiment.

5.5 Extreme Ultraviolet Self Emission Pinhole Imaging

We image the plasma self emission in the extreme ultraviolet (EUV or XUV) energy range ($\sim$10-100 eV). In LPS, we colloquially refer to the EUV imaging diagnostic using the jargon "quad-cams" (or "QCs," referencing quadrant cameras) because four pinholes image onto four regions of a microchannel plate (MCP) and a corresponding four frames of a charge coupled device (CCD) camera. The images have a $<$5 ns exposure time and the independently triggered four regions of the MCP provide a time history of 30 ns with 10 ns in between each successive frame. Furthermore, we have two EUV imaging setups that can either provide eight frames looking side-on (along a radius) or four frames side-on and four frames with a top-view (looking down along the central axis).

The microchannel plate imaging has the following specifications. The MCP has a gold coating on the side closest to the chamber and a phosphor fluorescent screen on the side away from the chamber that is facing the CCD camera. The gold coating thickness specifies the energy range of photons that interact with the gold (photoelectric effect); lower energy photons reflect off the gold and higher energy photons are absorbed. In between the gold coating and fluorescent screen, the MCP contains photomultiplier tubes (PMT) in four regions independently triggered with an externally applied voltage (5 kV). The lengths of the cables between the MCP quadrants and externally applied voltage determine the 10 ns frame spacing. The camera shutters are open for 4 seconds

during (and before and after) the experiment, so the time resolution (<5 ns) is based upon when the external voltage is applied to the MCP quadrant, allowing electrons to travel through the PMT and hit (brighten) the fluorescent screen. The PMT channels are 12 μm with 15 μm spacing, giving an effective spatial resolution of 27 μm (Δx in the paragraph below).

The EUV image resolution depends upon the setup geometry; see Fig. 5.8. As available in LPS, the diameter of the pinholes, D, can be configured to be 50 μm, 100 μm, 150 μm, or 200 μm. The image magnification, M, is given by Eq. 5.10, where L_O is the object feature length, L_I is the image feature length on the detector, d_O is the distance from the object to the pinhole, and d_I is the distance from the pinhole to the detector. The diffraction limit for no overlap of an image's Airy disk (first minimum) is given by Eq. 5.11, where λ is the photon wavelength and D is the pinhole diameter. To resolve the object feature, the detector spatial resolution, Δx, must be smaller than the image feature length, as shown in Eq. 5.12. Furthermore, due to the finite pinhole (aperture) size, a single point from the object will be projected to a region on the detector of length Δy, as shown in Eq. 5.13 (derived using geometric similar triangles of rays originating from the single object point); to prevent blurring, $\Delta x > \Delta y$ is desired.

$$M = \frac{L_I}{L_O} = \frac{d_I}{d_O} \tag{5.10}$$

$$\frac{L_I}{d_I} \geq 1.22\frac{\lambda}{D} \tag{5.11}$$

$$\Delta x < L_I = L_O\frac{d_I}{d_O} \tag{5.12}$$

$$\frac{\Delta y}{D} = \frac{d_O + d_I}{d_O} = 1 + M \tag{5.13}$$

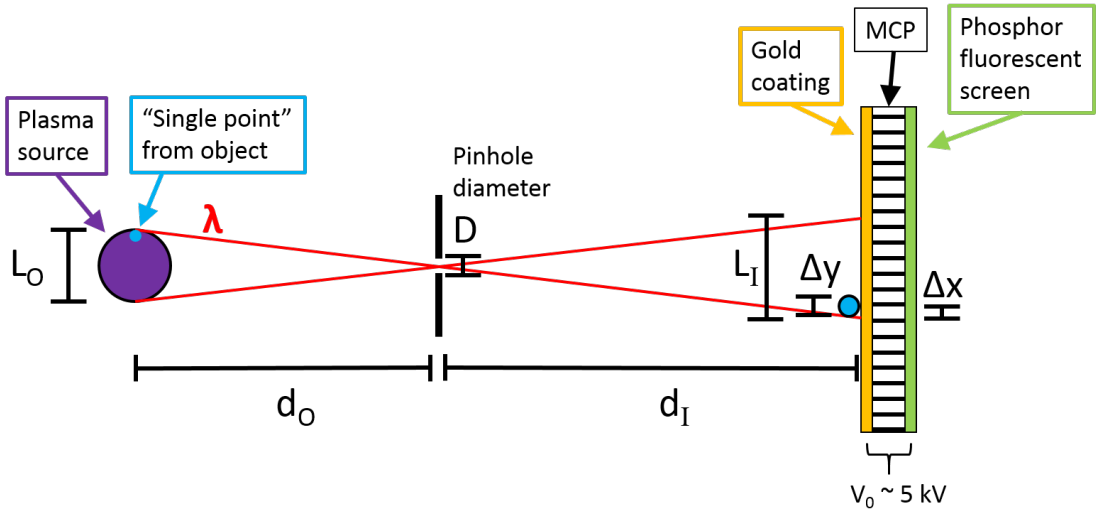

Figure 5.8: Schematic of a pinhole imaging setup.

For our experiments looking side-on in the COBRA chamber, we have $d_O \sim 53$ cm, $d_I \sim 38$ cm, and $\Delta x \sim 27$ μm. The magnification is therefore M ~ 0.72, using Eq. 5.10. Based on the detector resolution using Eq. 5.12, the minimum object feature size we could hope to image (ignoring Eq. 5.11 and Eq. 5.13) is $L_O = 38$ μm. However, using Eq. 5.13, we see that $\Delta y = 86$ μm for a D $= 50$ μm pinhole and $\Delta y = 344$ μm for a D $= 200$ μm pinhole. Since $\Delta x < \Delta y$, there is some blurring of the image. To further characterize the resolution, we take L_I to be the calculated Δy from Eq. 5.13 and use Eq. 5.11 to find the result that 50 μm pinholes correspond with photon wavelengths $\lambda < 9.3$ nm or energies E > 130 eV, and 200 μm pinholes correspond with photon wavelengths $\lambda < 150$ nm or energies E > 8.3 eV. In the present plasma jet research, we use 200 μm pinholes. The 50 μm pinholes did not provide qualitatively significant signal during the 5 ns imaging exposure time.

5.6 Optical Self Emission Fast-Framing Camera Imaging

We image the plasma self emission in the optical energy range ($\sim$1-3 eV) using a high speed camera (Invisible Vision Ultra UHSi 12/24). "High speed" means we can set the exposure time as low as 5 ns and time in between sequential frames also as low as 5 ns. Additionally, we can get up to 12 frames per experimental shot using this diagnostic. The image is focused based upon the (thin) lens equation given by Eq. 5.14, where d_O is the distance from the object to the lens, d_I is the distance from the lens to the camera, and f is the lens focal length. Given a relatively large lens diameter, image resolution is geometrically limited by Eq. 5.12.

$$\frac{1}{d_O} + \frac{1}{d_I} = \frac{1}{f} \tag{5.14}$$

Plasma self emission in any energy range is determined by the output radiated power. Generally, the power is some function of density and temperature; typically the electrons are a large source of the radiation, so P = P(n_e,T_e). The precise densities and temperatures determine what physical processes dominate the radiation: blackbody, line emission, or bremsstrahlung (along with recombination and cyclotron). In the present research, for our relatively "low" plasma temperatures $T_e \leq 100$ eV, bremsstrahlung radiation is less important than blackbody radiation. Plasmas can also lose energy by thermal diffusion, conduction (e.g. to the electrode hardware), and convection.

5.7 Time-Integrated Pinhole Imaging

Emission captured over the entire time of the experiment can provide information regarding what temperatures the plasma achieves. By covering the pinhole with different filter materials and thicknesses, one can observe over specified energy ranges. The photons radiated from the plasma will be diffraction limited through the pinhole (Eq. 5.11) and be passed through the filter based upon the material transmission (see: X-ray transmission of a solid from http://henke.lbl.gov/optical_constants/).

5.8 Laser Interferometry

To diagnose plasma density and density gradients, we use laser interferometry and laser backlighting shadowgraphy. The diagnostic laser is a 532 nm, 148 ps, 140 mJ pulse. The EKSPLA SL312 laser uses a Nd:YAG medium (1064 nm emitting) that is frequency doubled. The beam is split into three paths delayed with 10 ns time separation.

The laser beam is a monochromatic electromagnetic (EM) wave described by Eq. 5.15 with a phase velocity in free space of $v_{ph} = \omega/\mathrm{k}$, where **E** is the electric field, **r** is the spatial coordinate, t is time, **k** is the wave vector, k is the magnitude of the wave vector, ω is the frequency, and ϕ is the phase. EM waves in a (cold, temperature T —> 0) plasma satisfy the dispersion relation $\omega^2 = \omega_p^2 + k^2c^2$ or $\mathrm{k} = \frac{\omega}{c}\sqrt{1 - \frac{\omega_p^2}{\omega^2}}$, with speed of light, c, and plasma frequency, ω_p. The plasma refractive index is $n_p = \mathrm{c}/v_{ph} = \sqrt{1 - \frac{\omega_p^2}{\omega^2}}$. The (electron) plasma frequency $\omega_p = \omega_{p_e} = \sqrt{n_e q_e^2/\epsilon_0 m_e}$ is the frequency at which the plasma elec-

trons respond to a displacement from an electric field (like that of a propagating laser beam, for example), such that the plasma is opaque to waves at frequencies lower than the plasma frequency ($\omega < \omega_p$; meaning the refractive index n_p and wave vector k become imaginary).

$$\mathbf{E}(\mathbf{r}, t) = \mathbf{E_0}(\mathbf{r}, t)e^{i(\mathbf{k}\cdot\mathbf{r}-\omega t+\phi)} \tag{5.15}$$

The plasma critical density, n_C, is the (electron) density above which the plasma is opaque to the laser beam (at frequency ω), given by Eq. 5.16 with permittivity of free space ϵ_0, electron mass m_e, and elementary electric charge q_e. For our 532 nm beam, this critical density is $\sim 4*10^{21}\ cm^{-3}$. Although, below the critical density, while the laser can still propagate through the plasma, the laser can still be refracted by density (and index of refraction) gradients. The actual maximum density for which light will propagate through the plasma and still be detected depends upon the geometric "acceptance angle," α– the solid angle of the setup's collecting optics– using Eq. 5.17. [60] For our system setup's acceptance angle of $\alpha \approx 0.006$ steradians, the maximum density for which we can image the probing light is a factor of $\sim$12 less than the critical density. For larger densities, the light is refracted outside of the collection optics (at a larger angle than the acceptance angle).

$$n_C = \frac{\epsilon_0 m_e}{q_e^2}\omega^2 \tag{5.16}$$

$$\omega \geq \omega_p \alpha^{-1/2} \tag{5.17}$$

When an EM wave propagates through a plasma, the plasma index of refrac-

tion causes a change in the effective path length of the light (with wavelength λ) relative to its path length through free space. This path length change, ΔL, corresponds to a change in the phase, $\Delta\phi$ as shown in Eq. 5.18. The phase shift, $\Delta\phi$, is related to the line integrated electron density, $\int_0^L n_e dx$, by Eq. 5.19. For our interferometry measurements, two beams of light strike the detector. One beam passes through the plasma region of interest, and the other beam passes through a background region. The overlapping beams are the superposition of the two beams ($\mathbf{E_{tot}} = \mathbf{E_1}$+$\mathbf{E_2}$; see Eq. 5.15). Imaging records the light intensity (I proportional to $|\mathbf{E_{tot}}|^2$) that produces a fringe pattern; see Fig. 5.9. As written in Eq. 5.20, each sequential fringe is a change in phase of 2π, so a density perturbation (see Eq. 5.19) equivalent to a phase shift of 2π causes a "bump" in the fringe pattern of one fringe shift. The fringe shift (magnitude), F, is thereby related to the line integrated density by Eq. 5.21, for which an areal (line integrated) density of $\sim 4.2 * 10^{17}\ cm^{-2}$ corresponds to one fringe shift.

$$\Delta\phi = \frac{2\pi}{\lambda}\Delta L \tag{5.18}$$

$$\Delta\phi = -\frac{q_e^2}{2\omega c m_e \epsilon_0}\int_0^L n_e dx = -\frac{q_e^2 \mu_0 \lambda}{4\pi m_e}\int_0^L n_e dx = -\frac{\pi}{n_C \lambda}\int_0^L n_e dx \tag{5.19}$$

$$\Delta\phi = 2\pi F \tag{5.20}$$

$$F = \frac{1}{2 n_C \lambda}\int_0^L n_e dx \tag{5.21}$$

We measure densities using Mach Zender interferometry and "large shift" shearing interferometry. For our experimental setup, Mach Zender interferometry involves sending one laser beam through the chamber load region and one beam outside of the chamber. Then, the beams are combined to produce the interference fringe pattern. The beam paths will be close to the same length, but there will be a slight offset of angles and therefore a phase shift between beams

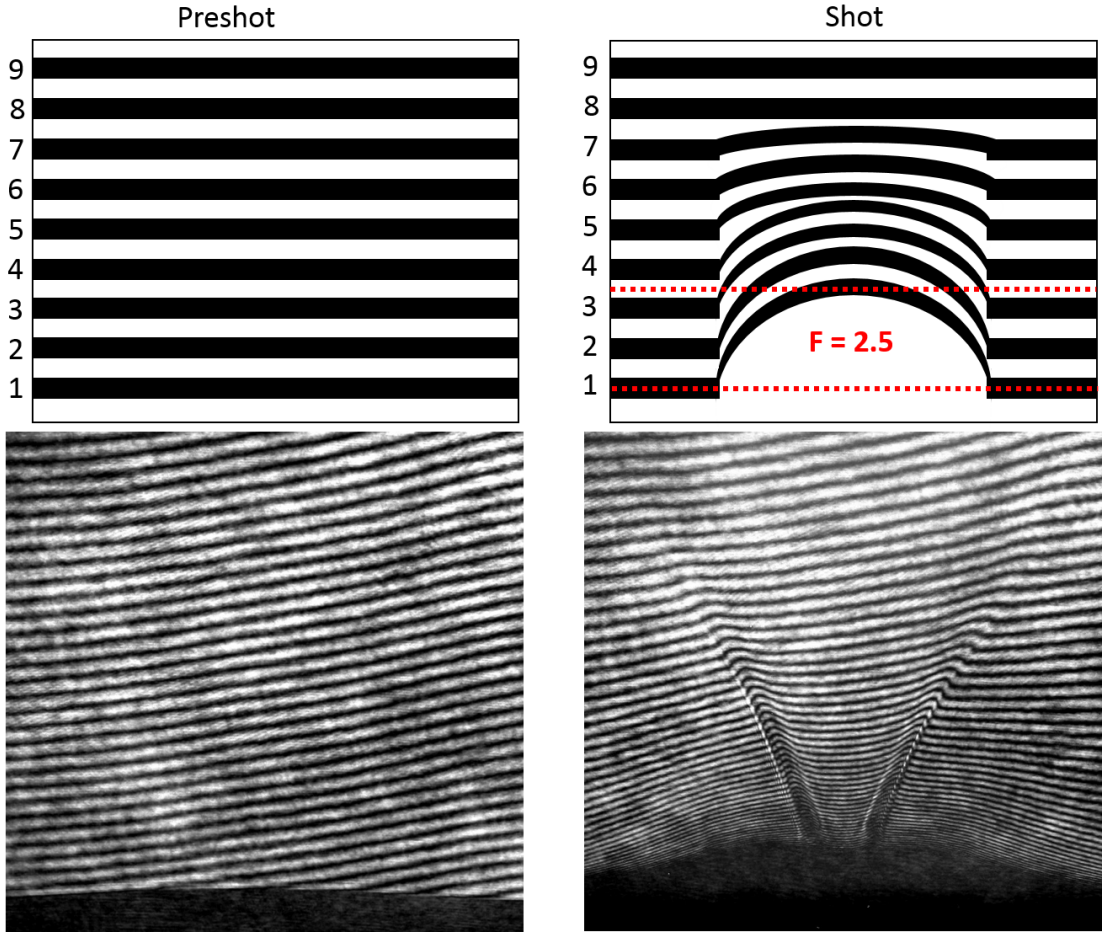

Figure 5.9: Top row: illustration of fringe patterns for a preshot (left) and shot (right), for which the bottom fringe (1) has a maximum fringe shift, F, of 2.5. Bottom row: experiment interferograms (Mach Zender) of plasma jet for preshot and shot 3702.

and a corresponding (reference) fringe pattern when the beams are combined even when there is no plasma in the chamber load region. Before the experiment, we take a preshot picture of this reference fringe pattern. Then, during a shot, we take another picture of the fringe pattern which shows the plasma perturbation when compared with the preshot. Contrastingly to Mach Zender interferometry, large shift shearing interferometry involves sending only one beam through the chamber load region. [61] Then, the beam is split with an air-wedge gap between two prisms, and the two beams overlap and combine at

the imaging detector. "Large-shift" refers to the beam area being large enough that the two beam images are offset such that a perturbed region on one beam image will overlap with an unperturbed background region on the other beam image. Thereby, the fringe shift can be related to the areal density similarly to the Mach Zender setup. We take a preshot picture and shot picture for the shearing interferometry, as well.

5.9 Laser Backlighting Shadowgraphy

$$\theta = \frac{d\phi}{dy}\frac{\lambda}{2\pi} = \frac{d}{dy}\int n_p d\ell \tag{5.22}$$

$$\frac{I_i}{I_d} = 1 + L\left\{\frac{d^2}{dx^2} + \frac{d^2}{dy^2}\right\}\left(\int n_p d\ell\right) \tag{5.23}$$

$$\frac{\Delta I_d}{I} = L\left\{\frac{d^2}{dx^2} + \frac{d^2}{dy^2}\right\}\left(\int n_p d\ell\right) \tag{5.24}$$

Using the same diagnostic laser as that used for interferometry, we can observe density gradients with laser backlighting shadowgraphy. As shown in Sec. 5.8, larger densities correspond with a larger effective path length of a propagating laser beam. Therefore, plasma density gradients will refract the laser beam wavefront. For the simple case of a planar slab of plasma with a density gradient perpendicular to the wavefront propagation direction, the refraction small angle deflection, θ, is given by Eq. 5.22 for which ϕ is the laser beam phase, y is the coordinate direction for deflection, λ is the wavelength, n_p is the refractive index, and ℓ is the coordinate direction along the laser beam path. The image intensity variations are given by Eq. 5.23 and Eq. 5.24 (now allowing for deflections in both the x and y directions), with incident beam intensity I_i, image intensity on detector $I_d \approx I$, fractional intensity variation $\Delta I_d \approx I_i - I_d$,

distance between refracting slab and detector L, refractive index n_p, and coordinate direction along the laser beam path ℓ. The density gradient deflection angle creates a bright-dark intensity fringe pair: a bright region where the light is deflected to and a dark region where the light is deflected away from. For further information on interferometry and shadowgraphy, the author directs the reader to (chapter 4 of) the book *Principles of Plasma Diagnostics* by I. H. Hutchinson. [60]

5.10 Thomson Scattering

The author would like to Jacob Banasek for his work on Thomson scattering, which helped to further experimentally confirm the rotation of the plasma jet under an applied B_z due to the $J_r B_z$ component of the $\mathbf{J} \times \mathbf{B}$ force. Our Thomson scattering laser produced a maximum 10 J, 3 ns, 526.5 nm pulse, focused to a 340 μm spot diameter, giving a laser irradiance of $3.7 * 10^{16}$ W/m^2.

Thomson scattering is the elastic scattering of an EM wave (e.g. laser) by oscillating charged particles (e.g. electrons). [62] In the non-collective regime, the laser wavelength is smaller than the plasma Debye length, and scattering is due to the motion of electrons. Our laboratory plasmas are in the collective regime, $\alpha = 1/k\lambda_{De} \approx 4 \geq 1$, so the collective motion of electrons across multiple Debye spheres is measured. Here, λ_{De} is the Debye length, and $\mathbf{k} = \mathbf{k}_s - \mathbf{k}_L$, where $\mathbf{k}_s$ is the scattered wave vector and $\mathbf{k}_L$ is the laser wave vector. In this work, we look at the scattering from electron motion associated with ion acoustic waves. The Thomson scattering spectrum can determine the ion velocities, electron velocities, ion temperature, and electron temperature; see Fig. 5.10. The

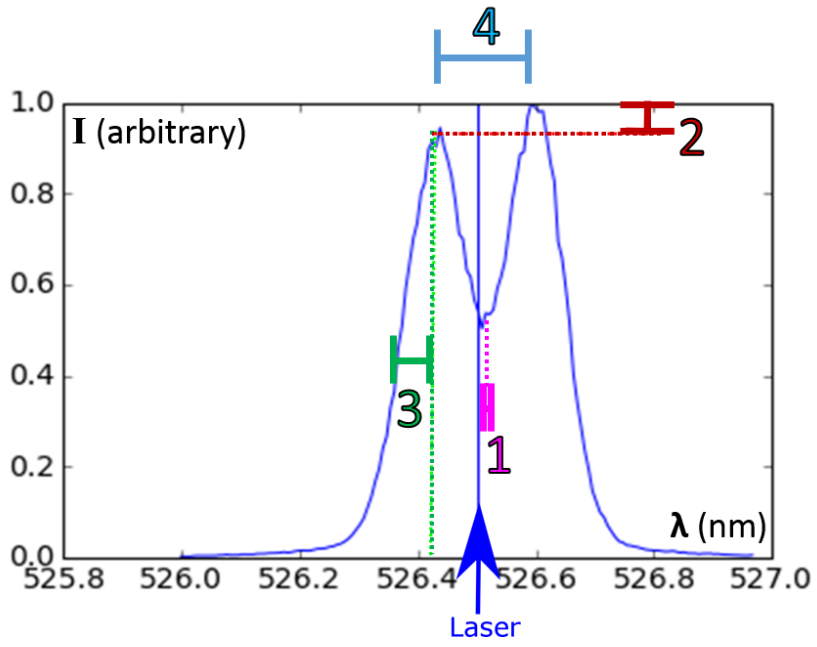

Figure 5.10: Example Thomson scattering spectrum (intensity vs. wavelength). Features related to 1) ion flow velocity, 2) electron-ion drift velocity, 3) ion temperature, 4) electron temperature. Thanks to J. T. Banasek.

ion flow velocity, $\mathbf{v}$, is determine from the Doppler shift, $\Delta\omega_d$, of the spectrum by $\Delta\omega_d = \mathbf{v} \cdot \mathbf{k}$. Furthermore, by looking at scattering from multiple directions, the components of the ion flow velocity can be decoupled to give radial, azimuthal, and axial velocities (in cylindrical coordinates, for example). The measurement of this azimuthal velocity component confirmed the plasma jet rotation.

CHAPTER 6

PERSEUS SIMULATION DESCRIPTION

In the Lab of Plasma Studies, we compare our high energy density experiments– wire arrays, gas puffs, cylindrical liners, and radial foils– with numerical simulations. We use the extended magnetohydrodynamics (XMHD) code, PERSEUS (an acronym standing for: Plasma as an Extended-MHD Relaxation System using an Efficient Upwind Scheme). Charlie Seyler and Matt Martin developed PERSEUS for Martin's PhD thesis in 2010 and the initial publication in 2011. [63, 14]

6.1 Fluid Equations and the Generalized Ohm's Law

The fluid equations derive from taking mathematical moments of the Boltzmann equation (from kinetic theory, Eq. 6.1) by integrating over velocity space; see Eq. 6.2. In Eq. 6.1, the phase space distribution function for all particles of species "s" is $\mathbf{f_s} = \mathbf{f_s}(\mathbf{x}, \mathbf{v}, t)$, with time t, spatial coordinate $\mathbf{x}$, velocity coordinate $\mathbf{v} = \partial\mathbf{x}/\partial t$, acceleration $\mathbf{a} = \partial\mathbf{v}/\partial t$, and a collision integral between species "s" and "s' " of $\sum_{s'} C_{ss'}(\mathbf{f_s}\ ,\ \mathbf{f_{s'}})$. Also, for clarity, $\partial\mathbf{f_s}/\partial\mathbf{x} = \nabla_x\mathbf{f_s}$, and, often, for example, $\mathbf{a} = (q_s/m_s)(\mathbf{E} + \mathbf{v}\ \times\ \mathbf{B})$ for the Lorentz force, with charge q_s, mass m_s, electric field $\mathbf{E}$, and magnetic field $\mathbf{B}$. The zeroeth moment gives the continuity equation (conservation of mass and particle number); the first moment gives conservation of momentum; the second moment gives conservation of energy; the third moment gives the heat transfer equation. Furthermore, the conservation equations can be written in "conservation form," shown in Eq. 6.3, where Q is some quantity (scalar or vector), $\mathbf{F}(Q)$ is the flux of Q, and S(Q) is the source of Q. The solution of each moment equation introduces

a higher order moment equation. Therefore, to close (solve for) the system of equations, we make an assumption about the highest-order moment equation that we consider. In the version of the PERSEUS code most commonly used by the author, we make an approximation to ignore the heat flow from the third moment equation, assuming (local) thermal equilibrium within a region, and we assume an ideal equation of state for an isotropic pressure $P_s = n_s k_B T_s$, with number density n_s, Boltzmann constant k_B, and temperature T_s. These assumptions give 5 moment equations (for each species): 1 for particle conservation, 3 for momentum conservation, and 1 for (isotropic) energy conservation. Then, the fluid conservation equations for species "s" are given by Eq. 6.4– Eq. 6.7, with fluid velocity $\mathbf{u_s}$, first moment of the collision integral $\sum_{s'} R_{ss'}$ (represents friction), energy ϵ_s, second moment of the collision integral $\sum_{s'} K_{ss'}$ (represents collisional heating rate and thermal equilibration), and adiabatic index γ_s ($= 5/3$ for ideal polytropic gas but can be less for partially-ionized ions, say $\sim$1.15 for Z=3 aluminum).

$$\frac{\partial \mathbf{f_s}}{\partial t} + \mathbf{v} \cdot \frac{\partial \mathbf{f_s}}{\partial \mathbf{x}} + \mathbf{a} \cdot \frac{\partial \mathbf{f_s}}{\partial \mathbf{v}} = \sum_{s'} C_{ss'}(\mathbf{f_s}\ ,\ \mathbf{f_{s'}}) \tag{6.1}$$

$$nth\ moment\ (with\ n\ \mathbf{v}'s\ in\ the\ parentheses) : \int_{-\infty}^{\infty} d\mathbf{v}\ (\mathbf{vv}...\mathbf{v})\ \mathbf{f_s} \tag{6.2}$$

$$\frac{\partial Q}{\partial t} + \nabla \cdot \mathbf{F}(Q) = S(Q) \tag{6.3}$$

$$\frac{\partial n_s}{\partial t} + \nabla \cdot (n_s \mathbf{u_s}) = 0 \tag{6.4}$$

$$\frac{\partial (m_s n_s \mathbf{u_s})}{\partial t} + \nabla \cdot (m_s n_s \mathbf{u_s} \mathbf{u_s} + \underline{\underline{\mathbf{I}}} P_s) = q_s n_s (\mathbf{E} + \mathbf{u_s} \times \mathbf{B}) + \sum_{s'} R_{ss'} \tag{6.5}$$

$$\frac{\partial \epsilon_s}{\partial t} + \nabla \cdot [\mathbf{u_s}(\epsilon_s + P_s)] = q_s n_s \mathbf{u_s} \cdot \mathbf{E} + \sum_{s'} K_{ss'} \tag{6.6}$$

$$where : \epsilon_s = \frac{1}{2} m_s n_s {\mathbf{u_s}}^2 + \frac{P_s}{\gamma_s - 1} \tag{6.7}$$

Among other assumptions, the plasma fluid approximation assumes 1) large enough collisionality for Maxwellian particle distributions (locally given by Eq. 6.8), 2) large enough length scales compared with the mean free path ($L_0 >> \lambda_{mfp}$; in Appendix A, see Table A.2 and Table A.3), and, typically, 3) electrical quasineutrality of the ions and electrons ($n_e = Z n_i$ with ionization state Z; this condition typically requires characteristic length scales larger than the Debye length, $L_0 >> \lambda_{D_e}$, and characteristic frequencies (inverse time scales) smaller than the electron plasma frequency $\omega_0 << \omega_{p_e}$). In the fluid approximation, plasma dynamics are determined by Maxwell's equations (Eq. 6.9– Eq. 6.12) and the fluid conservation equations. Additionally, in the magnetohydrodynamics approximation, the plasma is treated as a single fluid in the center of mass reference frame of the ions and electrons, with conservation equations given by Eq. 6.13– Eq. 6.21, where η is the electrical resistivity (in Appendix A, see Table A.3; here, taken as a scalar, although more generally a tensor quantity). As an approximation, because of the mass differences in this "single fluid" ($m_e << m_i$), the ions carry most of the momentum ($\mathbf{u} \approx \mathbf{u_i}$). In the single-fluid approximation, the electrons and ions have the same single-fluid temperature ($T = T_i = T_e$). In the extended magnetohydrodynamics formulation imple-

mented in the PERSEUS code that simulates the radial foil in 2D (finite volume (FV)), the two-fluid equations contain the physics of both the ions and electrons. In PERSEUS, the ions and electrons can have different temperatures because each species has its own energy conservation equation that includes thermal equilibration between species.

$$\mathbf{f_s}(\mathbf{x},\mathbf{v},t) = n_s(\mathbf{x},t)\left(\frac{m_s}{2\pi k_B T_s(\mathbf{x},t)}\right)^{3/2}\exp\left[\frac{-m_s\mathbf{v}^2}{2k_B T_s(\mathbf{x},t)}\right] \tag{6.8}$$

$$\nabla\cdot\mathbf{E} = \frac{\rho_c}{\epsilon_0} \tag{6.9}$$

$$\nabla\cdot\mathbf{B} = 0 \tag{6.10}$$

$$\nabla\times\mathbf{E} = -\frac{\partial\mathbf{B}}{\partial t} \tag{6.11}$$

$$\nabla\times\mathbf{B} = \mu_0\mathbf{J} + \frac{1}{c^2}\frac{\partial\mathbf{E}}{\partial t} \tag{6.12}$$

$$\rho = \sum_s m_s n_s \tag{6.13}$$

$$\mathbf{u} = \frac{1}{\rho} \sum_s m_s n_s \mathbf{u_s} \tag{6.14}$$

$$\frac{\partial \rho}{\partial t} + \nabla \cdot (\rho \mathbf{u}) = 0 \tag{6.15}$$

$$\frac{\partial \rho \mathbf{u}}{\partial t} + \nabla \cdot (\rho \mathbf{u}\mathbf{u}) = -\nabla P + \mathbf{J} \times \mathbf{B} \tag{6.16}$$

$$\frac{\partial \epsilon}{\partial t} + \nabla \cdot [\mathbf{u}(\epsilon + P)] = \mathbf{u} \cdot (\mathbf{J} \times \mathbf{B}) + \eta \mathbf{J}^2 \tag{6.17}$$

$$equivalently : \frac{\partial P}{\partial t} + \mathbf{u} \cdot \nabla P + \gamma P \nabla \cdot \mathbf{u} = (\gamma - 1)\eta \mathbf{J}^2 \tag{6.18}$$

$$where : \epsilon = \sum_s \epsilon_s \tag{6.19}$$

$$where : P = \sum_s P_s \tag{6.20}$$

$$where : \mathbf{J} = \sum_s n_s q_s \mathbf{u_s} \tag{6.21}$$

In order to mathematically solve for all variables in the system of equations of Maxwell's equations and the fluid equations, the Generalized Ohm's Law relates the single fluid velocity $\mathbf{u}$, electric field $\mathbf{E}$, magnetic field $\mathbf{B}$, and current density $\mathbf{J}$, as shown in Eq. 6.22 with simplifications in Eq. 6.23– Eq. 6.27, with elementary electric charge $e = q_e$. The Generalized Ohm's Law equation can be generated by combining the ion and electron momentum equations scaled by their respective charge to mass ratios (q_s/m_s). The Generalized Ohm's Law can be viewed 1) as an equation equating the electric field with contributing components or 2) as a time evolution equation for the current density. To close the system of equations, when the Generalized Ohm's Law equation is solved, the solved-for electric field and/or current density can then be substituted into the fluid conservation equations and Maxwell's equations: that is, 1) electric field put into Faraday's Law to time-evolve the magnetic field, called the Induction

equation, or 2) current put into Ampere-Maxwell's Law to time-evolve the displacement current ($(1/c^2)\partial\mathbf{E}/\partial t$).

$$\frac{m_e}{n_e e^2}\left(\frac{\partial \mathbf{J}}{\partial t} + \nabla\cdot\left[\mathbf{uJ} + \mathbf{Ju} - \frac{1}{n_e e}\mathbf{JJ}\right]\right) = \mathbf{E} + \mathbf{u}\times\mathbf{B} - \eta\mathbf{J} - \frac{\mathbf{J}\times\mathbf{B}}{n_e e} + \frac{\nabla P_e}{n_e e} \quad (6.22)$$

$$relaxed\ XMHD: 0 = \mathbf{E} + \mathbf{u}\times\mathbf{B} - \eta\mathbf{J} - \frac{\mathbf{J}\times\mathbf{B}}{n_e e} + \frac{\nabla P_e}{n_e e} \quad (6.23)$$

$$Hall\ MHD: 0 = \mathbf{E} + \mathbf{u}\times\mathbf{B} - \eta\mathbf{J} - \frac{\mathbf{J}\times\mathbf{B}}{n_e e} = \mathbf{E} + \mathbf{u_e}\times\mathbf{B} - \eta\mathbf{J} \quad (6.24)$$

$$with: \mathbf{u_e} = \mathbf{u} - \frac{1}{n_e e}\mathbf{J} \quad (6.25)$$

$$resistive\ MHD\ (for\ n=\infty): \mathbf{E} + \mathbf{u}\times\mathbf{B} = \eta\mathbf{J} \quad (6.26)$$

$$ideal\ MHD\ (for\ n=\infty\ and\ \eta = 0): \mathbf{E} + \mathbf{u}\times\mathbf{B} = 0 \quad (6.27)$$

Some useful comparisons can be made by taking the ratio of the terms in the Generalized Ohm's Law. First, we define the terms in Eq. 6.22 as: the electron inertial term on the left hand side, the electric field in the co-moving frame of the plasma $\mathbf{E}' = \mathbf{E} + \mathbf{u}\times\mathbf{B}$, the dynamo term $\mathbf{u}\times\mathbf{B}$, the resistive term $\eta\mathbf{J}$, the Hall term $(\mathbf{J}\times\mathbf{B})/n_e e$, and the electron pressure term $(\nabla P_e)/n_e e$. The ratio of the Hall term to the dynamo term scales as the ratio of the ion inertial length to the characteristic system scale (λ_i/L_0), and the ratio of the Hall term to the resistive term scales as the ratio of the electron cyclotron frequency to the collision frequency (ω_{c_e}/ν_{ei}; also the electron magnetization in Appendix A, see Table A.3). These ratios are further discussed in Sec. 7.1.2. Generally, the Hall term becomes important in low density regions– for example, at the interface between a dense plasma expanding into a vacuum.

6.2 PERSEUS Algorithm

The author would like to thank, in particular, Nat Hamlin and Charlie Seyler for helping me to understand (a bit about) how the PERSEUS code works.

The PERSEUS code solves Maxwell's equations, the fluid conservation equations, and the Generalized Ohm's Law. PERSEUS utilizes the Generalized Ohm's Law as a time evolution equation for the current density. In the most basic version of the code, there are 14 dependent variables: density, 3 velocity components, energy density, 3 magnetic field components, 3 electric field components, and 3 current density components. For a numerical simulation to efficiently calculate equations, putting the equation variables into a dimensionless form is important, so the computer does not have to keep track of unnecessarily large or small numbers; see Appendix G.

Some main advantages of PERSEUS compared to other codes include handling up to 9 orders of magnitude in density variation, the physical treatment of the plasma-vacuum interface, and computing Hall physics and electron inertial physics over large spatial and time scales (in a manner that is not "prohibitively computationally expensive"). For treatment of the plasma-vacuum interface, PERSEUS keeps the electron momentum equation and includes both Hall physics and electron inertial physics, thereby removing the need of a non-physical resistivity in MHD vacuum to prevent large currents. Furthermore, PERSEUS also has the capability to do (resistive) MHD modeling, permitting direct comparison to XMHD.

A "relaxation method" permits computationally efficient simulations of Hall physics and electron inertial physics without needing to explicitly resolve the

electron plasma frequency and electron inertial length. Here, computational efficiency refers to the ability to use large enough timesteps given the computational domain. The typical laboratory experiment occurs over more than 100 ns, but the typical electron cyclotron frequency timescale ($T = 2\pi/\omega$) is $1.8 * 10^{-2}$ ns, and the typical electron plasma frequency timescale is $6.4 * 10^{-5}$ ns (in Appendix A, see Table A.3). Additionally, the typical laboratory experiment system is larger than 10 mm, and the typical electron inertial length is $3.1 * 10^{-3}$ mm, and the typical (electron) Debye length is $2.4 * 10^{-5}$ mm (in Appendix A, see Table A.3). Explicitly resolving these timescales and length scales would require a "prohibitive amount" of computational time; additionally, resolving length scales much smaller than the collisional mean free path conflicts with the continuum fluid approximation (a non-kinetic treatment).

The relaxation method is formulated from the Ampere-Maxwell law (from Eq. 6.12) and the Generalized Ohm's Law (from Eq. 6.22) in conservation form (Eq. 6.3): shown in Eq. 6.28 and Eq. 6.29 using dimensionless code units, where "k" (superscript) is the time step and "k+1" is the subsequent time step. Here, the terms c^2/v_0^2 (square of the scaled speed of light) and L_0^2/λ_e^2 act as relaxation parameters that determine steady-state equilibrium (for large time steps; as the relaxation parameters approach ∞). This is a "local semi-implicit" scheme where the electric field and current density are implicitly time advanced, as they appear in the source terms only– not the flux terms (which have spatial derivatives). This avoids the need for a global implicit solver (a large matrix or linear system of equations solver).

$$\frac{\mathbf{E}^{k+1}-\mathbf{E}^{k}}{\Delta t}=\frac{c^2}{v_0^2}(\nabla\times\mathbf{B}^{k}-\mathbf{J}^{k+1}) \quad (6.28)$$

$$\frac{\mathbf{J}^{k+1}-\mathbf{J}^{k}}{\Delta t}=-\nabla\cdot\mathbf{F}^{k}+\frac{n_e^k L_0^2}{\lambda_e^2}(\mathbf{E}^{k+1}+\mathbf{u}^{k}\times\mathbf{B}^{k}-\frac{\lambda_i}{n_e^k L_0}\mathbf{J}^{k+1}\times\mathbf{B}^{k}-\eta\mathbf{J}^{k+1}) \quad (6.29)$$

The flux term in Eq. 6.29 ($\nabla\cdot\mathbf{F}^{k}$, including both the electron inertial flux and the electron pressure gradient) is computed separately with an explicit time advance. Explicitly time advancing the electron pressure term (which scales similarly to the Hall term) can introduce some numerical stability issues. For the other fluxes (particle density, momentum, and energy), the second order finite volume (FV) method uses neighboring cell data to compute the fluxes into and out of the cell boundaries (based on integrating the conservation equation Eq. 6.3 over the grid cell). Another option is the discontinuous Galerkin (DG) method, which assumes the conserved quantity takes some functional form throughout the grid cell, with separate evolution equations for each of the coefficients of the basis functions. [64] Compared to the FV code, the DG code is less numerically diffusive and allows for the modeling of shock structures and instabilities with a fewer number of grid cells. We briefly note here that PERSEUS is an Eulerian code, meaning the computational grid mesh is fixed.

As of this writing, the PERSEUS code is a work-in-progress. Possible future developments include 1) extending the fluid moment formulation to model heat flow (and effects like heat conduction and the Nernst effect), 2) incorporating multiple ion species, 3) using an anisotropic pressure tensor rather than scalar pressure, 4) incorporating radiation transfer and a self-consistent ionization model, 5) utilizing equation of state data (like from the SESAME tables or other better resources), and 6) incorporating relativistic modeling.

6.3 2D Radial Foil Simulations

In this thesis, most of the simulation results are from radial foil simulations. These finite volume (FV) simulations are 2D in the r-z plane (cylindrical coordinates) with a corresponding forced azimuthal symmetry. The grid is 20 mm (300 cells, r-direction) by 15 mm (225 cells, z-direction) with 67 μm spatial resolution. The initial conditions are as follows: an optional axial magnetic field (B_z, initially uniform), room temperature (0.026 eV), a background vacuum density of $6 * 10^{13}\ cm^{-3}$, a center pin with a density of $6 * 10^{22}\ cm^{-3}$ that is masked such that no particles have momentum within the pin grid cells, and a foil (aluminum) that is 1 grid cell thick (67 μm) with a density of $9 * 10^{21}\ cm^{-3}$. The initial foil density is smaller than solid density because a 67 μm solid density foil ablates slower than the experimental conditions of a 15-20 μm foil; therefore, decreasing the initial density in the simulation acts to increase the rate at which the current pulse will cause foil ablation. Furthermore, in this version of the code, the initial foil and the ablated plasma have a Spitzer resistivity.

Current through the foil is driven by applying an azimuthal (out-of-the-plane of the simulation) magnetic field along the lower-z boundary (below the foil) outside of the center pin radius, based on $B_\theta = \mu_0 I/2\pi r$. The current polarity (direction) can be changed by changing the mathematical sign of I, thereby changing the sign of B_θ. Unless otherwise noted, the simulation models the COBRA current pulse as $I(t) = I_{max} * \sin^2(0.5 * \pi * t/100)$ for the initial 100 ns rise time with time t in nanoseconds, where I_{max}= 1 MA. After 100 ns, we let $I(t) = I_{max}$. See Fig. 6.1 for a picture of the 2D radial foil simulation at time t = 0 ns; blue is the vacuum region, red is the center pin, and orange-yellow-green is the foil.

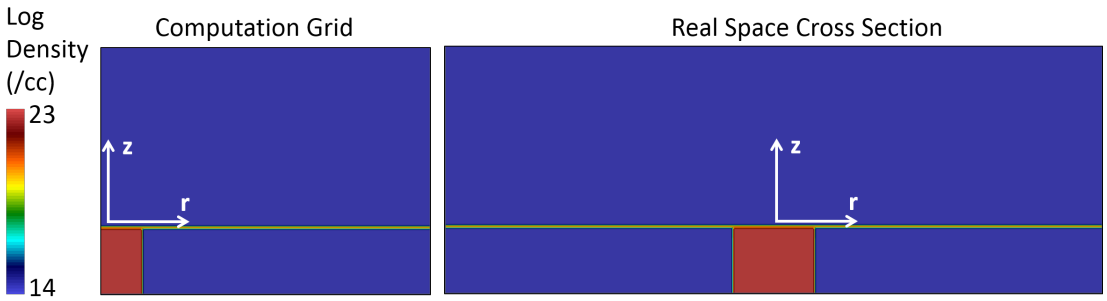

Figure 6.1: Density at initial time t = 0 ns for the computational domain (left) and a reflection showing a real space cross section for the azimuthally symmetric simulation (right). Here, the pin radius (left) is 2.5 mm, and pin diameter (right) is 5.0 mm.

6.4 3D Slab Simulations

In order to investigate fundamental material ablation physics related to the radial foil, we use a discontinuous Galerkin (DG) 3D simulation with Cartesian coordinates. [64] With the DG method, we use a linear basis with bilinear and trilinear elements {1,x,y,z,xy,yz,zx,xyz}. This version of the PERSEUS code treats the plasma as a single fluid with Hall MHD, including the Hall term in the Generalized Ohm's Law but not the electron pressure term due to numerical stability issues. The resistivity and equation of state (EOS) data for aluminum are interpolated using published experimental data from the solid phase to the plasma phase. [65, 66, 67, 68] In the plasma phase, we use the Spitzer conductivity and a plasma EOS (P = nkT).

The DG method allows for sufficient resolution to model a $\sim$20-25 μm thick foil. The DG method captures spatial variation locally within a single grid cell, and this allows for better resolution than the finite volume (FV) method, for which the function is assumed constant within the grid cell. Here, we are concerned with accurately modeling current diffusion through the solid foil thick-

ness rather than accurately modeling smaller scale structures within the foil. Full spatial resolution is important in order to correctly model diffusion of the current pulse through a foil that has an accurate electrical resistivity. The diffusion time, τ, is approximately related to the material thickness, δ, and resistivity, ρ, by $\tau \sim \mu\delta^2/\rho$, where μ is the permeability of the material. Examination of this parameter shows the importance of resolving the foil thickness in the simulation. Suppose the computation grid size (and minimum computation foil thickness, δ) is 4 times larger than the actual (experimental) foil thickness. Then, in order to achieve the same diffusion penetration time (τ) of the current pulse, the resistivity (ρ) of the foil material within the grid cell must be increased by a factor of 16. Furthermore, in order to have the same total foil material mass, a computation grid size 4 times larger than the foil thickness necessitates an initial density within the grid cell that is a factor of 4 times smaller than solid density. Because the material resistivity and EOS are important for the ablation physics investigated in this work, we want the foil thickness to be fully resolved and the foil initialized at solid density. Again for reference, we note that, for the 100 ns zero-to-peak COBRA current pulse, room temperature aluminum has a calculated skin depth of $\sim$40 μm for the experiments relevant to the simulation parameters presented here.

The computational grid is 2 mm (x direction) by 2 mm (y direction) by 2 mm (z direction) with 25 μm spatial resolution. We initialize the foil as a 2 mm by 2 mm by 25 μm aluminum block (or slab) in the x, y, and z directions, respectively. Figure 6.2 displays a diagram of the simulation setup. The foil grid cells have a (maximum) 0.5% random density perturbation. There are periodic boundary conditions in the x and y directions and open boundary conditions in the z directions. Current in the x direction through the foil, $J_x(t)$,

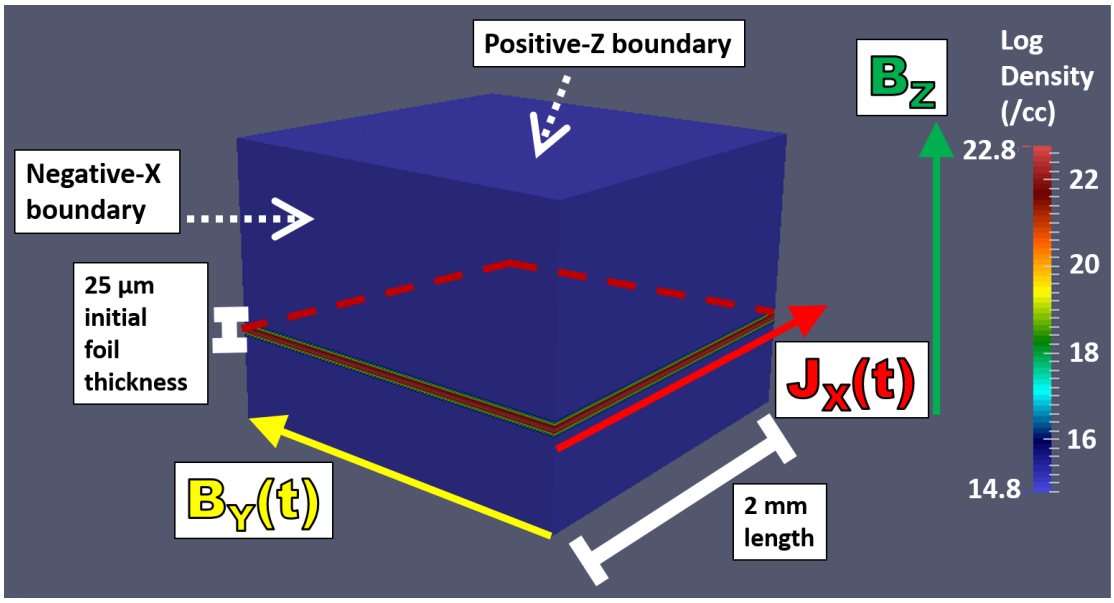

Figure 6.2: Computational domain (rectangular prism) at 45 ns into current pulse. Foil density has expanded slightly compared to 0 ns. Dashed red lines show the position of the foil edges that are not visible. Red arrow: current through foil in x direction. Yellow arrow: driving magnetic field in y direction applied along negative-z boundary. Green arrow: applied external magnetic field in z direction.

is driven by a magnetic field in the y direction, $B_y(t)$, placed as a boundary condition along the negative-z boundary of the computational domain. The $J_x B_y$ component of the J $\times$ B force accelerates the foil in the positive z direction. For the initial 100 ns rise time, the current, I, is modeled after the COBRA pulse as $I(t) = I_{max} \sin^2(0.5\pi t/100)$ with the time, t, in nanoseconds, and where I_{max} = 1 MA. The current density through the aluminum slab is set to be approximately equivalent to the current density that travels through the radial foil at the 2.5 mm pin radius. Additionally, an external magnetic field, B_z, can be applied along the z direction (the direction of the initial 25 μm foil thickness).

In these Cartesian simulations, we ignore the radial geometry of the radial foil experiments. If we consider the radial (cylindrical) geometry, taking one 2 mm edge of the foil to be at a radius of 2.5 mm, the foil edge at a radius of

4.5 mm would correspond to a distance of 3.6 mm; this piece of foil in the experiment is certainly not a Cartesian square. However, neglecting the effects of radial convergence and curvature, this block of foil material in Cartesian coordinates can approximate a section of the radial foil. The current $J_x(t)$ in the x-direction in the simulation corresponds with current along the radial direction for a radial foil, and the applied external magnetic field B_z in the simulation corresponds to an axial magnetic field (in the z-direction for a radial foil).

CHAPTER 7

RESULTS: EXPERIMENTS AND SIMULATIONS

7.1 Jet Development and XMHD Effects

In Fig. 7.1, Fig. 7.2, and Fig. 7.3, we present results from 2D radial foil PERSEUS simulations showing the plasma jet development for different cases. In Fig. 7.1, we show the jet time evolution in standard polarity with no applied magnetic field ($B_z = 0$ T) and a 1 T B_z. In Fig. 7.2, where the z-axis is on the left of the image, we display the in-plane (r-z) current density streamlines and magnetic field lines. In Fig. 7.3, we compare the influence of XMHD to (resistive) MHD when changing current polarities. The following subsections elaborate upon these plasma jet dynamics.

7.1.1 Dynamics Overview

First, we describe the overall plasma jet dynamics. As the COBRA current pulse travels through the radial foil, the Ohmic (Joule) heating power per unit length $P/(dr) = I^2R/(dr) = I^2\rho/2\pi rh \propto I^2/r$ causes the foil to ablate: melt, vaporize, and ionize into a surface plasma above the foil. Here, R is the resistance and ρ is the resistivity. The current I is dispersed within an annulus of the foil (with infinitesimal thickness dr) at radius r with cross-section area $A = 2\pi rh$, where h is the foil thickness. Therefore, the (radial) current density through the foil is $J_r = I/2\pi rh$. The current traveling through the center pin creates a magnetic field $B_\theta = \mu_0 I/2\pi r$ beneath the foil. Therefore, the force on the ablating foil plasma that causes expansion is $J \times B \sim J_r B_\theta = \mu_0 I^2/4\pi^2 r^2 h \propto 1/r^2$ in the

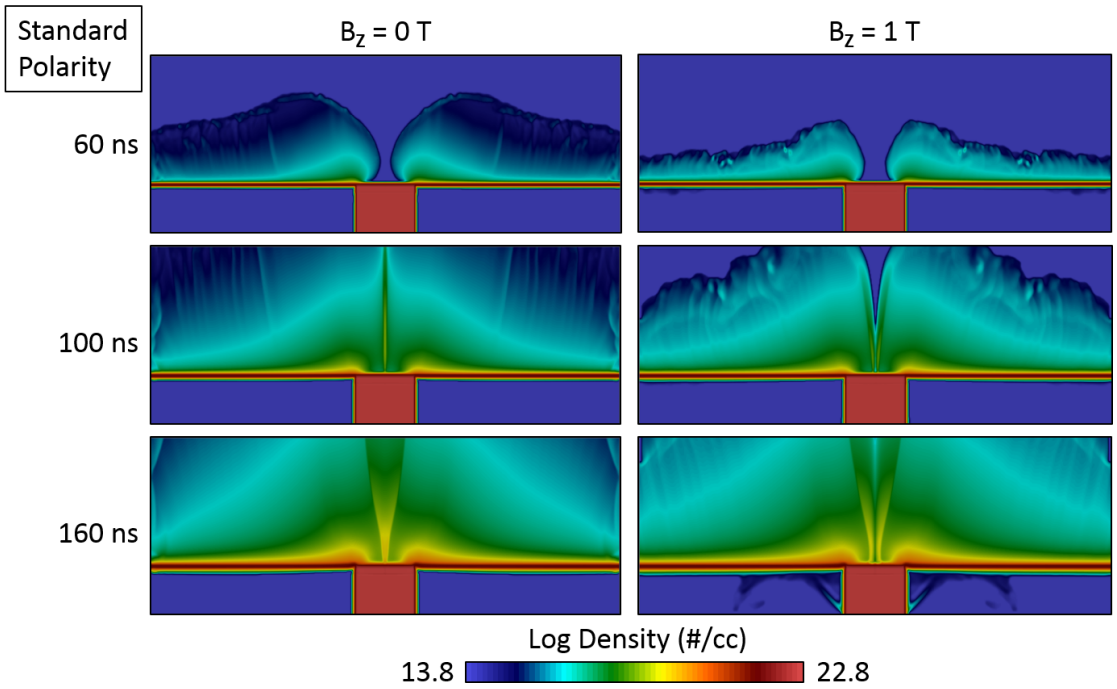

Figure 7.1: PERSEUS simulation time evolution for radial foil plasma jet ion density in standard polarity with no applied magnetic field and a 1 T B_z. 5 mm pin diameter.

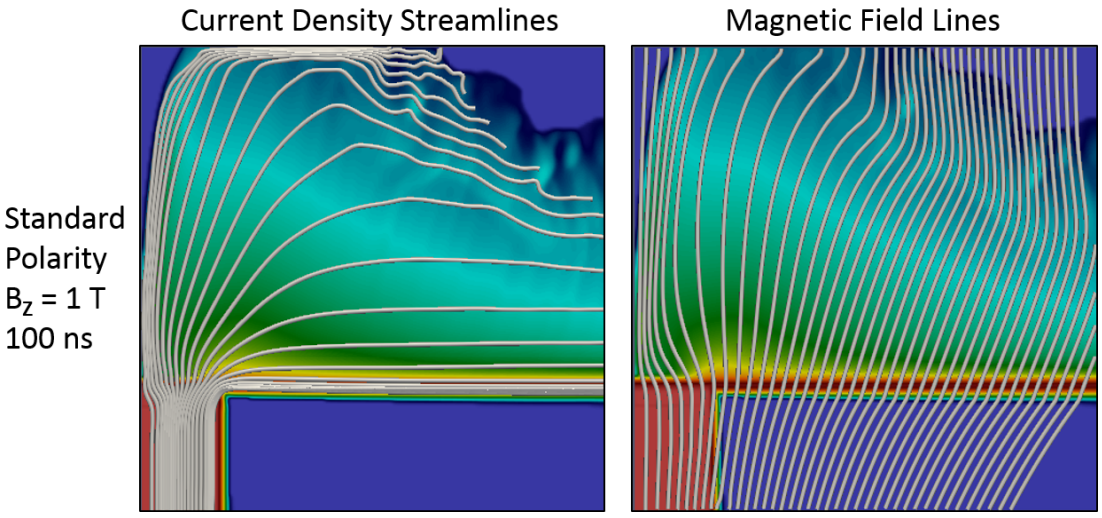

Figure 7.2: PERSEUS simulation showing in-plane (r-z) streamlines of current density and in-plane magnetic field lines, overlayed on ion density (color). 2.5 mm pin radius.

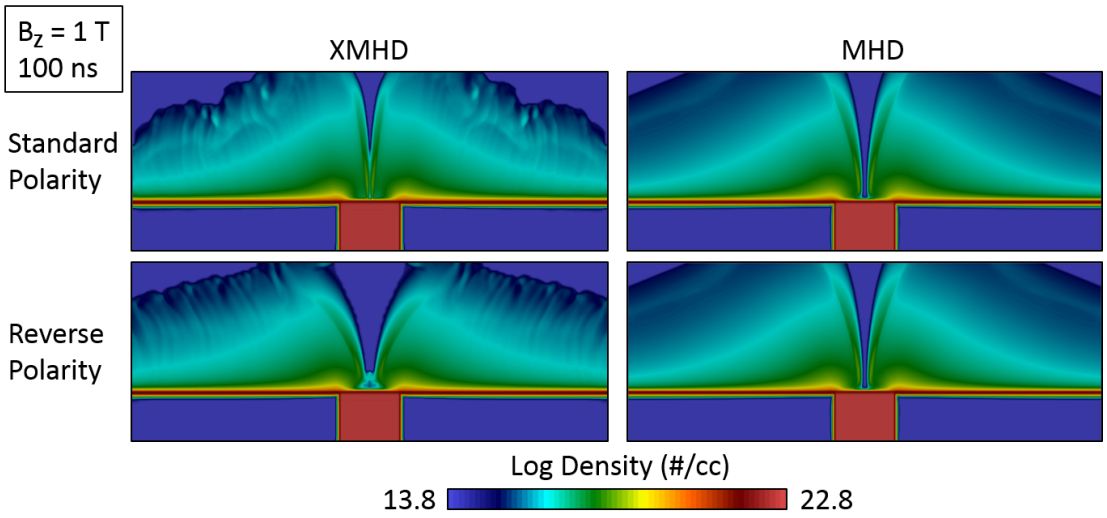

Figure 7.3: PERSEUS simulations for XMHD and MHD of plasma jets with $B_z = 1$ T under standard and reverse current polarities. Notice the MHD results are identical, while the XMHD results are not identical. 5 mm pin diameter.

positive z direction. The surface plasma expanding upward into the vacuum region has current traveling through the plasma in both the radial (r) and axial (z) directions; see Fig. 7.2 (left image). The axial current necessarily completes the electrical circuit through the plasma from anode to cathode. The axial current (J_z) self-generates a magnetic field (B_θ) which produces a well-collimated plasma jet on-axis due to converging plasma from the Z-pinch force ($J_z B_\theta$). Additionally, there is the pressure gradient force ($-\nabla P$) as the plasma expands into vacuum. The current in the plasma jet is estimated at around 2-5% of the total COBRA current using the 2D radial foil PERSEUS code at 100 ns (time of peak current) and estimated at around 5-10% using dB/dt (or B-dot) probes at 70 ns (using a 5 μm thick foil in previous experimental work). [30] The remainder of the COBRA current travels (radially) through the high-density solid-liquid foil and surface plasma directly above the foil.

The ablation process that generates the surface plasma from the initially

solid foil will be considered in further detail in Sec 7.5. Semi-quantitatively, one can think of the energy required to generate the plasma as $\Delta E = mc_v\Delta T + mL_f + mL_v + E_I^1$ with mass m, specific heat c_v, temperature T, latent heat of fusion (melting) L_f, latent heat of vaporization (boiling) L_v, and first ionization energy E_I^1. In general, the heat capacity is a function of temperature and phase (equation of state); furthermore, the heating power $P = dE/dt = I^2R$ depends upon the resistance R, which is also a function of temperature.

The higher-density jet is formed from the converging lower-density "background plasma." The boundary between the jet and background plasma is defined by the approximate radial force balance, taking the radial component of Eq. 6.16 and demanding $\partial(\rho u)/\partial t \approx 0$, as shown in Eq. 7.1 with plasma density ρ, fluid velocity u, current density J, magnetic field B, thermal pressure P, and radius r of the jet. From left to right the terms in Eq. 7.1 are the dynamical converging flow of background plasma toward the central z-axis (ram pressure; full term in brackets), the thermal pressure gradient, pinching force (Z-pinch), axial magnetic pressure related to field compression, and centrifugal rotation. The thermal pressure force, axial magnetic pressure, and centrifugal rotation force are directed radially outward. The dynamical pressure force and Z-pinch force are directed radially inward. With no applied axial magnetic field (B_z), the rightmost two terms are zero. By performing some math magic (algebra), one can solve for the jet radius at which there is an approximate radial force balance, $r^0(z)$, as written in Eq. 7.2 and illustrated in Fig. 7.4. Furthermore, an "outer" jet angle θ (between the jet and background plasma) can be defined by Eq. 7.3.

$$0 \approx \{-\frac{1}{r}\frac{\partial(r\rho u_r^2)}{\partial r} + \frac{\partial(\rho u_z u_r)}{\partial z}\} - \frac{dP}{dr} - J_z B_\theta + J_\theta B_z + \frac{\rho u_\theta^2}{r} \tag{7.1}$$

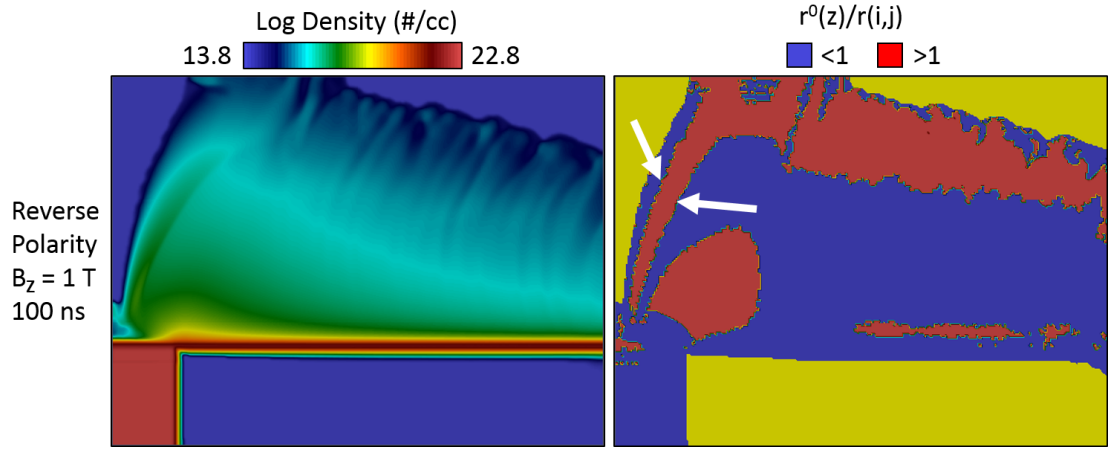

Figure 7.4: PERSEUS simulation of ion density and the ratio of the radius at which there is a calculated approximated radial force balance, $r^0(z)$, to the radius in the simulation, $r(i,j)$. A ratio of 1 means $r(i,j) = r^0(z)$. A ratio < 1 or > 1 does not provide information about the direction of the net radial force. The white arrows point to the inner and outer boundaries of the higher-density plasma jet at which there is an approximate radial force balance. 2.5 mm pin radius.

$$r^0(z) \approx \frac{\rho(u_r^2 - u_\theta^2)}{-\dfrac{\partial(\rho u_r^2)}{\partial r} + \dfrac{\partial(\rho u_z u_r)}{\partial z} - \dfrac{dP}{dr} - J_z B_\theta + J_\theta B_z} \tag{7.2}$$

$$\tan\theta = \frac{r^0(z) - r^0(0)}{z} \tag{7.3}$$

Experimentally, we test the importance of the Hall term in XMHD compared to MHD by changing the direction of current flow (radially inward or outward through the foil), referred to as changing current polarity. A basic understanding of how the current polarity can change the plasma dynamics is as follows. First, let us look at the electron velocity given in Eq. 6.25 as $\mathbf{u_e} = \mathbf{u} - \mathbf{J}/n_e e$ and take the radial component, $u_{e_r} = u_r - J_r/n_e e$. For the converging plasma, u_r is always negative, and J_r is negative for standard current polarity and positive for reverse polarity. Therefore, in reverse polarity compared to standard polarity, u_{e_r} is more negative, and, thereby, the radial convergence is enhanced and the

radial electric field is enhanced. Additionally, one can look at the Generalized Ohm's Law with Hall MHD in Eq. 6.24, rewritten as $\mathbf{E} = -\mathbf{u}\times\mathbf{B}+\eta\mathbf{J}+\mathbf{J}\times\mathbf{B}/n_e e$. First considering the case with no applied axial magnetic field (B_z), changing the current polarity corresponds to changing the mathematical sign of E, J, and B. Under this change of signs, the Hall term in the equation does not change sign while all other terms do. Therefore, without the Hall term (like for resistive MHD in Eq. 6.26), changing the current polarity does not influence the plasma dynamics, as seen in Fig. 7.3. The Hall term breaks the symmetry of the equation, and, experimentally, introduces anode-cathode asymmetries.

The primary effects of the applied axial magnetic field B_z on plasma jet dynamics are as follows: on-axis hollowing of plasma density (see Fig. 7.1); azimuthal rotation; and on-axis compression of the initially uniform applied field. As the lower-density background plasma converges toward the axis, the dynamical pressure forces advect and compress the B_z on-axis; see Fig. 7.2 (right image). The on-axis B_z compression causes the on-axis density hollowing due to the radial force balance (analogous to Eq. 7.1) at the "inner" boundary of the jet between the plasma jet and low-density (vacuum) region that contains the compressed B_z. The discontinuity between a larger compressed B_z on-axis within the vacuum and a smaller B_z within the plasma jet corresponds with an azimuthal current J_θ at the jet boundary needed to support the discontinuity in B_z. Furthermore, the B_z introduces a $J_r B_z$ component of the $\mathbf{J} \times \mathbf{B}$ force that causes azimuthal rotation of the plasma jet and background plasma.

The structural differences between standard and reverse current polarity jets are more apparent with an applied B_z than with $B_z = 0$ T. In reverse current polarity, the jet is wider and has a larger on-axis hollowing compared to standard

polarity. Furthermore, the jet formation can be altered by changing the center pin size (diameter), foil thickness, and foil material. A larger pin size tends to increase the time for the plasma to converge on axis and reduce the jet density on-axis because of the smaller $J_z B_\theta$ pinching force. A thicker foil tends to increase the time to form the jet because it takes longer for Joule heating of the foil to create a surface plasma. In addition to simply having different ion masses, different materials have different properties including radiative effects, conductivity, and equation of state– all of which can influence the plasma ablation process and jet structure.

7.1.2 Parameter Plots

While the estimates given in Appendix A provide approximations for certain parameter regimes within these radial foil experiments, the PERSEUS code can also be used to plot these parameters as a function of space and time. Of particular interest in this work are the following parameters: the ratio of the Hall term to the dynamo term in the Generalized Ohm's Law (from Eq. 6.22), given by Eq. 7.4; the ratio of the Hall term to the electric field in the co-moving frame with the plasma, given by Eq. 7.5; the ratio of the Hall term to the resistive term, given by Eq. 7.6; and the plasma beta, β (the ratio of thermal pressure to magnetic pressure), given by Eq. 7.7. Here, as in Appendix G, we use the notation where $\tilde{Q}$ is the dimensionless value (code units) of quantity Q. After nondimensionalizing the variables, the dimensionless scaling factor in the Hall-dynamo ratio (Eq. 7.4), λ_i/L_0, is the ratio of the ion inertial length to the characteristic length scale. Similarly, the dimensionless scaling factor in the Hall-resistive ratio (Eq. 7.6), ω_{c_e}/ν_{ei}, is the ratio of the electron cyclotron frequency to the electron-

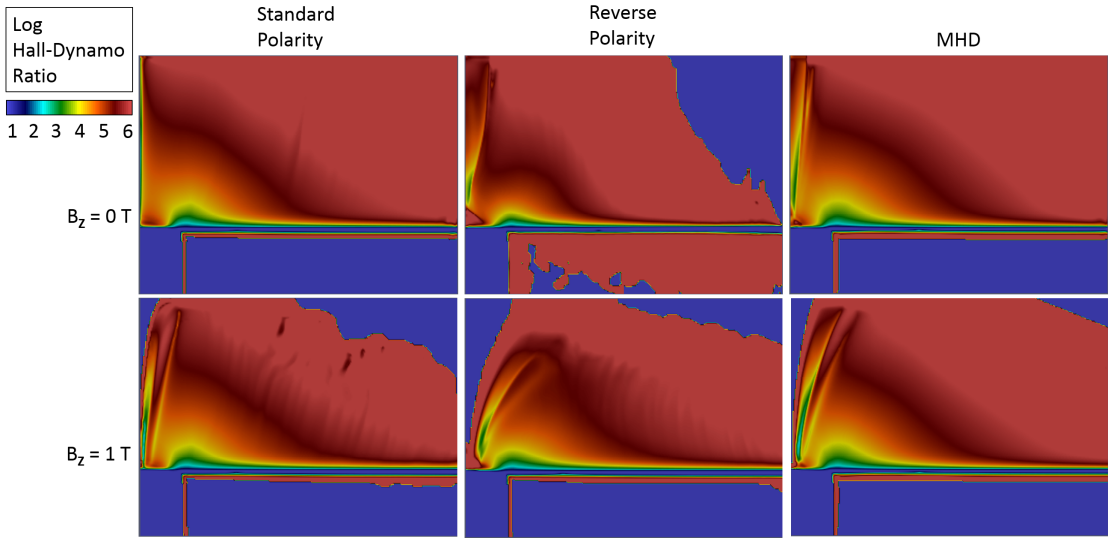

Figure 7.5: Ratio of the Hall term to the dynamo term in the Generalized Ohm's Law for opposite polarities in XMHD and for MHD.

ion collision frequency; this term is equivalent to the electron magnetization.

$$\frac{1}{n_e e}\frac{|\mathbf{J}\times\mathbf{B}|}{|\mathbf{u}\times\mathbf{B}|} = \frac{\lambda_i}{L_0}\frac{|\tilde{\mathbf{J}}\times\tilde{\mathbf{B}}|}{\tilde{n_e}|\tilde{\mathbf{u}}\times\tilde{\mathbf{B}}|} \tag{7.4}$$

$$\frac{1}{n_e e}\frac{|\mathbf{J}\times\mathbf{B}|}{|\mathbf{E}+\mathbf{u}\times\mathbf{B}|} = \frac{\lambda_i}{L_0}\frac{|\tilde{\mathbf{J}}\times\tilde{\mathbf{B}}|}{\tilde{n_e}|\tilde{\mathbf{E}}+\tilde{\mathbf{u}}\times\tilde{\mathbf{B}}|} \tag{7.5}$$

$$\frac{1}{n_e e}\frac{|\mathbf{J}\times\mathbf{B}|}{\eta|\mathbf{J}|} = \frac{\omega_{c_e}}{\nu_{ei}}\frac{|\tilde{\mathbf{J}}\times\tilde{\mathbf{B}}|}{\tilde{n_e}\tilde{\eta}|\tilde{\mathbf{J}}|} \tag{7.6}$$

$$\beta = \frac{n_i k_B T_i + n_e k_B T_e}{\mathbf{B}^2/2\mu_0} = \frac{\tilde{n_i}\tilde{T_i} + \tilde{n_e}\tilde{T_e}}{\tilde{\mathbf{B}}^2/2} \tag{7.7}$$

The Hall-dynamo ratio (Eq. 7.4) is plotted in Fig. 7.5. Here and for the subsequent parameter plots at 100 ns (peak current), we display the computational domain for which the central z-axis is on the left boundary of the image, and the pin radius is 2.5 mm. First, we note that the dimensionless scaling factor $\lambda_i/L_0 \propto m_i^{1/2}/Zn_i^{1/2}L_0$ depends upon the scale length L_0. This dependence means the Hall term is more important relative to the dynamo term for smaller

scales; therefore, the Hall term is more important for smaller laboratory experiments than for larger-scale astrophysical phenomena. In fact, we see that, based upon the characteristic length scale as defined in the simulation, the Hall term dominates the dynamo term within the entire plasma (above the foil), being larger by over 6 orders of magnitude in the low density background plasma. Now, we consider that the dynamo term is generally important due to how it relates to the electric field; thus, one can define the electric field in the co-moving frame of the plasma as $\mathbf{E}' = \mathbf{E} + \mathbf{u} \times \mathbf{B}$. This $\mathbf{E}'$ quantity may be more relevant when compared to the Hall term as in Eq. 7.5 and plotted in Fig. 7.6. Here, we again observe that the Hall term is relatively more important in the low density background plasma– including the low-density regions near the central axis when the B_z is applied. For reasons unknown to the author (likely a parallel processing issue), the computational output for this ratio (and only this ratio) did not process correctly for certain regions within the computational domain at certain times. These areas are marked off with white boxes. Notably, we see the importance of the Hall term in the MHD simulations that do not include the Hall term, again demonstrating the validity of using the XMHD code.

Next, the Hall-resistive ratio (Eq. 7.6) is plotted in Fig. 7.7. We note that the dimensionless scaling factor $\omega_{c_e}/\nu_{ei} \propto BT_e^{3/2}/Zn_e ln(\Lambda)$ does not involve an intrinsic scale length, unlike the dimensionless scaling factor for the Hall-dynamo ratio. Once again, we observe that the Hall term is important in the lower-density plasma regions that create the higher-density jet (when those regions merge as they converge toward the central z-axis). The dimensionless parameter ω_{c_e}/ν_{ei} is equivalent to the electron magnetization. This magnetization parameter includes all magnetic field components (notably B_θ and B_z); only including the B_z component still produces the same trends in the images.

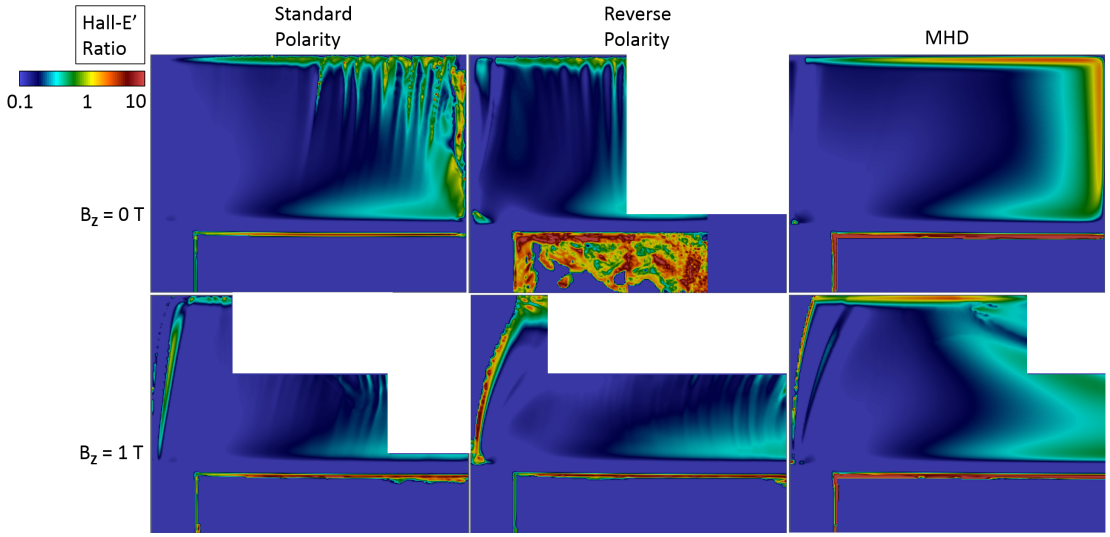

Figure 7.6: Ratio of the Hall term to the electric field in the co-moving frame of the plasma in the Generalized Ohm's Law for opposite polarities in XMHD and for MHD.

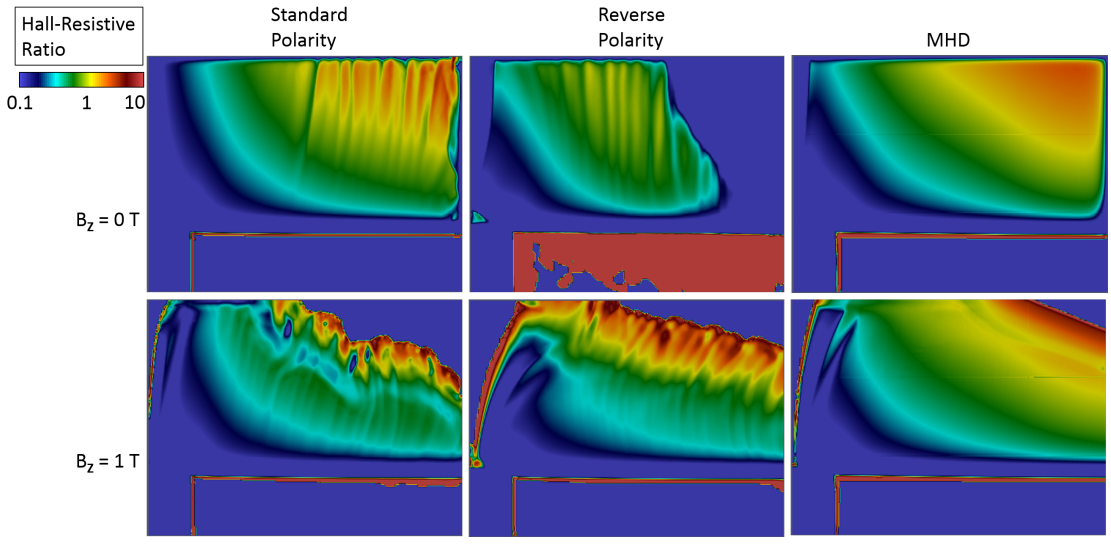

Figure 7.7: Ratio of the Hall term to the resistive term in the Generalized Ohm's Law for opposite polarities in XMHD and for MHD.

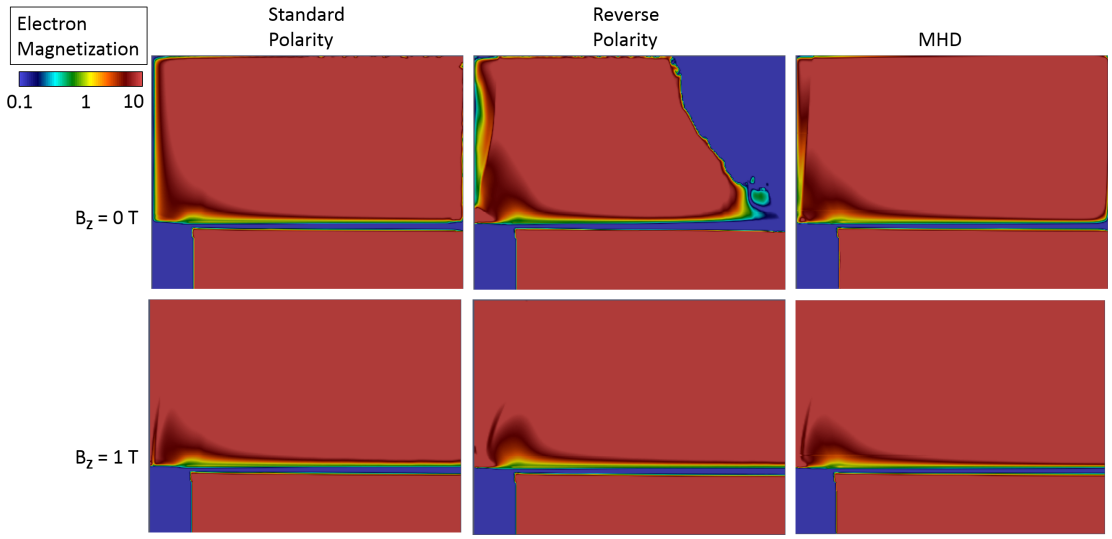

Figure 7.8: Ratio of the electron cyclotron frequency to the electron-ion collision frequency for opposite polarities in XMHD and for MHD.

As plotted in Fig. 7.8, we see that the background plasma electrons are highly magnetized ($\omega_{c_e}/\nu_{ei} > 10$), and the higher density jet is less magnetized. Jets with $B_z = 0$ T are less magnetized than jets with $B_z = 1$ T, again quantifying the influence of the applied magnetic field. Furthermore, we consider the ion magnetization, ω_{c_i}/ν_{ii}, as plotted in Fig. 7.9, which is less than the electron magnetization because $\omega_{c_i} << \omega_{c_e}$ since $1/m_i << 1/m_e$. Here, we find the ions are unmagnetized in most of the background plasma other than some areas near the plasma-vacuum boundary. Additionally, in reverse current polarity, the ions are nearly-magnetized ($\omega_{c_i}/\nu_{ii} \sim 1$) or weakly-magnetized ($1 < \omega_{c_i}/\nu_{ii} < 10$) near the central plasma jet.

Along with looking at how the electrons and ions are magnetized, we can visualize the influence of the applied magnetic field by plotting the plasma beta, β (Eq. 7.7), in Fig. 7.10. A plasma is thermally dominated for $\beta > 1$ and magnetically dominated for $\beta < 1$. For $B_z = 0$ T, we find that the central region near the jet is thermally dominated, and the outer background plasma region is mag-

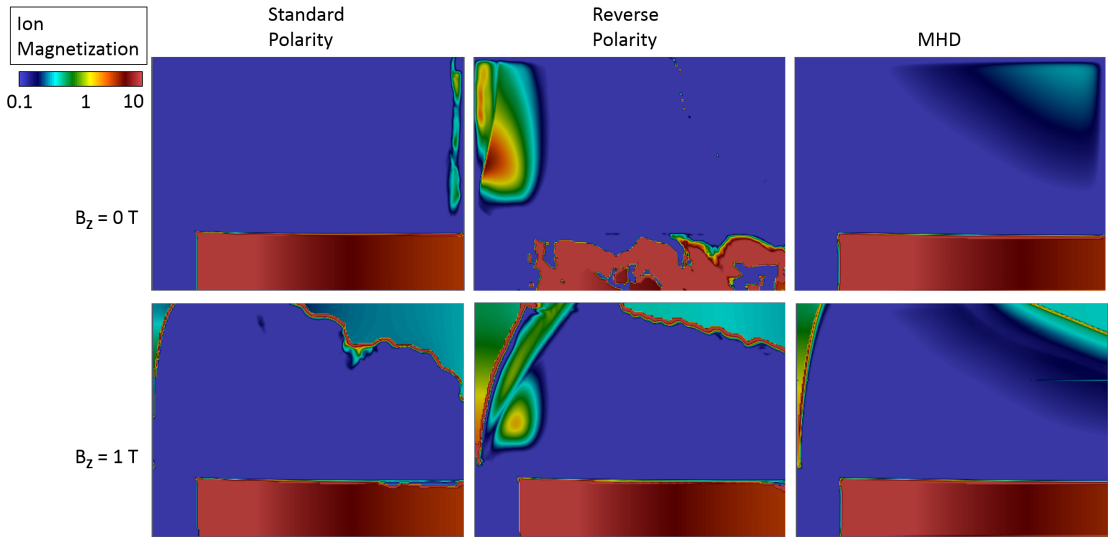

Figure 7.9: Ratio of the ion cyclotron frequency to the ion-ion collision frequency for opposite polarities in XMHD and for MHD.

netically dominated. For $B_z = 1$ T, the background plasma and central region near the jet z-axis is largely magnetically dominated, while the higher-density and higher-temperature jet is thermally dominated.

As a brief summary, from plotting the above parameters, we conclude that XMHD effects like the Hall term can be important in high energy density (HED) laboratory experiments– particularly when the high density plasma is created by the merging of initially lower density plasmas. For our case of the radial foil experiment, the central plasma jet is created by merging of the background plasma. Additionally, we state the plasma is magnetized in the sense that 1) when a magnetic field B_z is applied, there is an initial magnetic field that penetrates through the foil and generated plasma, 2) the background plasma region is magnetically dominated, 3) the electrons are highly magnetized ($\omega_{c_e}/\nu_{ei} > 10$) in the background plasma, and 4) for an initial $B_z = 1$ T, the electrons are magnetized ($\omega_{c_e}/\nu_{ei} > 1$) in the plasma jet, while for $B_z = 0$ T the electrons are either unmagnetized ($\omega_{c_e}/\nu_{ei} < 1$) or weakly magnetized ($1 < \omega_{c_e}/\nu_{ei} < 10$) within

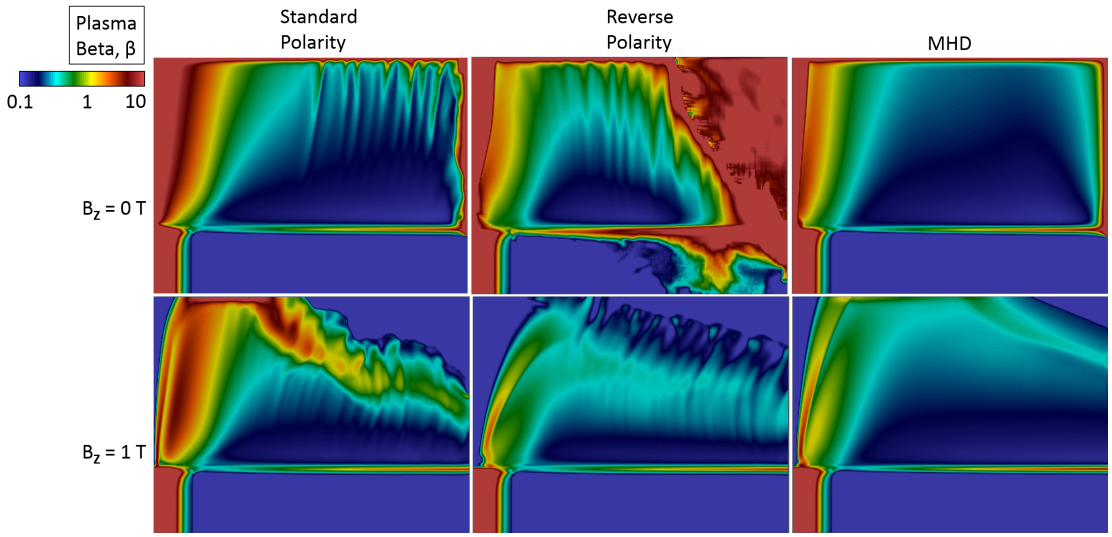

Figure 7.10: Ratio of the thermal pressure to magnetic pressure for opposite polarities in XMHD and for MHD.

the jet. On the other hand, the ions are largely unmagnetized ($\omega_{c_i}/\nu_{ii} < 1$). The parameters described in this subsection are an incomplete list of quantities that allow for further understanding of the physics involved with radial foil plasma jets.

7.1.3 Jet Angles and Widths

In Fig. 7.11, we display experimental images from multiple diagnostics for standard and reverse polarity aluminum jets with an applied $B_z \approx 1$ T: interferometry, shadowgraphy, EUV (or XUV) self-emission, and optical self-emission. We now compare the experimental images in Fig. 7.11 with the XMHD simulation results in Fig. 7.3.

Generally, the plasma jet boundary may have some curvature. Still, we can estimate an average jet angle. Comparing the interferometry and shadowgra-

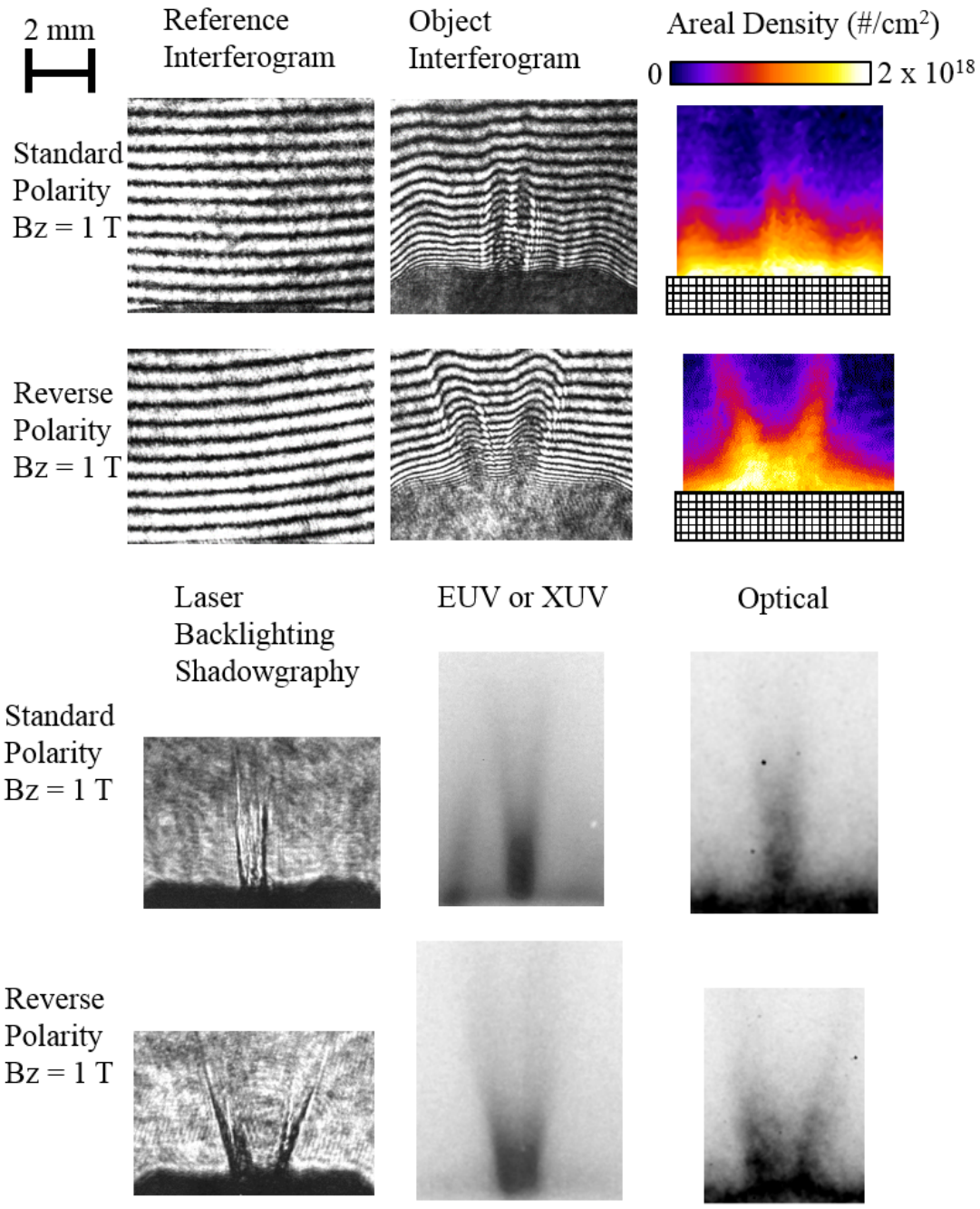

Figure 7.11: Multiple diagnostics showing a standard polarity jet (shot 3602) and a reverse polarity jet (shot 3541) with a 5 mm pin diameter and a 15 μm Al foil. Top two rows: interferometry (shot 3602 at 90 ns; shot 3541 at 130 ns). Bottom two rows: shadowgraphy (90 ns; 130 ns), EUV or XUV self-emission (100 ns; 135 ns), and optical self-emission (150 ns; 155 ns). Adapted from Byvank et al., 2016. [26]

phy experimental results to the simulation density predictions, we measure that reverse polarity jets have a jet angle (defined as twice the angle between the z-axis and the boundary between the jet and background plasma) of $\sim 30 \pm 2^\circ$ in experiments and $\sim 36 \pm 2^\circ$ in simulations, and standard polarity jets have a jet angle of $\sim 7 \pm 2^\circ$ in experiments and $\sim 15 \pm 2^\circ$ in simulations. Additionally, we measure that reverse polarity jets have a base width of $\sim 1.8 \pm 0.2$ mm in experiments and $\sim 1.1 \pm 0.2$ mm in simulations, and standard polarity jets have a base width of $\sim 0.9 \pm 0.2$ mm in experiments and $\sim 0.5 \pm 0.2$ mm in simulations. These quantities are in good agreement considering differences in diagnostic timings, current pulse shapes, foil nonuniformities, and differences between line-integrated experimental data compared with higher resolution simulation cross sections.

For EUV and optical self-emission images of reverse polarity jets, we measure a jet angle $\sim 20 \pm 2^\circ$, approximately 2/3 that of the angle from interferometry and shadowgraphy. For standard polarity jets, we measure approximately the same jet angles $\sim 7 \pm 2^\circ$ for all diagnostics. We measure EUV and optical self-emission jet widths of $\sim 1.5 \pm 0.2$ mm for reverse polarity and $\sim 0.8 \pm 0.2$ mm for standard polarity. Reverse current polarity jet angles are approximately 3 times larger than standard polarity angles, and reverse polarity jet base widths are approximately 2 times larger than standard polarity base widths with a $B_z \sim 1$ T for both experiments and PERSEUS XMHD simulations; resistive MHD simulations depict identical jets for standard and reverse current polarities (see Fig. 7.3). The experimental differences between standard and reverse polarity jets therefore support the XMHD simulations rather than the MHD simulations.

We note that the experimental results are not precisely reproducible because

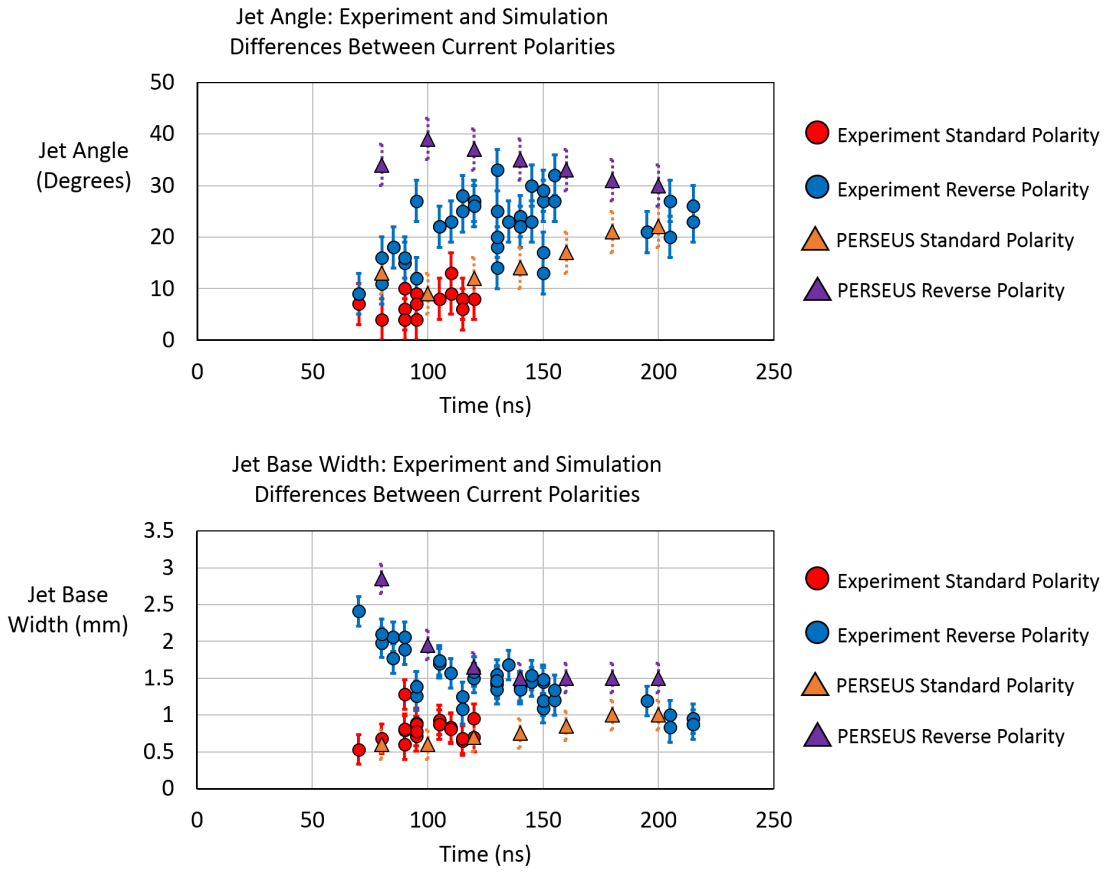

Figure 7.12: Top) jet angle and bottom) jet base width for $B_z \approx 1$ T for experiments (interferometry and shadowgraphy over multiple shots) and simulations (ion density) relative to the time after the start of the COBRA current pulse. Overall, reverse current polarity jets have larger angles and are wider than standard polarity jets.

of differences between experimental shots including diagnostic timings, current pulse shapes, and foil nonuniformities. Now, differently from above, we plot the jet angle defined as twice the angle between the central z-axis and the approximate density maximum within the jet. In Fig. 7.12 for both experiments (interferometry and shadowgraphy over multiple shots) and simulations (ion density), we show that reverse polarity jets have larger angles and are wider than standard polarity jets over the time of the experiment. In Fig. 7.13, we show jet angles relative to the applied B_z for different experiments using vari-

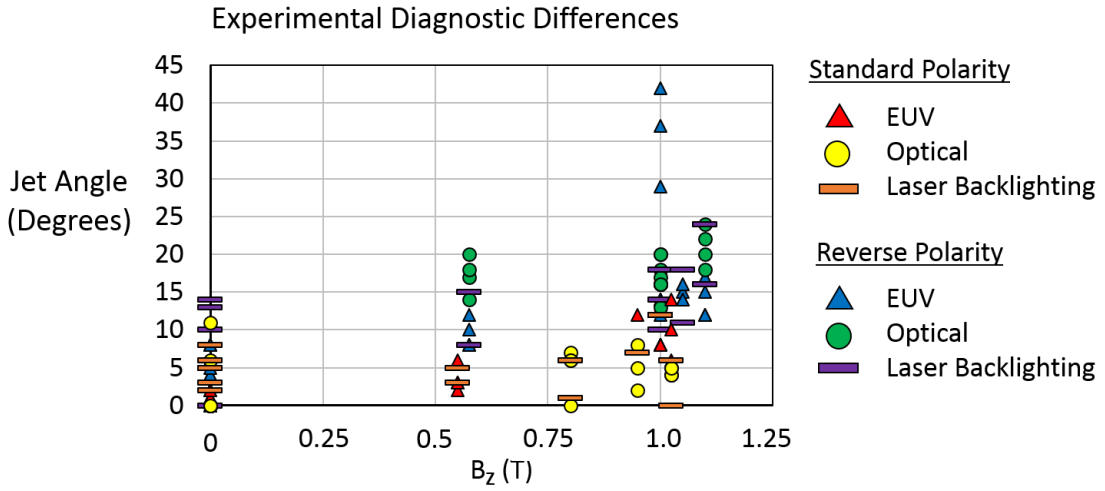

Figure 7.13: Experimental jet angles for various diagnostics relative to the applied B_z strength for standard and reverse current polarities. Overall, jet angles tend to increase with increasing B_z. Not shown: uncertainties taken to be $\pm 4^\circ$.

ous diagnostics. This plot does not contain an inclusive data set for all experiments but rather shows results from a few COBRA runs. This limited data set is the reason why some points are different from those shown in other graphs (for example, Fig. 7.12). One can see a spread among data even with the same diagnostics and applied B_z. Overall, one can still see that the reverse polarity jets have larger angles than standard polarity jet angles.

Next, we look at plasma jets made from a different foil material: titanium (Z = 22) rather than aluminum (Z = 13). The different material properties of these radial foils before (and during) plasma generation will be further considered in Sec 7.5. In regard to the jets already in the plasma phase, a larger ionization number correlates with more effects of radiation. Due to radiative cooling (meaning transfer of energy away from the hot titanium jet), we observe that titanium jets are skinnier than aluminum jets with no applied B_z, consistent with previous work showing higher atomic number jets having a higher degree of collimation. [37] This higher degree of collimation is likely due to

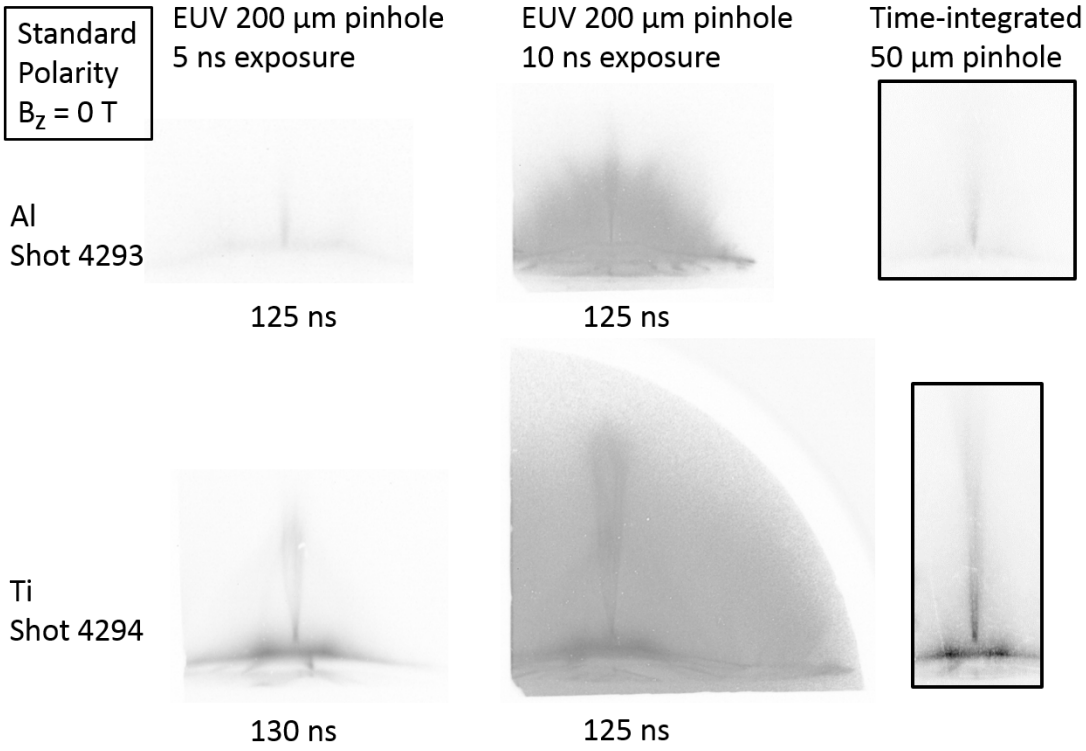

Figure 7.14: Experimental self-emission images for aluminum jets and titanium jets with no applied B_z, showing more emission (and a corresponding higher temperature) for titanium. For the time-integrated images, there was no filter material placed in front of the pinhole. Contrast not enhanced for any of these images. Darker areas mean more emission, but the darkness of the time-integrated (right-most) images should not be directly compared to the darkness of the other images. Time relative to the start of the COBRA current pulse.

there being relatively less thermal energy (or pressure gradient) in the jet (because the energy is radiated away) to resist the dynamic ram pressure, as shown by Eq. 7.1. Qualitatively in Fig. 7.14, we observe that titanium jets are hotter than aluminum jets by looking at self-emission pinhole imaging (as described in Sec. 5.5 and Sec. 5.7). Also, we observe the titanium jets to be more dense than the aluminum jets, qualitatively seen based on the height at which the interferometry fringes are hard to trace. Furthermore, using titanium as shown in Fig. 7.15, we again see current polarity differences between jets. As quantified in Fig. 7.16, larger applied B_z values correlate with larger jet angles and base

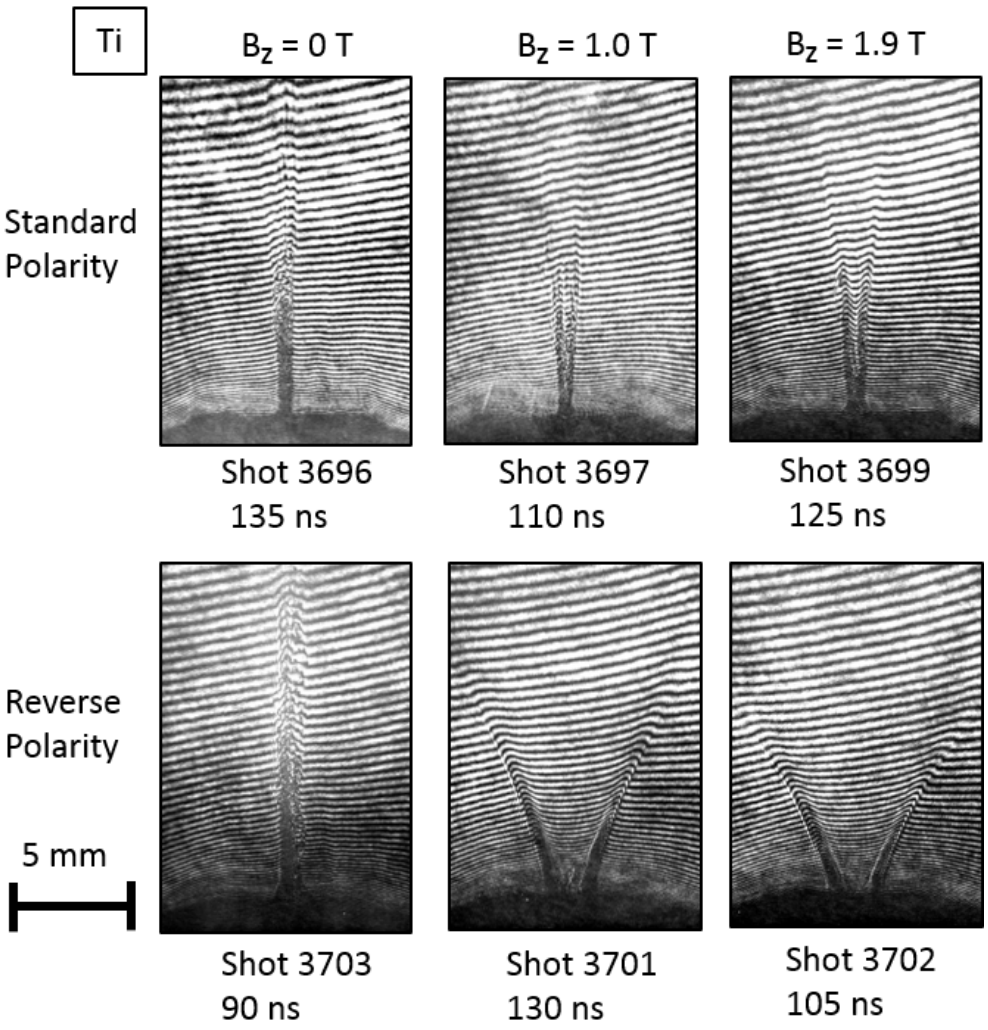

Figure 7.15: Experimental interferograms for titanium jets relative to the applied B_z strength for standard and reverse current polarities. Times relative to the start of the current pulse.

widths, more evident in reverse polarity than standard polarity.

We quickly review the main messages of this subsection. For a given B_z, reverse current polarity jets have larger jet base widths and larger jet angles than standard current polarity jets, keeping other parameters like pin size and foil thickness constant. We observe these current polarity effects using both experiments and simulations, using different experimental diagnostics, and using

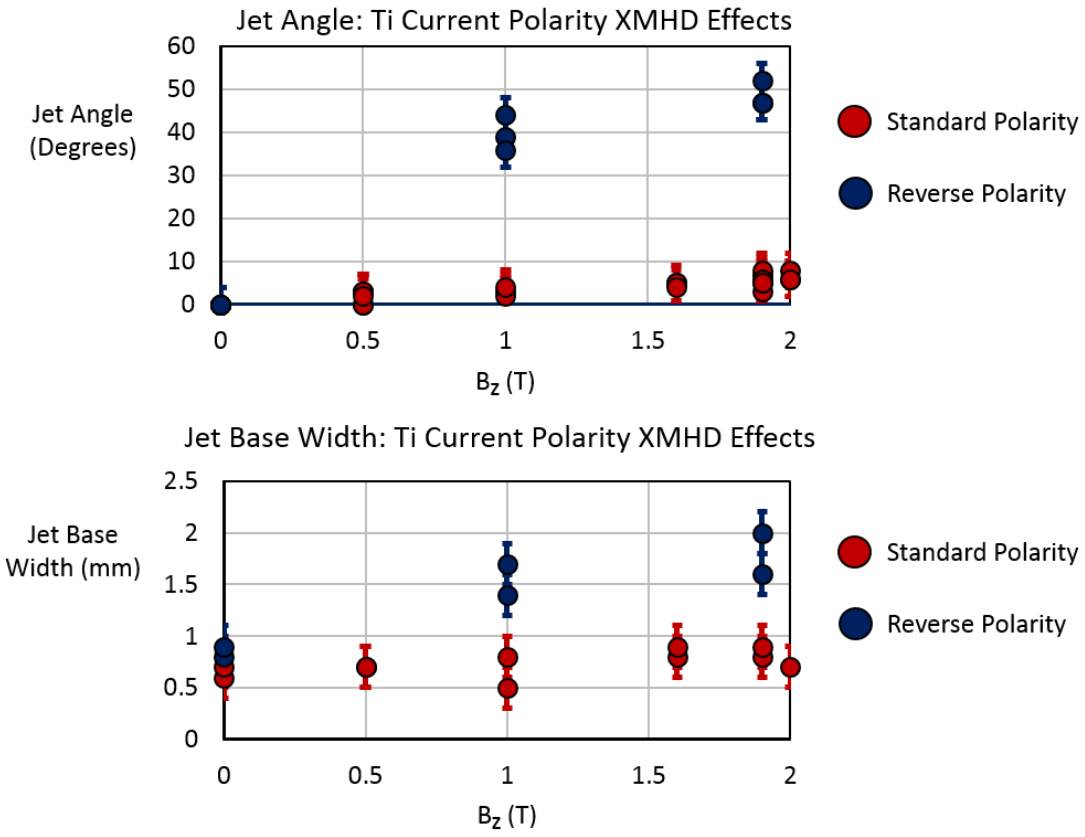

Figure 7.16: Experimental jet angles and base widths for titanium jets relative to the applied B_z strength for standard and reverse current polarities. Quantifying Fig. 7.15.

different radial foil materials. These polarity effects demonstrate the importance of XMHD compared to only MHD.

7.2 Current Filament Development and XMHD Effects

The surface plasma produced by the radial foil develops discrete paths of current flow. The structure is characteristic of an electrothermal filamentation plasma instability. [19, 40, 69, 70, 71, 72] The process of current filament forma-

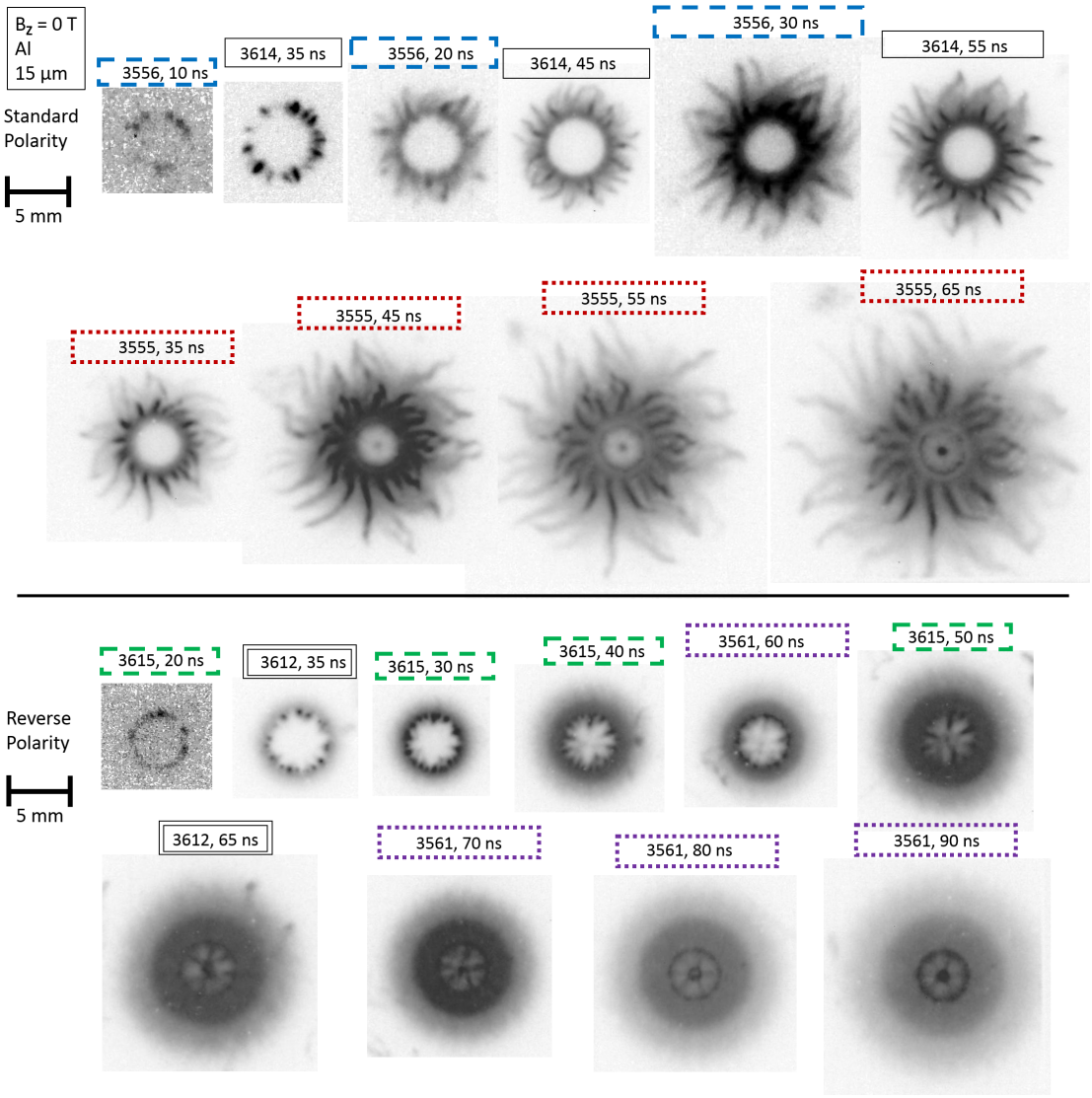

Figure 7.17: EUV images looking down onto the radial foil showing current filament time evolution for standard polarity (cathode pin, electrons flowing radially outward) and reverse polarity (anode pin, electrons flowing radially inward). All images are individually contrast enhanced (darker means more emission), so the intensities should not be compared between images. Images identified by their [shot number, time relative to the start of the COBRA current pulse].

tion is as follows. First we note that, by definition of resistivity, current tends to flow through less resistive (more conductive) paths; furthermore, current traveling through a path will Ohmically heat the area and increase the temperature. Next, we note that initial foil density nonuniformities can cause different plasma regions to have different resistivities (and/or different temperatures). Assuming that the plasma is in a (Spitzer-like) regime where the derivative of resistivity, η, with respect to temperature, T, is $\partial\eta/\partial T < 0$, then lower resistivity leads to higher temperatures and more current flowing through the paths of lower resistivity. This positive feedback generates discrete current filaments, which are present $<$ 2 mm above the foil. The filaments pinch under a $\mathbf{J} \times \mathbf{B_l}$ force $\propto I^2/r$, with B_l being the local B self-generated by the discrete current filament. The filaments radially expand over time as the foil heats (see Fig. 7.17), from the pin radius to eventually the foil outer radius. Under an applied axial magnetic field (B_z), $\mathbf{J} \times \mathbf{B}$ forces ($J_r B_z \, \hat{\theta}$) lead to azimuthal bending of the filaments (see Ti in Fig. 7.18). In EUV images of a top view of the foil, the azimuthal bending causes more washed out uniform emission.

Additionally, filamentation is different depending upon whether the central pin beneath the foil is held at the cathode or anode potential (see Fig. 7.17). In standard polarity with a cathode pin, electrons move from a location of higher current density (near the center pin) to a region of lower current density (near the outer annulus of the foil), and the initially high current density electron flow pinches into discrete filaments. In reverse polarity with an anode pin, electrons move from a region of lower current density (near the outer annulus of the foil) to a location of higher current density (near the center pin), and the initially lower current density electron flow only forms discrete filaments near the center pin (best seen early-on in time), where the current density is higher. This

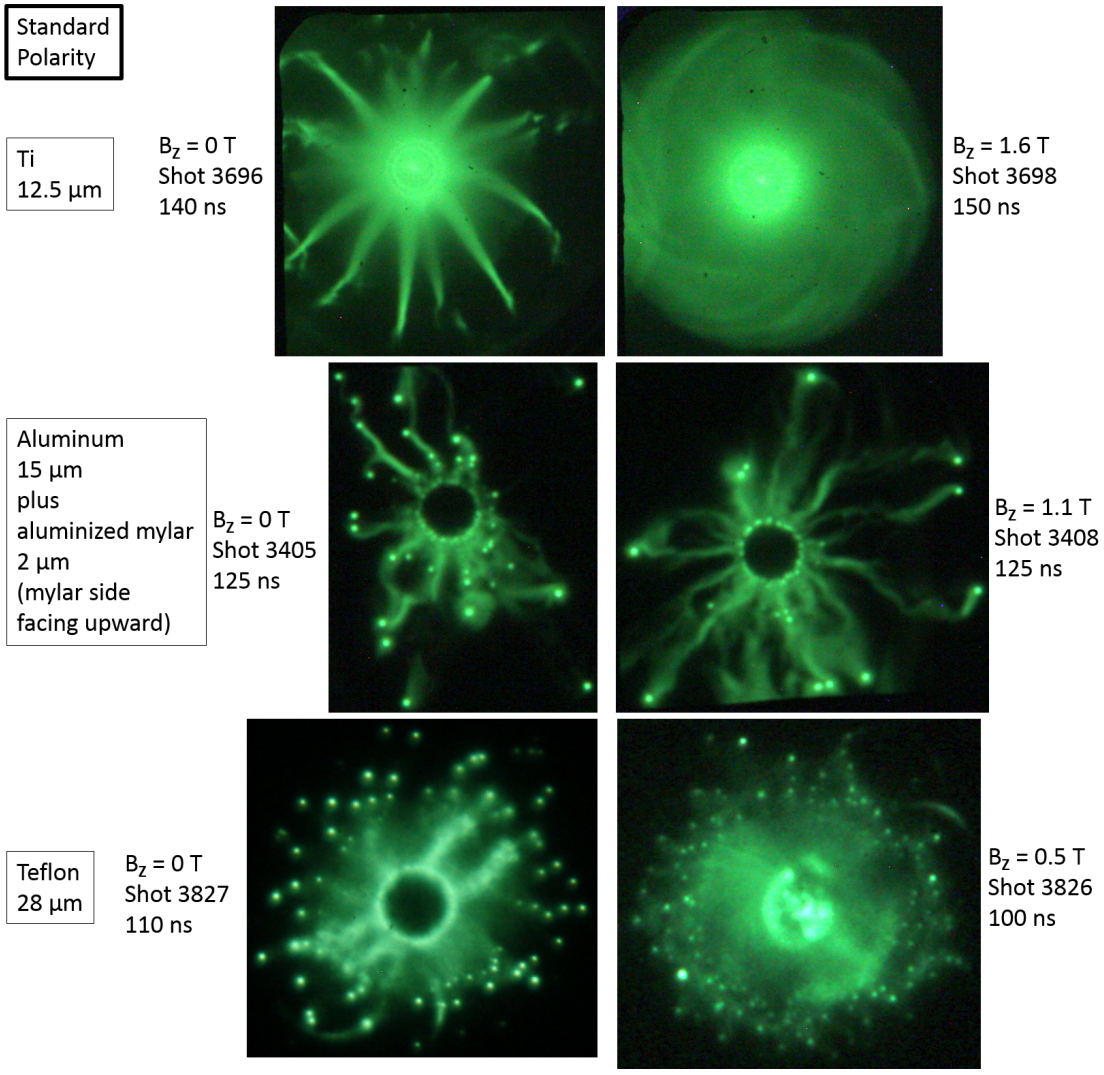

Figure 7.18: EUV images looking down onto different radial foil materials with different applied B_z strengths showing structure of current filaments. All images are individually contrast enhanced (lighter means more emission), so the intensities should not be quantitatively compared between images. Times relative to the start of the COBRA current pulse.

anode-cathode asymmetry represents an extended magnetohydrodynamics effect of Hall physics, whereby the electron flow and pinching force contribute to a more azimuthally uniform looking emission for the anode pin case (electrons flowing radially inward) relative to the cathode pin case (electrons flowing radially outward).

In Fig. 7.17, the images are ordered in a sequence that qualitatively shows the time evolution. Differences between effects like the precise current pulse shape can cause the absolute time dynamics to change between experimental shots (marked by different label borders). In standard polarity, we observe the filaments developing radially outward; in reverse polarity, we observe the filaments developing radially inward. The center point (darker, more emission) in some of the later-time images is the plasma jet.

In Fig. 7.18, we observe that insulators on the top of the foil surface lead to localized temperature hotspots (regions of more emission), and the current filaments travel along these hotspots (see bottom 4 images). We explicitly state here that there were no holes in the foil material before the experimental shot. As mentioned above, we note that, under an applied axial magnetic field (B_z), $\mathbf{J} \times \mathbf{B}$ forces lead to azimuthal bending of the filaments, and the azimuthal bending causes more washed out uniform emission. Also, we note that the images in Fig. 7.18 are aesthetically pleasing to emotional senses (i.e. they are beautiful).

We will revisit these current filaments produced by the electrothermal filamentation plasma instability when discussing the plasma jet disruption in Sec. 7.5.

7.3 Magnetic Field Compression

During formation of the plasma jet, as the lower-density background plasma converges toward the axis, the dynamical pressure forces advect and compress the B_z on-axis. We measure this B_z compression using dB/dt (or B-dot) probes (as described in Sec. 5.4). We place the dB/dt probe in the central hollow region

of a reverse polarity jet with an applied B_z, so we can minimize the perturbation to the jet density, azimuthal symmetry, and plasma current flow. Furthermore, we now use 10 mm diameter pins rather than 5 mm pins. The larger pin diameter changes the plasma dynamics and leads to a wider jet (and therefore more space to place a non-perturbing probe). There is a weaker $J_z B_\theta$ pinching force because the maximum $B_\theta \propto 1/r$ is smaller at the larger jet radius, and this weaker converging force also leads to less jet density and the jet forming at a later time for the 10 mm pin case than for the 5 mm pin case. As a side note, the 10 mm pin case also shows structural differences in standard polarity vs. reverse polarity for both the experiments and XMHD simulations (but not in MHD simulations), yet again validating the XMHD PERSEUS code.

In Fig. 7.19 on the left image, we see an interferogram of a titanium plasma jet with no probe, showing the conical jet shape. In the middle image, for a different experimental shot, we see an interferogram for the same conditions but with a dB/dt probe in the central hollow region of the jet. We see that the probe placed in the center of the jet does not significantly perturb the jet conical shape. Notably, we do observe fringe shifts and a corresponding plasma density near the surface of the probe. On the right image at about the same time as the middle image, using EUV self emission we observe little-to-no emission near the probe surface (compare with Fig. 7.23). Therefore, we conclude that the probe surface plasma is likely resistive (since T$<$ 10 eV) and therefore does not prevent magnetic field diffusion into the probe. The diffusion time, τ, is approximately related to the plasma distance (for the magnetic field to diffuse through), δ, and resistivity, ρ, by $\tau \sim \mu\delta^2/\rho$, where $\mu \sim \mu_0$ is the permeability of the plasma.

Furthermore, in Fig. 7.19 we do not see evidence of a shock structure around

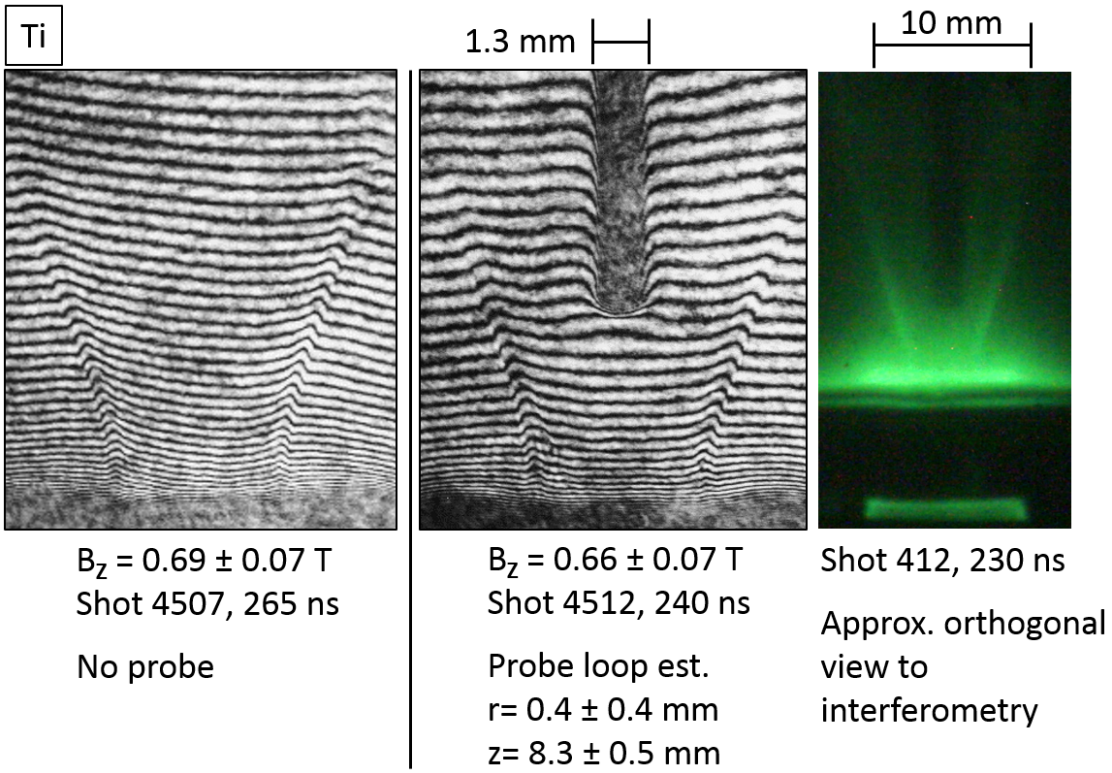

Figure 7.19: Placement of dB/dt probe in central hollow region of plasma jet, showing minimal perturbation. Left: interferogram of jet with no probe. Middle: interferogram of jet with probe. Right: EUV self emission of jet with probe. Times relative to the start of the current pulse.

the probe (compare with Fig. 7.23). If a shock is strong enough, the shock can be seen using laser backlighting shadowgraphy. However, even if a shock is weak and not visible to shadowgraphy, the shock can pose a problem for probe measurements by changing the direction of the magnetic field across the shock front. The probe will then measure a different component of the magnetic field compared to the ambient field on the other side of the shock. We note that, for a perfectly centered magnetic probe, the curved shock front surface normal will be parallel to the applied B_z at the center but not along the entire shock front. For reference to the reader, the formulas for these Rankine-Hugoniot jump conditions for ideal MHD shocks can be found on page 26 of the NRL Formulary. [73]

7.3.1 Characteristic dB/dt Signals

In Fig. 7.20, we show the raw dB/dt data vs. time for two differential measurements using double loop probes: left) a probe with loop orientations parallel and anti-parallel to the z-axis, and right) a probe with loop orientations parallel to the z-axis and parallel to the r-axis. On the left plot, we see that the two oppositely oriented probes lead to two opposite voltage signals (dark blue and light blue). The sum of these two signals should be proportional to the electric pickup of the probe and the difference proportional to the magnetic pickup (orange signal trace). We see that for the first $\sim$60 ns there is only a dominant electric field signal, negative because of the polarity of COBRA (cathode at a negative voltage with respect to the anode at ground). After 60 ns the two traces diverge indicating the start of the B_z compression. We see that the peak voltages relating to field compression occur at approximately the same time (125 ns after the start of current rise) for both probes. We see that the voltages return to their baseline values near 200 ns, implying no further B_z compression (after the red vertical line). However, at these times after 200 ns, the measurement of no voltage on the loops may have been the result of mechanisms causing an inaccurate dB/dt measurement.

The reason we question these late-time signals that do not show a decrease in B_z is because, when the current pulse is over, the current no longer drives the jet convergence (see blue traces in Fig. 7.26 on page 100 for example current pulses); therefore, we expect the compressed magnetic field pressure to push against the plasma jet pressure and eventually return the B_z to the initially uniform value produced by the Helmholtz coil while the plasma expands into vacuum. Still, we believe the probe voltage measurement is not failing at

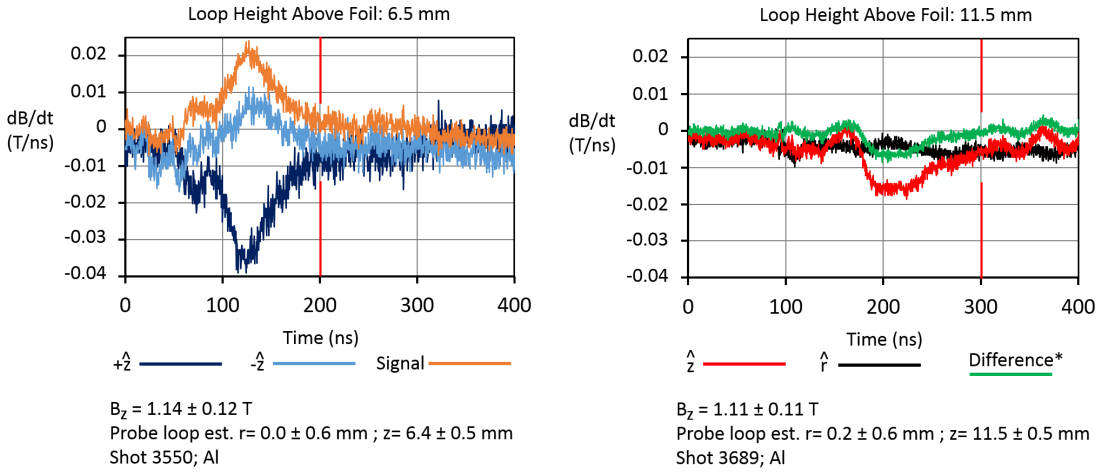

Figure 7.20: Measurements of dB/dt at different heights above the foil, showing more B_z compression closer to the foil surface. Times relative to the start of the current pulse. Adapted from Byvank et al., 2017. [27]

these times. The plasma environment in the present experimental work is more benign than in other situations in which these dB/dt probes have continued to reliably work. [59] Additionally, after the shot, we can (and do) check the probe continuity (connection) and calibrate to show the probes still function properly. If the flat dB/dt signal after approximately 200 ns is not a failure of the probe measurement, then the B_z in the probe loop region is not changing very fast. In this case, the plasma configuration must also be changing very slowly. At this time in the current pulse, the foil driving voltage is going to zero and reversing. This feature of the current pulse could result in resistive decay of currents above the foil. If the resistive decay time is relatively long, the plasma dynamics and magnetic fields will change very slowly. This situation is an open issue, and understanding this slow change in the magnetic field is the subject of further study.

In the right plot in Fig. 7.20, we see that the probe parallel to the z-axis gives a signal, while the probe parallel to the r-axis gives essentially no signal, and

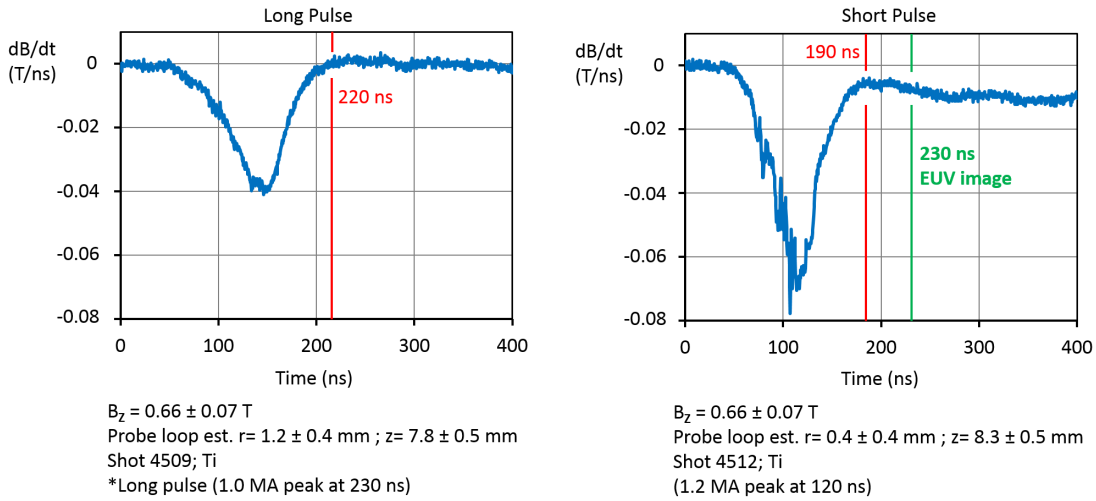

Figure 7.21: Measurements of dB/dt for different COBRA current pulse shapes, showing more B_z compression for a short pulse compared to a long pulse. Times relative to the start of the current pulse.

these combined signals confirm that we are measuring compression of the applied axial magnetic field rather than some non-axial (radial or azimuthal) component. We again mention that a misalignment of the probe loop parallel to the r-axis can produce a small component that may have measured B_z. Therefore, the difference between the r-axis and z-axis signals may not be exactly equivalent to the magnetic compression signal. The loops for the left graph in Fig. 7.20 are placed at a lower height of 6.5±0.5 mm above the foil compared to the loops for the right graph at 11.5±0.5 mm above the foil. Comparing the two plots, we see that there is larger B_z compression closer to the foil surface where there is larger plasma thermal pressure and dynamical ram pressure. Furthermore, we see that B_z compression starts earlier in time closer to the aluminum foil surface.

The details of the COBRA current pulse (such as rise time and peak current) influence the plasma jet development and corresponding B_z compression. COBRA can produce short pulses (nominally 100 ns and 1.0 MA) and long pulses (nominally 200 ns and 0.9 MA) by adjusting main switch pressures (see blue

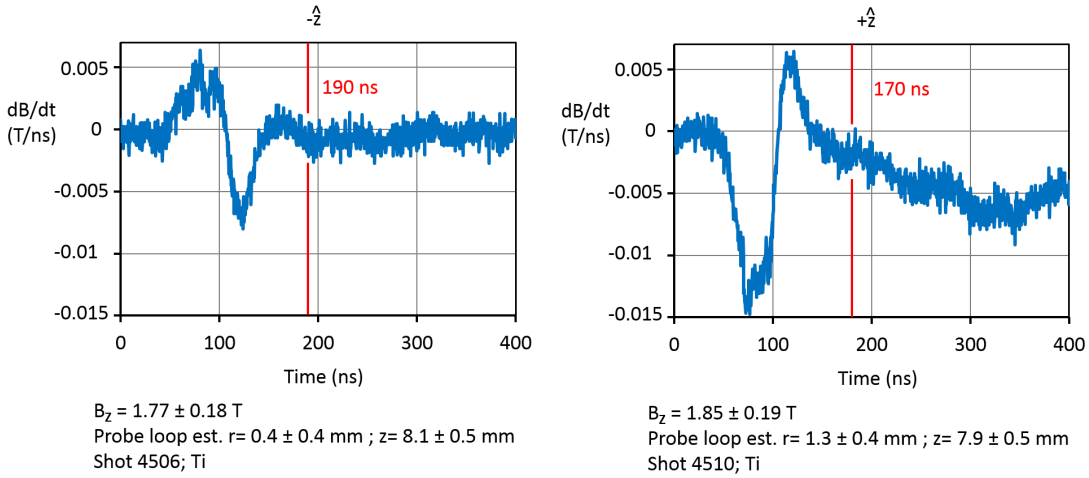

Figure 7.22: Measurements of dB/dt for opposite probe loop orientations for two separate shots, showing similar qualitative behavior with opposite signs. Times relative to the start of the current pulse.

traces in Fig. 7.26 on page 100 for example current pulses). In Fig. 7.21, we see less B_z compression for a long pulse (left plot) than for a short pulse (right plot), and we see the same general shape for the dB/dt traces. For each of these experiments, we use only one z-probe loop, hoping for less perturbation from a smaller final probe diameter compared with a double-loop probe. For the long pulse around 220 ns (red vertical line), we see no further B_z compression. For the short pulse around 190 ns (red vertical line), we see the start of a negative voltage signal that becomes a constant baseline, and we question the validity of the dB/dt measurement at this time. Perhaps this negative constant baseline signal is electrical pickup; however, the images for this shot in Fig. 7.19 show little-to-no probe perturbation, and these images are taken near 230 ns (green vertical line on plot). The precise time is not obvious at which we should start to not trust the probe voltage measurement to accurately record the dB/dt. Still, we do trust the measurement before 190 ns.

As expected for consistency, opposite probe loop orientations give opposite

voltage signals for different shots (as well as for the same shot, as shown in Fig. 7.20). In Fig. 7.22, we display dB/dt signals from oppositely oriented probe loops for similar shot conditions. We qualitatively see opposite signals: on the left plot, starting out positive and becoming negative; and on the right plot, starting out negative and becoming positive. This changing sign of the traces corresponds with a decrease in B_z after its initial compression. For the left plot, we again observe zero signal after 190 ns (red vertical line). For the right plot, we find a negative voltage signal after around 170 ns (or possibly earlier; red vertical line), qualitatively similar to that found in the right plot in Fig. 7.21.

The small negative voltage signals seen at late times in some of the above dB/dt plots is not disqualifying to the validity of the measurements. Firstly, the probes can be (and were) checked for continuity (connection) after the shot and calibrated again to show that the probes still function properly. Additionally, if the negative voltage actually is electrical pickup from the COBRA machine, the pickup (of around 10 V) is extremely small relative to the COBRA voltage of 100s kV (say $\sim$ 300 kV peak). The plot in Fig. 7.23 displays an example of when the COBRA current truly arcs to a probe; in this case (around 70 ns, red vertical line), the probe voltage immediately plummets to a negative value off-scale of the oscilloscope. A similar voltage spike and failure can occur if energetic electrons from the power feed or load region strike the probe tip; however, the reason is not clear why energetic electrons that were not stopped by the power feed or load region would be stopped by a dB/dt probe. We mention an additional related problem for which inaccurate dB/dt signals may occur is if a large current is carried on the outer conductor or in plasma on the outer insulation of the probe. This current can create unwanted components of the magnetic field that will be picked up by the loop, particularly dependent upon the loop

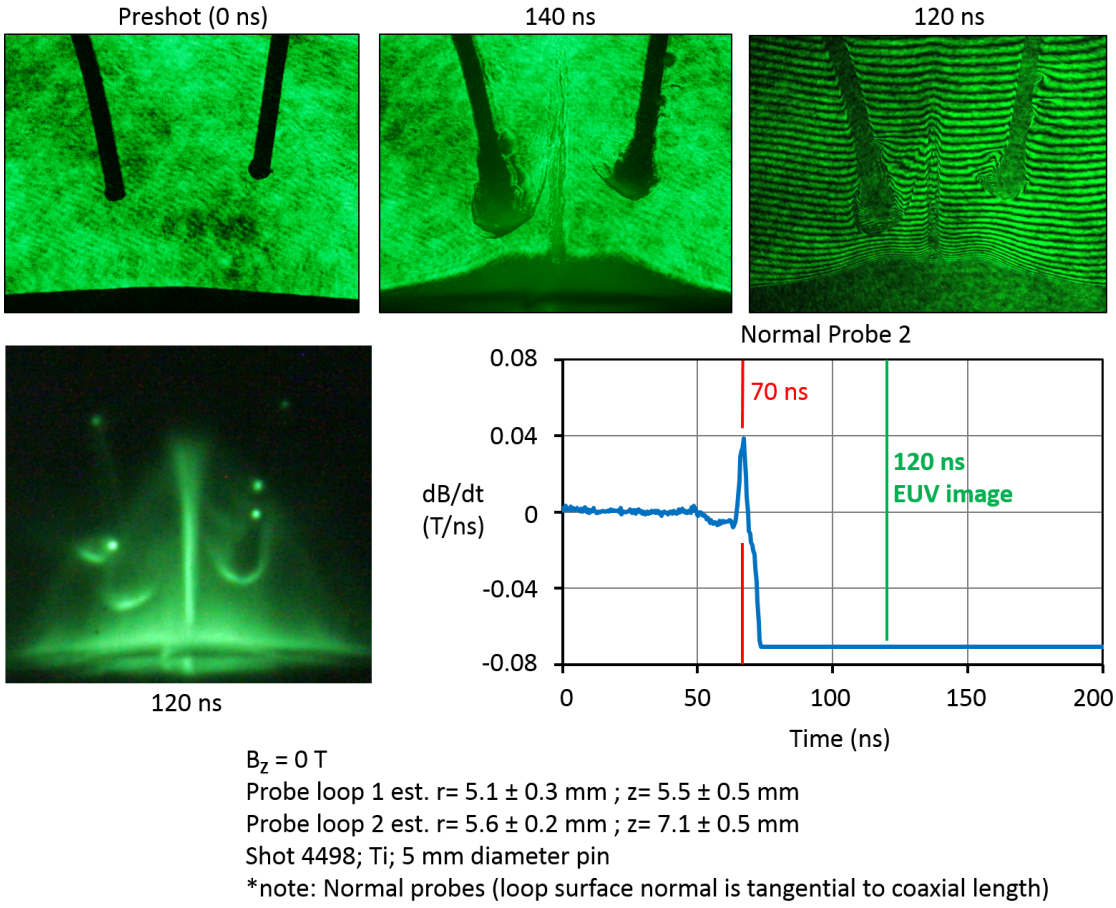

Figure 7.23: Example of a characteristic dB/dt probe measurement failure, showing a negative voltage spike when the COBRA plasma arcs to the probe. Images show probe surface plasma formation, shocks around probe tips, and EUV hot spots showing locations of insulation failure and arcing. Times relative to the start of the current pulse.

alignment.

Additionally, the EUV image (to the left of the graph) in Fig. 7.23 shows shock structures around the probes as well as bright hot spots at which the probe insulation has failed and the COBRA voltage can directly arc to the probe. The EUV emission near the probe surface suggests the plasma may be hot and conductive enough to limit magnetic field diffusion into the probe loop area. Looking at interferometry (top right), we observe regions of large density around the

probe surface– either from photoionization of the probe surface or from plasma buildup as the plasma converges on-axis for the $B_z = 0$ T jet. Lastly, we compare the preshot and shot laser backlighting shadowgraphy (top left two) images, for which we can again see shock structures and large amounts of plasma around the probe. This demonstration of probe measurements failing in Fig. 7.23 provides information to which we can compare the dB/dt signals that we believe are accurate.

To summarize, in this section we discussed how to interpret dB/dt signals that measure B_z compression. Placing the probe in the central hollow region of the jet permits accurate compression measurements. Differential measurements with probe loops oriented in different directions allow for confidence that we are measuring compression of the axial component of the magnetic field. Certain features in the dB/dt traces make us question the validity of the measurements at late enough times. In the next section, we look at the integrated dB/dt signals and compare experimental results with simulation predictions.

7.3.2 Compression Measurements

By adding the initial B_z produced by the Helmholtz coil to the integrated dB/dt signal– after taking into account the loop orientation and corresponding voltage sign– we can look at the B_z compression measured by the probes. In Fig. 7.24, we plot the B_z compression results from the dB/dt signals in Fig. 7.20 and compare with PERSEUS simulation predictions for the same locations as the probe loops. The experiment results are solid lines, and the simulation predictions are dashed lines. Compared to the simulation results, the experimental results

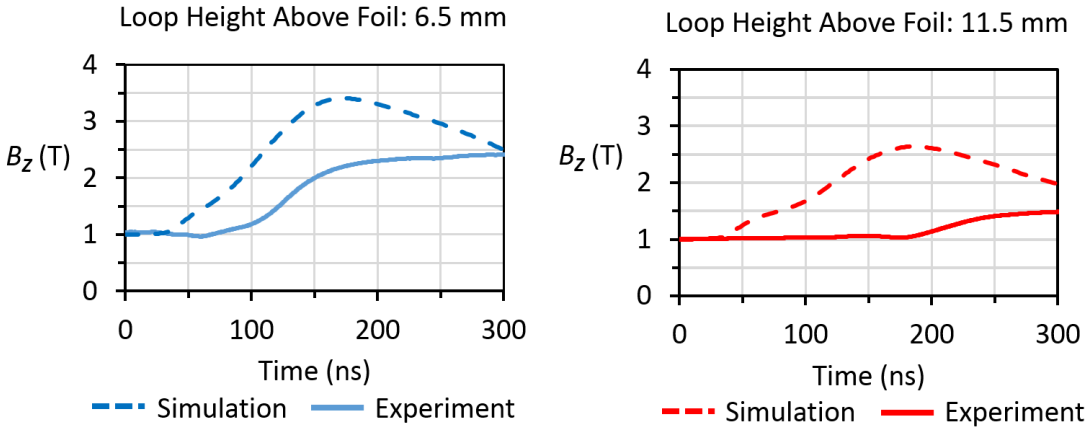

Figure 7.24: Integrated dB/dt signals show compression of the initially applied ~1 T B_z for simulations and experiments with left) experiment shot 3550; two loops oriented parallel and antiparallel to the z-axis, and right) experiment shot 3689; one loop oriented parallel to the z-axis and one loop oriented parallel to the r-axis. Note: the simulation result is for a loop height of ~11.0 mm rather than 11.5 mm due to the computational spatial domain. Time is relative to the COBRA current pulse with peak current at approximately 100 ns. Adapted from Byvank et al., 2017. [27]

show a smaller maximum B_z with compression starting later in time. Additionally, the simulation shows a decrease in the compressed B_z at around 200 ns, while in the experiments we do not observe a decrease in the compressed field at least until after 300 ns. The larger compression seen in the simulation results implies that there is more inward pressure (e.g. dynamical ram pressure and thermal pressure) in the simulation than was present in the experiment. Notably, the simulation did not include a radiation package, which could reduce this inward pressure.

The overall discrepancy between the simulation and experimental results is greater at a height of 11.5 mm than at 6.5 mm. We now look more closely and quantitatively at the B_z compression traces in Fig. 7.24. At 6.5 mm, the peak compression is 2.4±0.3 T at 200 ns in the experiment and 3.4 T at 180 ns in the simulation. Additionally, the simulation takes about 140 ns to increase the B_z

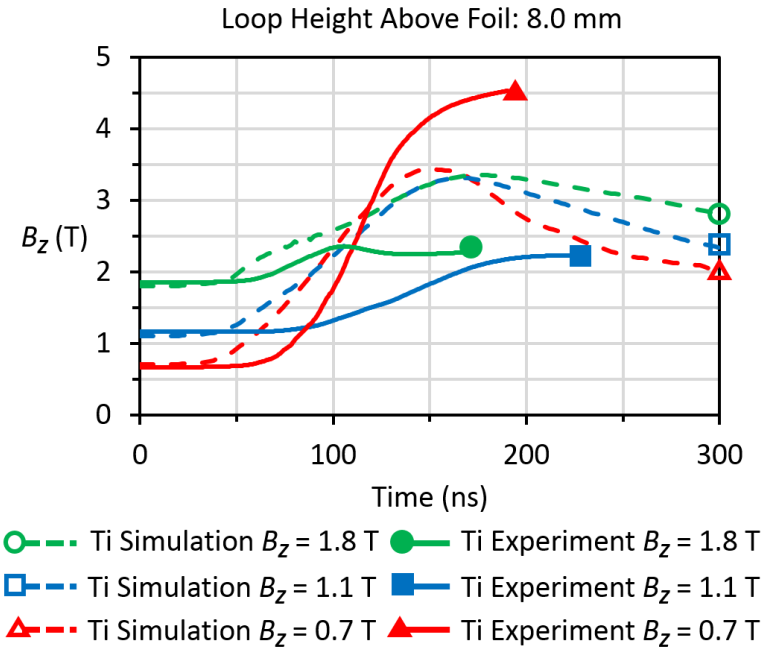

Figure 7.25: Integrated dB/dt signals show compression of different initial applied magnetic field strengths (B_z = 0.7 T, 1.1 T, 1.8 T) for titanium simulations and titanium experiments (shot 4512: B_z = 0.7 T; shot 4503: B_z = 1.1 T; shot 4510: B_z = 1.8 T). Time is relative to the COBRA current pulse (peak current around 100 ns). Adapted from Byvank et al., 2017. [27]

by 2.4 T, corresponding to an average dB/dt of 0.017 T/ns, which is close to the peak dB/dt in the experiment (see left plot in Fig. 7.20). At 11.5 mm, the peak compression is 1.5±0.2 T at 300 ns in the experiment and 2.6 T at 190 ns in the simulation. Furthermore, we see that the simulation predicts compression starting around 40 ns for both heights above the foil, while the experiments shows compression starting around 70 ns for the 6.5 mm height and 190 ns for the 11.5 mm height. Assuming the experimental results to be accurate, this discrepancy between the measurements at different heights suggests the simulations may be missing some physics in these low plasma density regions near the top of the jet– perhaps related to an experimental delay in jet formation and how much the magnetic field is truly tied to the electron flow.

Now using titanium jets, we look at the effects on field compression of varying the initial applied magnetic field strength at a height of about 8.0±0.5 mm above the initial (preshot) foil surface. Experimentally, we use titanium rather than aluminum because aluminum jets "disrupt" and do not form in a collimated manner above a B_z ∼1.1 T, as will be further discussed in Sec. 7.5. Radiation becomes more important for higher Z materials like titanium compared to aluminum. Without implementing radiation in the PERSEUS code, we model titanium instead of aluminum only by changing the ion mass, m_i, and ionization as a function of electron temperature, $Z(T_e)$.

In Fig. 7.25 we plot the total B_z as a function of time for these titanium experiments and compare them to the titanium simulations without radiation. As in Fig. 7.24, the titanium simulations show the B_z compression starting around 40 ns for all the initial applied field strengths 0.7-1.8 T. The experiments show B_z compression starting later in time than the simulations. For both experiments and simulations, we see the same trend of a larger change of B_z (peak value minus initial value) with a smaller initial applied magnetic field strength. This effect is most pronounced in the experimental results for the 0.7 T initial field strength. Experimentally at the probe location 8.0±0.5 mm above the foil, applying an initial B_z of 0.7±0.1 T leads to compression to a total B_z of 4.5±0.5 T at 190 ns (a B_z change of 3.8 T); applying an initial B_z of 1.1±0.1 T leads to compression to a total B_z of 2.2±0.2 T at 210 ns (a B_z change of 1.1 T); and applying an initial B_z of 1.8±0.2 T leads to compression to a total B_z of 2.4±0.3 T at 110 ns (a B_z change of 0.6 T). Simulations for titanium show compression of a 0.7±0.1 T B_z to a total 3.4 T at 150 ns (a B_z change of 2.7 T), compression of a 1.1±0.1 T B_z to a total 3.3 T at 170 ns (a B_z change of 2.2 T), and compression of a 1.8±0.2 T B_z to a total 3.3 T at 180 ns (a B_z change of 1.5 T). The larger peak B_z for the initial

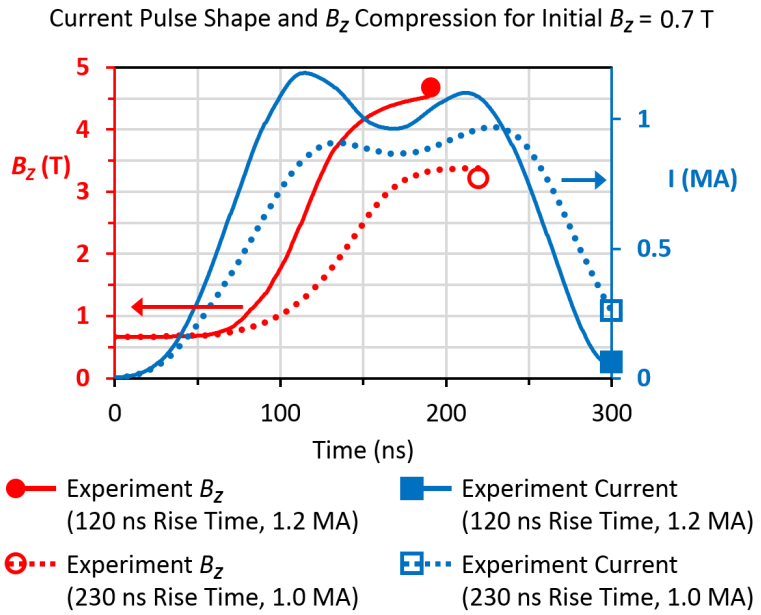

Figure 7.26: Current pulse shapes and B_z compression of an initial applied B_z = 0.7 T from an experimental short pulse (shot 4512; nominally 100 ns rise time, 1.0 MA peak current) and an experimental long pulse (shot 4509; nominally 200 ns rise time, 0.9 MA peak current). Adapted from Byvank et al., 2017. [27]

0.7 T field case corresponds with a larger peak magnetic pressure that must be supported by a larger dynamical ram pressure or pinching force (pressure from the B_θ field from the jet current). Furthermore, a larger initial B_z means more magnetic pressure to resist inward radial motion.

Experimentally, the rise time and peak current of the COBRA pulse influences the plasma jet development and the corresponding B_z compression. COBRA can produce short pulses (nominally 100 ns and 1.0 MA) and long pulses (nominally 200 ns and 0.9 MA) by adjusting main switch pressures. In Fig. 7.26, long and short COBRA pulses for this load are shown along with the magnetic compression traces for the jets they produce with an initial B_z of 0.7$\pm$0.1 T (integrated from dB/dt signals shown in Fig. 7.21). The shorter pulse with the larger peak current produces a higher peak value of the compression, 4.5$\pm$0.5 T, com-

pared to the longer pulse with the lower peak current, 3.4±0.4 T. This trend is due to the larger current for a short pulse providing a larger $\mathbf{J} \times \mathbf{B}$ force that collimates the plasma jet on-axis and increases the B_z compression.

In this section, we presented the experimental measurements for B_z compression, and we found quantitative differences with simulations but also similar qualitative trends. In both experiments and simulations, there is larger compression closer to the foil surface where there are larger inward dynamical and thermal pressures. In both experiments and simulations, there is a larger change in B_z for a smaller initially applied field. Experimentally, we find a difference in B_z compression based upon the current pulse shape. In the next section, we use the PERSEUS simulation to attempt to further understand aspects of the experiments– including the current pulse shape, among other experimental variables.

7.3.3 Simulation Insights

Exploring predictions made by the PERSEUS code can allow for better understanding of the importance of the physical processes involved with the B_z compression. As previously stated, experimentally for the compression measurements we use 10 mm pin diameters in reverse polarity to try to minimize how much the dB/dt probe perturbs the jet. Among many other regrets in life, the author regrets being unable to conduct compression measurements with 5 mm pins or in standard polarity that were "successful" in the sense of being confident that the probe signals were accurately measuring the dB/dt and not perturbing the plasma jet structure. We hope to utilize the PERSEUS simulations to

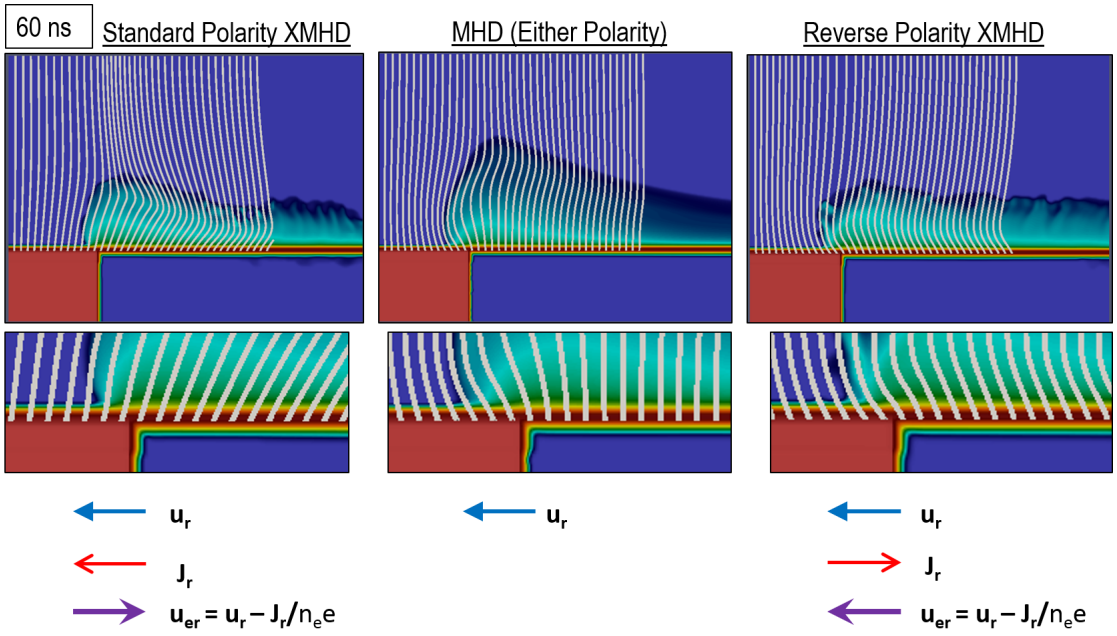

Figure 7.27: Magnetic field streamlines (in r-z plane) overlayed on plasma density at 60 ns in PERSEUS simulations for XMHD standard current polarity (left), MHD (middle), and XMHD reverse polarity (right). Lower images are zoomed-in sections of the above images. Below images, directions of vector radial components of fluid velocity u_r, current J_r, and electron velocity u_{e_r} are shown for the various cases. Note: for standard polarity, u_{e_r} may not be radially outward for all times if u_r inward is large enough. The images and vector directions demonstrate how the magnetic field is tied to the electrons in XMHD (or Hall MHD) and tied to the ions in MHD. Image central z-axis is on the left of all images with a 10 mm diameter pin (5 mm radius).

understand some of the physics that we did not experimentally measure.

PERSEUS shows different jet structures depending on current polarities and pin sizes, and these different jets correlate with different amounts of B_z compression. In Fig. 7.27 at 60 ns during the jet formation process, we see how the magnetic field is tied to the electrons in XMHD (or Hall MHD) and tied to the ions in MHD. This "tying" is based on the frozen-in-flux theorem and neglects resistive diffusion; see Eqs. 7.8-7.12 with magnetic flux Φ. Still, we see that the radially inward electron motion, u_{e_r}, enhances on-axis B_z compression for re-

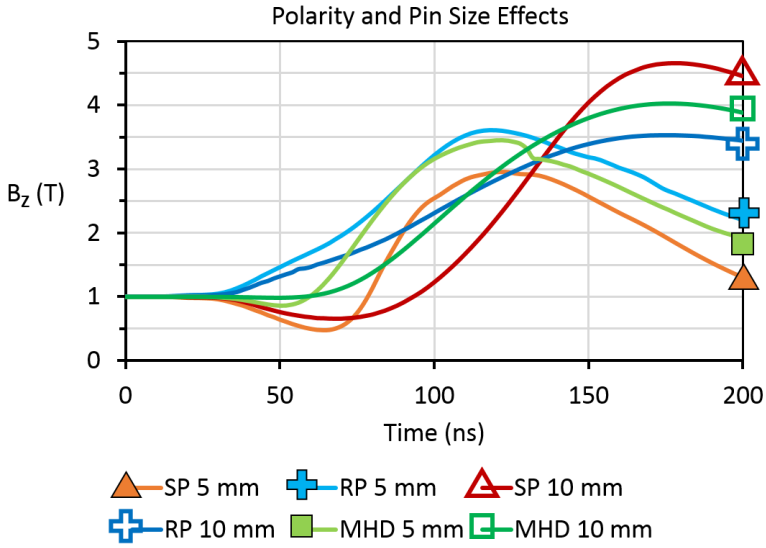

Figure 7.28: PERSEUS simulation B_z vs. time for different current polarities and pin sizes at a 6.5 mm height above the foil. The larger pin size delays jet development and B_z compression. The MHD results are typically in between the XMHD standard current polarity (SP) and reverse polarity (RP) results. Note: the experimental results are the RP 10 mm case.

verse polarity (field lines bent radially inward) and reduces B_z compression for standard polarity (field lines bent radially outward). For MHD, the B_z is compressed "only" by the radially inward ion motion, u_r. These XMHD or Hall MHD differences compared with MHD were highlighted in Sec. 6.1.

$$\Phi = \int_S \mathbf{B} \cdot d\mathbf{S} \tag{7.8}$$

$$\frac{d\Phi}{dt} = \int_S \frac{d\mathbf{B}}{dt} \cdot d\mathbf{S} + \int_S \mathbf{B} \cdot \frac{d\mathbf{S}}{dt} \tag{7.9}$$

$$\frac{d\Phi}{dt} = \int_S (-\nabla \times \mathbf{E}) \cdot d\mathbf{S} + \oint_C (\mathbf{B} \times \mathbf{u}) \cdot d\ell \tag{7.10}$$

$$\frac{d\Phi}{dt} = \oint_C (\mathbf{E} + \mathbf{u} \times \mathbf{B}) \cdot d\ell \tag{7.11}$$

$$for\ ideal\ MHD: \frac{d\Phi}{dt} = 0 \tag{7.12}$$

Quantitatively, in Fig. 7.28 we plot the B_z vs. time at a 6.5 mm height above the foil for 5 mm and 10 mm diameter pins and also for XMHD standard polarity (SP), XMHD reverse polarity (RP), and MHD (either polarity). As previously stated, the larger pin size delays jet development and B_z compression. For both pin sizes, we observe how the B_z in standard polarity initially decreases because of the radially outward electron motion advecting the B_z. However, as the plasma (both ions and electrons) converges toward the central z-axis, the B_z is compressed to above the initial field. For 5 mm diameter pins, reverse polarity (RP) gives the largest peak compression. For 10 mm pins, standard polarity (SP) gives the largest peak compression. The MHD results are typically in between the XMHD opposite current polarity results. We again note that the B_z compression is related to the radial force balance of the jet; see Sec 7.1.1 and Eq. 7.1. Using the frozen-in-flux theorem and assuming ideal MHD, we can make an oversimplified model for the B_z compression: a perfectly conducting plasma cylinder at the pin radius, R_0, compresses the initial applied field, B_0, to the final jet radius, R_f. We assume conservation of magnetic flux: $\Phi_0 = B_0 \pi R_0^2 = \Phi_f = B_f \pi R_f^2$. With this model, compressing an initial $B_z = B_0 = 1$ T from the 10 mm pin diameter ($R_0 = 5$ mm) to a jet radius of $R_f = 2$ mm would lead to a final compression of $B_f = 6.25$ T. The same result occurs by taking a 5 mm pin diameter and 1 mm final jet radius. This calculated result is the same order of magnitude as the simulation results, but the simulations include additional physics like finite resistivity and the Hall effect.

As previously discussed in the context of the frozen-in-flux theorem, finite material resistivity influences magnetic field diffusion. The dB/dt probe is fabricated from a coaxial cable conductor. The dB/dt loop is located to the side of the coaxial cable (see z-probe in Fig. 5.6), so the magnetic field lines do not have

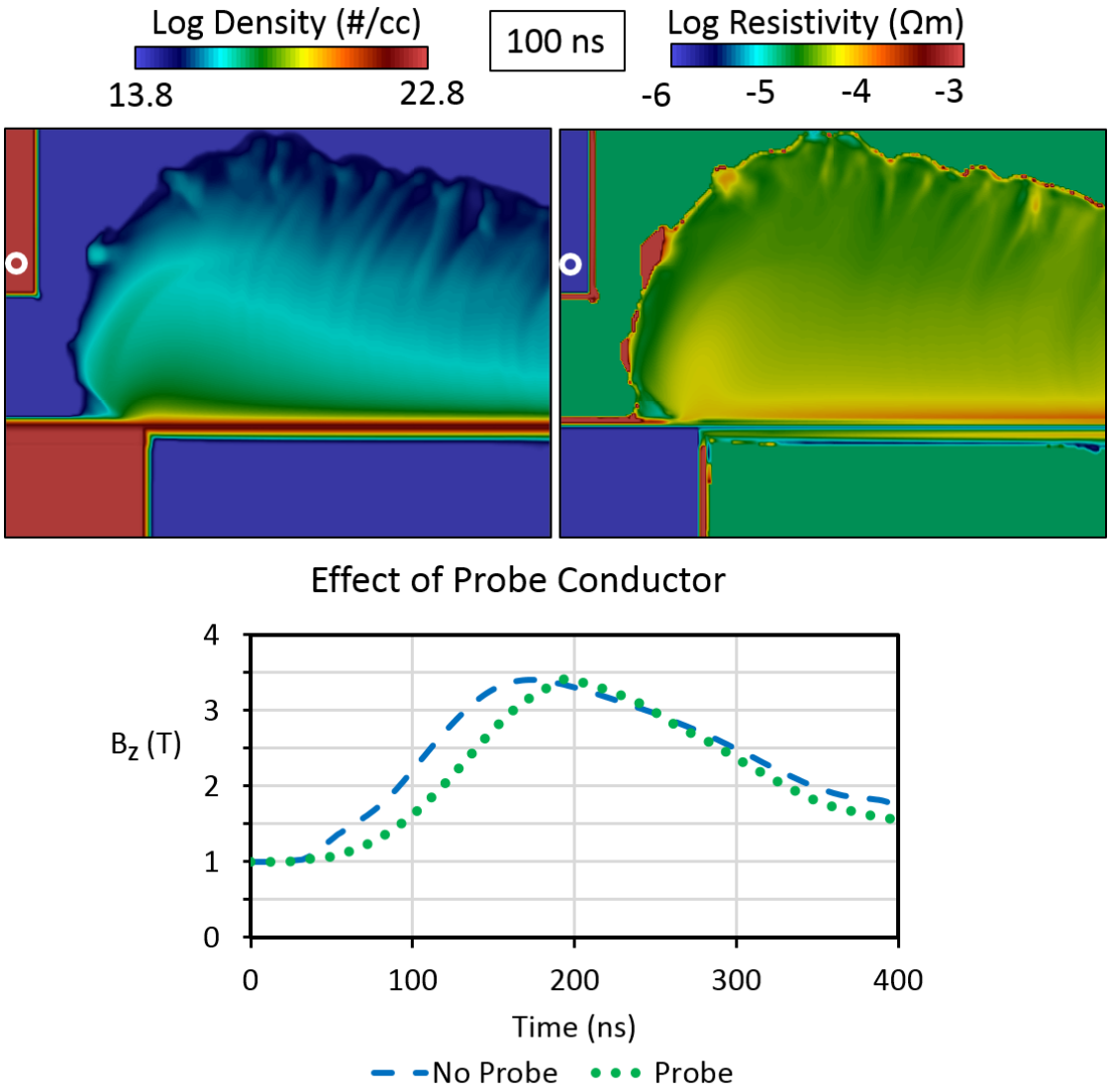

Figure 7.29: Simulation results when including a solid conductor at the dB/dt probe location, showing delayed compression due to magnetic field penetration into the conductor. B_z taken at a 6.5 mm height above the foil (white circles in images), with a 10 mm pin in reverse current polarity– the same conditions as in the experiments.

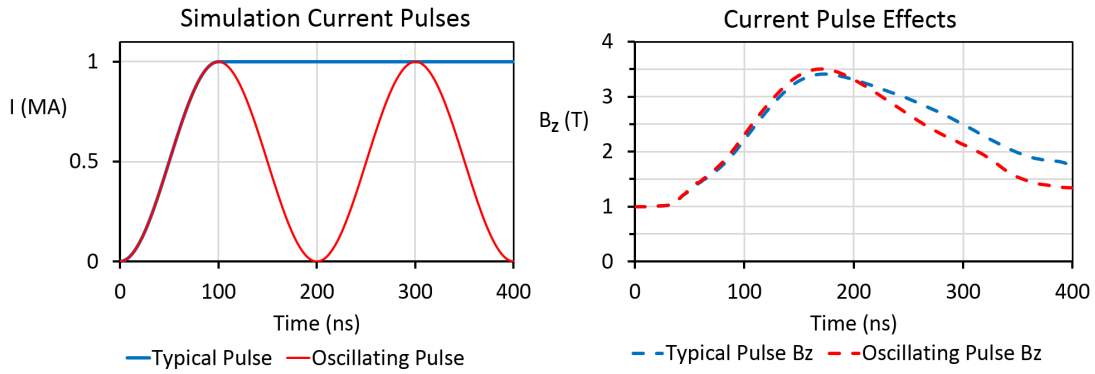

Figure 7.30: Simulation B_z compression (right plot) for different current pulses (left plot). The blue trace, typically used in the simulation for all results presented thus far, is a sine-squared waveform until peak current with constant current afterward. The red trace is an oscillating sine-squared waveform. There are minimal differences in the B_z compression for these two cases at the same 6.5 mm height above the foil with a 10 mm diameter pin in reverse polarity.

to penetrate the coaxial cable to induce a voltage in the loop. Still, we can model how a solid conductor influences the B_z compression in the center hollow region of the plasma jet. As shown in Fig. 7.29, we add a central solid conductor at the probe location in the PERSEUS simulation; the white circle denotes the approximate measurement location. A resistive plasma forms on the conductor surface. Relative to the situation for which there is no probe (as shown in all previous figures, like Fig. 7.4 for a smaller 5 mm diameter pin), the conductor delays the B_z compression by $\sim$15 ns, but the peak compression of 3.3-3.4 T is the same for both cases.

In the previous section, we found that the experimental current pulse shape (short pulse or long pulse) affected the B_z compression measurement. The PERSEUS simulation results presented thus far used a sine-squared waveform until peak current at 100 ns, with constant current afterward. The experimental current decreases slightly after the first peak and returns to zero after the sec-

ond peak (ignoring the possibility of crowbarring); see Fig. 7.26 for examples. To consider the effects of these current changes, we compare the typically-used current pulse in the simulation with an oscillating sine-squared waveform that is not held constant after a particular time. As shown in Fig. 7.30, the different current pulses do not greatly influence the B_z compression. A possible reason for this result is that, after the initial $\mathbf{J} \times \mathbf{B}$ force that drives the plasma convergence and jet formation, the already-generated dynamical ram pressure and thermal pressures are enough to compress the B_z. Additionally, the B_z decreases at late times even for the typical current pulse with a constant current after peak. Therefore, this B_z decrease may be due to diffusion into the plasma or may be due to plasma expansion (and a corresponding reduction in inward thermal and dynamical ram pressures).

Due to the current oscillations, there is a change in sign in dI/dt and corresponding voltage (see, for example, Eq. 5.3). This 2D PERSEUS simulation with only Spitzer resistivity (and ignoring the not-Spitzer resistivity in the solid-liquid part of the foil) may not accurately model the current reversal and diffusion (including phenomena like the reverse skin effect). Furthermore, we note that most of the current goes through the radial foil surface rather than the plasma jet, so the jet dynamics may not be as influenced by the oscillating current pulse compared to the surface plasma near the foil surface (on both the top and bottom sides of the foil). Notably, the process of current reversal late in the current pulse is one consideration (and possible explanation) for why we observe no dB/dt at late times, experimentally.

The 2D radial foil simulations with Spitzer resistivity have limitations regarding what they can accurately model. In Fig. 7.31, on the left plot we com-

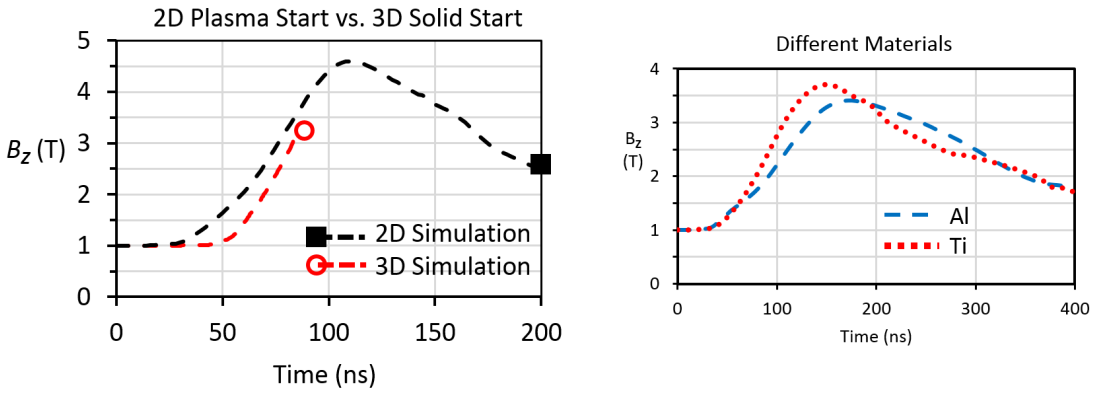

Figure 7.31: PERSEUS simulation B_z compression for various parameters. Left: comparing the 2D (r-z) code with Spitzer resistivity with the 3D code (DG) that includes equation of state and resistivity data starting in the solid phase, although the 3D code is not fully spatially resolved (both 2D and 3D cases for aluminum); 5 mm height with 5 mm diameter pin in reverse polarity. Adapted from Byvank et al., 2017. [27] Right: comparing aluminum and titanium results using the 2D code with no implemented radiation; 6.5 mm height with 10 mm pin in reverse polarity.

pare this 2D simulation (67 μm spatial resolution) with a 3D radial foil simulation using the DG method and including material equation of state and resistivity data (for aluminum) starting from the solid phase. However, due to limitations with computational resources (number of processors and running time), the 3D code grid resolution of 100 μm spatially under-resolves the foil thickness (15-20 μm). Due to these computational resource limitations, the 3D code was stopped at around 90 ns. Still, we do observe a $\sim$20 ns delay in B_z compression for 3D with a "solid" (but spatially under-resolved) start compared to 2D with a plasma start. Unfortunately, based on when the 3D simulation was stopped, we can not compare the peak compression values. Additionally, on the right plot in Fig. 7.31, we compare 2D simulations for aluminum and titanium without radiation effects, only changing the mass and ionization state. Likely due to its larger mass– ram pressure– and higher temperature– thermal pressure– titanium has a slightly higher peak compression from 1 T to 3.7 T at 150 ns compared to 3.4 T

at 190 ns for aluminum. Systematically changing parameters like these in the simulations allows for better physical understanding of the important physical processes involved with the B_z compression.

The Nernst effect– a current (force on electrons) present when there is a temperature gradient perpendicular to a magnetic field– is another process that we would like to consider in regard to B_z compression. [74, 75, 76] Qualitatively, the Nernst effect influences the electron motion that can advect the magnetic field (or create currents which can generate magnetic fields). Furthermore, the Nernst effect is more important with larger densities and larger temperature gradients– for example, more important near the ablating foil surface than in the ablated background plasma. Implementing heat transport into PERSEUS, including heat conduction and the Nernst effect, is presently being worked on (thanks to Jason Hamilton).

Semi-quantitatively, we can determine the importance of the Nernst effect by looking at the ratio of it with other terms present in the Generalized Ohm's Law. In the limit of strong (electron) magnetization, the Nernst effect adds a term contributing to the electron momentum equation of: $-(3/2)(n_e\nu_{ei}/\omega_{c_e})\hat{b} \times \nabla(k_B T_e)$, which has units of N/m^3 (force density). In the Generalized Ohm's Law, this term becomes a component to the electric field of: $-(3/2)(1/n_e e)(n_e\nu_{ei}/\omega_{c_e})\hat{b} \times \nabla(k_B T_e)$, which can also be written as $(3/2)(\nu_{ei}/m_e\omega_{c_e}^2)\nabla(k_B T_e) \times \mathbf{B}$ (to act analogously to the $\mathbf{u} \times \mathbf{B}$ dynamo term), both of which have units of $N/C = V/m$ (electric field). The ratio of the Nernst term to the Hall term is therefore: $[-(3/2)(n_e\nu_{ei}/\omega_{c_e})\hat{b} \times \nabla(k_B T_e)]/[\mathbf{J} \times \mathbf{B}]$. By scaling the terms (and making the oversimplified and, in general, incorrect approximation that the gradient scale lengths are the same for both the temperature and the magnetic field), the

Nernst-to-Hall ratio is given by $\sim (5 * 10^{-36}) n_e^2 \ln(\Lambda)/B^3 T_e^{1/2}$ where the electron density n_e is in cm^{-3}, the Coulomb logarithm is $\ln(\Lambda) \sim 5$, the magnetic field B is in Tesla, and the electron temperature T_e is in eV. For the radial foil experiments, taking $B = 2$ T and $T_e = 20$ eV, we find the Nernst effect is more important than the Hall effect for $n_e > 1 * 10^{18}\ cm^{-3}$. Therefore, the Nernst effect may influence the B_z compression by influencing field lines near the ablating foil surface.

7.4 Azimuthal Rotation (Overview)

Applying the B_z creates a $J_r B_z$ component of the $\mathbf{J} \times \mathbf{B}$ force that causes azimuthal rotation of the plasma (of both the background plasma and of the plasma jet that is formed by the converging background plasma). For completeness, so the reader gets a quantitative sense of the effects of the applied B_z, Fig. 7.32 shows research conducted by others studying this plasma rotation using optical spectroscopy and Thomson scattering. We note the different axis scales on each graph, but the main result is that the rotation direction is switched by changing the direction of the B_z or the current polarity.

Using the PERSEUS code, we can compare the rotation velocities predicted by the simulation to the experimental results. In Fig. 7.33, we find the same qualitative behavior for the rotation of the background plasma outside of the jet in the simulation as in the experiment (left plot in Fig. 7.32), for which the rotation velocity increases with radius. We also compare the ion fluid rotation velocity (caused by the $\mathbf{J} \times \mathbf{B}$ force) with the azimuthal component of the $\mathbf{E} \times \mathbf{B}$ drift velocity, $\mathbf{v_{E \times B}} = \mathbf{E} \times \mathbf{B}/\mathbf{B}^2$. From this comparison, we observe how the

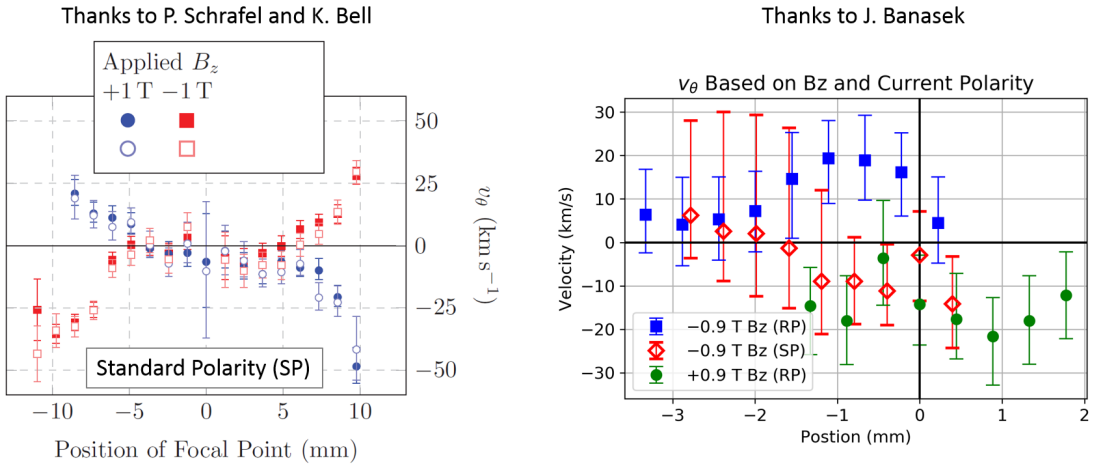

Figure 7.32: Experimental measurements of the plasma azimuthal rotation vs. radial position. Lineouts at a height 5 mm above the initial foil position. Note: the left and right images have different axis scales and different definitions of "positive" and "negative" rotation velocities. All quantities of the ion flow velocities are consistent with the $J_r B_z$ component of the $\mathbf{J} \times \mathbf{B}$ force. Left) optical spectroscopy measurements conducted by P. Schrafel and K. Bell showing rotation of the background plasma outside of the central jet, near $\sim$ 120 ns into the current pulse. Adapted from Schrafel et al., 2015. [40] Right) Thomson scattering measurements conducted by J. Banasek showing rotation of the central jet itself, at $\sim$ 160 ns into the current pulse. Adapted from Byvank et al., 2017. [27]

electric fields, magnetic fields, and current densities are set up to create the qualitative trends in rotation that we see in both the experiments and simulations. However, we also caution that the plasma rotation is not simply an $\mathbf{E} \times \mathbf{B}$ drift because the ion cyclotron radius is much larger that the collision mean free path ($r_{c_i} >> \lambda_{mfp_i}$; see, for example, Table A.3 in Appendix A); therefore, collisions dominate the fluid motion (rather than the particle gyroradius motion or particle guiding center drift dominating the fluid motion). Regarding the rotation of the plasma jet itself, simulations predict a peak azimuthal ion velocity that occurs at a very low-density region of plasma inside of the dense plasma jet ($\sim 10^{16}$ cm^{-3}, approximately two orders of magnitude lower than the peak jet density). The simulation peak ion velocity is much larger than what is seen with the experimental measurements. Qualitatively, this discrepancy is shown in the

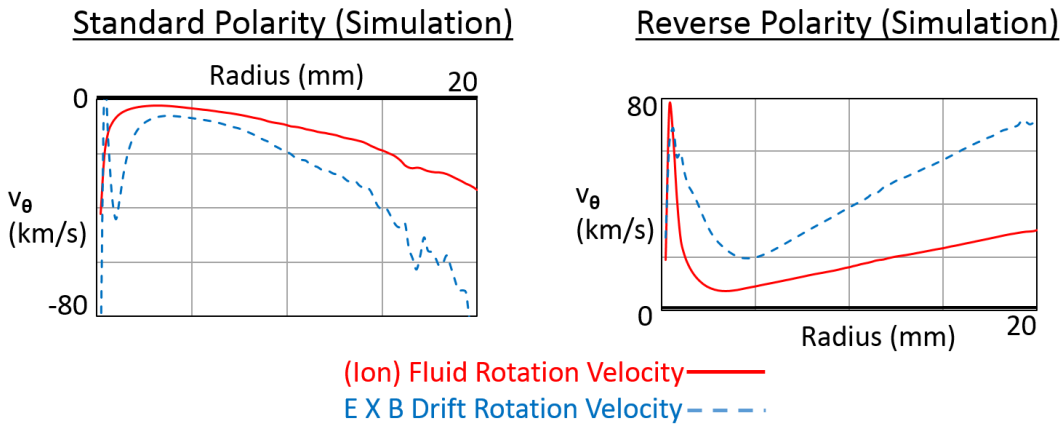

Figure 7.33: PERSEUS simulation for standard and reverse current polarities showing azimuthal rotation for plasma (ions) and comparison to the azimuthal component of the $\mathbf{E} \times \mathbf{B}$ drift velocity. The direction of the ion flow velocities are consistent with the $J_r B_z$ component of the $\mathbf{J} \times \mathbf{B}$ force. Lineouts at a height 2 mm above the initial foil position at 100 ns into the current pulse.

right image in Fig. 7.33 compared to the right image in Fig. 7.32, although here the lineouts are taken at different heights. Still, within the dense plasma jet itself (near the density peak), the simulation and experimental rotation velocities are similar (around 15-20 km/s).

On-axis compression of the applied axial magnetic field requires an azimuthal current to support the change in B_z across the plasma jet boundary. This current is a result of the relative electron-ion drift velocity. From the Thomson scattering measurements conducted, we were not able to obtain reliable values for the relative electron-ion drift velocities in our jets. However, experimental observations of the magnetic field compression and the jet rotation strongly indicate the presence of this azimuthal electrical current layer. For more information on these rotation measurements, we direct the reader to Schrafel et al., 2015 and Byvank et al., 2017. [40, 27]

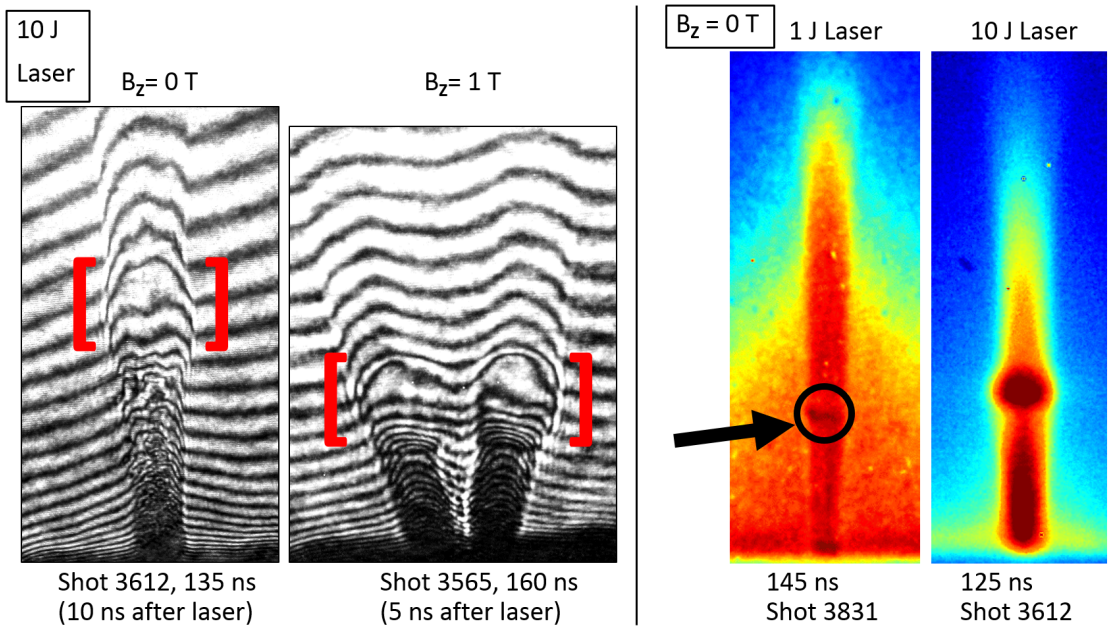

Figure 7.34: Interaction of the Thomson scattering laser with the plasma jet. Left: interferograms for plasma jets with different applied axial magnetic fields using a 10 J laser energy. Red brackets identify low-density bubble region. Right: EUV self emission with different laser energies using plasma jets with no B_z. Individual EUV images are contrast enhanced with dark red meaning more emission and blue meaning less emission. Black arrow points to slight heating even with a 1 J laser energy.

7.4.1 Spin-off from Thomson Scattering: Laser-Jet Interaction

While obtaining the Thomson scattering measurements using the 10 J laser, we observed an interaction between the laser and the plasma jet. This observation is important because Thomson scattering is intended to be a non-perturbing diagnostic to measure plasma parameters. The laser heats the plasma jet and creates a low-density bubble within the plasma jet that expands over time. Qualitatively, we observe the heating through the intensity of the plasma self-emission, and we observe the low-density bubble using interferometry (e.g. looking at the curvature of the fringes that depict a low-density bubble region between higher-density plasma regions in the plasma jet above and below the bubble);

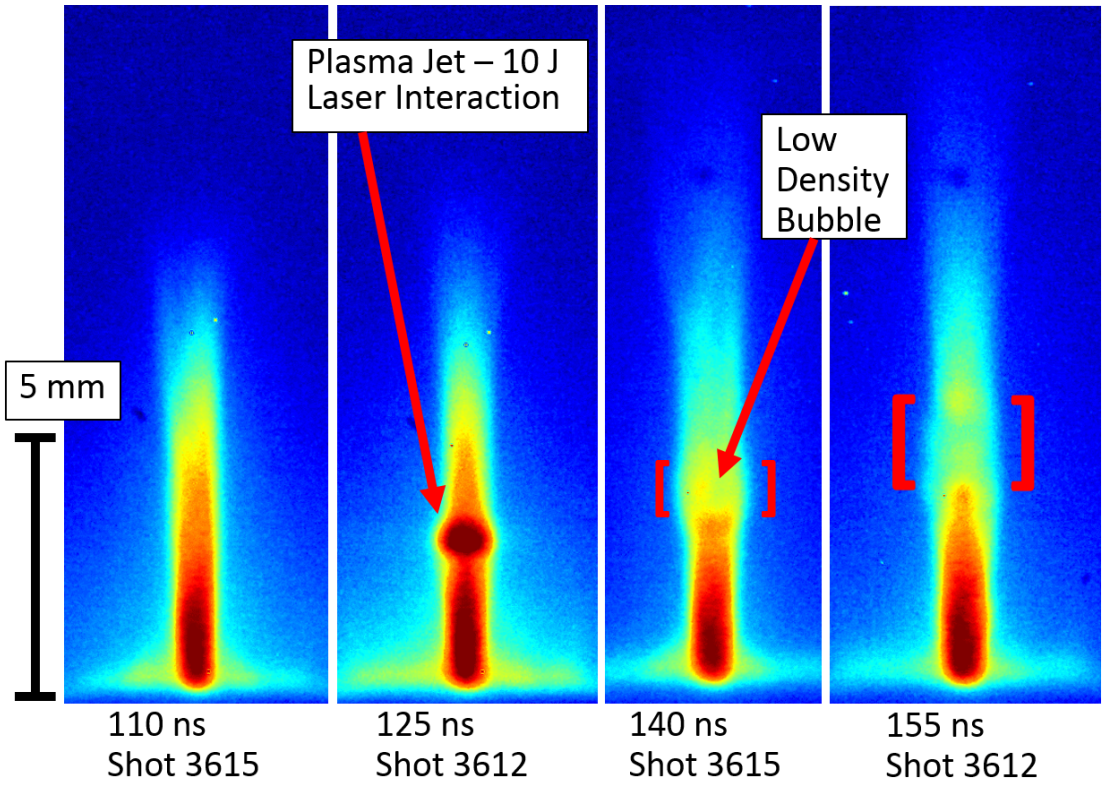

Figure 7.35: EUV self emission time development of laser-jet interaction with no B_z, showing: unperturbed plasma jet, heated and perturbed plasma jet, low density bubble formation, and bubble expansion. Individual images are contrast enhanced with dark red meaning more emission and blue meaning less emission.

see Fig. 7.34. Quantitatively, Jacob Banasek has observed heating of the plasma electron temperature over the timescale of the 3 ns laser pulse using streaked Thomson scattering. [77] The physical interpretation of this heating is that the laser electric field oscillates plasma electrons and deposits energy; this process is inverse bremsstrahlung absorption. The energy deposition that heats the plasma electrons (which heat the ions by collisions) then causes the plasma to expand (i.e. create a low-density bubble).

This time evolution is depicted in Fig. 7.35 using EUV self emision and in

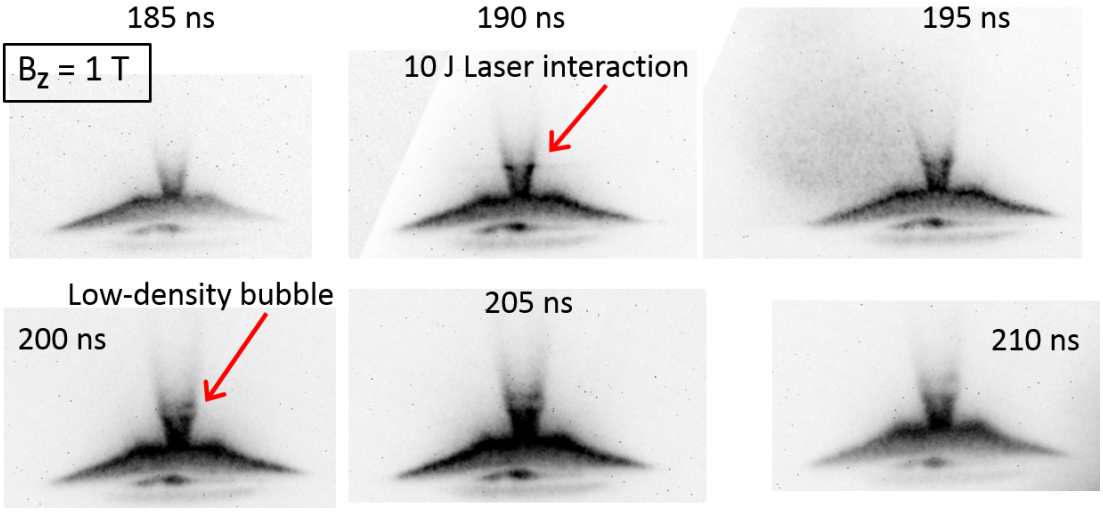

Figure 7.36: Optical self emission time development of laser-jet interaction with $B_z = 1$ T. Individual images are contrast enhanced with darker meaning more emission. Shot 3566.

Fig. 7.36 using optical self emission for different experiments. One feature that is sometimes, but not always, observed in the optical self emission is a "cloud" of emission intensity after the laser-jet interaction that occurs outside of the plasma jet on the "downstream" side of the laser (shown at 195 ns in Fig. 7.36; note: the laser is propagating from right to left in the images). This emission feature may be due to an interaction with the background plasma after some of the laser refracts away from the dense central plasma jet.

We can estimate the extent of the laser-jet interaction by comparing the deposited laser energy density to the plasma jet energy density. The jet thermal pressure (energy density), as given in Table A.3 in Appendix A, is $P_{th} \sim 2{*}10^7\ J/m^3$. For our laser specifications (wavelength, energy, irradiance), the absorption coefficient for the inverse bremsstrahlung process is $\kappa \sim 0.1\ cm^{-1}$ (see, for example, page 58 of the NRL formulary). [73] The energy density deposited into the plasma jet is estimated by $E_D = E_I(1 - \exp(-\kappa x)) \sim 1 * 10^9\ J/m^3$, where $x \sim 0.1\ cm$ is the characteristic jet width and E_I is the incident laser en-

ergy density (within the same volume as the deposited volume). We therefore semi-quantitatively find that $E_D > P_{th}$, so the energy deposited by the Thomson scattering laser is a significant perturbation to the plasma jet. We note that, using slightly different estimates, Banasek et al. gives a deposited laser energy estimate of $1.4 * 10^8\ J/m^3$. [77]

7.5 Plasma Disruption

When we vary the magnitude of the applied B_z, we expect differences in the amounts of effects like the jet density hollowing, magnetic field compression, and azimuthal rotation. Unexpectedly, at a B_z larger than a material-dependent critical B_z, we observe a different effect that we call a "disruption" of the plasma jet formation. We use the word "disruption" to refer to the breaking up of the well-aligned structure of the plasma jet. Below the critical B_z, the well-collimated jet structure and dynamics are determined as is discussed in previous sections. Above the critical B_z, the plasma erupts from the foil at various angles in discrete bursts in an uncollimated manner.

7.5.1 Experimental Jet Formation Disruption

First, we focus on experiments with a 15 μm aluminum foil and 5 mm diameter center pin. Up to B_z = 1 T, increasing B_z creates a larger on-axis hollowing of the well-collimated plasma jet. The aluminum jet disrupts for $B_z > 1.1 \pm 0.1$ T and is no longer well-collimated at any time within the experiment. Above the critical B_z, the jet may erupt as multiple bursts at various angles, not necessar-

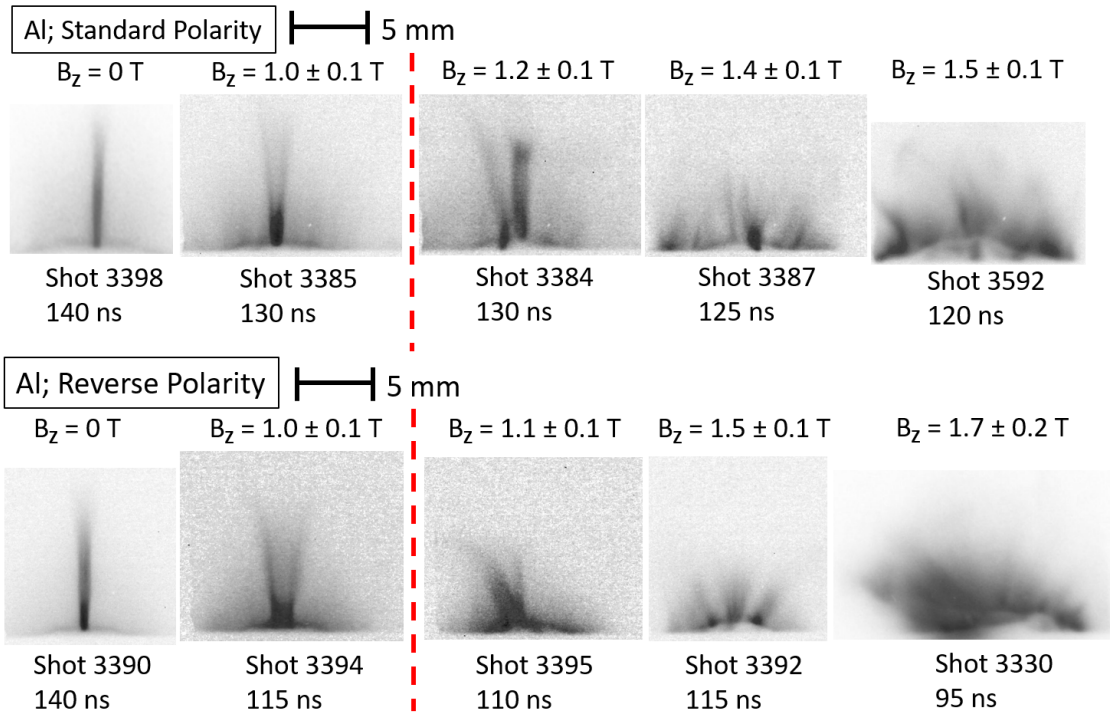

Figure 7.37: EUV self emission with increasing B_z from left to right, showing the plasma disruption above the critical B_z for standard polarity (top row) and reverse polarity (bottom row). Darker regions correspond to more emission. Contrast is enhanced for individual images. Adapted from Byvank et al., 2018. [78]

ily originating at the center of the foil. We show results using EUV self emission in Fig. 7.37 for both standard and reverse current polarities, displaying the same critical B_z independent of polarity. We show results using laser backlighting shadowgraphy in Fig. 7.38 for standard polarity. Additionally, as shown in Fig. 7.39, the disruption critical B_z appears independent of whether the B_z is oriented parallel or antiparallel to the z-axis (and the upward jet axial velocity direction). In order to limit the experimental parameter space while exploring the disruption phenomena with a finite number of COBRA shots, we choose to use standard polarity and a positive B_z (directed upwards) as a baseline case, for which we will vary parameters like pin size, foil thickness, and foil material.

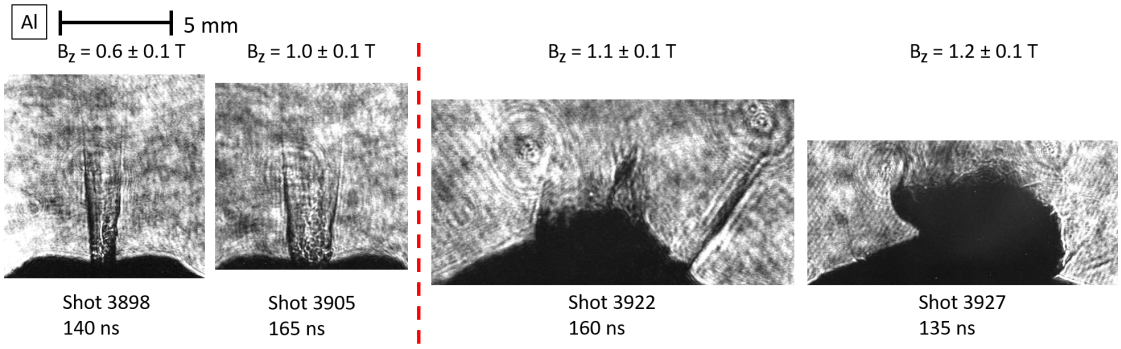

Figure 7.38: Laser backlighting shadowgraphy with increasing B_z from left to right, showing the plasma disruption above the critical B_z (in standard polarity). Adapted from Byvank et al., 2018. [78]

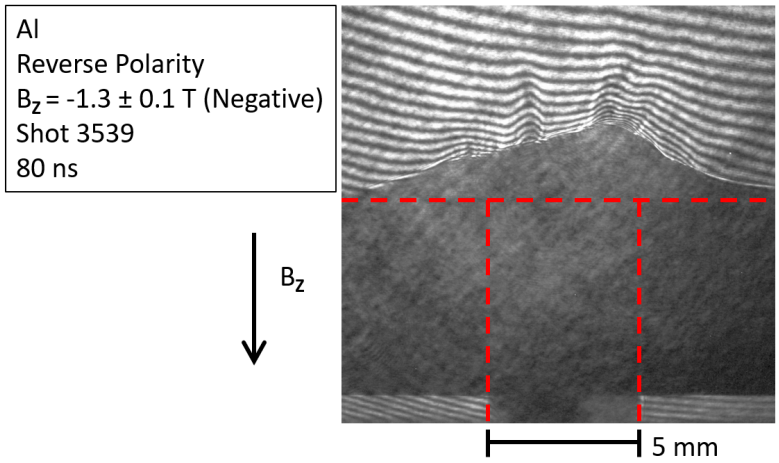

Figure 7.39: Interferogram showing disruption for a negative B_z (directed downward) in reverse polarity. Initial foil and pin location denoted by dashed red lines. Note the asymmetric ablation of the dense foil and discrete plasma bursts above the foil.

The disruption originates from the foil surface early-on in time– before or during the formation of the plasma jet. Therefore, the plasma disruption is not some effect like a kink instability or rotational instability of the already-formed jet. In Fig. 7.40 before the plasma jet forms, we compare the uniform and symmetric foil emission below the critical B_z to the discrete plasma bursts erupting from the foil above the critical B_z. Another notable aspect of the disruption critical B_z is not the precise magnitude but rather the sudden onset of the jet

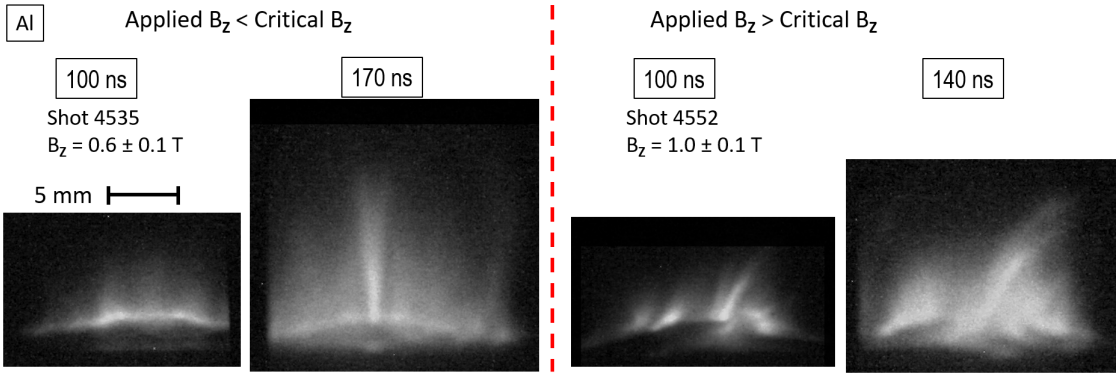

Figure 7.40: EUV self emission of plasma jet with no disruption (left) and disruption (right). For the disruption, plasma nonuniformities start during the foil ablation, before (or while) the jet would be forming. Brighter regions correspond to more emission. Contrast is enhanced for individual images.

disruption by changing the applied field strength by ∼10-20%. The mechanism causing the disruption is likely still present at lower B_z but does not dominate the plasma dynamics and jet formation.

Initial density perturbations and nonuniformities in the radial foil exacerbate the disruption. Bumps < 50 μm on the contact area between the foil and pin can lead to a more-pronounced disruption when there is an applied field. However, the critical B_z value does not change. The jet plasma typically erupts from the foil near the location of the density perturbation. When there is no applied field, the < 50 μm perturbations do not significantly alter the plasma dynamics, as observed by the plasma jet forming in a similar manner as seen using all diagnostics. The jet disruption still occurs even when perturbations are reduced to bumps < 0.5 μm. These bump sizes are estimated by eye comparing samples of known surface roughness.

We conduct experiments varying the center pin diameter to observe any effects on the critical B_z, while keeping the foil thickness constant at 15 μm. Varying the pin diameter changes the maximum B_θ and, therefore, maximum J $\times$ B

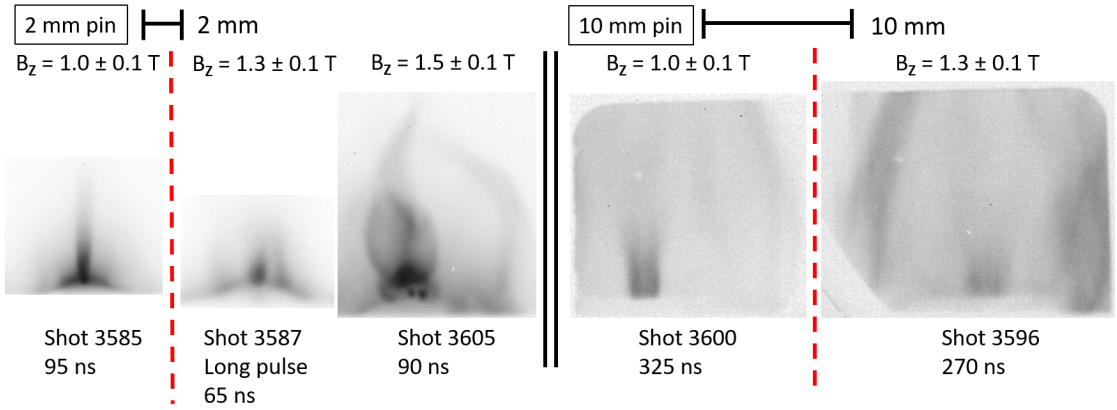

Figure 7.41: EUV self emission images with different center pin diameters, showing the plasma jet disruption above the critical B_z. Three images on the left are for 2 mm pins. Two images on the right are for 10 mm pins. Darker regions correspond to more emission. Contrast is enhanced for individual images. Adapted from Byvank et al., 2018. [78]

force that collimates the plasm jet on-axis. A smaller pin with a larger J $\times$ B force will create a collimated jet more quickly. As shown in Fig. 7.41, for 2 mm and 10 mm pins, we observe well-collimated plasma jets at a B_z below 1.1$\pm$0.1 T. For $B_z > 1.1\pm0.1$ T, we observe large amounts of background plasma bursts that do not form a single well-collimated central jet. Based on these results, the pin diameter does not appear to influence the disruption critical B_z. In particular, if there was a strong correlation between pin size and the disruption, we would expect a disruption at a $B_z < 1.0$ T (lower than the threshold for the 5 mm pin case) for one of the cases with pin diameters of either 2 mm or 10 mm. Still, we note that the plasma dynamics significantly change with these different pin sizes, so there may be other differences that influence the plasma jet structure. For instance, using 2 mm pins creates a magnetic bubble (after the well-collimated jet) that develops into a Z-pinch and x-ray burst that have been previously studied; see Fig. 1.1.

We conduct experiments varying the radial foil thickness to observe any ef-

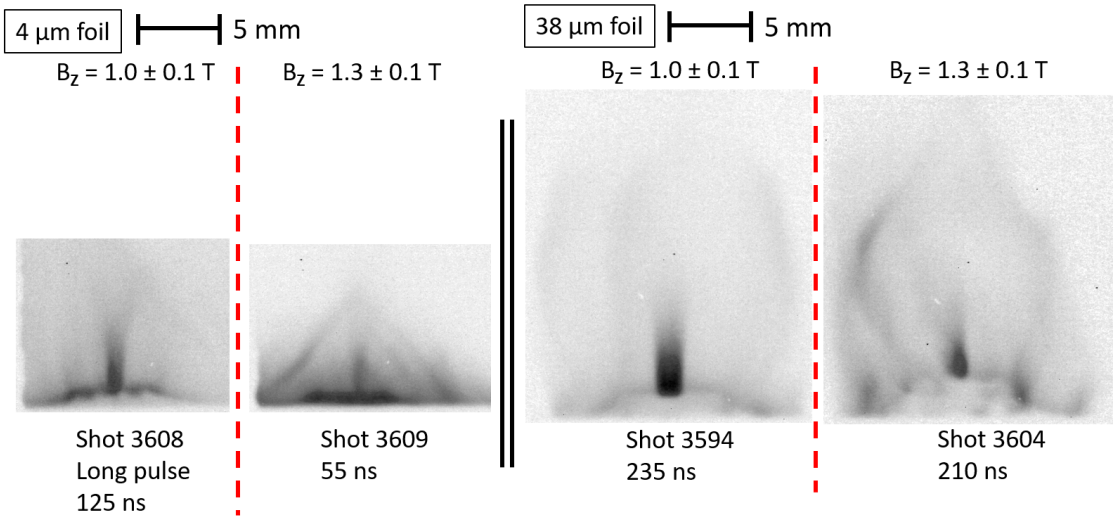

Figure 7.42: EUV self emission images with different foil thicknesses, showing the plasma jet disruption above the critical B_z. Two images on the left are for 4 μm foils. Two images on the right are for 38 μm foils. Darker regions correspond to more emission. Contrast is enhanced for individual images. Adapted from Byvank et al., 2018. [78]

fects on the critical B_z, while keeping the center pin diameter constant at 5 mm. Varying the foil thickness changes the amount of solid material available to become plasma and the heating time for plasma generation. However, we note that all foil thicknesses used in the present work are less than the skin depth of $\sim$40 μm for solid room temperature aluminum. As shown in Fig. 7.42, for 4 μm and 38 μm foil thicknesses, we observe well-collimated plasma jets at a B_z below 1.1$\pm$0.1 T. For $B_z > 1.1\pm0.1$ T, we again observe large amounts of background plasma bursts that do not form a single well-collimated central jet. However, in particular for the 4 μm case, for example, we do see a central jet in the middle of plasma bursts. This result is somewhat ambiguous: has the 4 μm thick foil disrupted for $B_z > 1.1\pm0.1$ T? Again, we observe that the disruption initiates early on as azimuthal nonuniformities in the foil and surface plasma, occurring before or during the time that the jet would be forming. We note that changing the foil thickness significantly alters the plasma dynamics; using 4 μm

foils creates a magnetic bubble (after the well-collimated jet) that develops into a Z-pinch and x-ray burst that have been previously studied. Thicker foils like 15 μm and 38 μm do not form a magnetic bubble that creates an x-ray burst. Additionally, using thicker foils like 38 μm delays time of plasma formation on the foil surface compared with thinner foils.

We change the foil materials from aluminum (Z=13) to titanium (Z=22), nickel (Z=28), copper (Z=29), zinc (Z=30), molybdenum (Z=42), and tungsten (Z=74). As shown in Fig. 7.43, we observe a disruption for the copper jets at a B_z = 0.95$\pm$0.1 T, which is measurably lower than that for aluminum. We observe a disruption for the zinc jets at a B_z = 1.6$\pm$0.2 T, which is measurably higher than that for aluminum. As shown in Fig. 7.44, we observe no disruption for titanium, nickel, molybdenum, and tungsten jets for applied field strengths up to B_z = 2.0$\pm$0.2 T, which is the maximum B_z experimentally applied in this work. The critical B_z of 0.95 T for copper foils, 1.1 T for aluminum foils, and 1.6 T for zinc foils, are lower than the dynamical fields of $>$5-10 T applied in previous pulsed power work and uniform fields of $\sim$20 T in laser-target irradiation that do not disrupt the laboratory plasma jets. [35, 42, 79, 80]

Because we observe that the disruption originates from the foil surface early on in time, solid material properties may be important if the disruption is seeded in the solid phase. We find a correlation between the plasma jet disruption and the foil material's electrical resistivity and equation of state. Material properties for the foils used in the present work are shown in Table 7.1 and Table 7.2 along with the critical B_z for the disruption. [81] Table 7.1 is ordered by increasing resistivity at the melting point temperature in the liquid phase (right column). This quantity serves to show the dependence of the disruption critical

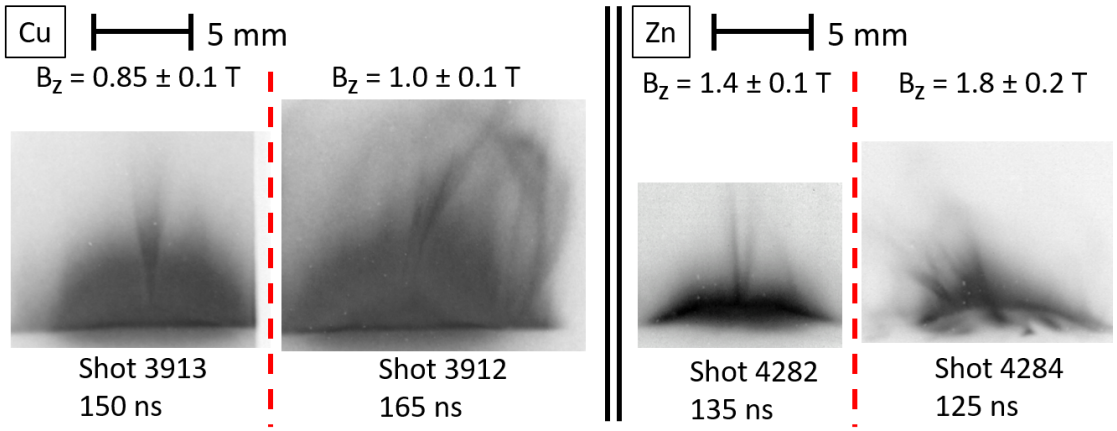

Figure 7.43: EUV self emission images with different foil materials, showing the plasma jet disruption above the critical B_z. Two images on the left are for Cu foils. Two images on the right are for Zn foils. Darker regions correspond to more emission. Contrast is enhanced for individual images. Adapted from Byvank et al., 2018. [78]

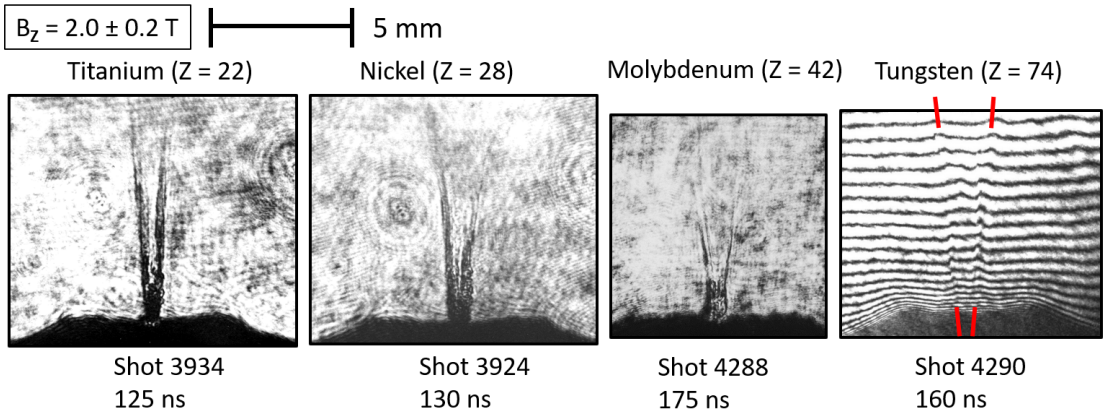

Figure 7.44: Laser backlighting shadowgraphy (and one interferogram) for radial foil experiments with different foil materials at the maximum experimentally applied B_z = 2 T, showing well-collimated jets (no disruption) for Ti, Ni, Mo, or W foils. For the interferogram, the red dashes are meant to guide the reader's eyes along the fringe shifts to see the conical jet angle for the well-collimated W jet. Adapted from Byvank et al., 2018. [78]

Table 7.1: Foil Material Properties [81] and Disruption Critical B_z

Material	Disruption Critical B_z (T)	Z	Melting Point (°C)	Solid Phase Melting Point Resistivity (nΩm)	Liquid Phase Melting Point Resistivity (nΩm)
Cu	0.95 ± 0.1	29	1085	110	220
Al	1.1 ± 0.1	13	660	110	250
Zn	1.6 ± 0.2	30	420	160	380
Ni	>2	28	1455	630	850
Mo	>2	42	2623	830	970
W	>2	74	3422	1200	1350
Ti	>2	22	1668	1620	1670

B_z on both electrical resistivity and equation of state. Table 7.2 is ordered by material identically to Table 7.1. We find a better correlation between the disruption critical B_z with the resistivity at the melting point (Table 7.1) than with the resistivity at either room temperature or the boiling point (Table 7.2). This dependence motivates numerical simulation modeling that includes the material conductivity and equation of state from the solid through plasma phases, including the phase transitions; see Sec. 7.5.3. Additionally, as we discuss in the simulations presented in Sec. 7.5.3, current nonuniformities originating in the solid-liquid phases appear to generate current and density nonuniformities within the plasma phase; the discrete plasma bursts in these simulations could lead to the discrete plasma bursts observed in the experimental disruption. Furthermore, we do not find a correlation of the disruption critical B_z with material atomic number, Z, which suggests that radiation effects (like radiative cooling and ionization) are not the primary factors influencing the disruption.

The plasma magnetization and anisotropy created by the applied B_z could prevent plasma and current transport radially inward toward the central jet axis. However, because the disruption appears to originate from the foil surface,

Table 7.2: More Foil Material Properties [81] and Disruption Critical B_z

Material	Disruption Critical B_z (T)	Z	Solid Phase Room Temperature Resistivity (nΩm)	Boiling Point (°C)	Liquid Phase Boiling Point Resistivity (nΩm)
Cu	0.95 ± 0.1	29	17	2562	1100 [extrapolate]
Al	1.1 ± 0.1	13	28	2470	490 [extrapolate]
Zn	1.6 ± 0.2	30	59	907	370
Ni	>2	28	69	2730	920
Mo	>2	42	53	4639	1160
W	>2	74	53	5930	1550
Ti	>2	22	420	3287	1900

the magnetization in the solid, liquid, and/or vapor phases may be more relevant than the plasma magnetization (ω_{c_k}/ν_{ki}, as shown in Fig. 7.8 and Fig. 7.9). Moreover, estimates for the electron and ion plasma magnetization suggest that the plasma disruption is not caused solely by the plasma being tied to and following the applied B_z field lines. The applied B_z causing anisotropic conductivity could influence current generation and plasma formation (i.e. Pederson σ_P, Hall σ_H, and parallel $\sigma_{||}$ conductivity components in the conductivity tensor $\overline{\overline{\sigma}}$; see Eqs. 7.13-7.16 with the parallel component referring to the magnetic field direction). Additionally, the current diffusion and foil heating time may influence how well initial density perturbations can equilibrate.

$$\overline{\overline{\sigma}} = \begin{bmatrix} \sigma_P & \sigma_H & 0 \\ \sigma_H & \sigma_P & 0 \\ 0 & 0 & \sigma_{||} \end{bmatrix} \tag{7.13}$$

$$\sigma_P = \frac{\nu_{ei}}{\omega_{c_e}^2 + \nu_{ei}^2} \frac{n_e e^2}{m_e} \tag{7.14}$$

$$\sigma_H = \frac{\omega_{c_e}}{\omega_{c_e}^2 + \nu_{ei}^2} \frac{n_e e^2}{m_e} \tag{7.15}$$

$$\sigma_{||} = \frac{1}{\nu_{ei}} \frac{n_e e^2}{m_e} \tag{7.16}$$

The well-collimated plasma jet carries axial current, I_z, which self-generates an azimuthal magnetic field, B_θ. Estimating that the jet carries 5% of the COBRA current, at a characteristic radius of r=1 mm at peak current (1 MA at 100 ns), the jet would produce a $B_\theta = \mu_0 I_z / 2\pi r = 10$ T. The ratio B_z/B_θ is therefore a factor of 0.1-0.2 for a B_z of 1-2 T. Additionally, at a 2.5 mm pin radius, the peak COBRA current through the center pin produces a maximum $B_\theta = 80$ T beneath the foil, substantially larger than the B_z. Yet, we find that a slight ($\sim$10%) change in B_z can dramatically influence the plasma dynamics. When the jet disruption occurs, a well-collimated plasma jet does not form and therefore does not generate an azimuthally symmetric B_θ. Furthermore, if we consider the disruption to initiate early in time while the surface plasma is ablating from the foil– say, around $\sim$50 ns– the relative ratio of B_z/B_θ at the ablating plasma surface would be even larger.

In this section, we have experimentally observed a breaking up of the azimuthally symmetric plasma jet into discrete bursts with a material-dependent critical B_z for the disruption. The disruption originates from the foil surface early in time and occurs based on a $\sim 10 - 20\%$ change in the applied B_z. In

the following sections, we look at a top view of the disrupting foil, conduct 3D simulations to study ablation of a section of the foil, and try to amalgamate evidence to better elucidate the disruption phenomena.

7.5.2 Experimental Current Filament Disruption

The process of current filament formation of the radial foil surface plasma is described in Sec. 7.2. For 15 μm thick aluminum foils with 5 mm pin diameters, the disruption of the discrete current filaments appears for $B_z > 1.1 \pm 0.1$ T, the same threshold as for the jet disruption; see Fig. 7.45. Nonuniformities in the foil and pin-foil contact exacerbate the current filament disruption, but the disruption still occurs for small perturbations (bumps < 0.5 μm on pin and foil surfaces). While there is approximately azimuthally symmetric EUV emission at $B_z < \ 1.1 \pm 0.1$ T, for $B_z > \ 1.1 \pm 0.1$ T there are discrete bursts of plasma filaments in addition to the approximately symmetric emission. The disruption is therefore consistent with breaking the azimuthal symmetry of the current and plasma formation.

7.5.3 Foil Ablation Simulations

We define the term "ablation" of a solid foil to be the heating process by which the initially solid material melts, vaporizes, ionizes, and produces a plasma. The author would like to thank Dr. Charlie Seyler for running these 3D simulations and for giving me the code output files to inspect, dissect, and analyze. The specifications for these slab simulations are given in Sec. 6.4. The intention is

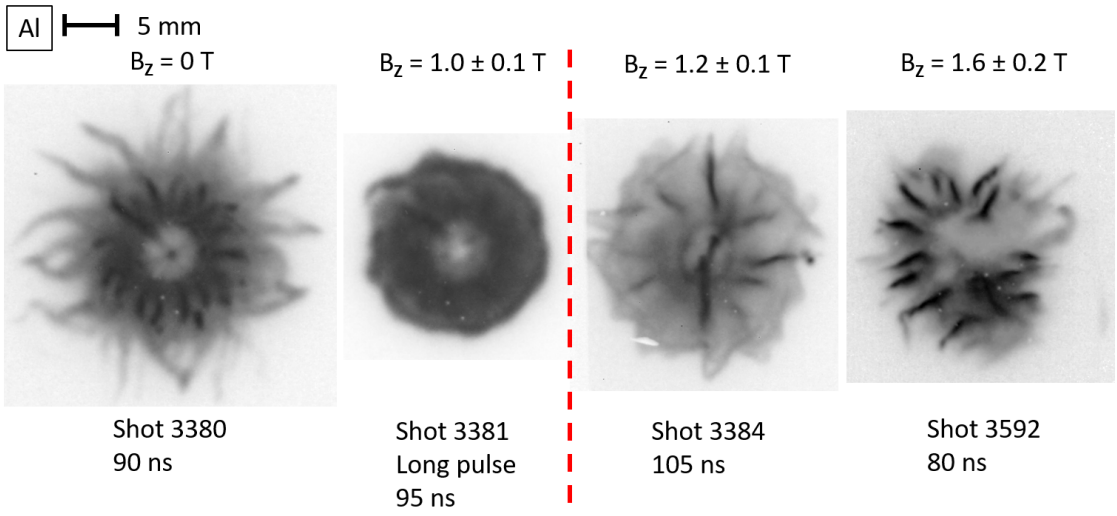

Figure 7.45: EUV self emission images looking down onto the radial foil surface with increasing B_z from left to right, showing the plasma (current filaments) disruption above the critical B_z in standard polarity. For reverse polarity (not shown), we also see discrete plasma bursts for the disruption. Darker regions correspond to more emission. Contrast is enhanced for individual images. Adapted from Byvank et al., 2018. [78]

that studying the Cartesian slab ablation can serve as an analog to understanding the local disruption process that occurs during ablation of the radial foil.

2D azimuthally symmetric PERSEUS simulations reproduce the aluminum jet structure for $B_z < 1.1 \pm 0.1$ T, but the simulations do not reproduce the jet disruption for $B_z > 1.1 \pm 0.1$ T. Furthermore, these 2D simulations initialize the foil as a plasma with Spitzer resistivity. The disruption is inherently a 3D process that breaks azimuthal symmetry of the current and plasma distributions. Additionally, the experimentally observed material effects on the disruption critical B_z suggest that material properties like electrical conductivity and equation of state (EOS) are important influencing factors in the foil ablation process. We would like to conduct a 3D radial foil simulation with detailed aluminum conductivity and EOS data from the solid through plasma phases with full spatial resolution. However, due to limited computational resources, we instead

present 3D results of the ablation process of a small aluminum slab that represents a section of the radial foil (as specified in Sec. 6.4).

We begin by discussing simulation results that most pertain to the disruption in the plasma phase. Then, we explore the ablation process in more detail, including dynamics that occur in the denser solid and liquid phases. We consider cases for which there is 1) no applied B_z, 2) a 1 T B_z, 3) a 4 T B_z, and 4) a 1 T B_z for which we artificially increase the material resistivity by a factor of 5 from the solid phase until the plasma phase, at which point we use Spitzer resistivity. For this "fake material" in the last case, we still use the aluminum EOS, and the idea is to observe the isolated influence of resistivity to stand in for titanium or another one of the higher-resistivity materials that we did not experimentally observe to disrupt. We did not have conductivity or EOS data for any of the materials used in the experiments other than aluminum; we did have beryllium conductivity and EOS data for the simulation, but there was a lack of desire to experimentally explode beryllium foils due to plebeian health concerns like beryllium poisoning.

Within this thesis subsection, we display two main types of images from the simulation results. First, as displayed in Fig. 7.46, we show images of a (number) density contour of the foil. This contour is a 3D surface (that has x, y, and z dimensions) of the ablating foil at a particular (number) density. Then, we color the contour to show the current density magnitude at the position on the (number) density contour. Here, this contour structure is always (number) density, and the color is always current density magnitude. The height of the contour above the initial foil position is labeled as Δz (for the contour on the upper side of the foil). Second, as displayed in Fig. 7.47, we show images of

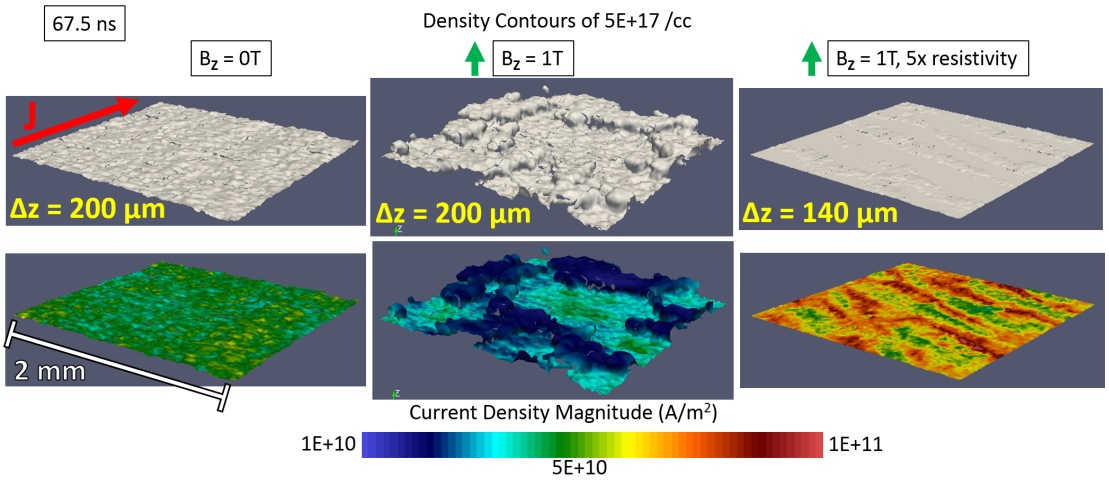

Figure 7.46: 3D slab simulations of density contours at $5 * 10^{17}\ cm^{-3}$, showing differences in the ablated plasma (top row) and current density (color overlay in bottom row) structure for a 0 T B_z, a 1 T B_z, and a 1 T B_z with an artificially enhanced resistivity by a factor of 5 from the solid phase until the plasma phase, for which we use Spitzer resistivity. Time relative to the start of the current pulse. Adapted from Byvank et al., 2018. [78]

the computational spatial domain: the cube faces that show cross sections of the bulk system. Here, this bulk system can show different parameters– as labeled– including (number) density, current density magnitude, and temperature. The axial position of the initial (time zero) foil is marked as z_0.

First, we look at the surface of the ablating slab that corresponds to the top surface of the radial foil. In Fig. 7.46 in the top row, we plot contours of constant density at $5 * 10^{17}\ cm^{-3}$, which is in the plasma phase. We observe discrete and nonuniform humps ($\sim$150 μm height) of plasma for the 1 T B_z case (center), while there is smoother and more-uniform ($\sim$10 μm height humps) plasma ablation for both the 0 T B_z case (left) and 1 T B_z case with artificially increased resistivity (right). Additionally, in the bottom row of Fig. 7.46, we overlay a colorscale for the current density magnitude onto the density contour. When comparing the 0 T and 1 T cases, we see that the plasma nonuniformities also

correlate with current nonuniformities. These discrete plasma bursts in these Cartesian slab simulations could lead to the plasma and current nonuniformities in the radial foil experiments that cause the discrete plasma bursts observed in the disruption. For the case with a 1 T B_z and artificially enhanced resistivity, the ablating plasma is uniform, but there are also noticeable current nonuniformities. This difference compared to the 0 T case is due to significant changes in the ablation dynamics for the case with artificially enhanced resistivity. For example, at the same 67.5 ns time, the $5 * 10^{17}\ cm^{-3}$ contour is at a height above the initial (time zero) solid foil location of Δz =200 μm for both the 0 T case and 1 T case (at the "lower" position of the nonuniform humps), but the contour for the case with a 1 T B_z and artificially enhanced resistivity is at a lower height of Δz =140 μm. Overall, the simulations show the same trend as the experiments: a disruption (nonuniform discrete bursts) with an applied B_z and a lower resistive material but not for the two cases with either no B_z or with a B_z but a higher resistive material.

Now that we have shown the simulation results in the plasma phase that are most analogous to the experimental disruption, we will analyze the ablation process in more detail. In Fig. 7.47 for a 0 T and 1 T B_z, we look at the time evolution of the density and current. Around 45-50 ns into the current pulse, the foil has significantly expanded from its original 25 μm thickness to $\sim$80 μm. Then, plasma starts forming above the denser foil surface. More plasma forms above the foil than below because the J $\times$ B force is directed upward.

At 55 ns, we observe more ablating plasma for the 0 T case than the 1 T case (a thicker region of $\sim 10^{17}\ cm^{-3}$ (cyan) above the $> 10^{22}\ cm^{-3}$ foil (red) in Fig. 7.47 A than B). The current is distributed mostly in the solid foil ($> 10^{22}\ cm^{-3}$ (red)

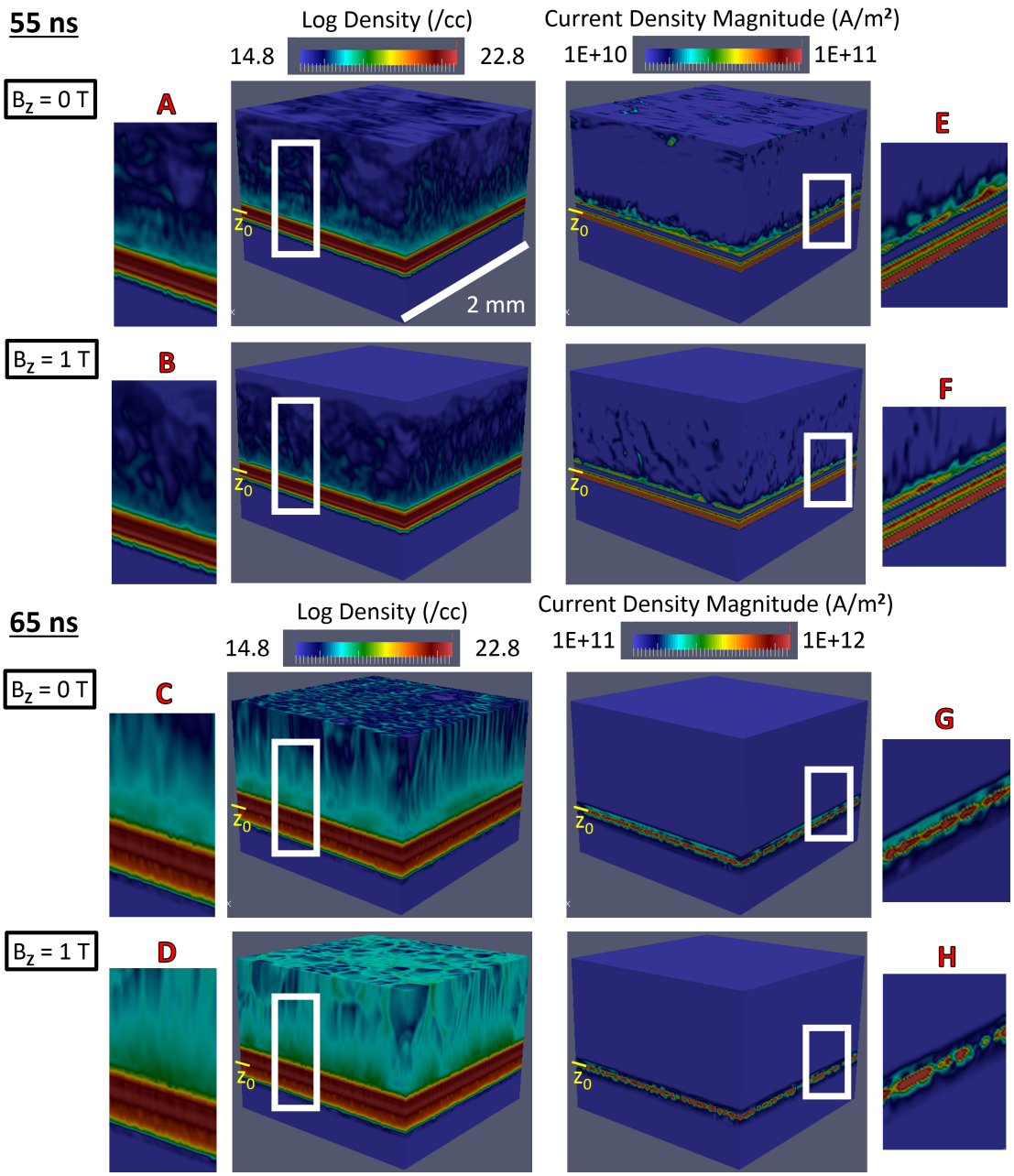

Figure 7.47: 3D slab simulations showing density and current time evolution with external B_z= 0 T and 1 T. The density color scales are the same for all parts (A-D), but the current density color scales are different between the 55 ns cases (E, F) than the 65 ns cases (G, H). Time relative to the start of the current pulse. Adapted from Byvank et al., 2018. [82]

in Fig. 7.47 A and B), but there is also a layer of current in the ablating surface plasma ($\sim 10^{18}\ cm^{-3}$ (green) and $\sim 10^{17}\ cm^{-3}$ (cyan) in A and B). Additionally, there is a gap of little-to-no current between these two current layers ($< 10^{10}\ A/m^2$ (blue) region between the two $\sim 10^{11}\ A/m^2$ (orange to red) regions in Fig. 7.47 E and F). This current gap occurs in an intermediate density range in the material ($\sim 10^{20} - 10^{21}\ cm^{-3}$ (orange to dark red) in Fig. 7.47 A and B). Furthermore, the lowermost $> 10^{10}\ A/m^2$ region in Fig. 7.47 E and F consists of two $\sim 10^{11}\ A/m^2$ (red) regions separated by $> 4 * 10^{10}\ A/m^2$ regions (green to dark red); this situation corresponds with a medium current layer in between two high current layers. While we plot the current density magnitude, we note that the vast majority of the current is moving in the x direction (not shown).

Looking an additional 10 ns later, at 65 ns we now see more plasma for the 1 T case than the 0 T case (a thicker region of $\sim 10^{18}\ cm^{-3}$ (green) above the $> 10^{22}\ cm^{-3}$ (red) in Fig. 7.47 D than C). Therefore, between 55 ns and 65 ns in this simulation, the external 1 T B_z is facilitating more plasma ablation from the upper foil surface. We believe the physical reason for this changing plasma ablation relates to the B_z generating nonuniform currents in the higher-density phases, which nonuniformly heats the foil and produces ablated plasma from the heated locations. Furthermore, electrothermal instabilities are likely candidates for why 1) there are initial nonuniformities in the higher-density (solid-liquid) foil that do not equilibrate and smooth out, and 2) the nonuniform plasma propagates from these initial solid-liquid nonuniformities. As previously stated, most of the current is traveling in the high density near-solid foil ($> 10^{21}\ cm^{-3}$) rather than the surface plasma ($< 10^{19}\ cm^{-3}$). At 65 ns, we observe that more current is flowing more uniformly in the near-solid foil for the 0 T case than the 1 T case (more current $> 3 * 10^{11}\ A/m^2$ (cyan) distributed in Fig. 7.47

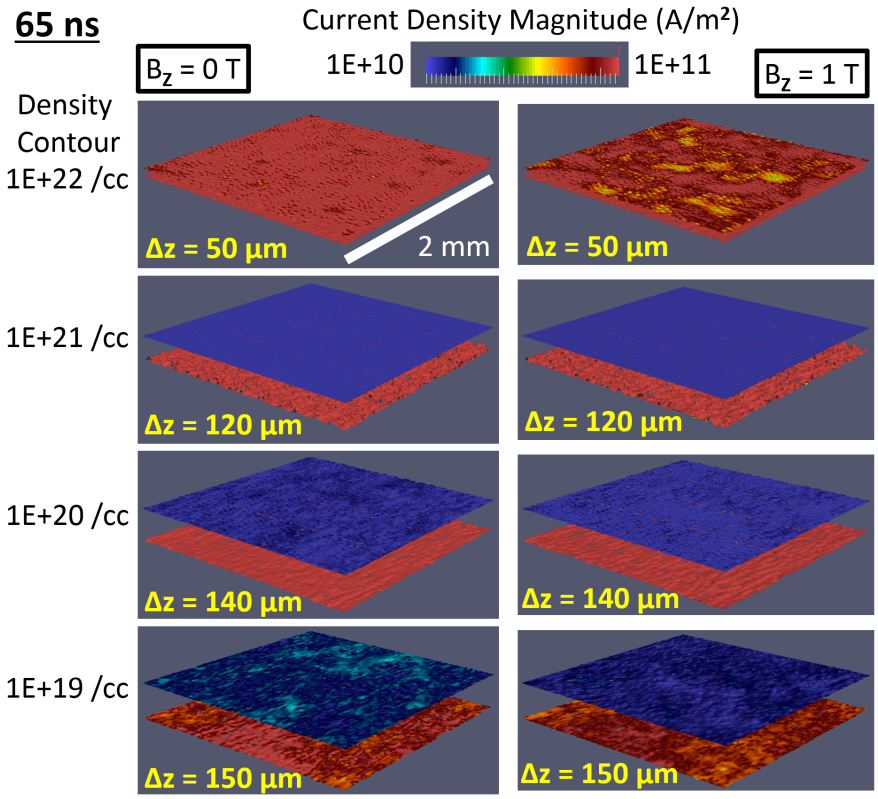

Figure 7.48: 3D slab simulations showing current density of specified (number) density contours within the slab for B_z= 0 T and 1 T. There are two contours (one above the other) at each density because the foil expands and generates plasma on both its upper and lower surface. Time relative to the start of the current pulse. Adapted from Byvank et al., 2018. [82]

G than H). Although both images G and H saturate the displayed color scheme (with currents $> 10^{12}\ A/m^2$), the maximum current densities for both simulations at this time are close: $\sim 8 * 10^{12}$ A$/m^2$ for the 0 T case and $\sim 9 * 10^{12}$ A$/m^2$ for the 1 T case. At this 65 ns time, the little-to-no current region shown in the images at 55 ns is still present but not displayed due to the color scale change. The current density distribution is fundamentally related to the temperature, number density, and amount of ablated plasma.

We plot the current within individual density contours at 65 ns in Fig. 7.48 and from 50-72.5 ns in a lower density plasma phase in Fig. 7.49. Each surface

contour in each image has a specific density as labeled, and we overlay the current magnitude as the color scale. There are two contours (one above the other) at each density because the foil expands and generates plasma on both its upper and lower surface. Here, we are focusing on the upper surface corresponding to the top side of the radial foil. At a given number density, the upper surface typically has less current density compared to the lower surface because the upward plasma ablation reduces the magnetic field magnitude and shear within the plasma that drives the current (in other words, reducing the $\partial B_y/\partial z$ that drives the J_x). For the slice with the highest density, $1 * 10^{22}\ cm^{-3}$, we observe that applying the 1 T B_z causes current nonuniformities (dispersed lower current $\sim 6 * 10^{10}$ A$/m^2$ represented by yellow regions) compared to the 0 T case. The $1*10^{21}\ cm^{-3}$ contours are similar for both cases, showing little-to-no current in the upper foil surface. The $1 * 10^{20}\ cm^{-3}$ contours are also similar, with there being somewhat more current (more $\sim 2 * 10^{10}$ A$/m^2$ (dark blue) regions rather than $< 2 * 10^{10}$ A$/m^2$ (blue) regions) for the 0 T case than the 1 T case. Then, considering the lower density plasma contours, at $1 * 10^{19}\ cm^{-3}$ we again see larger differences, where the applied 1 T B_z has lower current than the 0 T case (again, we note that the current scale minimum is 10^{10} A$/m^2$ (blue), and the 1 T case has $1 - 3 * 10^{10}$ A$/m^2$ (blue and dark blue) regions, while the 0 T case has mostly $2 - 4 * 10^{10}$ A$/m^2$ (dark blue and cyan) regions). The main result is that the applied 1 T B_z leads to current nonuniformities in the solid through plasma phases.

Now, in Fig. 7.49 we look more closely at the time evolution of the plasma density contour at $5 * 10^{17}\ cm^{-3}$, which is similar to the density of the ablated surface plasma and background plasma that forms the plasma jet or plasma disruption in the radial foil experiments. Again, we overlay the current density

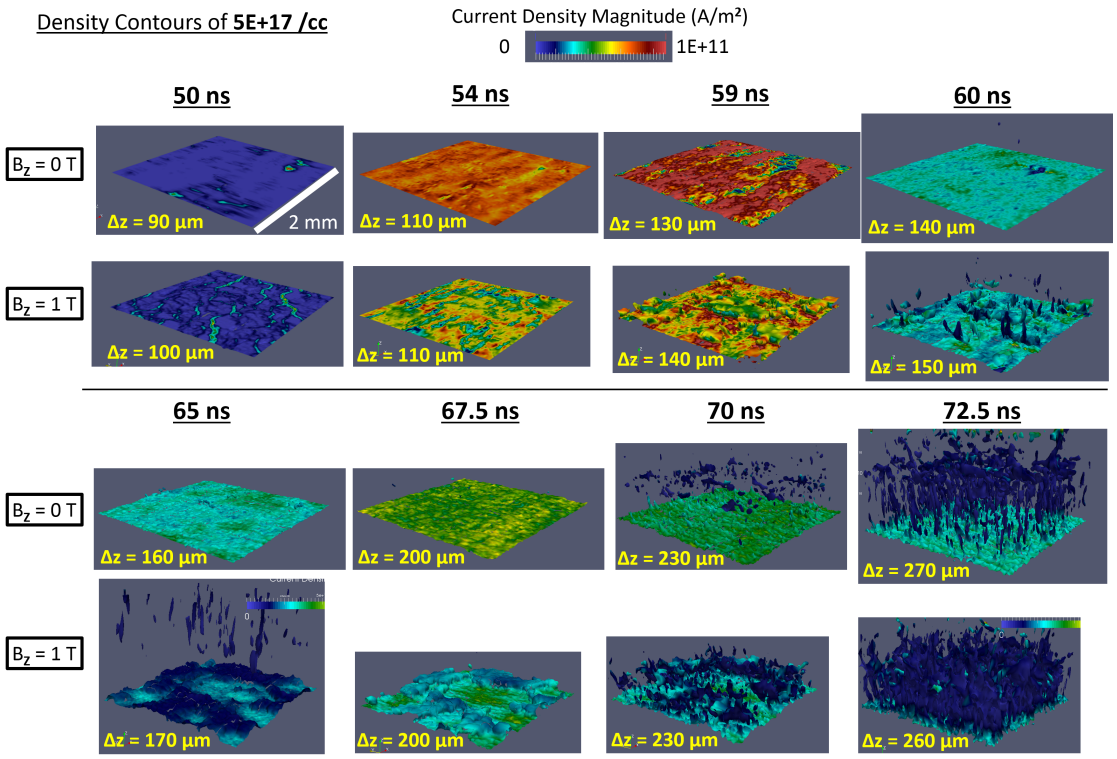

Figure 7.49: 3D slab simulations showing current density of the $5 * 10^{17}\ cm^{-3}$ (number) density contour on the top surface of the slab for B_z= 0 T and 1 T. Time relative to the start of the current pulse.

magnitude as the color scale. Throughout the ablation process, the applied 1 T B_z facilitates current nonuniformities, which cause temperature nonuniformities (from Joule heating) and nonuniformities in plasma generation. From 50 ns to 59 ns, current increases at this density layer. Then, current decreases from 59 ns to 65 ns, and the plasma density contour becomes noticeably less uniform for the 1 T case than the 0 T case. For reference, current increasing physically corresponds to current moving into this density layer, and current decreasing corresponds to current moving into a different density layer. From 65 ns (note: the same time as shown in Fig. 7.47 C and D) to 70 ns, the current increases and the plasma nonuniformities for the different cases become most clear (as shown in Fig. 7.46 at 67.5 ns). After around 70 ns, the plasma expansion from the foil

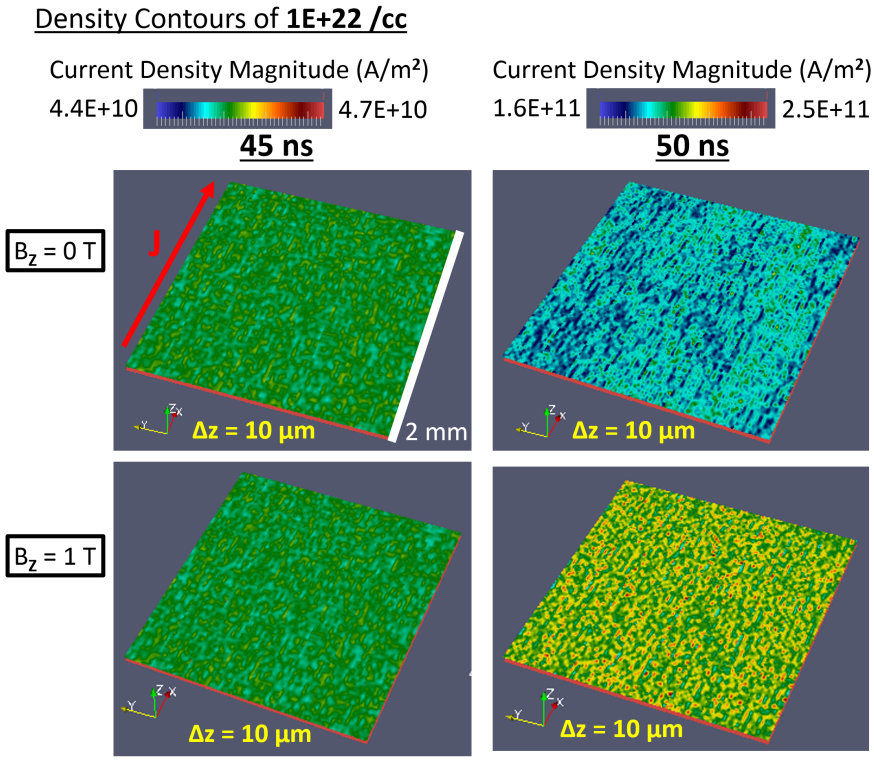

Figure 7.50: 3D slab simulations showing current density of the $1 * 10^{22}\ cm^{-3}$ (number) density contour within the slab for B_z= 0 T and 1 T. Time relative to the start of the current pulse.

surface makes structural comparisons difficult to analyze.

Next, in Fig. 7.50 we look again at contours of the higher density at $1 * 10^{22}\ cm^{-3}$ at times of 45 ns and 50 ns. As seen in Fig. 7.49, current is just barely starting to flow in the $5 * 10^{17}\ cm^{-3}$ plasma at the 50 ns time. At this 50 ns time when plasma is just starting to be generated on the foil's top surface, the higher density $1 * 10^{22}\ cm^{-3}$ contour is already starting to show differences between the current distributions for the 0 T B_z and 1 T B_z cases. The applied B_z is leading to larger variations (meaning more nonuniformities) in the current. Even earlier in time at 45 ns, the current distributions at this high density are similar for the 0 T B_z and 1 T B_z cases; considering the color scale bar, we find the current distribution at this time to be very uniform for both cases (a variation of less than

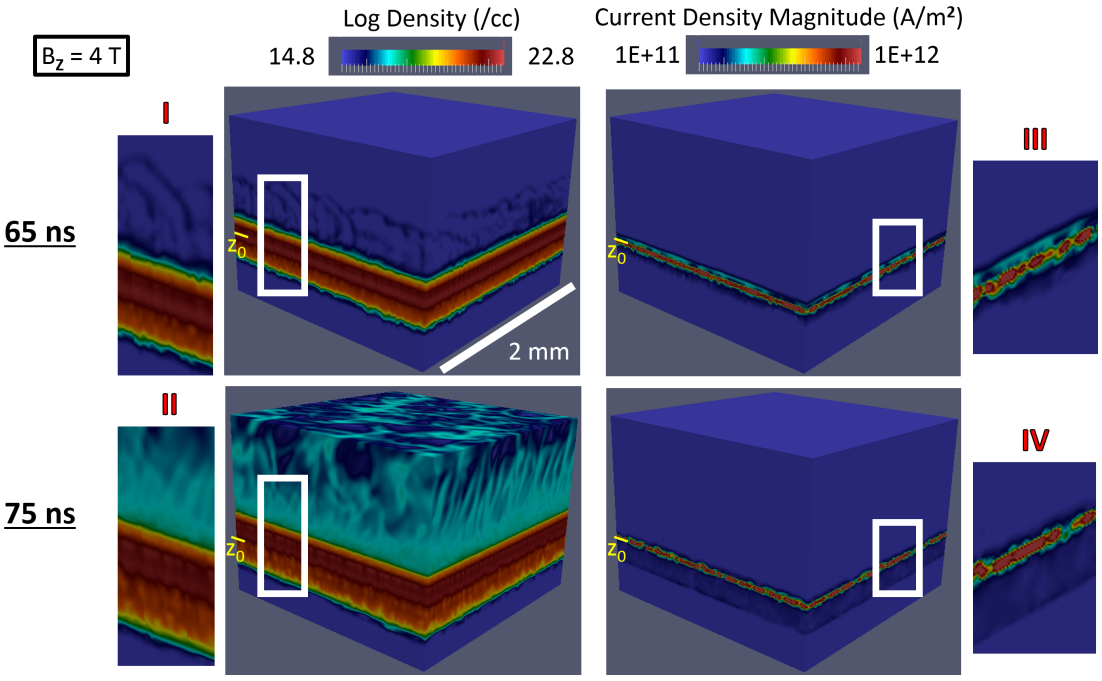

Figure 7.51: 3D slab simulations showing density and current time evolution of slab with external B_z= 4 T. Time relative to the start of the current pulse. Adapted from Byvank et al., 2018. [82]

2%). We also note that current which is not present within this density contour may be distributed within a different density.

So far, the simulation results look promising in regards to matching with the trends shown by the experimental disruption. We would expect an even larger applied B_z to exacerbate the disruption and plasma density nonuniformities. However, in these slab simulations, when an even larger B_z= 4 T is applied, we find a delayed and more uniform ablation compared to the 1 T case.

With a B_z= 4 T in Fig. 7.51 at 65 ns, the higher densities $> 10^{20}\ cm^{-3}$ of the foil (orange to red) have expanded with only minimal surface plasma of $10^{17} - 10^{18}\ cm^{-3}$ (cyan and green) compared to the 0 T and 1 T cases (Fig. 7.51 I compared to Fig. 7.47 C and D). The ablation is delayed in time, and when the surface plasma does form, it is more uniform for B_z= 4 T than B_z= 1 T

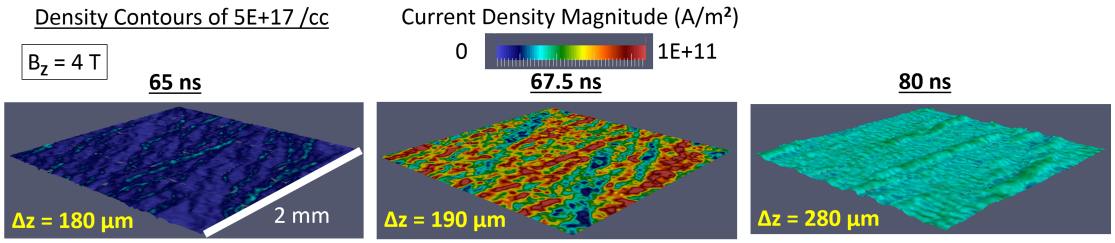

Figure 7.52: 3D slab simulations showing current density of the $5 * 10^{17}\ cm^{-3}$ (number) density contour on the top surface of the slab for B_z= 4 T. Time relative to the start of the current pulse.

(uniform $10^{17}\ cm^{-3}$ (cyan) at 75 ns in Fig. 7.51 II compared to less uniform $10^{17} - 10^{18}\ cm^{-3}$ (cyan and green) at 65 ns in Fig. 7.47 D). The physical reason for this delay in plasma expansion above the foil is presently an open question. One possible cause is that anisotropic conductivity due to the applied B_z influences the plasma dynamics. Another explanation is that the larger magnetic pressure ($B^2/2\mu_0$) into which the plasma must expand causes this delay for the B_z= 4 T case compared to the 0 T and 1 T cases. As the ablating plasma expands above the foil, the simulations show advection of the external B_z for which the field lines bend and distort, creating non-axial (x and y) components of the magnetic field above the foil. We note that, if the field lines did not bend, expansion upward in the z direction would not be prevented by the B_z field lines (oriented along the expansion direction). The more uniform density distribution correlates with a more uniform current distribution (Fig. 7.51 III has more distributed current $\sim 3 * 10^{11}$ A$/m^2$ (cyan) like Fig. 7.47 G rather than Fig. 7.47 H). At these 65 ns and 75 ns times for B_z= 4 T, the little-to-no current region shown in the B_z= 0 T and 1 T images at 55 ns (Fig. 7.47 E and F) is still present but not displayed due to the color scale change.

Furthermore, the ablation nonuniformities are not only delayed in time but also suppressed, as the surface plasma is still largely uniform at 90 ns.

In Fig. 7.52, we show the time evolution of the plasma density contour at $5*10^{17}\ cm^{-3}$ with an overlay of the current density color scale. Here with the 4 T B_z, current nonuniformities do not produce significant density nonuniformities. Comparing Fig. 7.52 to Fig. 7.49, 65 ns with a 4 T B_z looks similar to 50 ns with a 0 T or 1 T B_z, 67.5 ns at 4 T looks similar to around 54 ns (or earlier) at 0 T or 1 T, and 80 ns at 4 T looks similar to 60 ns at 0 T or 1 T. These differences between a 4 T and 1 T B_z raise questions about the critical B_z for the plasma disruption. Experimentally, would a larger B_z (say, 4 T) stabilize the nonuniform plasma ablation for aluminum? In the slab simulations, would the density nonuniformities still exist for 1.5 T or 2 T, and would a lower field of 0.5 T or 0.1 T produce uniform ablation? At present, these simulations have not been run.

Next, we look in more detail at the ablation with a 1 T B_z with an artificially increased resistivity by a factor of 5, as previously shown on the right in Fig. 7.46. The larger material resistivity decreases the current diffusion time and leads to quicker ablation dynamics as shown in Fig. 7.53 with significant expansion of the foil from its original thickness starting around 40 ns (compared to around 50 ns for the lower resistivity material; see Fig. 7.47). Current prefers not to travel in the more resistive material (by definition), and this effect significantly changes the ablation dynamics– ultimately leading to more uniform plasma on the top surface (as shown in Fig. 7.46 on the right).

Furthermore, as shown in Fig. 7.54 at 67.5 ns, we can compare the density, current, and temperature for the ablating slabs with a B_z of 0 T, 1 T, and 1 T with the increased resistivity. For this last case, we see that the current density does not want to flow in the higher resistive dense material and, therefore, tends to flow in the plasma on the bottom side of the foil. This effect (of minimal current

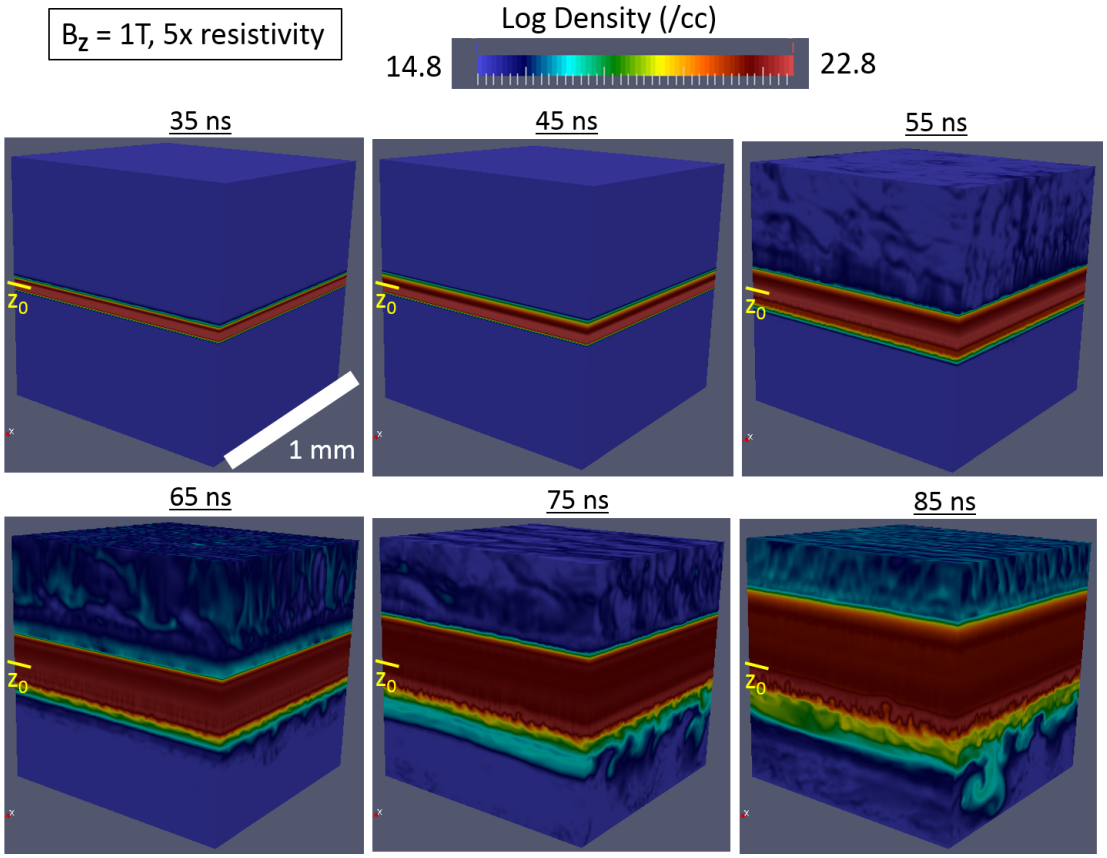

Figure 7.53: 3D slab simulations showing density time evolution of a slab with an external B_z= 1 T and artificially high resistivity. Time relative to the start of the current pulse. Note: computation domain shown has a 1 mm length (instead of 2 mm).

in the top side of the foil) correlates with minimal current nonuniformities that lead to minimal density nonuniformities in the ablating surface plasma. Additionally, we observe that the change in current flow changes the plasma temperature for the different cases. For the higher resistivity case, because the initial generation of ablating surface plasma is quicker due to faster current diffusion, the plasma temperature on the top surface is higher– around 50 eV compared to around 20-30 eV for the lower resistivity cases. Finally, we would like to caution one more time that this higher resistivity material is a "fake" material with aluminum EOS from the solid through plasma phases but with artificially

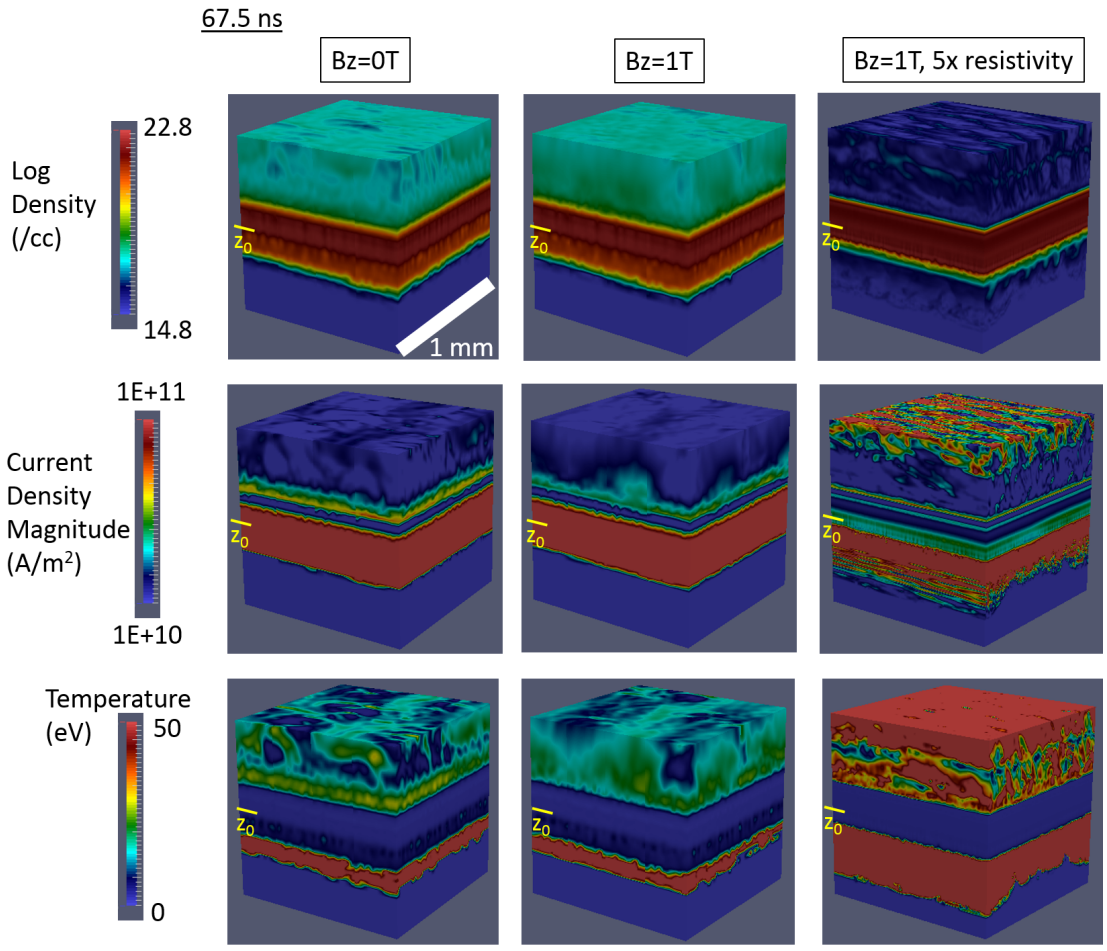

Figure 7.54: 3D slab simulations showing density, current, and temperatures of slabs with external B_z= 0 T, 1 T, and 1 T with an artificially high resistivity. Time relative to the start of the current pulse. Note: computation domain shown has a 1 mm length (instead of 2 mm).

enhanced resistivity.

The main results for this section are as follows. The B_z= 1 T case generates a more nonuniform plasma ablation than the 0 T, 4 T, and 1 T with artificially high resistivity cases. The current and density nonuniformities occur both in the higher density solid-liquid phases and lower density plasma phases. The artificially high resistivity material causes faster initial plasma ablation and a higher temperature plasma on the top side of the slab.

7.5.4 Physical Mechanism for Disruption

We first summarize the evidence regarding the jet disruption. The aluminum jet disruption at $B_z > 1.1 \pm 0.1$ T remains independent of changing the experimental parameters of current polarity, B_z direction, foil thicknesses, and center pin diameter. Changing the foil material from aluminum to titanium, nickel, molybdenum, or tungsten prevents the disruption up to the maximum applied field strengths of $B_z = 2.0 \pm 0.2$ T. Copper jets disrupt at $B_z > 0.95 \pm 0.1$ T. Zinc jets disrupt at $B_z > 1.6 \pm 0.2$ T. Increasing perturbations on the pin-foil contact area exacerbate the disruption, but the disruption occurs even for smooth pins (surface roughness < 0.5 μm); the initial density perturbations likely help seed the disruption. During experiments with aluminum foil and $B_z > 1.1 \pm 0.1$ T, copper foil and $B_z > 0.95 \pm 0.1$ T, or zinc foil and $B_z > 1.6 \pm 0.2$ T, the jet is not well-collimated at any time within the experiment (i.e. does not form), meaning the jet does not start out collimated and then later becomes uncollimated. Furthermore, we believe the disruption-causing mechanism is likely still present for lower applied fields than the critical B_z, just not to a large-enough extent that the mechanism prevents formation of the well-collimated azimuthally symmetric plasma jet.

The disruption involves bursts of current-carrying plasma that are not azimuthally symmetric, initialize from the foil surface, and grow in time. The plasma and current that would otherwise form the azimuthally symmetric plasma jet instead develop into discrete (spatially localized) bursts. Once a discrete plasma burst forms, the current may follow this established current path and continue to propagate in time– similarly to the electrothermal filamentation plasma instability as discussed in Sec. 7.2. We now consider how the cur-

rent and density nonuniformities are created and how the foil material properties along with the applied magnetic field can generate these discrete plasma bursts. Density nonuniformities in the radial foil exist due to creases from hardware contacts, impurities within the material, and adsorbed impurities on the surface. Current nonuniformities develop due to different resistivities between these density nonuniformities compared to the rest of the foil. Above the critical B_z, the B_z causes these nonuniformities to become discrete bursts of plasma. The precise physical mechanism for this phenomena is still not well understood. One possibility is that the B_z leads to anisotropic conductivity that helps propagate the current nonuniformities (in the solid through plasma phases) and plasma nonuniformities, thereby breaking the azimuthal symmetry required for the plasma jet formation.

We find a correlation between the plasma jet disruption and the foil material's electrical resistivity and equation of state. Foil materials with higher resistivity (like Ti) tend to increase the critical B_z for the plasma disruption. A larger resistivity decreases the magnetic diffusion timescale into the foil. We note that the Ohmic heating rate from the COBRA current driver to the foil is P = I^2R, and the corresponding voltage drop along the foil is V = IR. Therefore, a higher resistive material correlates with a larger voltage, and this larger voltage may cause quicker breakdown and formation of plasma on the foil surface. With plasma forming earlier in time, relatively more energy goes into the plasma rather than the denser foil. Therefore, with a higher resistivity material, there is possibly less time for initial solid nonuniformities to seed plasma nonuniformities later in time during the ablation process. However, we note that changing the heating time by changing the foil thickness for Al did not appear to change the disruption threshold. Although, the foil thicknesses for all materials used in

this work are smaller than the COBRA current pulse skin depth. A much larger foil thickness would change the heating time more significantly and influence the ablation dynamics.

Larger applied field strengths may lead to more magnetized plasma preventing radial transport and collimation, or a separate mechanism may cause large enough fields to stabilize the jet disruption. Increasing the magnetic field for the titanium, nickel, molybdenum, and tungsten jets to some $B_z > 2.0$ T should also lead to a disruption unless there is a mechanism that stabilizes the jet for all applied field strengths (like radiative cooling to minimize temperature and current nonuniformities). There may also be a separate physical effect that leads to jet collimation at even larger applied magnetic fields (some $B_z > 2.0$ T) for all materials, including the copper, aluminum, and zinc that disrupt.

In summary, we hypothesize that the disruption of the central jet is caused by the B_z acting along with the material electrical conductivity to create discrete bursts of plasma from the ablating foil surface. Current then flows in these discrete plasma bursts that break the azimuthal symmetry which would otherwise form the collimated central plasma jet. The B_z influences the current distribution in the dense solid foil and in the ablating surface plasma. Anisotropic conductivity caused by the B_z may prevent radial transport that would equilibrate the uniformities. Initial density perturbations may help propagate this breaking of azimuthal symmetry under the conditions of a B_z larger than the material-dependent critical field. The $\sim$10% change in the applied B_z that breaks plasma and current azimuthal symmetry motivates further understanding of ablation physics in the warm dense matter regime between the initial room temperature solid state and final plasma state above the foil.

CHAPTER 8

CONCLUSION

We conclude by copying verbatim the contents of Sec. 4.2. Then, we rant about possible next steps for the research.

Both experiments and the PERSEUS extended magnetohydrodynamics (XMHD) code show differences in jet structures under a change in current polarities, while an MHD code shows identical jets. These polarity differences are particularly noticeable with an applied B_z. Reverse current polarity jets are wider, have a larger conical angle, and have more on-axis density hollowing than standard current polarity jets. The jet structure is determined by an approximate radial force balance between competing dynamical (ram) pressures, thermal pressures, and magnetic pressures. Additionally, we observe polarity effects (i.e. anode-cathode asymmetries) of the current filamentation that forms on the radial foil surface. The addition of the Hall term in the Generalized Ohm's Law permits the XMHD code to be more accurate than an MHD code.

As the plasma converges toward the central axis to form the jet, the plasma compresses the applied B_z. In both experiments and simulations, we find larger B_z compression at a height closer to the foil surface compared to higher up. Simulations predict a larger peak B_z compression than what is measured in the experiments (other than one case, for a Ti foil and a 0.7 T B_z). Simulations show compression starting earlier in time than in the experiments. Furthermore, simulations show a decrease in B_z strength at late enough times, but the experiments do not show this decrease and the compression measurements become questionably-reliable at late enough times. Both simulations and experiments

show the same trend of a larger change in B_z (peak value minus initial value) for a smaller initial B_z. We also consider the effects on B_z compression of the current pulse shape, current polarities, the probe conductor, 2D vs 3D effects, and foil materials. Differences between simulations and experiments are larger than the estimated experimental measurement uncertainty of $\sim$10%. Considering discrepancies between experiments and simulations can allow for better understanding of the physical effects involved in the plasma dynamics.

Applying the B_z creates a $J_r B_z$ component of the $\mathbf{J} \times \mathbf{B}$ force that causes azimuthal rotation of the plasma (of both the background plasma and of the plasma jet that is formed by the converging background plasma). Measurements of this rotation were conducted by other graduate students using optical spectroscopy and Thomson scattering (with my support, for the latter). When using the 10 J laser for Thomson scattering, the laser can interact with the plasma jet by heating from inverse bremsstrahlung absorption, which causes the plasma to expand and produce a low-density bubble. For an accurate measurement (e.g. of electron temperature), the goal is to minimize the plasma perturbation by the diagnostic.

Under application of a large enough B_z, rather than simply forming a wider jet as expected by the 2D PERSEUS simulations, we experimentally observe a disruption of the plasma jet collimation for which plasma erupts from the foil surface as discrete bursts early on in time. The critical B_z for the onset of the disruption correlates with material properties like electrical resistivity and equation of state. Lower resistivity materials like aluminum disrupt at a B_z for which higher resistivity materials like titanium produce well-collimated jets. 3D simulations of the ablation process of a slab (that represents a small section of the

radial foil) that starts from the solid phase reproduce some of the experimental trends such as the material resistivity and B_z dependence on generation of current nonuniformities and plasma nonuniformities. Understanding the dynamics of a plasma that is generated from a source (like a solid foil) can require detailed understanding of material phase transitions in the solid, liquid, and vapor states.

8.1 Next Steps

Realistically, most– if not all– of the following research avenues will not be explored. Gas puffs are just too cool. Still, the author would like to share an incomplete list of thoughts. Firstly, some of the experimental results presented in this thesis could be repeated to get more shot statistics for verification, including looking at the disruption critical B_z for different pin sizes, foil thicknesses, and B_z directions (upward or downward). With that said, we now consider new experiments.

Future work could apply an independent pre-pulser to the radial foil early-on into or slightly before the COBRA current. The pre-pulse may form an initial surface plasma over the foil. If the plasma disruption originates from initial solid nonuniformities, an initial surface plasma may mitigate the growth of the nonuniformities, thereby leading to formation of a well-collimated plasma jet by the COBRA current pulse at larger B_z that would otherwise cause the disruption. As an extension to this surface modification concept, baking the foil with an external heat source or illuminating the foil with a UV light may improve foil purity by reducing absorbed particles.

Taking radiographs of the radial foil may provide useful insights into the foil structure in order to compare the disruption with formation of a well-collimated jet. We already have great imaging diagnostics, but combining X-pinches with the radial foil load hardware is problematic. An independent pre-pulser that triggers the X-pinch burst could potentially allow for more flexibility with the setup geometry.

The dB/dt probes may be used above the critical B_z for the disruption to measure the distortion of the applied B_z as well as the current distribution within the discrete plasma bursts, possibly permitting characterization of the instability growth rates. Foreseeable difficulties of these measurements include the probes perturbing the disrupting plasma bursts. Furthermore, below the critical B_z, the dB/dt probes may be used to study and characterize the current filamentation and growth rates for different materials.

Development and use of the already-developed Faraday rotation diagnostic could allow for measurements of the B_θ and corresponding current within the plasma jet. A laser path through a radial cord would be parallel to B_θ on one side of the jet and antiparallel on the other side, creating opposite polarization rotation angles. Because Faraday rotation requires both a plasma density and a magnetic field parallel to the path direction, conducting Faraday rotation along the z-axis of the hollow (zero or very low density) plasma jet would likely not provide usable measurements of B_z compression.

In regard to the applied magnetic field, increasing the experimental B_z would allow for exploration of larger critical B_z for materials that did not disrupt below 2 T. Tilting the orientation of the applied field to create a B_x or $B_x\hat{x} + B_z\hat{z}$ would break the azimuthal symmetry. The B_x would also permit

studying foil ablation for which the current direction is simultaneously parallel, antiparallel, and perpendicular to the radial current flow in separate regions of the foil.

As already seen in this thesis work, the material of the radial foil can significantly change plasma dynamics. The results for insulator materials as shown in Fig. 7.18 (for standard polarity) could be conducted in reverse polarity to observe polarity differences in the formation of the hot spots and current filaments. Additionally, using a material like a dense foam foil may provide an experimental platform to study the Nernst effect. For the Nernst effect to be significant, a system needs large (electron) temperature gradients perpendicular to a magnetic field. The radial foil Joule heating power per unit length $P/(dr) \propto I^2/r$ could potentially provide a large radial temperature gradient near the pin (particularly for diameters < 2 mm), and there is a perpendicular magnetic field B_θ whose direction could be changed with addition of the applied B_z. Research could investigate the compression and expansion of the foam foil under $\mathbf{J} \times \mathbf{B}$ forces and how the Nernst effect influences the dynamics.

Thinking about this prospective fun research almost makes me want to be a grad student for another 5 years– almost.

APPENDIX A

PARAMETER ESTIMATES

See the NRL formulary and other introductory plasma textbooks as references for these quantities. [73, 83, 84] These approximate and derived parameters should only be considered as "order of magnitude" (or 2) estimates for our radial foil plasma jet systems. As Bruce would say, "do you even know what an order of magnitude *is*?"

Table A.1: Constants

Symbol	Description	Value
A_{Al}	aluminum atomic mass number	27
c	speed of light	$3 * 10^8$ m/s
k_B	Boltzmann constant	$1.38 * 10^{23}$ J/K
m_e	electron mass	$9.1 * 10^{-31}$ kg
$m_i = A_{Al} m_p$	aluminum ion mass	$27 * 1.67 * 10^{-27}$ kg
m_p	proton mass	$1.67 * 10^{-27}$ kg
$q_e = e$	elementary charge	$1.6 * 10^{-19}$ C
ϵ_0	permittivity of free space	$8.8542 * 10^{-12}$ F/m
μ_0	permeability of free space	$4\pi * 10^{-7}$ H/m

Table A.2: Approximate Parameters

Symbol	Description	Plasma Jet Value
B_0	characteristic magnetic field strength	2 T
L_0	characteristic length	1 mm
L_{jet}	jet height	1 cm
ln(Λ)	Coulomb logarithm	5
γ	adiabatic index	5/3
n_e	electron density	$3 * 10^{18}\ cm^{-3}$
n_i	ion density	$5 * 10^{17}\ cm^{-3}$
T_e	electron temperature	30 eV $= 3.5 * 10^5\ K$
T_i	ion temperature	20 eV $= 2.3 * 10^5\ K$
t_0	characteristic timescale	20 ns
u_0	characteristic speed	50 km/s
Z	ionization state	6

Table A.3: Derived Parameters

Symbol	Description	Formula	Plasma Jet Value
C_s	ion sound speed	$\sqrt{\gamma Z k_B T_e / m_i}$	$3.3 * 10^4\ m/s$
c_{p_e}	e- specific heat capacity	k_B / m_e	$1.5 * 10^7\ \frac{m^2}{s^2 K}$
Lu	Lundquist number	$\mu_0 v_A L_0 / \eta$	0.8
M	Mach number	u_0 / C_s	1.5
N_D	Debye number	$\frac{4\pi}{3} n_e \lambda_{D_e}^3$	$1.6 * 10^2$
Pe	Peclet number	$u_0 L_0 / \alpha_e$	4.4
P_{th}	thermal pressure	$n_i k_B T_i + n_e k_B T_e$	$1.6 * 10^7\ \frac{kg}{m\ s^2}$
P_M	magnetic pressure	$B_0^2 / 2\mu_0$	$1.6 * 10^6\ \frac{kg}{m\ s^2}$
Re	Reynolds number	$n_i m_i u_0 L_0 / \mu_i$	$3.2 * 10^5$
R_M	magnetic Reynolds number	$u_0 L_0 / \eta_M$	3.5
r_{c_e}	electron cyclotron radius	$m_e v_{th_e} / q_e B_0$	$6.5 * 10^{-6}\ m$
r_{c_i}	ion cyclotron radius	$m_i v_{th_i} / Z q_e B_0$	$2.0 * 10^{-4}\ m$
v_A	Alfven speed	$B_0 / \sqrt{\mu_0 n_i m_i}$	$1.2 * 10^4\ m/s$
v_{th_e}	electron thermal speed	$\sqrt{k_B T_e / m_e}$	$2.3 * 10^6\ m/s$
v_{th_i}	ion thermal speed	$\sqrt{k_B T_i / m_i}$	$8.4 * 10^3\ m/s$
α_e	electron thermal diffusivity	$\kappa_e / n_e m_e c_{p_e}$	$11.3\ m^2/s$
α_i	ion thermal diffusivity	$\kappa_i / n_i k_B$	$6.3 * 10^{-4}\ m^2/s$
β	plasma beta	P_{th} / P_M	10
η	Spitzer resistivity	$m_e \nu_{ei} / n_e q_e^2$	$1.8 * 10^{-5}\ \Omega\ m$
η_M	magnetic diffusivity	η / μ_0	$14.3\ m^2/s$
κ_e	e- thermal conductivity	$3.2 n_e k_B^2 T_e / \nu_{ei} m_e$	$4.7 * 10^2\ \frac{kg\ m}{s^3 K}$
κ_i	ion thermal conductivity	$3.9 n_i k_B^2 T_i / \nu_{ii} m_i$	$4.3 * 10^{-3}\ \frac{kg\ m}{s^3 K}$
λ_{D_e}	electron Debye length	$\sqrt{\epsilon_0 k_B T_e / n_e q_e^2}$	$2.4 * 10^{-8}\ m$
λ_e	electron inertial length	c / w_{p_e}	$3.1 * 10^{-6}\ m$
λ_i	ion inertial length	c / w_{p_i}	$2.7 * 10^{-4}\ m$
λ_{mfp_e}	electron mean free path	v_{th_e} / ν_{ei}	$1.5 * 10^{-6}\ m$
λ_{mfp_i}	ion mean free path	v_{th_i} / ν_{ii}	$1.9 * 10^{-8}\ m$
μ_e	electron dynamic viscosity	$0.73 n_e k_B T_e / \nu_{ei}$	$7.0 * 10^{-6}\ \frac{kg}{m\ s}$
μ_i	ion dynamic viscosity	$0.96 n_i k_B T_i / \nu_{ii}$	$3.5 * 10^{-6}\ \frac{kg}{m\ s}$
ν_{ee}	e-e collision freq	$\frac{1}{16\pi} \frac{q_e^4}{\epsilon_0^2} \frac{n_e \ln(\Lambda)}{m_e^{1/2} (k_B T_e)^{3/2}}$	$2.5 * 10^{11}\ s^{-1}$
ν_{ei}	e-i collision freq	$\frac{1}{16\pi} \frac{q_e^4}{\epsilon_0^2} \frac{Z n_e \ln(\Lambda)}{m_e^{1/2} (k_B T_e)^{3/2}}$	$1.5 * 10^{12}\ s^{-1}$
ν_{ii}	i-i collision freq	$\frac{1}{16\pi} \frac{q_e^4}{\epsilon_0^2} \frac{Z^4 n_i \ln(\Lambda)}{m_i^{1/2} (k_B T_i)^{3/2}}$	$4.4 * 10^{11}\ s^{-1}$
ω_{c_e}	electron cyclotron freq	$q_e B_0 / m_e$	$3.5 * 10^{11}\ rad/s$
ω_{c_i}	ion cyclotron freq	$Z q_e B_0 / m_i$	$4.3 * 10^7\ rad/s$
ω_{c_e} / ν_{ei}	electron magnetization	$\lambda_{mfp_e} / r_{c_e}$	0.23
ω_{c_i} / ν_{ii}	ion magnetization	$\lambda_{mfp_i} / r_{c_i}$	$9.4 * 10^{-5}$
ω_{p_e}	electron plasma frequency	$\sqrt{n_e q_e^2 / \epsilon_0 m_e}$	$9.8 * 10^{13}\ rad/s$
ω_{p_i}	ion plasma frequency	$\sqrt{n_i Z^2 q_e^2 / \epsilon_0 m_i}$	$1.1 * 10^{12}\ rad/s$

APPENDIX B

COBRA FIRING SEQUENCE

Between the time that the COBRA operator presses a button and they hear a "bang," many signals are traversing many cables to provide diagnostic timings with (hopefully) nanosecond accuracy (realistically, one accepts at least 5-10 ns jitter for diagnostics). See Figs. B.1, B.2, B.3, and B.4 for a timing diagram.

Temporarily ignoring diagnostic triggering, the COBRA operator presses the button on the 22 V pulser, which sends a signal [300 V after the "Glory Box," see below] to the PT-55 (55 kV) switch (PT is "pulse trigger"), which sends a [5 kV] signal to the TG-70 (70 kV) switch (TG is "trigger generator"), which sends a [40 kV] signal to the Trigger Marx, which sends a [320 kV] signal to the Marx Generator.

Now, considering diagnostic triggering, before the 22 V pulser signal reaches the PT-55, it passes through the "Glory Box" (triggering circuit). Along with the 22 V pulser signal, the Glory Box requires a 5 V DC power supply and a 10 Hz signal generator. The 10 Hz generator also sends a signal to start the diagnostic laser. The Glory Box outputs a square pulse, which characteristically has a rising and falling edge. The rising edge "first pass" sends a signal to 1) a delay generator to trigger the B_z Helmholtz coil capacitor bank (as well as the puff valve and preionizer for gas puff experiments) and 2) a "master" delay generator that will trigger the streak camera, bolometer, 10 J laser, fake Bdot (for testing signals without a shot), and PT-55 delay generator. (For gas puff experiments, a preionizer monitor signal is also input into the PT-55 delay generator.) The PT-55 delay generator sends a signal to the COBRA charging panel that triggers the oscilloscopes (in the "screen room") and the PT-55 power

supply. (See the previous paragraph for the triggering sequence from PT-55 to Marx and Sec. 5.1 for the signal from Marx to pulse forming lines (PFL).)

When the PFLs start charging, the South PFL sends a signal to the Glory box that forces a falling edge to the Glory Box's square pulse [due to a Bdot on the side of the pulse line]. The falling edge "second pass" sends a signal to two delay generators that trigger the rest of the diagnostics: to fire the diagnostic laser, extreme ultraviolet (EUV) self emission quadrant cameras ("quad cams" or "QCs") 1 and 2, optical self emission fast framing camera ("12-frame"), and to fire the 10 J laser and trigger the spectrometer.

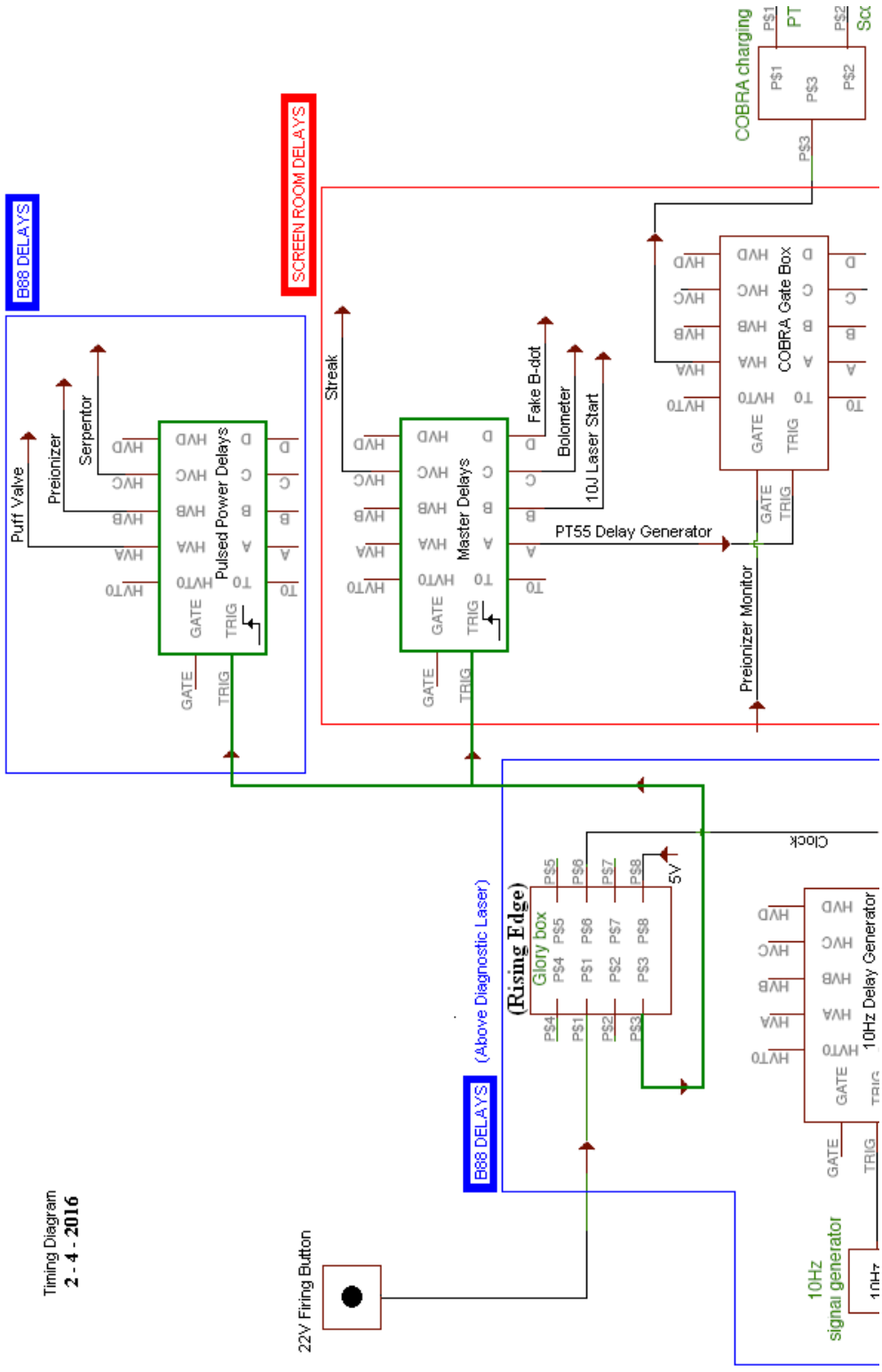

Figure B.1: Diagram of COBRA triggering, top left quadrant. Made by W. Potter.

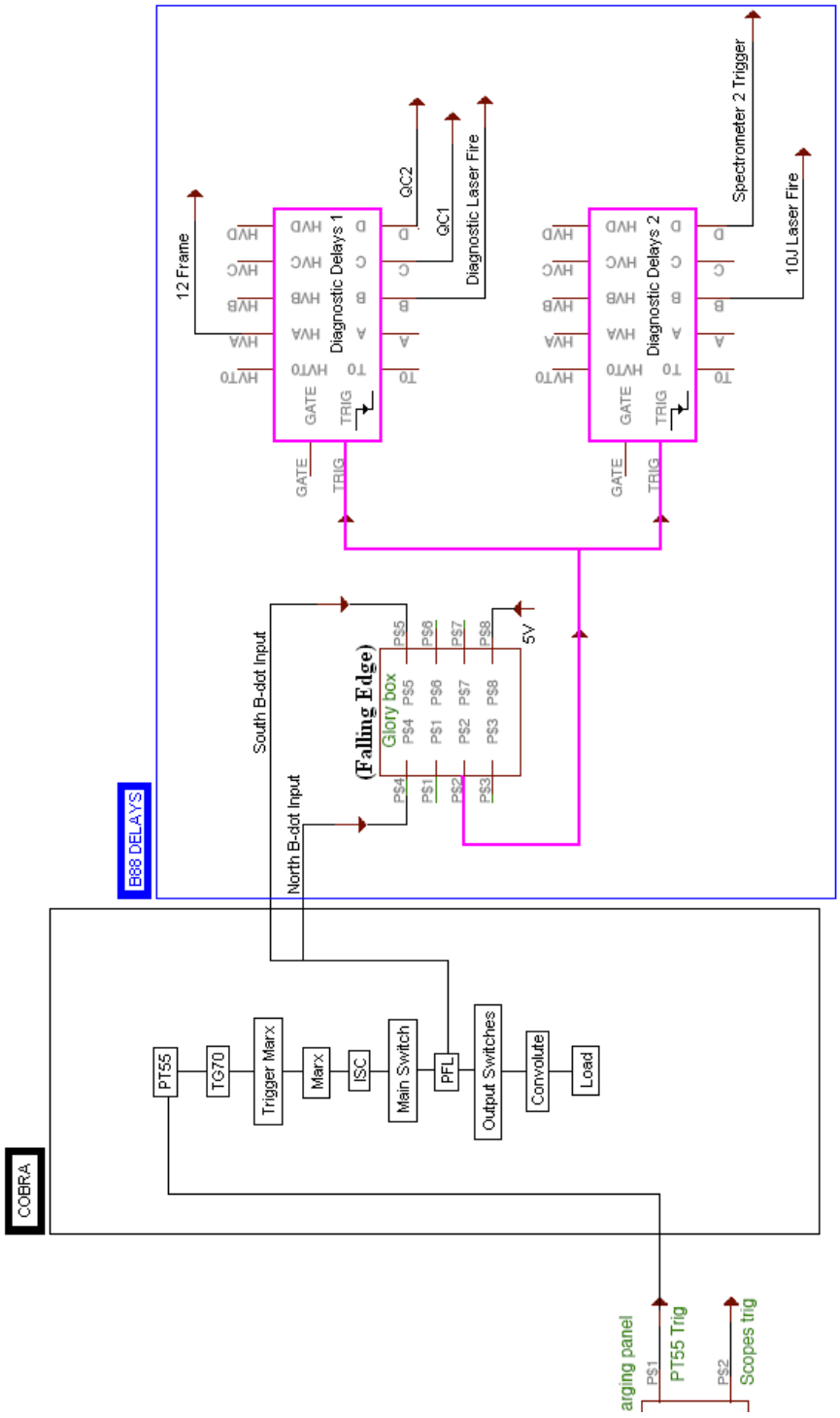

Figure B.2: Diagram of COBRA triggering, top right quadrant. Made by W. Potter.

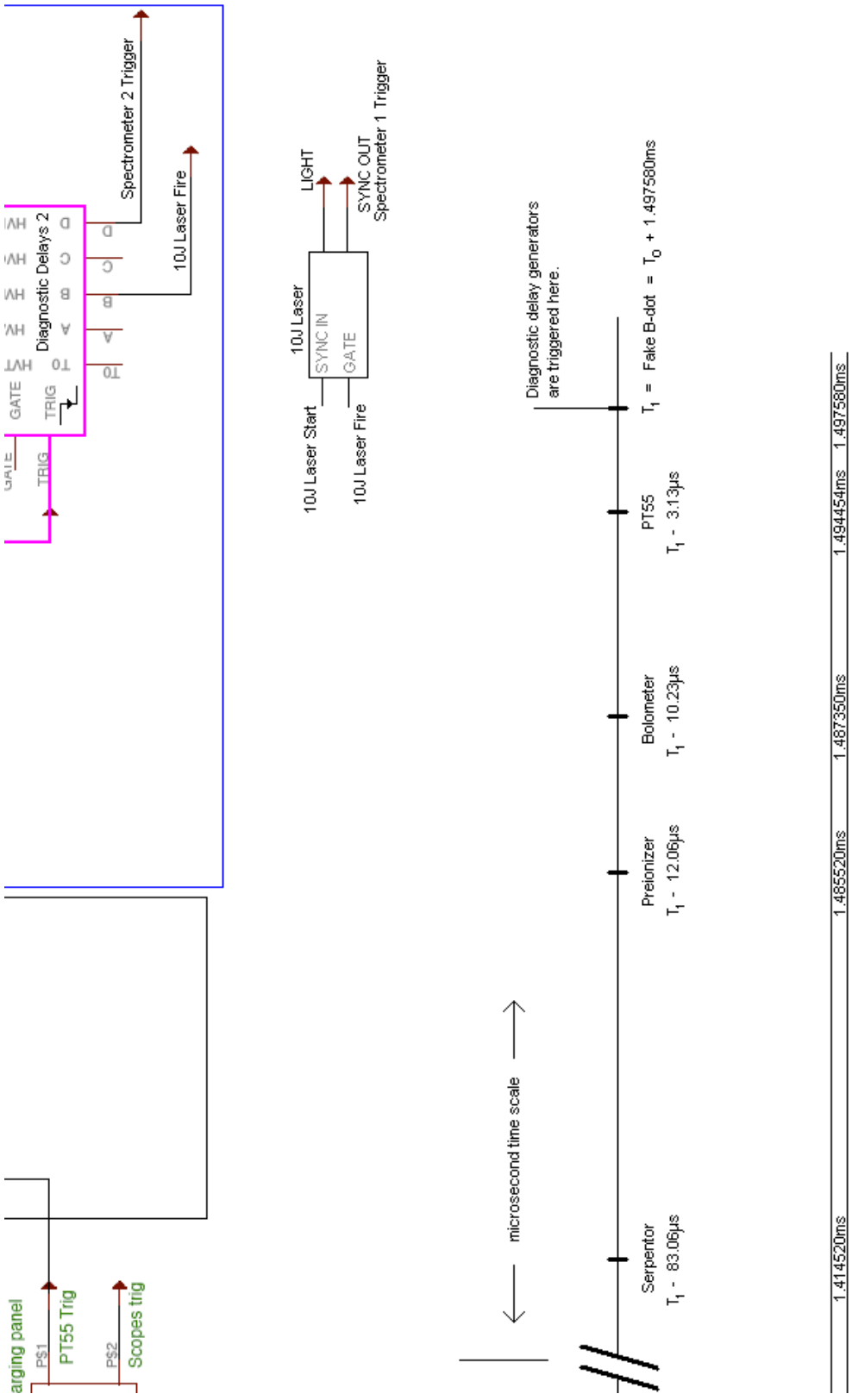

Figure B.3: Diagram of COBRA triggering, bottom right quadrant. Made by W. Potter.

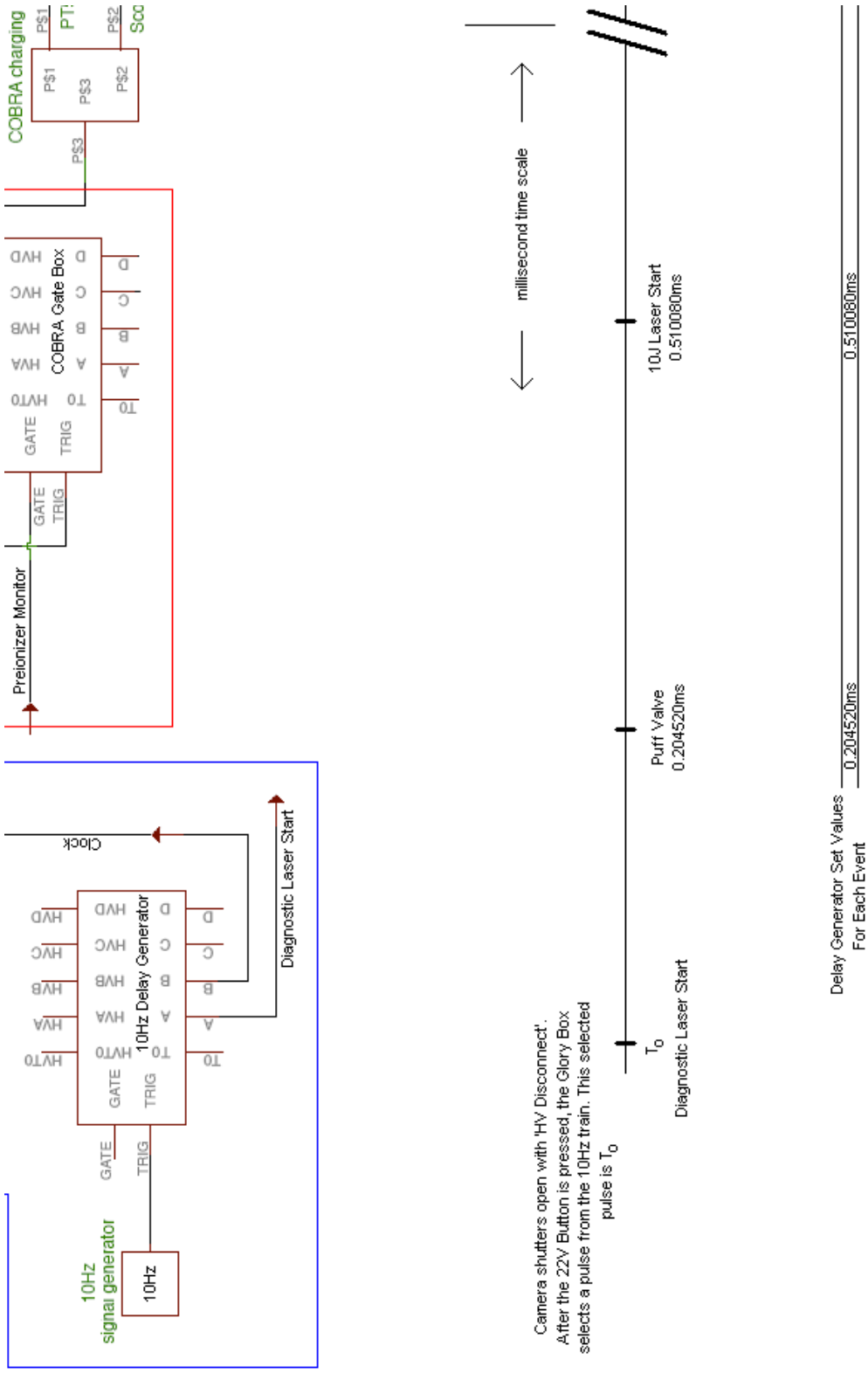

Figure B.4: Diagram of COBRA triggering, bottom left quadrant. Made by W. Potter.

APPENDIX C

COBRA OPERATING INSTRUCTIONS

To any anxious grad student reading this, please get a current COBRA operator's training, supervision, and permission to fire COBRA. Additionally, be aware that there may be changes in the procedure from what is written in this section. Thanks to Harry "Wizard" Wilhelm.

Before Shot:

Outside of COBRA in firing area:

Be sure the SF6 valve on gas cylinder is open. If you need to change the SF6 pressures in switches, edit the Run document found on the desktop. Make sure to save the file after changing the values. At SF6 control computer enter "power,0". Vent N and S Marxes to about 3 psi by manually flipping orange vent switches. Remember to close them when done. At control computer enter "power,1" and then "script,run" *. Wait for numbers to stabilize (about 2 minutes). Check TG70 pressure; it should be 17 psi**. Check water resistivity for N and S ISC; the resistivity number should be above 2.

*If computer not register command, enter power,0; script,run; power,1; script,run

**If not:
Panel inlet, switch down –> out, fills
Panel outlet, out goes from panel to TG70
Vent, lowers pressure

On top level of COBRA:

Check vacuum via ion gauge; want pressure to be at 5E-5 (Torr) or lower. If OK then turn off ion gauge controller, unplug controller, valve off ion tube, and remove wires connected to ion tube. Connect cables for top axial QC if necessary. Turn on high voltage power supplies for quadrant cameras (in box under optical table). Make sure COBRA power boxes are all on (there are two boxes, each with 3 switches; 1 box is on North side, 1 on South side).

Using ladder:

Turn off oil recirculation (white switch on front of blue pump). Close valves on left (marked from cans); want lever perpendicular to lines.

On bottom level of COBRA:

Water circulation. Turn off pump on both sites: A) white switch by South, B) box by North: auto –> off. Turn off and unplug the pulseline bubble/oil/water detector box.

During Shot:

Optional before shot: Trigger test (for North and South Trigger Marx fire output signals). Only TG ON (and TG-70), wait for trigger voltages to charge up, then press 22 V pulser.

Computer SF6 control enter "power,0".

TG on and Arm (press buttons). Wait until trigger voltages (kV) charge up (4 readouts; wait for 2nd to left to read $\sim$15.5).

HV on and TG-70. ***Make sure resistivity meter switch (below orange square light) is down.** Make sure TG-70 bottom white switch is on and the

power supply switch above that is on. Check dials below TG-70 [button]; current goes up and voltage, then current drops (about 3 seconds).

Watch that current is stable. Voltage should rise to ∼68 kV on all 4 capacitor banks, then you should see the current falling. (Watch for voltage hanging up at around 10 kV indicating a bad diode board.) ***If voltage exceeds 70 kV and/or if current does not fall, then promptly press discharge [big red button].**

Wait for all currents to go to less than 1.0 mA.

∼Do a final look around: pressures, dials, resistivity meter switch down, etc.

...

Disconnecting–3 [button]

Wait ∼1/2 second in between

2–open clamps

Wait ∼1/2 second in between

1–flip open gate valve controls (switches)

∼pause ∼1 sec; wait for gate valves to show green

–> FIRE: press 22 volt pulser button

***Discharge**

<u>After Shot:</u>

On SF6 pressure control computer, turn off system by entering "power,0" (unless already did so before shot). Curse slowness of keyboard response; curse a second time. When it has been accepted, vent N and S Marxes by manually flipping orange buttons ***and dont forget to close after they reach ∼3 psi. *Back at control panel, stop venting Marxes.** Enter "power,1" and then "script,clean"*. Watch that the pressure gauges of Marxes go up together, indi-

cating that you are running the clean script.

*If computer does not register command, enter power,0; script clean; power, 1; script,clean.

Enter COBRA area.

Turn on oil monitoring (pulseline indicator box) system. 4 green lights are good– anything else indicates a problem. Open 2 flaps by diagnostic laser and delay generators; turn off diagnostic laser; close laser shutter. Be sure the upper flap is chained open so the delay generators stay cool.

Debubble 4 pulselines:
(1) Fill air tank (switch up), then switch down.
(2) Fill NE, then once filled put switch down.
Repeat (1) and (2) for the other 3 pulselines.
(3) Put all switches up except for the green fill air tank.
*red indicates oil; yellow/orange indicates air

In COBRA area, using ladder, *while draining air from pulselines*: Get flashlight. Climb ladder to blue oil recirculation pump. On a gas puff shot, look at water level in marble column, a drop may indicate a broke upper barrier. Open top valve on left; shine flashlight in flow indicator, and turn on switch. Look for about 10 seconds to see if bubbles appear. Switch off; close valve. Repeat for valves 2, 3, and 4. Open all valves, turn on pump, and verify that oil is circulating. ***Every time you open a valve, look at oil level [indicator on front] to see if it is dropping**– this dropping indicates a barrier problem.

*If there are bubbles, shut pump off and get help– means arc in can.

After pictures have been downloaded, go to COBRA platform, turn off cameras and high voltage. Disconnect cables from top axial QC if necessary.

Once pulseline indicator box shows all green, you can turn all switches on box down ("Chalenski sweep") and turn on water circulation switches (South white switch and North box off –> hand (or auto)). ***Hand (/manual) is probably better than auto.** *If there's a yellow light on the North box, auto won't work. Need to re-do turning on circulation if cylinder stuck in top/bottom of flow meter rather than in middle.

Check for bubbles near the 4 barriers using borescope; check for bubbles on barrier and edges. If there are bubbles, then repeat "Debubble pulseline" procedure for the problem barriers. *When done, don't forget to screw on the caps.

Only if water circulation box set to auto: *IF water circulation has stopped, there will be a yellow light on the control panel in the corner (NE) of the COBRA room indicating low water on north or south. Turn off circulation pump. Close valves from pulse lines; open valve to roughing filters; open H2O valve supplying building water (N of N Marx, green lever with stop watch/ timer on it). Set timer to about 2 minutes. Wait until the low water LED goes out, then add another 2 minutes of water. Close the water supply valve and set the other 2 valves the way they were. Start circulation.

Things to monitor/ check:

Monitor gas (in cylinders): SF6 outside; Nitrogen by pulseline.
If water levels are low.
Adder water circulation.

Oil flowing in Marx circulation.

Leaks near pulseline-can connections.

End of Day:

Turn off power supplies on top of COBRA.

Close SF6 valve on cylinder (behind firing area).

APPENDIX D

HELMHOLTZ COIL CHARGING BANK OPERATING INSTRUCTIONS

Thanks to Peter Schrafel.

0. Make sure the current paths from the power supply bank to the coil are connected and properly insulated.

1. Turn down powerstat dial.

2. Flip on toggle power switch (red light comes on).

3. Press "charge" button to activate charging relays.

4. When turning up powerstat, try to keep current gauge below $\sim$30 μA DC.

5. Turn up powerstat to desired firing voltage (top left gauge: kV DC), accounting for voltage drop when disconnecting.

6. Press "disconnect" to isolate capacitors and ignitron from voltage supply. (If firing during a COBRA shot, do this at the same time the COBRA operator says or presses "disconnect" on COBRA.)

7. Press COBRA trigger 22 V pulser.

8. Press "dump" and flip off toggle power switch after firing. (And turn down powerstat.)

APPENDIX E

MAGNETIC (B-DOT) PROBE FABRICATION

The dB/dt probes are fabricated with the following procedure:

Acquire the Following Ingredients:

1. semi-rigid coaxial cable: 0.020″ outer diameter (OD) with copper outer conductor [Pasternack; part #PE-20SR]

2. connector: SMA straight female solder jack for 0.047″ semi-rigid cable, 50 Ohm, gold plated brass [Field Components Inc.; part #FC10DSF-B15-1-R1; cage code: 5ZF66]– includes pin, brass adapter, insulator plug

– brass adapter dimensions: 0.0895″ OD, ∼0.0435″ inner diameter (ID), 0.0230″ wall thickness

3. structural stabilizer adapter: tinned copper semi-rigid cable, 0.047″ OD, 0.035″ ID

4. base tubing (plastic, possibly FEP): 0.125″ OD, ∼0.625″ ID, 0.030(5)″ wall thickness

5. long extension tubing: FEP industrial tubing, 0.063″ OD, 0.031″ ID, 0.015″ wall thickness [Small Parts; part #FEP-IT063-C]

6. Kapton (polyimide) tubing:

a) [used for normal probes and for making the loop area of z-probes] polyimide trp. walltube AWG 23, 0.0226″ ID, 0.0030 wall thickness [Small Parts; part #TWPT-022-12-10]

b) [used for normal probes and for making the loop area of z-probes] tubing polyimide, 0.0290″ ID, 0.00300″ wall thickness [Advanced Polymers; Vention Medical; part #141-0046]

c) [used for outside of single z-probe loop] polyimide trp. walltube AWG 16,

0.0508" ID, 0.00375" wall thickness [Small Parts Inc.; part #TWPT-050-12-10]

d) [used for outside of double-z-probe loop(s); largest] tubing polyimide, 0.0800" ID, 0.00375" wall thickness

e) [other "medium size"] tubing polyimide, 0.043" ID, 0.00300" wall thickness [Advanced Polymers; Vention Medical; part #141-0074]

7. calibration pulser; oscilloscope

8. solder; soldering iron; 5 minute epoxy, stirrer; vice

9. tools: razor blade, tweezers, needle-nose pliers, flush cutter, file, ruler, spring-loaded punch

To Assemble the Connector:

– Insert white insulator plug into connector and indent connector (2-3 times, every $\sim 120^\circ$ near center of where white plug is)

– Put brass adapter and structural stabilizer adapter into connector; solder to connector; *afterward, make sure can still see through hole in connector (solder not blocking)

– Note: to "score," 1) twist the wire under a blade or 2) press down with the blade; remove blade; rotate wire; press with blade; repeat as needed

– Score around coax copper outer conductor (OC) $\sim$4 mm from end; bend around and pull OC off

– Score around coax white insulator $\sim$2 mm from end; pull off

– Attach pin and coax: solder inner conductor wire to inside of pin (on the opposite side of the pin to what will connect to a SMA male connector)

– Slide coax into connector; at some time, pin won't want to go into plug further; then, start inserting the pin with pliers, then press on it with a blunt tool (like blunt end of a file), then press against a table, and then with a blunt tool again; so, pin ends up stuck into plug as far as it can go

– "Lightly" (not a thick glob) solder outer conductor to shielding

– Note: make sure structural stabilizer adapter does not go into the connector, or else it may short circuit (connecting inner conductor with outer conductor), plus it will be hard to put the pin into the plug

To Make a Normal Loop:

0. Assemble the connector

– Note: to "score," 1) twist the wire under a blade or 2) press down with the blade; remove blade; rotate wire; press with blade; repeat as needed

– Score around coax copper outer conductor (OC) $\sim$3 mm from end; bend around and pull OC off

– Score around coax white insulator, leaving $\sim$1 mm from OC; pull off

– Flick tip (of inner conductor (IC)) while holding bottom of cable to make sure the tip doesn't break

– Make loop by bending inner conductor down to touch the outer conductor (the loop area is determined by the length of the white insulator); *make sure the loop is "in-plane"

– Solder loop connection point between IC and OC

– Note: to solder a small amount: after soldering iron is hot, make sure tool tip is clean (can use wet sponge and/or gold pipe cleaner), put bead of solder on tool tip, then flick the tip to throw most of the bead on the floor (this gets the tip hot); then, 1) put a tiny bit more solder onto the tip, press onto loop connection to make joint ($\sim$1 sec), and push/ pull the tool tip away to minimize bulge in solder joint, or 2) make loop connection, solder material and tool tip meet together ($\sim$1 sec), and push/pull tool tip away

– Note: if there's too much of a solder joint bulge, may use file to remove necessary amount

– Slide Kapton over loop (and over solder joint– without breaking it) and move down to cover ∼2-3 cm of coax from the top of the loop; and cut Kapton ∼0.5-1 mm above the top of the loop

– Attach base tubing (enough length to extend past and cover the structural stabilizer adapter) to long extension tubing (long enough that it covers ∼1 cm of Kapton once it slides onto the probe)

– Slide long extension tubing over Kapton and coax

– Epoxy the probe tip (with 5 min epoxy), making sure the epoxy gets far down to insulate the loop, and let dry

– Note: can slightly bend coax to denote loop orientation

– Calibrate probe loop area using calibration pulser

– Note: test probe continuity (as needed)

To Make a z-probe Loop:

0. Assemble the connector

– Slide a piece of Kapton tubing with a slit (to act as the loop area) down the coax

– Note: to "score," 1) twist the wire under a blade or 2) press down with the blade; remove blade; rotate wire; press with blade; repeat as needed

– Score around coax copper outer conductor (OC) ∼3-4 mm from end; bend around and pull OC off

– Slice ∼3 mm of the outer conductor, along the axis of the coax

– Bend out both of the sides of the sliced OC

– Tilt the insulator (and inner conductor) wire 90° out from the coax

– *Carefully* cut off the bent insulator while not cutting the inner conductor (cut or score around the insulator with a razer blade and pull it off with tweezers)

– Crimp together the outer conductor sliced sides to make metal contact above

what will become the probe loop

– Slide up the Kapton piece with a slit

– To create the probe loop: bend inner conductor wire around the Kapton piece (pay attention to loop orientation)

– Solder end of IC to OC

– Slide down larger Kapton tubing over the loop

– Epoxy the probe tip (with 5 min epoxy), making sure the epoxy gets far down to insulate the loop, and let dry

– Calibrate probe loop area using calibration pulser

– Note: test probe continuity (as needed)

To Make a Double-z-probe Loop:

0. Assemble the connector

1. Make two z-probes with the following changes:

– After "slide down larger Kapton tubing over the loop," put the two probe ends together and slide down another even larger Kapton tubing over the two probe ends; if the "even larger" Kapton tubing does not fit, can put the "larger" Kapton tubing over only one of the probe loops

– Epoxy the probe tip (with 5 min epoxy), making sure the epoxy gets far down to insulate the loop, and let dry

– Note: may want to calibrate individual probe loops before combining, but it is still good to calibrate after combining them

– Note: test probe continuity (as needed)

APPENDIX F

PROBE CALIBRATION PULSER

The dB/dt probe loop areas are calibrated using a well-characterized pulser described here. The pulser current travels through a copper sheet bent to a horseshoe-shaped loop (with a gap), creating a magnetic field within the horseshoe loop. The probe loops are placed through a small hole in the copper sheet. The magnetic field (dB/dt) will induce a voltage in the probe loop based upon the loop orientation relative to the magnetic field. Along with measuring the voltage when the loop area is aligned with the magnetic field, it may be useful to also record any voltage pickup when the loop area is (nominally) perpendicular to the magnetic field. If due to the loop area (mis)alignment, this off-axis component pickup could produce voltage signals from dB/dt components other than in the direction of interest.

Using the calibration pulser, a dB/dt probe loop of well known area (i.e. larger than the typical loop areas for experiments) is placed through the small hole in the copper sheet. An oscilloscope records the voltage of the dB/dt loop and the pulser current from a Rogowski coil. The loop dB/dt signal is integrated by the oscilloscope. The peak-to-trough (twice the amplitude) oscilloscope voltage of the integrated waveform is averaged between both loop orientations (parallel and antiparallel to the dB/dt). To compare relative probe areas, this voltage value for the known loop area is compared with the value measured while calibrating an experiment probe loop.

For our calibration pulser when calibrating a probe with unknown area, after recording the average peak-to-trough voltage (in nV) of the integrated dB/dt signal for both loop orientations, dividing $600 * 10^{10}$ by this recorded value will

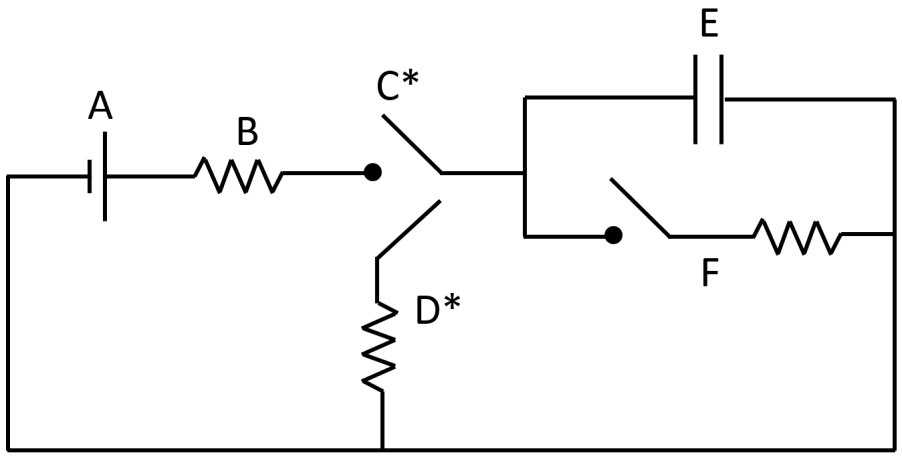

Figure F.1: Simplified circuit diagram of the dB/dt probe calibration pulser. A: power supply, B: charging resistor, C: charge relay (switch), D: dump resistor (and relay), E: capacitor, F: air self break switch and load (copper sheet loop).

provide a calibration factor in units of Gauss/(seconds*Volt) that will convert a voltage to a dB/dt.

The specifications for the calibration pulser in LPS are as follows (see Fig. F.1 for reference). Power supply (A): 30 kV, 5 mA; with 4A fuse (note: voltage gauge and dial measures across power supply). Charging resistor (B): 75 Ω, 50 W. Charge relay (C): rated for 40 kV, linked to dump resistor relay (D); charge button closes relay, dump button opens relay. Dump resistor (D) [with a "large" resistance]: linked to charge relay (C); dump button closes relay, charge button opens relay. Capacitor (E): 0.2 μF, rated for 50 kV, 0.02 μH, voltage across this capacitor causes air gap switch (F) to break. Air self break switch and load (F): switch ($\sim$1 cm gap) always open until voltage across $>$ 25 kV, then breakdown pulse through air; pulse then travels through load– a $\sim$25 mm diameter Cu loop (horseshoe with a gap), $\sim$50 mm wide sheet– with a hole through the Cu sheet for the dB/dt probe loop to enter. Lastly, we note that to measure current with the oscilloscope, the Rogowski coil has a calibration factor of 2.17 kA/V.

APPENDIX G

NONDIMENSIONALIZING THE GENERALIZED OHM'S LAW

From Sec. 6.1, we have the Generalized Ohm's Law (GOL) shown in Eq. G.1. As mentioned: for a numerical simulation to efficiently calculate equations, putting the equation variables into a dimensionless form is important, so the computer does not have to keep track of unnecessarily large or small numbers.

$$\frac{m_e}{n_e e^2}\left(\frac{\partial \mathbf{J}}{\partial t} + \nabla \cdot \left[\mathbf{uJ} + \mathbf{Ju} - \frac{1}{n_e e}\mathbf{JJ}\right]\right) = \mathbf{E} + \mathbf{u} \times \mathbf{B} - \eta \mathbf{J} - \frac{\mathbf{J} \times \mathbf{B}}{n_e e} + \frac{\nabla P_e}{n_e e} \quad \text{(G.1)}$$

A dimensional quantity Q is put in dimensionless form by writing $Q = Q_0 \tilde{Q}$ where Q_0 is a characteristic value of the quantity with dimensions, and $\tilde{Q}$ is dimensionless. Thereby, we can work with $\tilde{Q}$ in the equation. See Table G.1 for (possible) characteristic values of the quantities in the GOL. Of note: the gradient operator and time derivative have units that need to be considered, the magnetic field and velocity are related by the Alfven speed, and the pressure (energy density) can be scaled in multiple ways.

Then, dividing all quantities in Eq. G.1 by E_0 and simplifying (see Appendix A as necessary), we get the dimensionless GOL, Eq. G.2, where the tildes are dropped from the variables (meaning Q refers to $\tilde{Q}$). We see the electron inertial length is important for the electron inertia term, and the ion inertial length

Table G.1: Characteristic Values for Nondimensionalization

Description	Symbol	Characteristic Value
length	L_0	$1.0 * 10^{-3}$ m
time	t_0	$1.0 * 10^{-7}$ s
number density	n_0	$6.0 * 10^{28}$ $\#/m^3$
(Al ion) mass	m_0	$m_i = 27 * 1836 * m_e$
gradient operator	∇_0	L_0^{-1}
time derivative	$(\partial/\partial t)_0$	t_0^{-1}
velocity	u_0	L_0/t_0
magnetic field	B_0	$u_0\sqrt{m_0 n_0 \mu_0}$
electric field	E_0	$u_0 B_0$
current density	J_0	$B_0/\mu_0 L_0$
resistivity	η_0	$\mu_0 L_0^2/t_0$
pressure	P_0	$\beta B_0^2/\mu_0$ or $m_0 n_0 u_0^2$

is important for the Hall and electron pressure terms.

$$\frac{\lambda_e^2}{L_0^2}\left(\frac{\partial \mathbf{J}}{\partial t} + \nabla \cdot \left[\mathbf{uJ} + \mathbf{Ju} - \frac{\lambda_i}{n_e L_0}\mathbf{JJ}\right]\right) = n_e(\mathbf{E} + \mathbf{u} \times \mathbf{B} - \eta \mathbf{J} - \frac{\lambda_i}{n_e L_0}\mathbf{J} \times \mathbf{B} + \frac{\beta \lambda_i}{n_e L_0}\nabla P_e) \quad \text{(G.2)}$$

BIBLIOGRAPHY

[1] Bruce A. Remington, R. Paul Drake, and Dmitri D. Ryutov. Experimental astrophysics with high power lasers and Z pinches. *Reviews of Modern Physics*, 78(3):755–807, August 2006. URL: http://link.aps.org/doi/10.1103/RevModPhys.78.755, doi:10.1103/RevModPhys.78.755.

[2] D. Ryutov, R. P. Drake, J. Kane, E. Liang, B. A. Remington, and W. M. Wood-Vasey. Similarity Criteria for the Laboratory Simulation of Supernova Hydrodynamics. *The Astrophysical Journal*, 518(2), June 1999. URL: http://iopscience.iop.org/0004-637X/518/2/821, doi:10.1086/307293.

[3] D. D. Ryutov, R. P. Drake, and B. A. Remington. Criteria for Scaled Laboratory Simulations of Astrophysical MHD Phenomena. *The Astrophysical Journal Supplement Series*, 127(2), April 2000. URL: http://iopscience.iop.org/0067-0049/127/2/465, doi:10.1086/313320.

[4] D. D. Ryutov, B. A. Remington, H. F. Robey, and R. P. Drake. Magnetohydrodynamic scaling: From astrophysics to the laboratory. *Physics of Plasmas*, 8(5), 2001. URL: http://scitation.aip.org/content/aip/journal/pop/8/5/10.1063/1.1344562, doi:10.1063/1.1344562.

[5] S. Bouquet, E. Falize, C. Michaut, C.D. Gregory, B. Loupias, T. Vinci, and M. Koenig. From lasers to the universe: Scaling laws in laboratory astrophysics. *High Energy Density Physics*, 6(4):368–380, December 2010. URL: http://linkinghub.elsevier.com/retrieve/pii/S1574181810000224, doi:10.1016/j.hedp.2010.03.001.

[6] Michael D. Smith. *Astrophysical jets and beams*. Number 49 in Cambridge astrophysics. Cambridge University Press, Cambridge ; New York, 2012.

[7] R. V. E. Lovelace. Dynamo model of double radio sources. *Nature*, 262(5570):649–652, August 1976. URL: http://www.nature.com/doifinder/10.1038/262649a0, doi:10.1038/262649a0.

[8] R. V. E. Lovelace, J. C. L. Wang, and M. E. Sulkanen. Self-collimated electromagnetic jets from magnetized accretion disks. *The Astrophysical Journal*, 315:504, April 1987. URL: http://adsabs.harvard.edu/doi/10.1086/165156, doi:10.1086/165156.

[9] Richard VE Lovelace, Marina M. Romanova, Patrick Lii, and Sergei Dyda. On the origin of jets from disc-accreting magnetized stars. *Computational Astrophysics and Cosmology*, 1(1):1–10, September 2014. URL: http://link.springer.com/article/10.1186/s40668-014-0003-5, doi:10.1186/s40668-014-0003-5.

[10] Sergey V. Lebedev, editor. *High Energy Density Laboratory Astrophysics*. Springer Netherlands, Dordrecht, 2007. DOI: 10.1007/978-1-4020-6055-7. URL: http://link.springer.com/10.1007/978-1-4020-6055-7.

[11] John I. Castor. Astrophysical Radiation Dynamics: The Prospects for Scaling. *Astrophysics and Space Science*, 307(1-3):207–211, March 2007. URL: http://link.springer.com/10.1007/s10509-006-9236-3, doi:10.1007/s10509-006-9236-3.

[12] R. F. Coker, B. H. Wilde, J. M. Foster, B. E. Blue, P. A. Rosen, R. J. R. Williams, P. Hartigan, A. Frank, and C. A. Back. Numerical Simulations and Astrophysical Applications of Laboratory Jets at Omega. *Astrophysics and Space Science*, 307(1-3):57–62, March 2007. URL: http://link.springer.com/10.1007/s10509-006-9268-8, doi:10.1007/s10509-006-9268-8.

[13] Radu Presura, Stephan Neff, and Lucas Wanex. Experimental Design for the Laboratory Simulation of Magnetized Astrophysical Jets. *Astrophysics and Space Science*, 307(1-3):93–98, March 2007. URL: http://link.springer.com/10.1007/s10509-006-9286-6, doi:10.1007/s10509-006-9286-6.

[14] C. E. Seyler and M. R. Martin. Relaxation model for extended magnetohydrodynamics: Comparison to magnetohydrodynamics for dense Z-pinches. *Physics of Plasmas (1994-present)*, 18(1), January 2011. URL: http://scitation.aip.org/content/aip/journal/pop/18/1/10.1063/1.3543799, doi:10.1063/1.3543799.

[15] M Koenig, A Benuzzi-Mounaix, A Ravasio, T Vinci, N Ozaki, S Lepape, D Batani, G Huser, T Hall, D Hicks, A MacKinnon, P Patel, H S Park, T Boehly, M Borghesi, S Kar, and L Romagnani. Progress in the study of warm dense matter. *Plasma Physics and Controlled Fusion*, 47(12B):B441–B449, December 2005. URL: http://stacks.iop.org/0741-3335/47/i=12B/a=S31?key=crossref.60cd5d6fe3e344e34b0a45bdb0790b17, doi:10.1088/0741-3335/47/12B/S31.

[16] M. C. Jones, D. J. Ampleford, M. E. Cuneo, R. Hohlfelder, C. A. Jennings, D. W. Johnson, B. Jones, M. R. Lopez, J. MacArthur, J. A. Mills, T. Preston, G. A. Rochau, M. Savage, D. Spencer, D. B. Sinars, and J. L. Porter. X-ray power and yield measurements at the refurbished Z machine. *Review of Scientific Instruments*, 85(8):083501, August 2014. URL: http://aip.scitation.org/doi/10.1063/1.4891316, doi:10.1063/1.4891316.

[17] M. G. Haines. A review of the dense Z-pinch. *Plasma Physics and Controlled Fusion*, 53(9), September 2011. URL: http://iopscience.iop.org/0741-3335/53/9/093001, doi:10.1088/0741-3335/53/9/093001.

[18] Dmitri D. Ryutov. Characterizing the Plasmas of Dense Z -Pinches. *IEEE Transactions on Plasma Science*, 43(8):2363–2384, August 2015. URL: http://ieeexplore.ieee.org/document/7169570/, doi:10.1109/TPS.2015.2453265.

[19] D. D. Ryutov, M. S. Derzon, and M. K. Matzen. The physics of fast Z pinches. *Reviews of Modern Physics*, 72(1):167–223, January 2000. URL: http://link.aps.org/doi/10.1103/RevModPhys.72.167, doi:10.1103/RevModPhys.72.167.

[20] S. A. Slutz, M. C. Herrmann, R. A. Vesey, A. B. Sefkow, D. B. Sinars, D. C. Rovang, K. J. Peterson, and M. E. Cuneo. Pulsed-power-driven cylindrical liner implosions of laser preheated fuel magnetized with an axial field. *Physics of Plasmas*, 17(5):056303, May 2010. URL: http://aip.scitation.org/doi/10.1063/1.3333505, doi:10.1063/1.3333505.

[21] I. H. Mitchell, J. M. Bayley, J. P. Chittenden, J. F. Worley, A. E. Dangor, M. G. Haines, and P. Choi. A high impedance megaampere generator for fiber *z* pinch experiments. *Review of Scientific Instruments*, 67(4):1533–1541, April 1996. URL: http://aip.scitation.org/doi/10.1063/1.1146884, doi:10.1063/1.1146884.

[22] J. B. Greenly, J. D. Douglas, D. A. Hammer, B. R. Kusse, S. C. Glidden, and H. D. Sanders. A 1 MA, variable risetime pulse generator for high energy density plasma research. *Review of Scientific Instruments*, 79(7), 2008. URL: http://scitation.aip.org/content/aip/journal/rsi/79/7/10.1063/1.2949819, doi:10.1063/1.2949819.

[23] D. J. Ampleford, S. V. Lebedev, A. Ciardi, S. N. Bland, S. C. Bott,

J. P. Chittenden, G. Hall, C. A. Jennings, J. Armitage, G. Blyth, S. Christie, and L. Rutland. Formation of Working Surfaces in Radiatively Cooled Laboratory Jets. *Astrophysics and Space Science*, 298(1-2):241–246, July 2005. URL: http://link.springer.com/article/10.1007/s10509-005-3941-1, doi:10.1007/s10509-005-3941-1.

[24] D. Ampleford, S. Lebedev, A. Ciardi, S. Bland, S. Bott, G. Hall, N. Naz, C. Jennings, M. Sherlock, J. Chittenden, J. Palmer, A. Frank, and E. Blackman. Supersonic Radiatively Cooled Rotating Flows and Jets in the Laboratory. *Physical Review Letters*, 100(3), January 2008. URL: http://link.aps.org/doi/10.1103/PhysRevLett.100.035001, doi:10.1103/PhysRevLett.100.035001.

[25] Tom Byvank, Peter Schrafel, Pierre Gourdain, Charles Seyler, and Bruce Kusse. Plasma jets subject to adjustable current polarities and external magnetic fields. In *AIP Conference Proceedings*, volume 1639, pages 84–87. AIP Publishing, December 2014. URL: http://scitation.aip.org/content/aip/proceeding/aipcp/10.1063/1.4904783, doi:10.1063/1.4904783.

[26] T. Byvank, J. Chang, W. M. Potter, C. E. Seyler, and B. R. Kusse. Extended Magnetohydrodynamic Plasma Jets With External Magnetic Fields. *IEEE Transactions on Plasma Science*, 44(4):638–642, April 2016. URL: http://ieeexplore.ieee.org/document/7416619/, doi:10.1109/TPS.2016.2530634.

[27] T. Byvank, J. T. Banasek, W. M. Potter, J. B. Greenly, C. E. Seyler, and B. R. Kusse. Applied axial magnetic field effects on laboratory plasma jets: Density hollowing, field compression, and azimuthal rotation. *Physics of Plasmas*, 24(12):122701, December 2017. URL: http://aip.scitation.org/doi/10.1063/1.5003777, doi:10.1063/1.5003777.

[28] A. Ciardi, S. V. Lebedev, A. Frank, E. G. Blackman, D. J. Ampleford, C. A. Jennings, J. P. Chittenden, T. Lery, S. N. Bland, S. C. Bott, G. N. Hall, J. Rapley, F. A. Suzuki Vidal, and A. Marocchino. 3d MHD Simulations of Laboratory Plasma Jets. *Astrophysics and Space Science*, 307(1-3):17–22, March 2007. URL: http://link.springer.com/10.1007/s10509-006-9215-8, doi:10.1007/s10509-006-9215-8.

[29] Andrea Ciardi, Sergey V. Lebedev, Adam Frank, Francisco Suzuki-Vidal, Gareth N. Hall, Simon N. Bland, Adam Harvey-Thompson, Eric G. Blackman, and Max Camenzind. Episodic magnetic bubbles and jets: astrophysical implications from laboratory exper-

iments. *The Astrophysical Journal*, 691(2):L147–L150, February 2009. URL: http://stacks.iop.org/1538-4357/691/i=2/a=L147?key=crossref.a7512e58d0fdb7fd2cf5b38fa6c58aa3, doi:10.1088/0004-637X/691/2/L147.

[30] P.-A. Gourdain, I. C. Blesener, J. B. Greenly, D. A. Hammer, P. F. Knapp, B. R. Kusse, and P. C. Schrafel. Initial experiments using radial foils on the Cornell Beam Research Accelerator pulsed power generator. *Physics of Plasmas*, 17(1), 2010. URL: http://scitation.aip.org/content/aip/journal/pop/17/1/10.1063/1.3292653, doi:10.1063/1.3292653.

[31] P. A. Gourdain, I. C. Blesener, J. B. Greenly, D. A. Hammer, P. F. Knapp, B. R. Kusse, S. A. Pikuz, and T. C. Shelkovenko. High energy density plasmas generated by radial foil explosions. *Plasma Physics and Controlled Fusion*, 52(5), 2010. URL: http://iopscience.iop.org/0741-3335/52/5/055015.

[32] P.A. Gourdain, J.B. Greenly, D.A. Hammer, P.F. Knapp, B.R. Kusse, S.A. Pikuz, P.C. Schrafel, and T.C. Shelkovenko. The Impact of Cathode Diameter on Radial Foil Explosions. *IEEE Transactions on Plasma Science*, 38(12):3363–3369, December 2010. doi:10.1109/TPS.2010.2083696.

[33] P.-A. Gourdain, J. B. Greenly, D. A. Hammer, B. R. Kusse, S. A. Pikuz, C. E. Seyler, T. C. Shelkovenko, and P. F. Knapp. Magnetohydrodynamic instabilities in radial foil configurations. *Physics of Plasmas (1994-present)*, 19(2), February 2012. URL: http://scitation.aip.org/content/aip/journal/pop/19/2/10.1063/1.3677887, doi:10.1063/1.3677887.

[34] P.-A. Gourdain and C. E. Seyler. Impact of the Hall Effect on High-Energy-Density Plasma Jets. *Physical Review Letters*, 110(1), January 2013. URL: http://link.aps.org/doi/10.1103/PhysRevLett.110.015002, doi:10.1103/PhysRevLett.110.015002.

[35] P.-A. Gourdain, C. E. Seyler, L. Atoyan, J. B. Greenly, D. A. Hammer, B. R. Kusse, S. A. Pikuz, W. M. Potter, P. C. Schrafel, and T. A. Shelkovenko. The impact of Hall physics on magnetized high energy density plasma jets. *Physics of Plasmas (1994-present)*, 21(5), May 2014. URL: http://scitation.aip.org/content/aip/journal/pop/21/5/10.1063/1.4872022, doi:10.1063/1.4872022.

[36] P.-A. Gourdain and C. E. Seyler. Modeling of strongly colli-

mated jets produced by high energy density plasmas on COBRA. *Plasma Physics and Controlled Fusion*, 56(3), March 2014. URL: http://iopscience.iop.org/0741-3335/56/3/035002, doi:10.1088/0741-3335/56/3/035002.

[37] S. V. Lebedev, J. P. Chittenden, F. N. Beg, S. N. Bland, A. Ciardi, D. Ampleford, S. Hughes, M. G. Haines, A. Frank, E. G. Blackman, and T. Gardiner. Laboratory Astrophysics and Collimated Stellar Outflows: The Production of Radiatively Cooled Hypersonic Plasma Jets. *The Astrophysical Journal*, 564(1):113–119, January 2002. URL: http://stacks.iop.org/0004-637X/564/i=1/a=113, doi:10.1086/324183.

[38] S. V. Lebedev, D. Ampleford, A. Ciardi, S. N. Bland, J. P. Chittenden, M. G. Haines, A. Frank, E. G. Blackman, and A. Cunningham. Jet Deflection via Crosswinds: Laboratory Astrophysical Studies. *The Astrophysical Journal*, 616(2), December 2004. URL: http://iopscience.iop.org/0004-637X/616/2/988, doi:10.1086/423730.

[39] S V Lebedev, A Ciardi, D J Ampleford, S N Bland, S C Bott, J P Chittenden, G N Hall, J Rapley, C Jennings, M Sherlock, A Frank, and E G Blackman. Production of radiatively cooled hypersonic plasma jets and links to astrophysical jets. *Plasma Physics and Controlled Fusion*, 47(12B):B465–B479, December 2005. URL: http://stacks.iop.org/0741-3335/47/i=12B/a=S33?key=crossref.3ccd52594e540b9c26ea4fdc920f2d0a, doi:10.1088/0741-3335/47/12B/S33.

[40] Peter Schrafel, Kate Bell, John Greenly, Charles Seyler, and Bruce Kusse. Magnetized laboratory plasma jets: Experiment and simulation. *Physical Review E*, 91(1), January 2015. URL: http://link.aps.org/doi/10.1103/PhysRevE.91.013110, doi:10.1103/PhysRevE.91.013110.

[41] F. Suzuki-Vidal, S. V. Lebedev, A. Ciardi, S. N. Bland, J. P. Chittenden, G. N. Hall, A. Harvey-Thompson, A. Marocchino, C. Ning, C. Stehle, A. Frank, E. G. Blackman, S. C. Bott, and T. Ray. Formation of episodic magnetically driven radiatively cooled plasma jets in the laboratory. *Astrophysics and Space Science*, 322(1-4):19–23, August 2009. URL: http://link.springer.com/10.1007/s10509-009-9981-1, doi:10.1007/s10509-009-9981-1.

[42] Francisco Suzuki-Vidal, Sergey V Lebedev, Simon N Bland, Gareth N Hall, Adam J Harvey-Thompson, Jeremy P Chittenden, Alberto Marocchino, Simon C Bott, James Palmer, and Andrea Ciardi. Effect of Wire

Diameter and Addition of an Axial Magnetic Field on the Dynamics of Radial Wire Array Z-Pinches. *IEEE Transactions on Plasma Science*, 38(4):581–588, April 2010. URL: http://ieeexplore.ieee.org/lpdocs/epic03/wrapper.htm?arnumber=5382586, doi:10.1109/TPS.2009.2036730.

[43] F. Suzuki-Vidal, S. V. Lebedev, M. Bocchi, M. Krishnan, G. Swadling, G. Burdiak, S. N. Bland, P. de Grouchy, G. N. Hall, A. J. Harvey-Thompson, E. Khoory, L. Pickworth, J. Skidmore, J. P. Chittenden, K. Wilson-Elliot, R. Madden, and A. Ciardi. Experimental study of shock waves from the interaction of a supersonic plasma jet with an ambient gas. *Shock Waves*, 22(3):249–251, May 2012. URL: http://link.springer.com/10.1007/s00193-012-0360-4, doi:10.1007/s00193-012-0360-4.

[44] F. Suzuki-Vidal, M. Bocchi, S. V. Lebedev, G. F. Swadling, G. Burdiak, S. N. Bland, P. de Grouchy, G. N. Hall, A. J. Harvey-Thompson, E. Khoory, S. Patankar, L. Pickworth, J. Skidmore, R. Smith, J. P. Chittenden, M. Krishnan, R. E. Madden, K. Wilson-Elliot, A. Ciardi, and A. Frank. Interaction of a supersonic, radiatively cooled plasma jet with an ambient medium. *Physics of Plasmas*, 19(2), 2012. URL: http://scitation.aip.org/content/aip/journal/pop/19/2/10.1063/1.3685607, doi:10.1063/1.3685607.

[45] F. Suzuki-Vidal, M. Bocchi, S.V. Lebedev, J. Skidmore, G. Swadling, G. Burdiak, A.J. Harvey-Thompson, P. de Grouchy, S.N. Bland, G.N. Hall, E. Khoory, L. Pickworth, L. Suttle, J.P. Chittenden, M. Krishnan, K. Wilson-Elliot, R. Madden, A. Ciardi, and A. Frank. Jet-ambient interaction of a supersonic, radiatively-cooled jet in laboratory experiments. *EAS Publications Series*, 58:127–131, 2012. URL: http://www.eas-journal.org/10.1051/eas/1258020, doi:10.1051/eas/1258020.

[46] F Suzuki-Vidal, S V Lebedev, M Krishnan, M Bocchi, J Skidmore, G Swadling, A J Harvey-Thompson, G Burdiak, P de Grouchy, L Pickworth, L Suttle, S N Bland, J P Chittenden, G N Hall, E Khoory, K Wilson-Elliot, R E Madden, A Ciardi, and A Frank. Laboratory astrophysics experiments studying hydrodynamic and magnetically-driven plasma jets. *Journal of Physics: Conference Series*, 370, June 2012. URL: http://stacks.iop.org/1742-6596/370/i=1/a=012002?key=crossref.441cb480ab4a01d4242d138a264779a1, doi:10.1088/1742-6596/370/1/012002.

[47] F. Suzuki-Vidal, S.V. Lebedev, M. Krishnan, J. Skidmore, G.F. Swadling, M. Bocchi, A.J. Harvey-Thompson, S. Patankar, G.C. Burdiak,

P. de Grouchy, L. Pickworth, S.J.P. Stafford, L. Suttle, M. Bennett, S.N. Bland, J.P. Chittenden, G.N. Hall, E. Khoory, R.A. Smith, A. Ciardi, A. Frank, R.E. Madden, K. Wilson-Elliot, and P. Coleman. Interaction of radiatively cooled plasma jets with neutral gases for laboratory astrophysics studies. *High Energy Density Physics*, 9(1):141–147, March 2013. URL: http://linkinghub.elsevier.com/retrieve/pii/S1574181812001292, doi:10.1016/j.hedp.2012.11.003.

[48] H Bluhm. *Pulsed Power Systems*. Power Systems. Springer-Verlag, Berlin/Heidelberg, 2006. DOI: 10.1007/3-540-34662-7. URL: http://link.springer.com/10.1007/3-540-34662-7.

[49] Isaac Blesener. *Initiation, Ablation, Precursor Formation, And Instability Analysis Of Thin Foil Liner Z-Pinches*. PhD thesis, Cornell, Ithaca, NY, 2012. URL: http://hdl.handle.net/1813/31212.

[50] Kate Blesener. *Spectroscopic Determinations Of Magnetic Fields, Electron Temperatures, And Electron Densities In Single Wire Aluminum Plasmas*. PhD thesis, Cornell, Ithaca, NY, 2012. URL: http://hdl.handle.net/1813/31222.

[51] Adam Cahill. *An Investigation Of The Aluminum K-Edge By Spatially Resolved X-Ray Absorption Spectroscopy*. PhD thesis, Cornell, Ithaca, NY, 2016. URL: http://hdl.handle.net/1813/44264.

[52] David Chalenski. *A Parametric Study Of Polarity, Contact And Current Risetime Effects On Wire Array Z-Pinches*. PhD thesis, Cornell, Ithaca, NY, 2010. URL: http://hdl.handle.net/1813/14883.

[53] Jonathan Douglass. *An Experimental Study of Tungsten Wire-Array Z-Pinch Plasmas Using Time-Gated Point-Projection X-Ray Imaging*. PhD thesis, Cornell, Ithaca, NY, 2008. URL: http://hdl.handle.net/1813/10891.

[54] Cad Hoyt. *Noncollective X-Ray Thomson Scattering Diagnostic Development Based On A Titanium Hybrid X-Pinch X-Ray Source*. PhD thesis, Cornell, Ithaca, NY, 2015. URL: http://hdl.handle.net/1813/40611.

[55] Patrick Knapp. *Investigation Of Conditions In Closely Spaced Parallel Exploding Aluminum Wires Using Point Projection X-Ray Absorption Spectroscopy*. PhD thesis, Cornell, Ithaca, NY, 2011. URL: http://hdl.handle.net/1813/30771.

[56] Ryan McBride. *Implosion Dynamics, Radiation Characteristics, And Spectroscopic Measurements Of Wire-Array Z-Pinches On The COrnell Beam Research Accelerator (COBRA)*. PhD thesis, Cornell, Ithaca, NY, 2008. URL: http://hdl.handle.net/1813/11578.

[57] Peter Schrafel. *Magnetized Plasma Jets In Experiment And Simulation*. PhD thesis, Cornell, Ithaca, NY, 2014. URL: http://hdl.handle.net/1813/38899.

[58] Milton Ohring. *Materials science of thin films: deposition and structure*. Academic Press, San Diego, CA, 2nd ed edition, 2002.

[59] John Greenly, Matthew Martin, Isaac Blesener, David Chalenski, Patrick Knapp, Ryan McBride, Bruce R. Kusse, and David A. Hammer. The Role of Flux Advection in the Development of the Ablation Streams and Precursors of Wire Array Z-pinches. pages 53–56. AIP, 2009. URL: http://aip.scitation.org/doi/abs/10.1063/1.3079752, doi:10.1063/1.3079752.

[60] I. H. Hutchinson. *Principles of Plasma Diagnostics*. Cambridge University Press, Cambridge, 2 edition, 2002. DOI: 10.1017/CBO9780511613630. URL: http://ebooks.cambridge.org/ref/id/CBO9780511613630.

[61] S. A. Pikuz, V. M. Romanova, N. V. Baryshnikov, Min Hu, B. R. Kusse, D. B. Sinars, T. A. Shelkovenko, and D. A. Hammer. A simple air wedge shearing interferometer for studying exploding wires. *Review of Scientific Instruments*, 72(1):1098–1100, January 2001. URL: http://aip.scitation.org/doi/10.1063/1.1321746, doi:10.1063/1.1321746.

[62] John Sheffield, Dustin Froula, Siegfried H Glenzer, and Neville C Luhmann, Jr. *Plasma scattering of electromagnetic radiation: experiment, theory and computation*. Elsevier, Amsterdam ; Boston, 2011.

[63] Matthew Martin. *Generalized Ohm's Law At The Plasma-Vacuum Interface*. PhD thesis, Cornell, Ithaca, NY, 2010. URL: http://hdl.handle.net/1813/17095.

[64] Xuan Zhao, Yang Yang, and Charles E. Seyler. A positivity-preserving semi-implicit discontinuous Galerkin scheme for solving extended magnetohydrodynamics equations. *Journal of Computational Physics*, 278:400–415, December 2014. URL: http://linkinghub.elsevier.com/retrieve/pii/S0021999114006202, doi:10.1016/j.jcp.2014.08.044.

[65] M. P. Desjarlais, J. D. Kress, and L. A. Collins. Electrical conductivity for warm, dense aluminum plasmas and liquids. *Physical Review E*, 66(2), August 2002. URL: https://link.aps.org/doi/10.1103/PhysRevE.66.025401, doi:10.1103/PhysRevE.66.025401.

[66] M. Desjarlais. *QMD Simulations of Warm Dense Matter in Support of High Energy Density Physics Experiments on the Z Machine*. Pleasanton, CA, USA, February 2006. URL: http://hifweb.lbl.gov/public/AcceleratorWDM/proceedings/1.Wednesday.Feb.22/pm01.15.M.Desjarlais.pdf.

[67] V. Morel, A. Bultel, and B. G. Chron. The Critical Temperature of Aluminum. *International Journal of Thermophysics*, 30(6):1853–1863, December 2009. URL: http://link.springer.com/10.1007/s10765-009-0671-6, doi:10.1007/s10765-009-0671-6.

[68] Aaron Ward. *Investigation of Aluminum Equation of State Generation*. PhD thesis, Marquette, Milwaukee, WI, 2011. URL: http://epublications.marquette.edu/theses_open/124/.

[69] M. G. Haines. Thermal Instability and Magnetic Field Generated by Large Heat Flow in a Plasma, Especially under Laser-Fusion Conditions. *Physical Review Letters*, 47(13):917–920, September 1981. URL: https://link.aps.org/doi/10.1103/PhysRevLett.47.917, doi:10.1103/PhysRevLett.47.917.

[70] V. I. Oreshkin. Thermal instability during an electrical wire explosion. *Physics of Plasmas*, 15(9):092103, September 2008. URL: http://aip.scitation.org/doi/10.1063/1.2966121, doi:10.1063/1.2966121.

[71] Kyle J. Peterson, Daniel B. Sinars, Edmund P. Yu, Mark C. Herrmann, Michael E. Cuneo, Stephen A. Slutz, Ian C. Smith, Briggs W. Atherton, Marcus D. Knudson, and Charles Nakhleh. Electrothermal instability growth in magnetically driven pulsed power liners. *Physics of Plasmas*, 19(9):092701, September 2012. URL: http://aip.scitation.org/doi/10.1063/1.4751868, doi:10.1063/1.4751868.

[72] T. J. Awe, E. P. Yu, K. C. Yates, W. G. Yelton, B. S. Bauer, T. M. Hutchinson, S. Fuelling, and B. B. Mckenzie. On the Evolution From Micrometer-Scale Inhomogeneity to Global Overheated Structure During the Intense Joule Heating of a z-Pinch Rod. *IEEE Transactions on Plasma Science*, 45(4):584–

589, April 2017. URL: http://ieeexplore.ieee.org/document/7859463/, doi:10.1109/TPS.2017.2655450.

[73] J. D Huba. *2016 plasma formulary: handbook of data and tables for plasma physics and engineering*. Wexford Press, Washington DC: Naval Research Laboratory, 2016. URL: https://www.nrl.navy.mil/ppd/content/nrl-plasma-formulary.

[74] S. I. Braginskii. Transport Processes in a Plasma. *Reviews of Plasma Physics*, 1, 1965. URL: http://adsabs.harvard.edu/abs/1965RvPP....1..205B.

[75] E. M. Epperlein. The accuracy of Braginskii's transport coefficients for a Lorentz plasma. *Journal of Physics D: Applied Physics*, 17(9), September 1984. URL: http://iopscience.iop.org/0022-3727/17/9/007, doi:10.1088/0022-3727/17/9/007.

[76] M G Haines. Heat flux effects in Ohm's law. *Plasma Physics and Controlled Fusion*, 28(11):1705–1716, November 1986. URL: http://stacks.iop.org/0741-3335/28/i=11/a=007?key=crossref.a0b5555b45e232ee7d94e49cd9ced230, doi:10.1088/0741-3335/28/11/007.

[77] J. T. Banasek, T. Byvank, S. V. R. Rocco, W. M. Potter, B. R. Kusse, and D. A. Hammer. Time-Resolved Thomson Scattering on Laboratory Plasma Jets. *IEEE Transactions on Plasma Science*, 2018. Submitted.

[78] T. Byvank, N. Hamlin, L. Atoyan, C. E. Seyler, and B. R. Kusse. Plasma Jet Disruption from a Critical Applied Uniform Axial Magnetic Field. *Physics of Plasmas*, 2018. Not yet submitted.

[79] B. Albertazzi, J. Bard, A. Ciardi, T. Vinci, J. Albrecht, J. Billette, T. Burris-Mog, S. N. Chen, D. Da Silva, S. Dittrich, T. Herrmannsdrfer, B. Hirardin, F. Kroll, M. Nakatsutsumi, S. Nitsche, C. Riconda, L. Romagnagni, H.-P. Schlenvoigt, S. Simond, E. Veuillot, T. E. Cowan, O. Portugall, H. Ppin, and J. Fuchs. Production of large volume, strongly magnetized laser-produced plasmas by use of pulsed external magnetic fields. *Review of Scientific Instruments*, 84(4), 2013. URL: http://scitation.aip.org/content/aip/journal/rsi/84/4/10.1063/1.4795551, doi:10.1063/1.4795551.

[80] B. Albertazzi, A. Ciardi, M. Nakatsutsumi, T. Vinci, J. Beard, R. Bonito, J. Billette, M. Borghesi, Z. Burkley, S. N. Chen, T. E. Cowan, T. Herrmanns-

dorfer, D. P. Higginson, F. Kroll, S. A. Pikuz, K. Naughton, L. Romagnani, C. Riconda, G. Revet, R. Riquier, H.-P. Schlenvoigt, I. Y. Skobelev, A. Y. Faenov, A. Soloviev, M. Huarte-Espinosa, A. Frank, O. Portugall, H. Pepin, and J. Fuchs. Laboratory formation of a scaled protostellar jet by coaligned poloidal magnetic field. *Science*, 346(6207):325–328, October 2014. URL: http://www.sciencemag.org/cgi/doi/10.1126/science.1259694, doi:10.1126/science.1259694.

[81] G. T. Dyos and T. Farrell, editors. *Electrical resistivity handbook*. Number 10 in IEE materials & devices series. Peter Peregrinus on behalf of the Institution of Electrical Engineers, London, U.K, 1992.

[82] T. Byvank, N. Hamlin, L. Atoyan, C. E. Seyler, and B. R. Kusse. External Magnetic Field Effects on Ablation of Current-Driven Foils Using an Extended Magnetohydrodynamics Simulation. *IEEE Transactions on Plasma Science*, 2018. Submitted.

[83] Francis Chen. *Introduction to Plasma Physics and Controlled Fusion*. Springer International Publishing, Cham, 2016. DOI: 10.1007/978-3-319-22309-4. URL: http://link.springer.com/10.1007/978-3-319-22309-4.

[84] Paul Murray Bellan. *Fundamentals of Plasma Physics*. Cambridge Univ. Press, Cambridge, 2008. OCLC: 227031861.